DEVELOPMENT OF THERMOPLASTIC 3D PRINTING FEEDSTOCK UTILISING BIOMASS

A Thesis submitted by

Xianglian Xiao, MSc

For the award of

Doctor of Philosophy

2020

Abstract

3D printing feedstock constituted by bio-based thermoplastic and biomass filler is increasingly gaining prominence for fused deposition modelling (FDM). Biomass fillers are abundantly available and sustainable resources, which are widely applied in biocomposites for producing cost-effective and sustainable materials. The incorporation of biomass filler in bio-based and biodegradable polylactide (PLA) has obtained considerable attention for FDM 3D printing application.

In this thesis, hemp hurd (HH), the waste product of hemp fibre industry, and bamboo powder (BP), the waste product of bamboo-pole slicing and bamboo-plank sanding, were used as biomass fillers for the preparation of FDM feedstock by melt-compounding and extrusion. Due to the toughness decrease with the inclusion of biomass powder, the toughening modification of PLA biocomposites was investigated using poly(butylene adipate-co-terephthalate, PBAT) combined with ethylene-methyl acrylate-glycidyl methacrylate random terpolymer (EGMA), a commercially-available core-shell acrylic impact modifier (BPM520), and polycaprolactone (PCL). The toughening efficacy was compared in PLA/BP biocomposite, and the processability and printability of the toughened biocomposites were examined. PDLA-PCL-PDLA (PCDL) tri-block copolymers were investigated as compatibilizers for addressing the phase-separation of PLA/PCL blend and enhancing the toughness of PLA/BP/PCL biocomposite. The optimal toughening agent PBAT/EGMA was used for studying the effects of the biomass powder loading levels and particle sizes on PLA/HH and PLA/BP biocomposites as FDM feedstock. The melt flow, rheological, thermo-mechanical, and mechanical properties of biocomposite pellets, filament quality, and finish quality of FDM-printed parts were systematically investigated.

The key findings of this research include understanding the relationship between toughness enhancement, loading levels and particle size distributions of HH and BP biomass species, and a major range of properties of PLA biocomposites, including melt flow, rheological, thermo-mechanical, and mechanical properties of biocomposite pellets, filament quality, and finish quality of FDM-printed parts, and the associated mechanisms. Also, PLA/HH and PLA/BP feedstocks were developed and appropriately applied in FDM 3D printing.

Experimental results showed that PLA/BP biocomposite toughened by PBAT/EGMA exhibited higher toughness, superior filament quality, improved processability, and lower surface roughness than BPM520-toughened feedstock, and enhanced toughness than commercial PLA feedstock for both FDM-printed and injection-moulded (IM) specimens. PCDL efficiently improved the compatibility between PLA and PCL, leading to improved toughness. The increment in the toughness of PLA/BP biocomposite using PCL as toughening agent and PCDL as compatibilizer was insignificant. Among the three toughening agents, PBAT/EGMA was optimum with respect to toughness enhancement and processability, together with printability. Increasing biomass loading levels resulted in increased complex viscosity and decreased melt flow, while the FDM filament retained diameter tolerance (within ±0.03 mm) and roundness (0.04 mm) meeting the requirement in GB/T 37643-2019 standard. IM specimens filled with 40 phr HH exhibited 10.8% increase in tensile strength, 12% increase in flexural strength, 62.5% increase in flexural modulus, whereas 38.5% decrease in impact strength, compared to the base polymer matrix. FDM-printed parts with up to 30 phr HH or BP incorporation showed higher impact toughness than the parts fabricated from the commercial PLA filament control (46±2.5 J/m). Also, the FDM-printed parts exhibited greater dimensional accuracy (decreased shrinkage) than the samples from PLA control. The shrinkage of all PLA/HH samples was lower than that of PLA (0.33±0.04 %) and decreased from 0.30±0.06 % (PLA-HH-0) to 0.03±0.01 % (PLA-HH-40), indicating the dimensional accuracy improved with increasing HH loading. The porosity increased from 5.8% for PLA-HH-0 to 17.9% for PLA-HH-40, and 16.9% for PLA-BP-40. The increase in biomass loading levels and particle sizes did not change the average surface roughness (R_a and R_q) when the particle size of biomass was smaller than the printing layer thickness, while increased the peak-to-valley height (R_z and R_{max}) of FDM-printed parts. HH and BP particle sizes exhibited opposite effects on the melt flow and complex viscosity ($|\eta^*|$) at low frequency, increased particle size led to increased MFR and decreased $|\eta^*|$ for PLA/HH while decreased MFR and increased $|\eta^*|$ for PLA/BP biocomposites. Larger particle size was advantageous for obtaining higher impact strength for both IM and FDM-printed specimens for both PLA/HH and PLA/BP. The impact strength was improved from 41.3±3.0 J/m to 54.4±4.3 J/m for PLA/HH biocomposites. Impact strength was retained at around 55

J/m for FDM parts although the porosity increased from 4.86% to 9.85%, with concomitant particle size increase from 35 to 160 μm. PLA-BP-3 exhibited an impact strength of 13% and 38% higher than PLA-BP-1 for IM and FDM parts, respectively.

This thesis contributes to the utilization of biomass filler in 3D printing for obtaining renewable and sustainable feedstock. This research reinforces the understanding of the influence of toughening modification, biomass filler contents, and particle size distributions on the melt flow, mechanical properties, processability, and printability of PLA biocomposites, and the underlying mechanisms. The potential of producing PLA biocomposites and application in FDM are investigated, the future work is discussed.

Thesis certification

This thesis is entirely the work of **Xianglian Xiao** except where otherwise acknowledged. The work is original and has not previously submitted for any other award, except where acknowledged.

Principal Supervisor: Hao Wang

Associate Supervisor: Venkata S. Chevali

Student and supervisors' signature of endorsement is held at the University.

Acknowledgements

I would like to thank my principal supervisor, Prof. Hao Wang, for offering me the opportunity to earn my doctorate and great support throughout this research. This work would never be completed without his guidance and encouragement. I also thank Dr. Venkata S. Chevali and Prof. Pingan Song, gave many discussions on the project, and reviewed the work throughout the process. I appreciate that Dr. Yihu Yang provided experimental equipment at Shenzhen Esun Industrial Co., Ltd and resources used in this project. Thanks for the assistance from Prof. Zhanhui Zhang on SEM characterization, the assistance from Dr. Jianying Wang and Dr. Tonghui Hao on rheology determination. Dr. Dongning He helped me on the characterization of the particle size distribution of biomass powder. In addition, many thanks to Dr. Fengmei Cheng, Dr. Man Xi, Prof. Xiaoming Liu, Prof. Chuncheng Zuo, Dr. Bo Xing, Mr. Jiabing Feng, Dr. Weidi Liu, Mr. Feng Wang, Dr. Zhiguang Xu, Dr. Friederike Susette Eberhard, Mr. Chengliang Dong, Mr. Hao Yuan, Wayne Crowell, Martin Geach, Mohan Trada, Adrian Blokland, and Ms. Yanru Wang for their support on this journey.

The scholarship support of USQ Postgraduate Research Scholarship (USQ PRS) is acknowledged. The Forest and Wood Products Australia [Grant No. PNA360-1516] and the financial support from China-Australia Institute for Advanced Materials and Manufacturing in Jiaxing University [Grant No. 701170120] are also acknowledged.

I thank my family, my husband, my daughter, my parents, my brothers, and my sisters, for their love, understanding, support, and encouragement on the way of pursuing this degree.

Lastly, I would like to thank my colleagues, friends, and everyone who shared their time and knowledge in the completion of this thesis.

Publications

Journals

X. Xiao, V. S. Chevali, P. Song, D. He, H. Wang 2019, 'Polylactide/hemp hurd biocomposites as sustainable 3D printing feedstock', Composites Science and Technology, p.107887.

X. Xiao, V. S. Chevali, P. Song, B. Yu, Y. Yang, H. Wang 2020, 'Enhanced toughness of PLLA/PCL blends using poly(d-lactide)-poly(ε-caprolactone)-poly(d-lactide) as compatibilizer', Composites communication, p100385.

X. Xiao, V. S. Chevali, P. Song, J. Feng, H. Wang, Rheological, mechanical, and surface properties of polylactide/hemp hurd biocomposite for 3D printing: hemp hurd particle size. (In submission)

X. Xiao, V. S. Chevali, P. Song, H. Wang, Polylactide/bamboo powder biocomposite for 3D printing: Effect of bamboo powder content and particle size. (In progress)

Conference proceedings

X. Xiao, V. S. Chevali, H. Wang 2019, 'Toughening of polylactide/bamboo powder biocomposite for 3D printing', In ICCM 22 conference proceedings; Melbourne, Australia.

Table of Contents

List of Figures

List of Tables

List of Abbreviations

3D	Three-dimensional
3DP	Three-dimensional Printing
ABS	Acrylonitrile-butadiene-styrene
ACR	Acrylic impact modifiers
AM	Additive manufacturing
BF	Bamboo fibre
BP	Bamboo powder
CT	X-ray computer tomography
d_{10}	Particle size at 10% undersize
d_{50}	Volume-median-diameter/Particle size at 50% undersize
d_{90}	Particle size at 90% undersize
DSC	Differential scanning calorimetry
DTG	Derivative thermogravimetric
ε_b	Elongation-at-break
EBM	Electron beam melting
EBS	Ethylene bis stearamide
EGMA	Ethylene-methyl acrylate-glycidyl methacrylate random terpolymer
$\lvert\eta^*\rvert$	Complex viscosity
FDM	Fused Deposition Modelling
FTIR	Fourier transform infrared
G'	Storage modulus
G''	Loss modulus
GMA	Glycidyl methacrylate
GPC	Gel permeation chromatography
ΔH_{cc}	Crystallization enthalpy
ΔH_m	Melting enthalpy
HH	Hemp hurd
HNMR	H nuclear magnetic resonance
IM	Injection-moulded
l/d	Aspect ratio

L/D	Length/Diameter
LENS	Laser engineered net shaping
LDI	Lysine-based diisocyante
LOM	Laminated object manufacturing
$\bar{M}_n$	Number-averaged molecular weight
$\overline{M}_\eta$	Viscosity-average molecular weight
M_p	Peak molecular weight
$\bar{M}_w$	Weight-averaged molecular weight
MAH	Maleic anhydride
MDI	Methylene diphenyl diisocyanate
MFR	Melt flow rate
MNC	Micro/Nanocellulose
PBAT	Poly (butylene adipate-co-terephthalate)
PCL	Polycaprolactone
PDI	Polydispersity index
PDLA	Poly (D-lactic acid)
PEAA	Poly(ethylene–acrylic acid) copolymer
PEG	Polyethylene glycol
PHAs	Polyhydroxyalkanoates
PLA	Polylactide/Polylactic acid
PLLA	Poly (L-lactic acid)
PLA-g-MAH	Maleic anhydride-grafted poly(lactic acid)
POE	Polyolefin elastomer
ppm	Parts per million
R_a	Arithmetic mean roughness
R_q	Root mean square roughness
R_z	Mean peak-to-valley height
R_{max}	Maximum peak-to-valley height
RPM	Round per minute
SEM	Scanning electron microscopy
SLA/SL	Stereolithography
SLS	Selective Laser Sintering

STL	Stereolithographic file
Tan δ	Loss factor
TGA	Thermogravimetric analysis
T_5	Temperature at 5% weight loss
T_{50}	Temperature at 50% weight loss
T_g	Glass transition temperature
T_m	Melting temperature
T_{max}	Temperature of the maximum mass loss rate/Maximum thermal degradation temperature
T_{onset}	Weight loss onset temperature/Onset degradation temperature
TPU	Thermoplastic polyurethane
TS	Tensile strength
UV	Ultraviolet
WF	Wood powder/wood flour
X_c	Degree of crystallinity
XRD	X-ray diffraction

Chapter 1: Introduction

3D printing is an additive manufacturing (AM) technology widely used in numerous fields. 3D printing technology has advantages in designing and construction of complex geometries with a problem to produce by traditional techniques [1], and benefits of flexible design, mass production, low amount of waste while with desired geometric accuracy [2], rapid and cost-effective fabrication, and automation [3]. Among the 3D printing technologies categorized by the deposition principles, fused deposition modelling (FDM) has gained prominence because of its cost-effectiveness in the fabrication of 3D parts with high resolution [4-6]. The feedstock for FDM are thermoplastics, among which acrylonitrile-butadiene-styrene (ABS) and polylactide (PLA) are prevalent [7]. Because of less warping, less cracking, less odour, and lower printing temperature, PLA is often the foremost choice for FDM feedstock.

The utilization of biomass powder in FDM feedstock as filler offers reduced carbon footprint, economical value, and aesthetics of wood. However, the challenges of biomass powder addition to PLA matrix to produce PLA biocomposite feedstock for FDM are the decreased melt flow and increased viscosity [8-14], decreased toughness [8, 9, 12, 15-21], decreased surface quality [22], and inadequate melt strength compared to the matrix without biomass powder, hence causing inconsistent diameter and roundness for filament. These changes in properties of PLA biocomposite and filament quality cause decreases in processability and printability for PLA biocomposite, and interruptions occur during filament manufacturing and FDM printing. Therefore, a modification for PLA biocomposite is often required, especially improvement for toughness. The comprehensive properties of PLA biocomposites are dependent on the amount and particle size distribution of biomass powder in the formulations, which requires systematic investigation.

The objective of this research was to develop PLA biocomposites using hemp hurd (HH) and bamboo powder (BP) as biomass fillers to reduce the cost of materials through melt-compounding and extrusion. The obtained PLA biocomposites were aimed to be used in FDM 3D printing. To address the toughness issue brought about by the inclusion of biomass filler, the toughening modification of PLA biocomposites was investigated before the systematic study of the relationship between the loading levels and particle size distributions of the biomass powder, and the overall

properties of PLA biocomposites. HH and BP with various particle size distributions were analysed in detail before utilization in the biocomposite. The characterization of melt rheology of PLA biocomposites, filament quality, thermal and mechanical properties, and finish quality of FDM-printed products were conducted. A comparison between the biocomposites and the PLA control was performed to determine the applicability of the biocomposites as FDM feedstock.

This thesis consists of 9 chapters. Chapter 1: Introduction briefly introduces the background of this research, highlights the benefits and the concerns of PLA/biomass biocomposites for FDM application. The research objectives and the structure of this thesis are also presented. Chapter 2: Literature review focuses on the survey of the literature of the 3D printing technologies, FDM technology and feedstock. The effect of content and particle size of biomass powder on the properties of PLA biocomposites, the application of PLA biocomposites in FDM, and the toughness modification has been conducted in PLA biocomposites are summarized. Chapter 3 highlights the research gaps, research objectives and research workflow. Chapter 4 describes the materials and methodology utilized throughout the research in detail. Chapter 5 describes the characterisation and analysis of constituent materials. Chapter 6 to Chapter 8 contain studies addressing the objectives of this research. Chapter 6 investigates the toughening modification of PLA biocomposite. Chapter 7 studies the PLA/HH and PLA/BP biocomposites through parametric analysis of HH and BP loading levels, and Chapter 8 investigates the PLA/HH and PLA/BP biocomposites through parametric analysis of HH and BP particle size distributions. The effect of toughening enhancement, biomass filler loading levels and particle size on melt flow, rheology, and thermal properties of biocomposites, filament quality, finish quality of FDM-printed parts, and mechanical properties for both injection-moulded (IM) and FDM-printed parts were assessed systematically.

Chapter 9 presents the conclusions and the key findings of this research and proposes the recommendations for the future development of PLA/biomass feedstock.

Chapter 2: Literature review

This comprehensive literature review covers 3D printing technology, FDM technology and feedstock, and the characteristics of PLA/biomass biocomposites and their application in FDM. The effect of biomass content and particle size on melt flow, mechanical properties, especially on the impact strength of PLA biocomposites is reviewed. The toughness modification for the PLA/biomass biocomposites is also reviewed.

2.1 3D printing technology

3D printing is an AM technology that uses layer-by-layer deposition of materials. It was developed by Charles Hull in 1986 in a technique called stereolithography (SLA/SL). With the development in 3D printing technology, new techniques emerged, including FDM, three-dimensional printing (3DP), selective laser sintering (SLS), polyjet, laminated object manufacturing, and paste extrusion printing, which employed a range of deposition principles [23, 24]. These 3D printing techniques were classified into (i) liquid-based, (ii) solid-based and (iii) powder-based according to the state of constituents, as displayed in **Figure 2-1**. The schematic diagrams of the widely used 3D printing techniques are presented in **Figure 2-2**. The associated feedstock, working principle, and features of the popular 3D printing techniques are summarized in **Table 2-1**. The common feedstock for 3D printing are thermoplastics, UV-curable resins, polymer powders, metals, and gypsum.

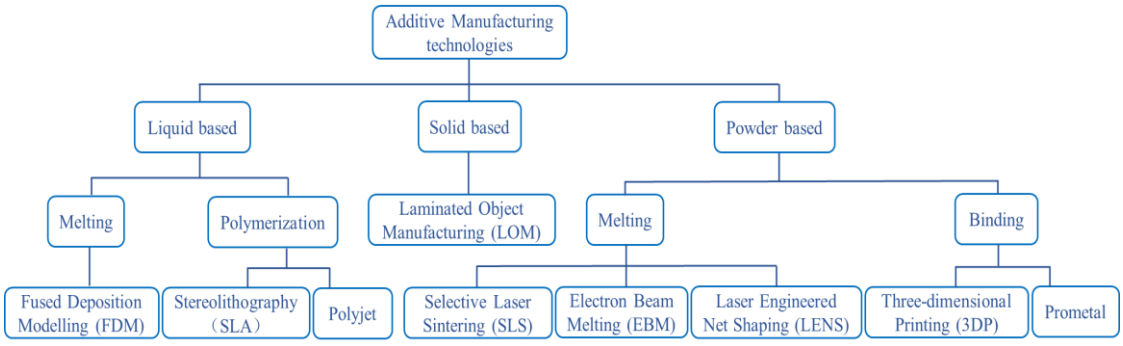

Figure 2-1 3D printing technologies [25].

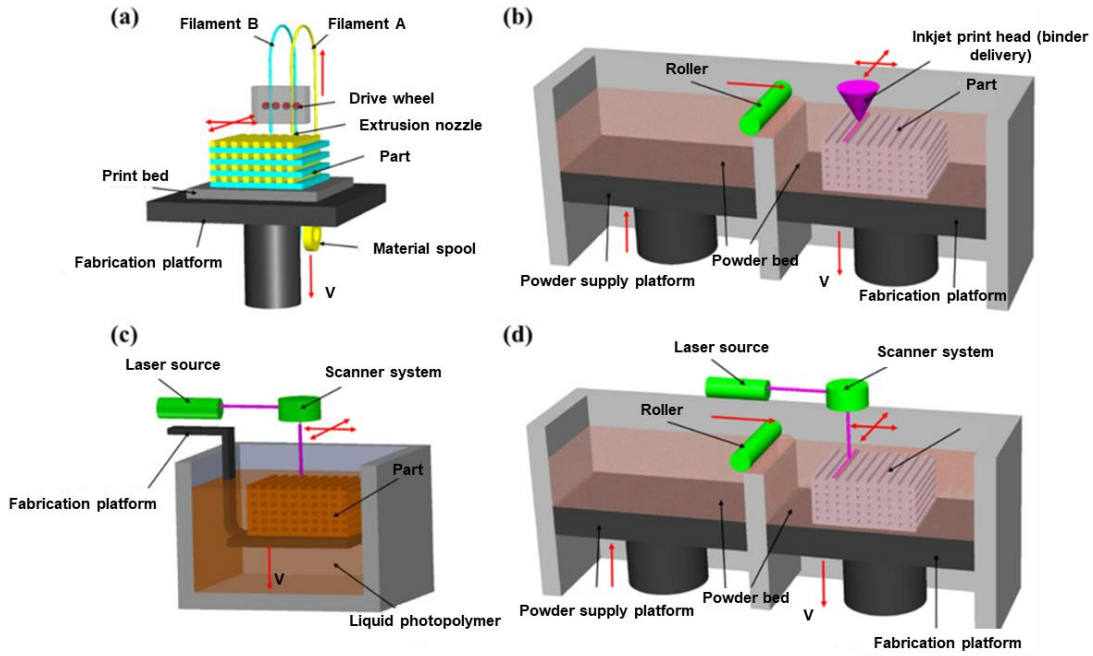

Figure 2-2 Schematic diagrams of main 3D printing techniques: (a) FDM, (b) 3DP, (c) SLA, and (d) SLS [26].

Table 2-1 A summary of common 3D printing technologies [26].

3D printing technology	Form of feedstock	Feedstock	Working principle	Resolution (μm)	Advantages	Disadvantages	Ref.
FDM	Filament	Thermoplastics, such as PLA, ABS, HIPS, PETG, PC and nylon	Extrusion and deposition	50-200	Low cost, good strength, multi-material capability	Anisotropy, nozzle clogging	[27, 28]
SLA	Liquid UV resin	Photo-curable resin (epoxy or acrylate-based resin)	Laser scanning and UV curing	10	High printing resolution	Material limitation, cytotoxicity, high cost	[29-31]
SLS	Powder	Polyamide powder and PCL	Laser scanning and heat-induced sintering	80	Good strength, easy removal of support powder	High cost, powdery surface	[32, 33]
3DP	Powder	Any materials can be supplied as a powder, binder needed	Drop-on-demand binder printing	100-250	Low cost, multi-material capability, easy removal of support powder	Clogging of binder jet, binder contamination	[34]

3D printing technology is mainly utilised in the areas of rapid prototyping (25%), product design (16%), and innovation (11%) according to the 2014 Gartner Report [35] (**Figure 2-3**). 3D printing technology is well-developed in the industry, including aerospace industries for the fabrication of complex lightweight geometries [36], automotive, and architectural industries for printing structural models [3, 25]. 3D printing is also employed in construction, art for replicating artefacts, education, biomedical applications for preparing tissues and organs [37], biomechanical, and fashion industries [3, 26, 38]. The most widespread application of the technology can be found in industrial and business machines (18.5%), aerospace (12.3%) and medical (13.7%), utilized for creating low-volume and high-value products, according to Wohler's report in 2014 [39] (**Figure 2-4**). However, aerospace was deemed to be the most encouraging application in the future, accounting for 18.2% of the total AM market, biomedical application constituted 11% of the market, and architectural applications shared 3% of the total AM market, according to Wohler's report 2017 [3]. A latest Wohler's report forecasts that the AM industry will grow to USD23.9 billion by the year 2022 and USD35.6 billion by the year 2024 [40].

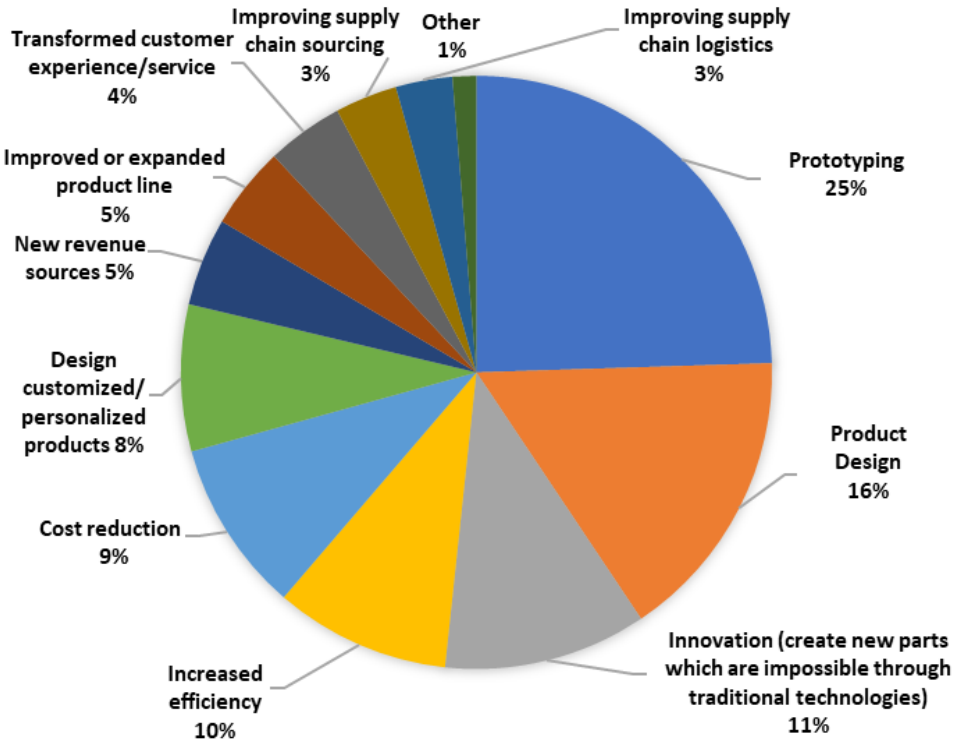

Figure 2-3 Applications of 3D printing technology. Source: Gartner report 2014 [35].

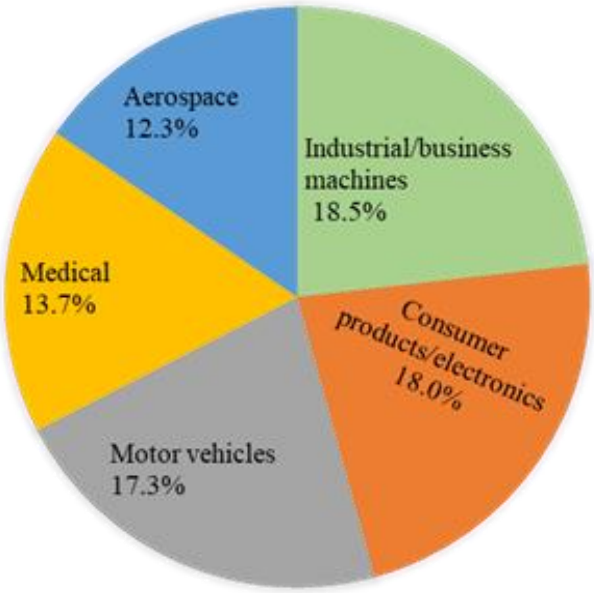

Figure 2-4 The progress in industrial applications of 3D printing. Source: Wohler's report in 2014 [39].

2.2 FDM technology and feedstock

FDM technique adopts a layer-by-layer deposition of low melting temperature thermoplastic feedstock. Dr. Scott Crump first introduced FDM technology in 1988, and the first commercial device was developed in 1991. The thermoplastic filament is melted and extruded through a heated nozzle, then solidified on the print bed or top of the last layer under room temperature or a chamber temperature below the solidification temperature, thus forming as designed by digital model files [41], as shown in **Figure 2-2a**. FDM is a heat-assisted process driven by heat transfer and phase transitions and dictated by the rheology, fluid mechanics, and material mechanics of the polymer/filler/additives [42]. FDM technology has advantages in its cost-effectiveness due to no need of using a laser as SLS and SLA [43], marginal wastage, reliability, fast fabrication, feedstock availability, and simplicity, although they have insufficient mechanical properties, the existence of voids, and layered structure in fabricated parts. The printability of materials is dependent on:

i) FDM printer and process parameters, such as nozzle diameter, nozzle temperature [44], layer thickness, filling ratio, raster angle [45], print speed, print bed temperature, environment temperature [46], and cooling system;
ii) Characteristics of produced parts, including their dimension, structure, geometry,

and the orientation [44];

iii) Properties of feedstock, like the melt flow and viscosity of the compositions [26], the surface quality of the filament and the consistency in filament diameter, the strength and toughness of the feedstock.

The melt flow and viscosity of feedstock in the molten state is the most important concern to guarantee continuous printing and adhesion between layers together with the surface quality of the created items [47]. The toughness of the feedstock dictates the printability and the end-user application of the materials.

ABS, PLA, polyethylene terephthalate glycol, polyamide or nylon, high impact polystyrene, polycarbonate, polymethyl methacrylate, polycaprolactone (PCL), polyethylene and polypropylene are commercially available feedstock for FDM technology. PLA and ABS are the most common feedstock materials, whereas PLA has clear benefits in processing and properties in comparison to ABS, including lower printing temperature, no odour emission, and lower propensity to warp and crack, thus making PLA a widely used feedstock for FDM.

PLA is a biobased and biodegradable thermoplastic polymer, with the largest production capacity and the highest cost-effectiveness among biopolymers. PLA can be manufactured by direct condensation polymerization of lactic acid or by ring-opening polymerization of lactide. The raw material, i.e., lactic acid monomer is obtained from the fermentation of carbohydrates from corn starch, sugarcane, or tapioca [48]. PLA has been commercially applied as a substitute for petroleum-based polymers [49-51]. The application of neat PLA in FDM is witnessing an increase because of:

i) Good printability due to less warping and less cracking, without odour emission during the FDM process and the lower melting temperature compared to ABS.

ii) The environmental-friendliness: using PLA filament in FDM could address the wastage issue emerged accompanied by the easier access to 3D printing for more people, due to its renewability, biodegradability and composability [52];

iii) Excellent mechanical properties of 3D-printed parts, including higher tensile strength and elastic modulus over traditional petrochemical polymers [53].

PLA has been applied in the biomedical field by FDM 3D printing, particularly in the fabrication of tissue engineering scaffolds. PLA contributes to the cell adhesion and

proliferation and creates a promising biological and mechanical environment for the cell [54].

Nevertheless, PLA is relatively less cost-effective and has lower toughness compared with traditional plastics, which limits the utilization of PLA in wide application [55]. Incorporation of fibre or filler [56] and cellulose nanofibers [57] to PLA can improve the mechanical properties of PLA and reduce its cost in the biocomposite blend form.

2.3 PLA biocomposites feedstock

Using PLA biocomposites filled with biomass filler is advantageous for obtaining cost-effective, sustainable, improved strength and dimensionally stable feedstock for FDM, compared to neat PLA. As renewable resources, biomass wastes utilization in FDM feedstock can be beneficial for lowering hazards associated with synthetic materials, and reducing carbon dioxide emission, compared with non-renewable alternatives [58]. Biomass resources have numerous benefits, including higher mechanical performances than synthetic fibres, without emission of toxic materials, and cost-saving [59]. Moreover, biomass can create a wood-like appearance [24], which is a crucial characteristic of biomass compounding with polymers [58]. Additionally, the usage of woody materials can lower the cost of feedstock [60]. Furthermore, the employment of biomass powder in FDM would add value for wood/biomass waste.

Biomass is a term for all plant materials, including algae, trees, and crops. The main types of biomass are categorized into woody plants, herbaceous plants/grasses, aquatic plants, and manures [61]. Biomass comprises primarily of three main constituents, including hemicellulose, cellulose, and lignin [62], in which the fractions of cellulose are 40-50 wt.% and hemicellulose is 20-40 wt.%, respectively [61]. The chemical constitutions of the main biomass fibre/fillers are summarized in **Table 2-2**. The thermal decomposition of biomass occurs at several steps with rising temperature. At temperatures below 220°C, the moisture evaporates, between 220-315°C, principally hemicellulose decomposes, at 315-400°C, cellulose decomposes, and above 400°C, lignin decomposes [62].

Various forms of biomass have been investigated in PLA biocomposites, including bamboo powder (BP) [47, 63], bamboo fibre [64], kenaf fibre [16], poplar wood powder [8, 9, 65, 66], ironwood sawdust [17], paulownia wood flour [67], hemp hurd

(HH) [68, 69], hemp fibre and harakeke fibre [70], jute fibre [71], beechwood [72], aspen wood fibre [38], date seed powder [10] and thermomechanical pulped fibres [73]. Lignin [19, 74] and cellulose [11] were also investigated in PLA biocomposites. The range of biomass content in the study varied from 0 to 50% in weight fraction. The particle size investigated is above 75 μm. The effect of biomass filler content and particle size on the properties of PLA biocomposites have been investigated, which are summarized in detail as below. Some of the studies investigated the modification of PLA biocomposites to improve interfacial compatibility and toughness properties. Parts of these biocomposites have been investigated for FDM application.

Table 2-2 Chemical constitutions of main biomass fibre/fillers [75]

Fibre/Filler	α-Cellulose (wt.%)	Hemicellulose (wt.%)	Lignin (wt.%)	Extractive (wt.%)	Ash (wt.%)
Hemp	70.2-74.4	17.9-22.4	3.7-5.7	1.6	-
Bamboo	48.2	25.1	21.4	9.9	2.3
Banana	63.9	1.3	18.6	10.6	1.5
Coir	44.2	12.1	32.8	6.4	2.2
Cotton	90.0	6.0	-	0.4	-
Flax	64-74	11-17	2-3	1.5	-
Hardwood	31-64	25-40	14-34	0.1-7.7	<1
Hemp hurd	39-49	16-23	16-23	2-4	2-4
Jute	60-65	6-8	5-10	-	1.2
Kenaf	63.5	17.6	12.7	4	2.2
Pineapple	73.4	7.1	10.5	5.5	2.0
Ramie	68.6-76.2	13.1-16.7	0.6-0.7	6.4	-
Sisal	60-67	10-15	8-12	1.7-6.0	0.14-0.87
Softwood	30-60	20-30	21-37	0.2-8.5	<1

2.3.1 PLA biocomposites: Effect of biomass content

The biomass content affects the melt flow and processability, mechanical properties, surface finish and density of PLA biocomposites, as summarized in **Table 2-3**. Generally, the addition of biomass filler decreased melt flow, mechanical strength, ductility, and toughness, whereas increased complex viscosity and modulus for PLA biocomposites.

Table 2-3 A summary of PLA biocomposites filled with increasing loading of biomass

Biomass species	Particle size	Filler content (wt.%)	Properties	Reference
Date seed powder (DSP)	<60 μm	0, 10, 20, 30, 40	With increasing DSP content, $\|\eta^*\|$ increased, whereas yield stress and strain decreased. Tensile modulus increased with the addition of DSP, then decreased with the increasing content of DSP.	[10]
Coconut shell powder (CSP)	38 μm	0, 15, 30, 45, 60	Increasing CSP content decreased the tensile strength and elongation-at-break and increased the modulus of elasticity of the PLA/CSP biocomposites.	[76]
Kenaf fibre	200 μm	0, 10, 20, 30, 40, 50	With increasing kenaf content, impact strength, tensile strength and modulus, and flexural properties decreased.	[16]
Bamboo fibre (BF)	Length/diameter: 500 μm/70 μm	0, 10, 20, 30, 40, 50	With increasing BF content, tensile strength, and elongation-at-break decreased, Young's modulus increased.	[64]
Poplar wood powder	325 mesh	0, 10, 20, 30, 40, 50	Tensile strength decreased with increasing wood flour (WF) content for both PLA/WF and PLA-g-MAH/WF.	[65]
Cork particles	446 μm	0, 5, 10, 15, 20, 25, 30, 50	With increasing cork granules content, tensile strength, modulus, elongation-at-break, impact strength, and density decreased.	[18]
Lignin		0, 20, 40	Tensile strength, modulus, and elongation-at-break decreased with the addition of lignin.	[74]

Biomass species	Particle size	Filler content (wt.%)	Properties	Reference
Poplar wood powder	100 to 120 mesh	0, 10, 20, 30, 40	With increasing wood flour content, $\|\eta^*\|$ increased, mechanical properties decreased.	[8]
Hemp hurd (HH)	44 ± 10 μm, Maximum: 400 μm	0, 10, 20, 30	Increasing HH content increased elastic modulus, flexural modulus, decreased tensile strength, flexural strength, elongation-at-break, and impact strength.	[68]
American wood fibres	425 μm	0, 5, 10, 20, 30, 40	The tensile strength decreased with the addition of wood fibre (WF), then increased with increasing WF content, tensile modulus and impact strength increased, elongation-at-break decreased with increasing WF content.	[77]
Rubberwood sawdust	500 μm	0, 5, 10, 20, 30	Tensile strength and modulus increased, and the elongation-at-break and impact strength decreased with increasing sawdust content.	[20]
Hemp fibre Harakeke fibre	Diameter: 28.3±8.3 μm; 12.3±1.7 μm	0, 10, 20, 30	With increasing fibre content, tensile strength decreased, Young's modulus increased. The surface finish is uneven and coarser with increasing fibre content.	[70]
Micro/Nanocellulose (MNC)		0, 10, 30, 50	MNC decreased MFR. MNC up to 30% improved tensile strength, flexural strength, and elongation-at-break.	[11]

2.3.1.1 Melt flow and complex viscosity

The effect of biomass filler addition and content on the melt flow of PLA biocomposites is shown in **Figure 2-5**. It is observed that the increasing poplar wood flour and date seed powder content caused increases in complex viscosity [8-14]. The effect of Micro/Nano cellulose on the melt flow rate (MFR) of Micro/Nano cellulose/PLA has also been investigated [11]. Results showed that 30 wt.% Micro/Nano cellulose decreased MFR from 2.2 g/10 min for neat PLA to 0.17 g/10 min for PLA biocomposite.

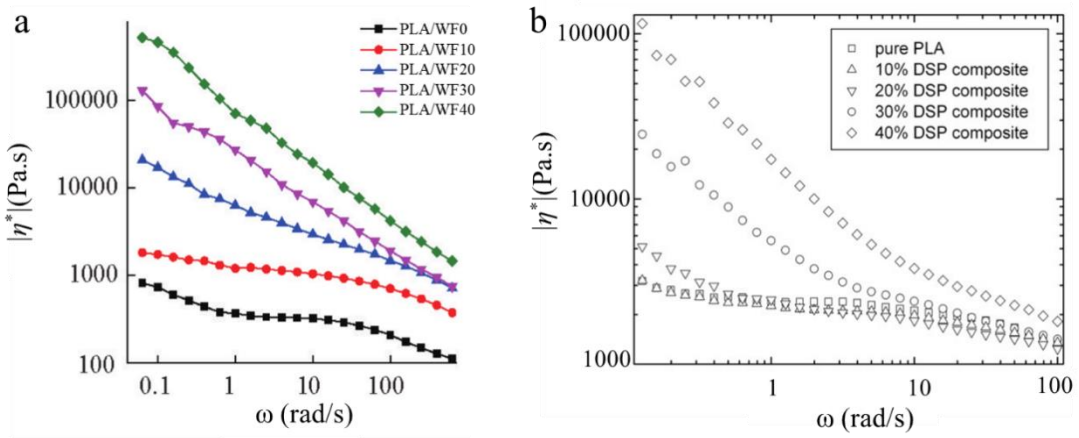

Figure 2-5 Complex viscosity, $|\eta^*|$ with increasing biomass content as a function of dynamic frequency (a) PLA/poplar wood flour (WF) [8] and (b) PLA/date seed powder (DSP) biocomposites [10].

2.3.1.2 Tensile properties

The effect of biomass filler content on the tensile strength of PLA biocomposites is shown in **Figure 2-6**. The tensile strength decreased with the increasing content of biomass filler [8-10, 16-18, 63-65, 70, 74, 76], 40 wt.% normal and special poplar WF decreased tensile strength by 26.5% and 22.9% [8]. It is also seen that the incorporation of 15 wt.% bamboo flour in PLA decreased tensile strength from 58 MPa to 42.5 MPa [15], 10 wt.% poplar wood flour decreased tensile strength from 38 MPa to 21 MPa [9], 30 wt.% untreated sawdust addition to PLA decreased tensile strength from 45.5 MPa to 39 MPa [17], ascribed to the poor interfacial adhesion between biomass and the matrix and the poor distribution of biomass powder in the polymer matrix.

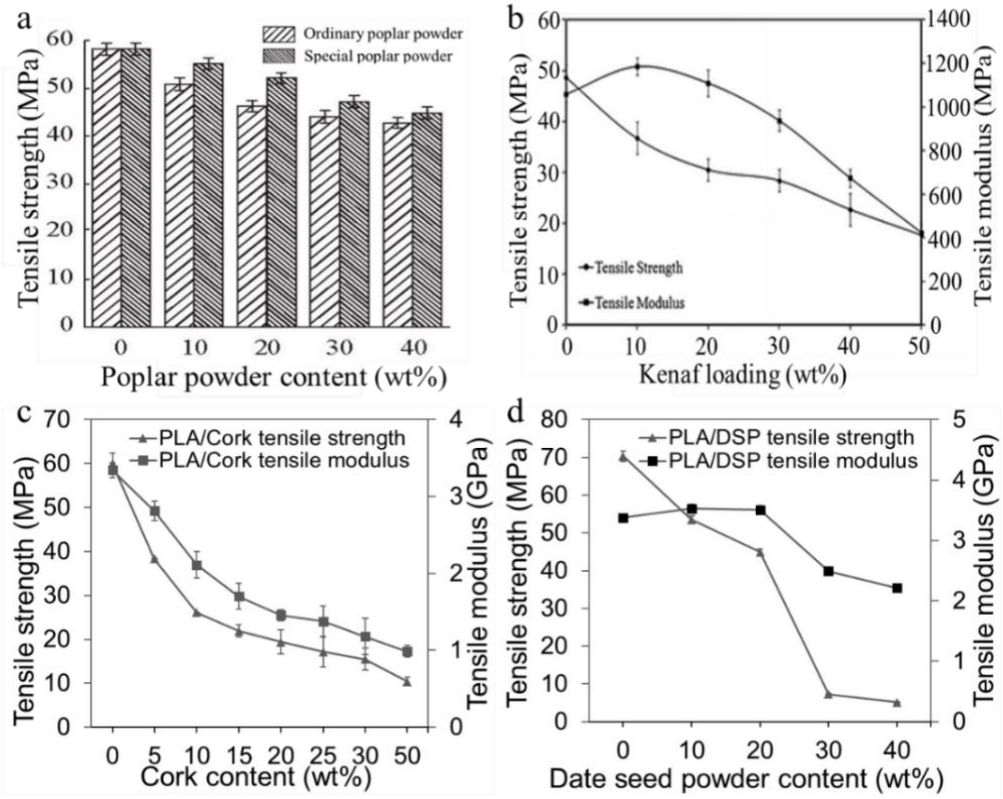

Figure 2-6 Tensile strength and modulus of PLA/biomass composites as a function of biomass content (a) PLA/poplar wood flour [8], (b) PLA/kenaf fibre [16], (c) PLA/cork [18], and (d) PLA/DSP [10].

Elongation-at-break decreased [17, 18, 20, 63, 64, 74, 76-78] with the increasing biomass content, as shown in **Figure 2-7**, due to the decrease in polymer chain disentanglement and chain mobility of the polymer matrix restricted by the rigid biomass particles [76, 79]. 30 wt.% untreated sawdust addition to PLA also decreased elongation-at-break from 5% to 2.7% [17].

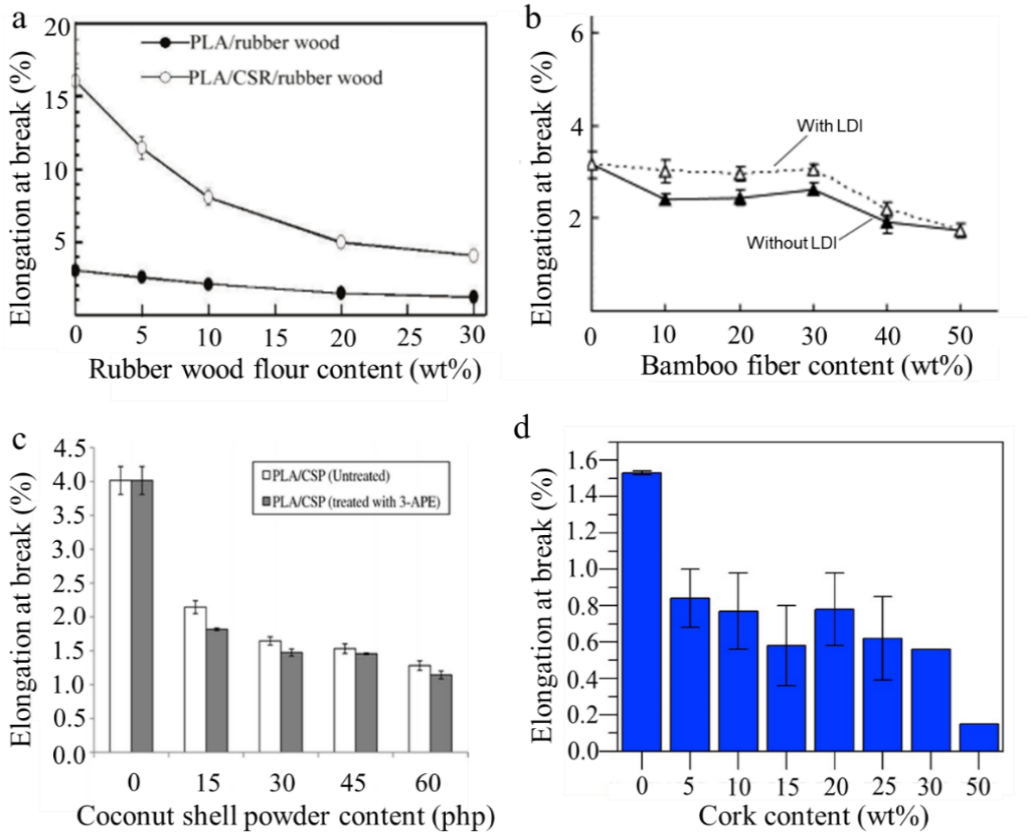

Figure 2-7 Elongation-at-break of (a) PLA/rubber wood and PLA/core-shell rubber/rubber wood [20], (b) PLA/bamboo fibre [64], (c) PLA/coconut shell powder [76], and (d) PLA/cork [18] biocomposites as a function of biomass content.

The tensile modulus or Young's modulus generally increased [20, 64, 70, 76, 77, 80] with the inclusion of biomass powder, as shown in **Figure 2-8**, which is common in the biocomposite reinforced with a rigid and stiff filler [64], attributed to the restrained movement of polymer chains by the biomass filler [66]. 30 wt.% untreated sawdust addition to PLA also increased tensile modulus from 1.1 GPa to 1.48 GPa [17]. For kenaf fibre and date seed powder reinforced PLA, the tensile modulus increased with the addition of biomass firstly, then decreased with further biomass content as shown in **Figure 2-6b**, **d**, related with the random dispersion of biomass in the matrix due to the inadequate interfacial interaction between biomass and the matrix. The tensile modulus decreased with increasing cork content [18] as shown in **Figure 2-6c**, ascribed to the high proportion of suberin (33-50%) and a low fraction of cellulose (6-25%) in cork.

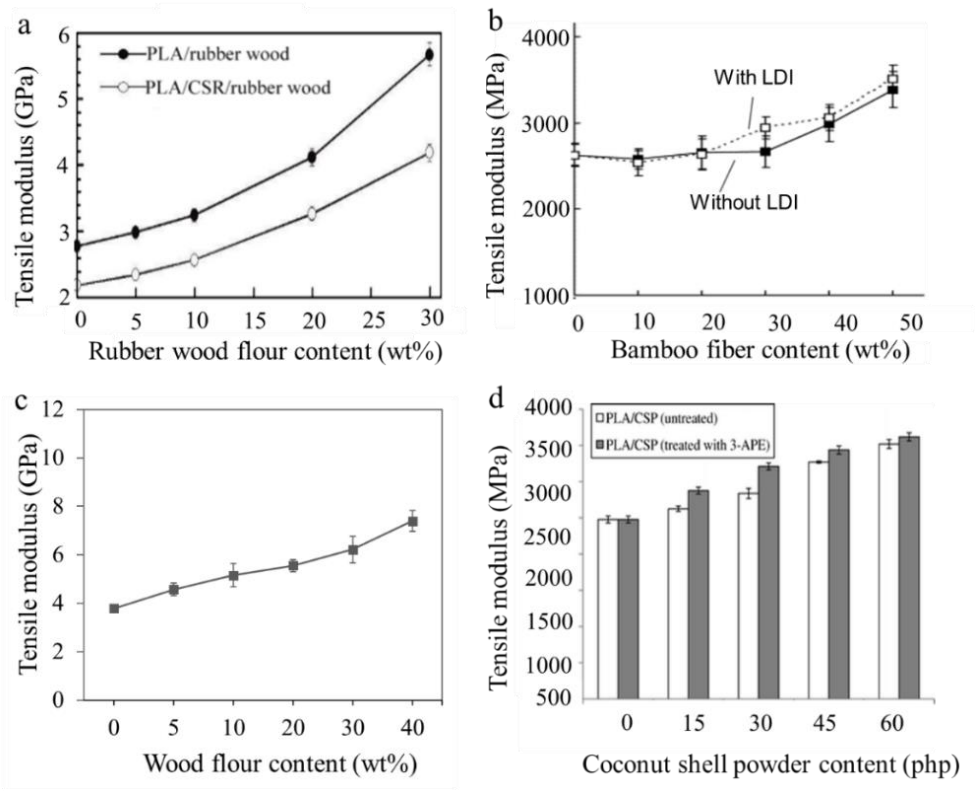

Figure 2-8 Tensile modulus of (a) PLA/rubber wood and PLA/core-shell rubber/rubber wood [20], (b) PLA/bamboo fibre [64], (c) PLA/wood flour [77], and (d) PLA/coconut shell powder [76] biocomposites as a function of biomass content.

2.3.1.3 Flexural properties

Flexural strength usually decreased with increasing biomass content [8, 9, 16, 19], as shown in **Figure 2-9**. 10 wt.% poplar wood flour decreased flexural strength from 70 MPa to 47 MPa [9], 40 wt.% normal and special poplar WF caused 30.3% and 14.5% decrease in flexural strength [8], due to the insufficient interfacial adhesion between the filler and matrix, and insufficient wetting of fibres with the matrix, resulting in efficient stress transfer between the polymer and fibre. Nevertheless, the increasing rubberwood sawdust increased flexural strength due to the inclusion of rigid rubberwood sawdust particles [20].

The increase in biomass content led to increasing flexural modulus as a result of the addition of stiff and higher modulus biomass [20, 81]. Flexural modulus increased with the addition of biomass, then decreased with increasing biomass content, Flexural modulus even might be decreased to a level lower than the control without biomass [16] due to the weak distribution of biomass in the matrix.

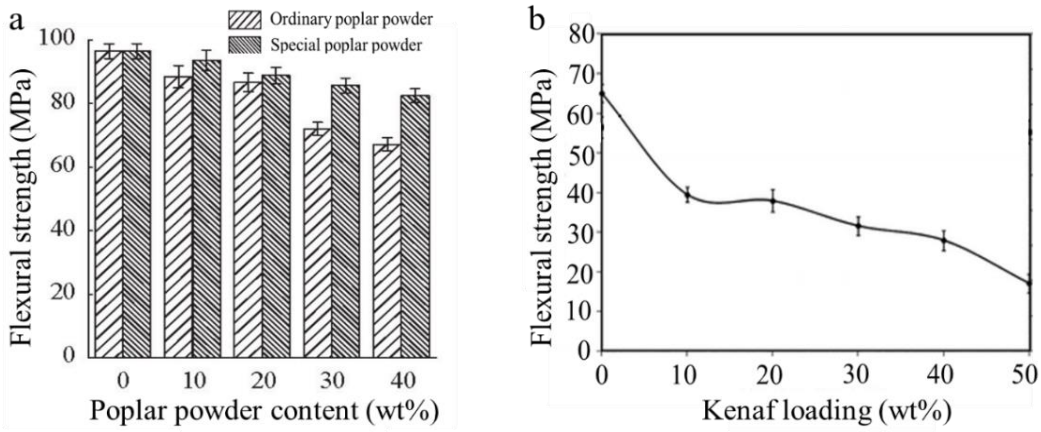

Figure 2-9 Flexural strength of PLA/biomass composites as a function of biomass content (a) PLA/poplar wood flour composites [8] and (b) PLA/kenaf fibre [16].

2.3.1.4 Impact strength

Commonly, impact strength decreased [8, 9, 12, 15-21] with the increasing biomass content, as shown in **Figure 2-10**, due to insufficient biomass/matrix interfacial adhesion to offer effective resistance to crack propagation during impact tests [79]. 15 wt.% bamboo flour incorporation to PLA decreased impact strength from 13.6 kJ/m^2 to 7.5 kJ/m^2 [15], 10 wt.% poplar wood flour decreased impact strength from 14 kJ/m^2 to 11 kJ/m^2 [12], and from 8 kJ/m^2 to 5.5 kJ/m^2 [9], 30 wt.% untreated sawdust decreased impact strength from 15 kJ/m^2 to 8 kJ/m^2 [17]. The addition of 40 wt.% normal poplar WF and special poplar WF caused 82.2% and 72.9% decrease in impact strength [8]. On the other hand, impact strength increased with increasing biomass content due to the increasing resistance to crack propagation from biomass filler to matrix or effective stress transfer from filler to matrix, because of the large particle size and high aspect ratio of biomass filler [14, 77, 82-84].

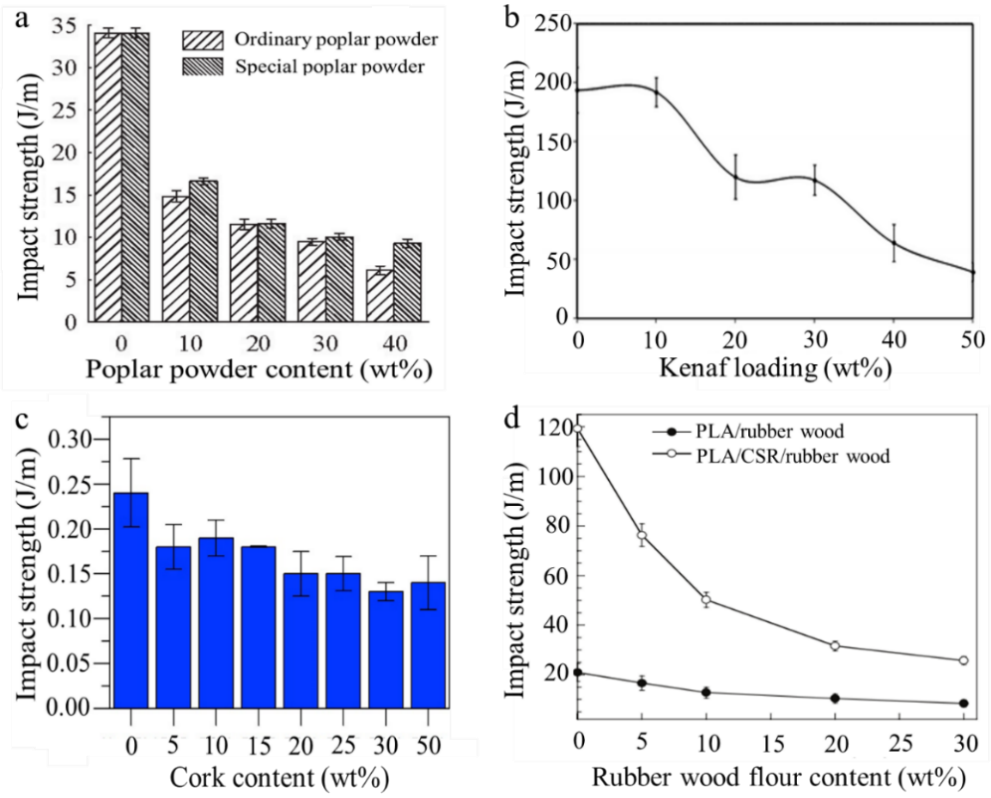

Figure 2-10 Impact strength of PLA/biomass composites as a function of biomass content: (a) PLA/poplar wood flour [8], (b) PLA/kenaf fibre [16], (c) PLA/cork [18], and (d) PLA/rubber wood and PLA/core-shell rubber/rubber wood [20].

For PLA biocomposites filled with a high loading of biomass, hot-pressing is used to form the biocomposites [65, 71]. Using hot-pressing, the melt strength and melt flow, which are critical for the extrusion process, are not required, the addition of high content of biomass filler is possible. With the increasing content of biomass powder, the melt flow and toughness of biocomposites decreased, there is potentially problematic for consistent processing of FDM feedstock [16, 64]. Toughness improvement for PLA biocomposites is necessary if considering the application in FDM [8].

2.3.2 PLA biocomposites: Effect of biomass particle size

There are a few investigations studied the effect of the particle size of biomass on the properties of PLA biocomposites, as summarized in **Table 2-4**.

Table 2-4 A summary of PLA biocomposites filled with biomass having different particle sizes

Biomass species	Particle size	Filler content (wt.%)	Properties	Reference
Poplar fibres	<180, 180−425, 425−850, and 850−2360 μm	20	The composites derived from poplar fibre <180 μm had a suitable viscosity range for 3D printing. Tensile strength of the composites increased from 34 to 54 MPa as the poplar fibre size decreased from 850−2360 to <180 μm, failure strain decreased with decreasing particle size.	[66]
Paulownia wood flour	30 mesh, 40 mesh, 60 mesh, 80 mesh, 140 mesh, 200 mesh	25	Density decreased, while smaller particle size below 200 mesh, the density is higher than neat PLA. Smaller particle size filled biocomposites obtained higher tensile strength and Young's modulus, elongation-at-break is lower than neat PLA but close to each other.	[67]

2.3.2.1 Complex viscosity

The effect of biomass particle size on complex viscosity of PLA biocomposites is shown in **Figure 2-9**, which shows no trend in the complex viscosity with respect biomass particle sizes. The poplar fibre with particle size under 180 µm led to the optimum viscosity range in biocomposites [66]. With the presence of poplar fibre, PLA biocomposites exhibited shear-thinning behaviour, with the increasing dynamic frequency, the complex viscosity decreased, which is favourable for 3D application. At the lower shear rate, cork with smaller particle size resulted in higher shear viscosity for PP composites, as shown in **Figure 2-10**, due to an improved wetting of the smaller cork particles because of their larger specific surface area [85].

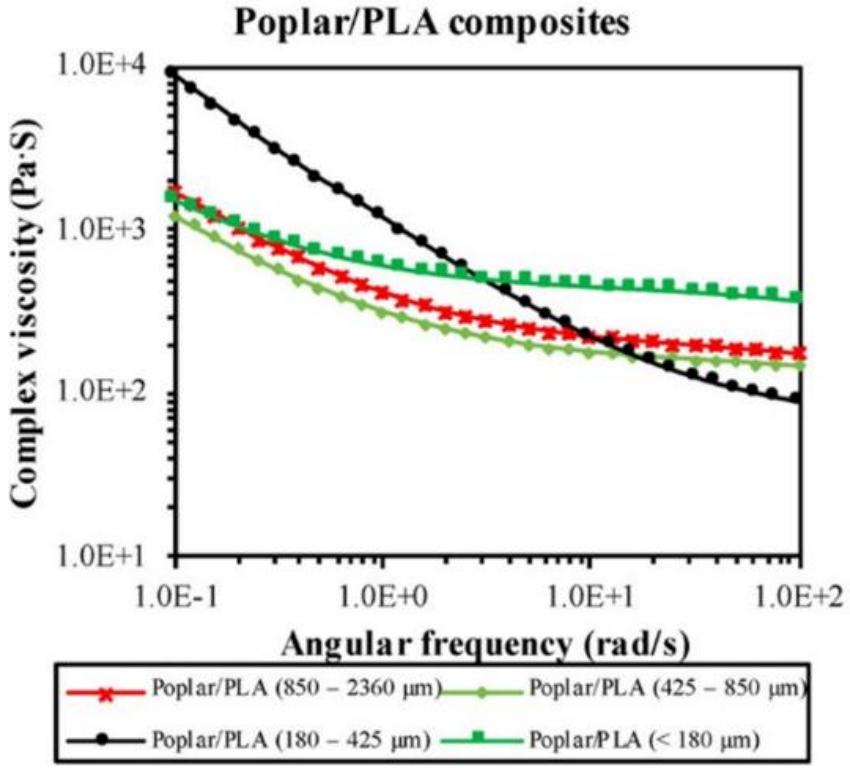

Figure 2-9 Complex viscosity of Poplar/PLA with varying poplar sizes [66].

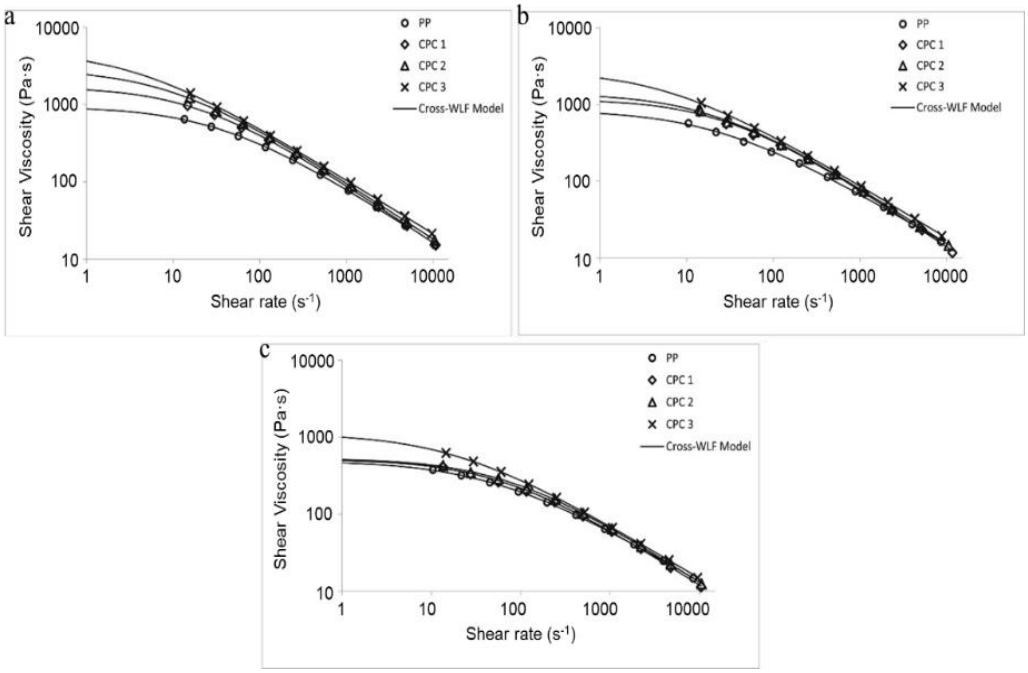

Figure 2-10 Shear viscosity of Cork/PP composites (CPC) at (a) 180°C, (b) 200°C and (c) 220°C [85]. CPC 1: 596 μm, CPC 2: 276 μm, CPC 3: 70 μm.

2.3.2.2 Tensile properties

Generally, the tensile strength and tensile modulus increased with decreasing particle size of biomass, as shown in **Table 2-5** and **Figure 2-11**. Elongation-at-break could increase (**Table 2-5**), or remain similar (**Figure 2-11**), even slightly decrease [86] with particle size decreasing, depends on the polymer matrix/biomass filler interfacial adhesion. Tensile strength increased as the poplar fibre size decreased from 850−2360 μm to <180 μm, due to more uniform dispersion of PLA and smaller fibre size, and enhanced interaction between PLA and fibre, which create higher mechanical interlocking. Failure strain increased with decreasing particle size, related to the plasticizing effect of small fibres [66]. In the particle size range of paulownia wood flour (PWF) between 30 mesh and 200 mesh, smaller particle size resulted in higher tensile strength and Young's modulus, because of the enhanced wood-PLA interaction, which is harder to break compared to PLA matrix punctured with fewer but larger wood particles. The reason is that the finer particles filled composites exhibited a heterogeneous matrix of PLA and particles, the "web-like" matrix contains huge numbers of PLA-particles interaction. The elongation-at-break was negligibly affected by the particle size [67]. Tensile strength and elongation-at-break and Young's modulus also increased as the bacterial cellulose particle size

decreased from 150-180 μm to <90 μm [87]. Tensile modulus increased with an improved aspect ratio of biomass filler [88].

Table 2-5 The effect of poplar fibre size on the tensile properties of composites [66]

Poplar/PLA composite	Tensile strength (MPa)	Young's modulus (MPa)	Failure strain (%)
Poplar: 850–2360 μm	34 ± 4 (1.8)	3847 ± 207 (93)	2.7 ± 0.5 (0.2)
Poplar: 425–850 μm	37 ± 7 (3.1)	3813 ± 579 (259)	4.8 ± 1.2 (0.5)
Poplar: 180–425 μm	39 ± 5 (2.2)	4220 ± 241 (108)	3.7 ± 1.1 (0.5)
Poplar: <180 μm	54 ± 2 (0.9)	4254 ± 255 (114)	4.8 ± 0.3 (0.1)
Neat PLA	54 ± 1 (0.4)	3172 ± 131 (59)	2.8 ± 0.4 (0.2)

* The values in the bracket are standard error.

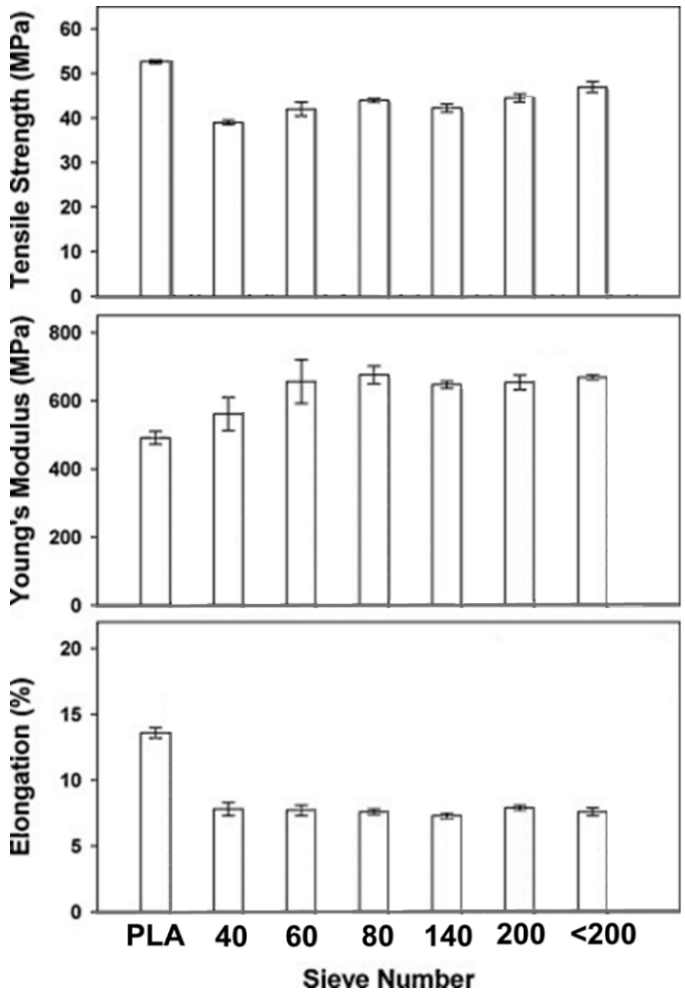

Figure 2-11 Mechanical properties of PLA/25% paulownia wood composites [67].

2.3.2.3 Flexural properties

The research is lacking in the effect of biomass particle size on flexural properties of PLA biocomposites to the author's knowledge. The effect of particle size on the flexural properties depends on the balance between the aspect ratio of biomass particles and interfacial adhesion between biomass filler and polymer matrix. The larger particle size favours to the flexural properties of PE/wood flour composites because the larger wood flour particles have a higher aspect ratio, showing enhanced reinforcement for composites. The flexural strength and modulus increased by 10.4% and 56.3%, respectively, when the particle size of wood flour increased from 100 μm to 850 μm, as shown in **Figure 2-12a** [89]. In contrast, flexural strength and modulus of PVC/rice hull composites increased with decreasing rice hull particle size, as shown in **Figure 2-12b**, **c**, due to the larger voids and larger defects created within the composites by the larger rice hull particles [86].

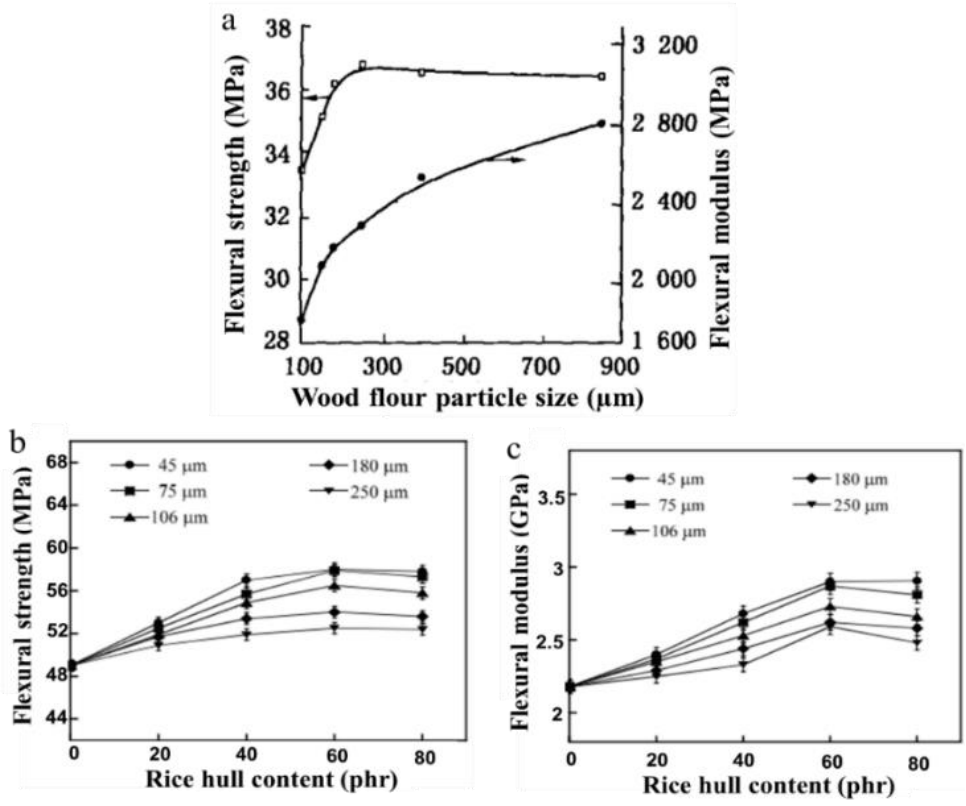

Figure 2-12 Flexural properties of (a) HDPE/wood flour [89] and (b, c) PVC/rice hull [86] composites with varies particle size.

2.3.2.4 Impact strength

Regarding the effect of biomass particle size on the impact strength of biocomposites, there is rarely studies on biomass-filled biocomposites based on PLA, only a few of studies based on HDPE, PVC and PP matrix, it is observed that larger particle size favours for higher impact strength [86, 89, 90], as shown in **Figure 2-13**, because more cavities were created and acted as internal defects reducing the energy transfer within the composites filled with smaller particles [86].

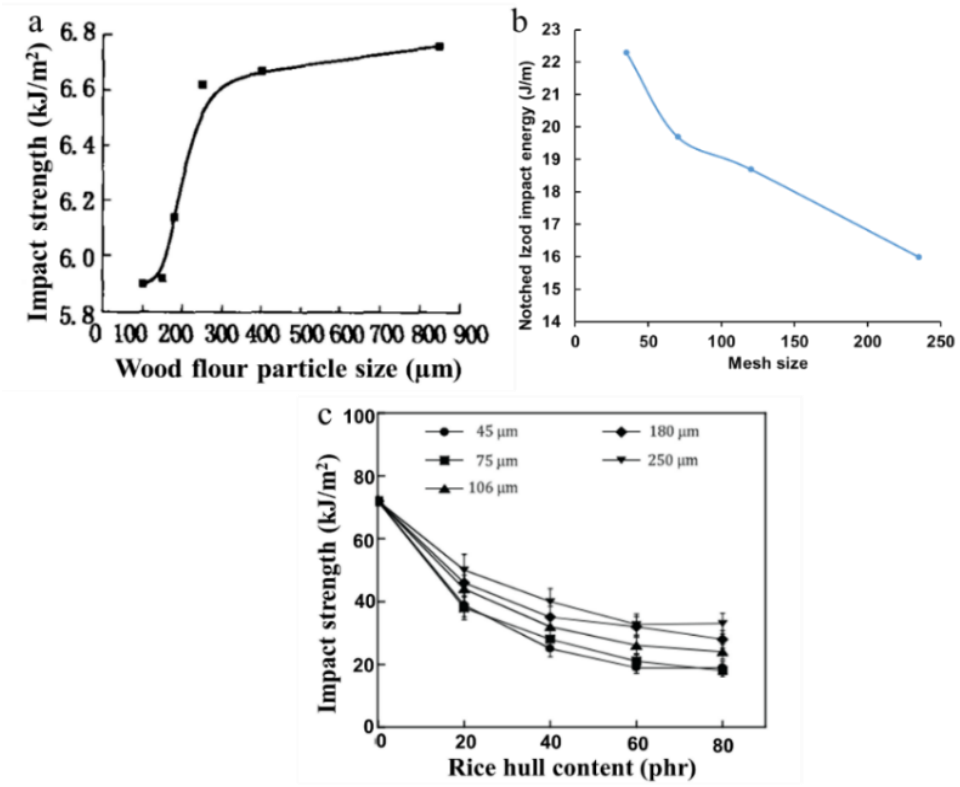

Figure 2-13 Impact strength of (a) HDPE/wood flour [89], (b) PP/wood flour [90], and (c) PVC/rice hull [86] composites with varies particle size.

2.3.3 PLA biocomposites: FDM Applications

The market portions of biocomposites in industrial areas, i.e. automotive, structure, thermal and sound insulation materials are increasingly significant [1, 91]. A range of biomass including bamboo, birch, cedar, coconut, ebony, olive, pine, and willow are utilized in commercial FDM filaments. The biocomposites are 3D-printed out to big parts for art design and installation (**Figure 2-14**). Commercial PLA biocomposite filaments were developed as summarized in [92]. The research in the

application of PLA biocomposites in FDM 3D printing is summarized in **Table 2-6**. The effect of biomass addition on melt flow of 3D printing materials, filament quality, and finish quality of 3D-printed parts, including mechanical properties, surface finish, and density was reviewed.

Figure 2-14 (a) 3D printing pavilions by researchers at Oak Ridge National Laboratory used a bamboo biocomposite material (Photo Credit: Oak Ridge National Laboratory) [93] and (b) installation Aguahoja I created by Neri Oxman and the Mediated Matter group with cellulose, chitosan, and pectin (Source: Mediated Matter Group) [93].

Table 2-6 A summary of the research of PLA biocomposites application in FDM

Biomass species	Particle size	Filler content (wt.%)	Properties	Reference
Beechwood	<0.237 mm	0, 10, 20, 30, 40, 50	The density of filament and 3D printed parts decreased as wood content increased; filament tensile strength increased from 55 MPa to 57 MPa (10 wt.% wood), decreased to 30 MPa (50 wt.% wood). The surface became rougher with increasing wood content.	[72]
Beechwood	<0.237 mm	0, 10, 20, 30, 40, 50	The surface roughness of FDM-printed samples of PLA/wood flour increased with WF content.	[22]
Cork particles	446 μm	0, 5, 10, 15, 20, 25, 30, 50	3D-printed specimens had lower elastic modulus and tensile yield strength, but higher elongation-at-break than compression moulded bars.	[18]
Hemp fibre Harakeke fibre	Diameter: 28.3±8.3 μm; 12.3±1.7 μm	0, 10, 20, 30	With increasing fibre content, the tensile strength of FDM-printed samples decreased, Young's modulus increased, the surface finish is uneven and coarser with increasing fibre content.	[70]
Kraft Lignin, Organosolv Lignin, Lignosulfonate		0, 5, 10, 15	Kraft Lignin increased melt volume rate because of the degradation of PLA. Flexural and impact strength of the FDM-printed bars decreased with increasing lignin loading. Lignosulfonate/PLA blends showed promising behaviour for 3D-printing.	[19]

Biomass species	Particle size	Filler content (wt.%)	Properties	Reference
Lignin		0, 20, 40	Tensile strength, modulus, and elongation-at-break of PLA/lignin FDM-printed samples decreased with the increasing content of lignin.	[74]
Micro/Nanocellulose (MNC)		0, 10, 30, 50	MNC decreased MFR. The optimum formulation of MNC/PLA composites for 3D printing was 30 wt.% MNC modified with 1% KH550, 5 wt.% PEG6000, and 65 wt.% PLA. The 3D parts with the optimum formula have a comparable mechanical property to neat PLA, with elongation-at-break of 12%, a tensile strength of 59.7 MPa and flexural strength of 50.7 MPa.	[11]
Aspen wood flour	14 μm	5	The addition of wood flour enhanced the elastic modulus of FDM-printed bars by 30%.	[38]
Poplar fibres	<180, 180−425, 425−850, 850−2360 μm	20	Poplar fibres <180 μm are in a favourable size range for additive manufacturing applications. The composites derived from poplar fibre <180 μm had a suitable viscosity range for 3D printing.	[66]
Poplar powder	<100 μm	10	10 wt.% poplar powder decreased impact strength from 14 kJ/m^2 of neat PLA to 11 kJ/m^2 and fluidity of FDM-printed parts, TPW604 also decreased impact strength, whereas improved fluidity. POE improved the fluidity and impact strength of FDM-printed parts.	[12]

2.3.3.1 FDM Feedstock: Melt flow and printability

With the addition of biomass filler, the melt flow of PLA biocomposites generally decreased. For FDM application, the melt flow is essential for printability, the melt flow should be low enough to keep the printed shape and high enough for smooth printing. Although the decrease in melt flow with the addition of biomass filler [11, 12], there was no problem in 3D printing the materials through optimization of the formulations, various products were FDM-printed out as shown in **Figure 2-15**. Some work put efforts to improve the melt flowability using additives. Lubricant (TPW604) and polyolefin elastomer (POE) efficiently improved the MFR of PLA/poplar powder composites [12] (**Figure 2-16**). 5 wt.% polyethylene glycol (PEG) 6000 increased MFR of PLA/30 wt.% MNC composites from 0.17 g/10 min to 0.57 g/10 min [11], the material had comparable mechanical properties with neat PLA. Xie *et al.* [94] investigated glycerol and tributyl citrate (tributyl 2-hydroxypropane-1,2,3-tricarboxylate) as plasticizers for PLA/poplar wood flour filament, the filament with 4% glycerol showed the highest melt index. Zhao [47] investigated the printability of PLA/BP (200 mesh) using PEG600 to tailor the melt flow. The particle size of biomass powder affected the melt flow and viscosity of PLA biocomposites (**Figure 2-9**) [66]. Particles sieved under 250 μm-filled PLA caused clogging in nozzle although the nozzle diameter was 400 μm, so ultra-fine wood powder is necessary for FDM feedstock to avoid nozzle blocking [95]. A problem was also observed during FDM printing of the wood-only composites (PLA-Osage orangewood and PLA-paulownia wood 75/25 in w/w), due to the brittleness and clogging in the nozzle, even the particle size was smaller than 63μm [96].

Figure 2-15 (a) Large-scale 3D printing process and (b) a completed 3D-printed podium base using poplar/PLA composite [66], and (c) the FDM printed products with PLA/30% MNC composite [11].

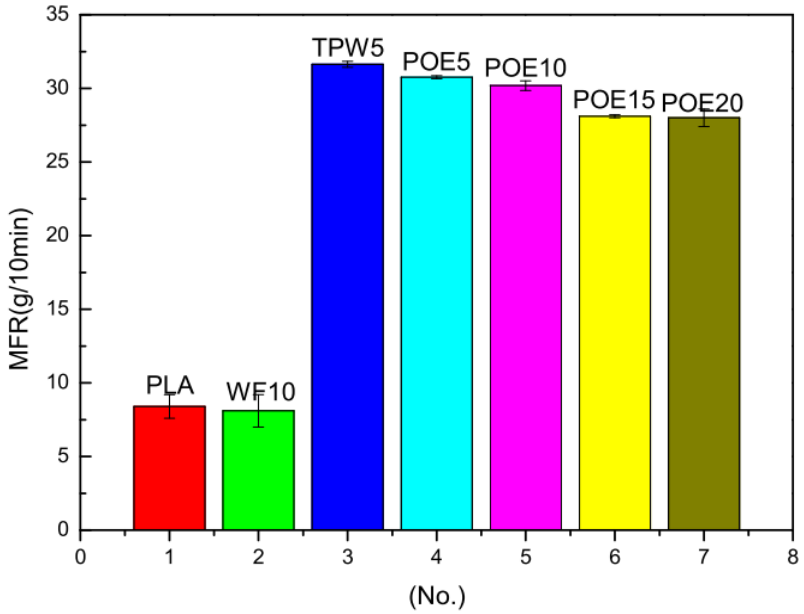

Figure 2-16 Melt flow rate of 3D printing materials with different additives [12].

2.3.3.2 FDM-printed products: Mechanical properties

The mechanical properties of FDM-printed parts fabricated by PLA biocomposites have been investigated, including the tensile properties, flexural properties, and impact strength. Generally, with the addition and increasing biomass content, tensile strength and elongation-at-break of the FDM-printed parts decreased due to the poor interfacial adhesion between biomass filler and matrix and insufficient interlayer

adhesion [38, 70, 74], the tensile modulus could increase or decrease, similar as IM parts. The addition of 20 wt.% and 40 wt.% lignin to PLA decreased the tensile strength from 58 MPa to 39 MPa and 32 MPa, elongation-at-break from 2.5% to 1.8% and 1.8%, tensile modulus from 2.89 GPa to 2.46 GPa and 1.96 GPa, respectively [74]. The inclusion of 5% aspen wood flour in the PLA matrix decreased the tensile stress and strain, however, enhanced the elastic modulus of FDM-printed bars by 30% [38]. The tensile modulus of PLA/hemp and PLA/harakeke was improved with fibre content due to its high aspect ratio [70]. Shin [97] compared three types of bamboo flour (*Phyllostachys bambusoides*, *Phyllostachys nigra var. henonis*, and *Phyllostachys pubescens*) in PLA composites, with the bamboo flour/PLA ratios of 10/90, 20/80, and 30/70 in w/w. The result showed that 10/90 of *Phyllostachys bambusoides* flour/PLA was an optimal candidate for 3D printing filament due to the highest tensile strength. Daver *et al.* [18] found that FDM-printed parts of PLA/cork composites exhibited slightly lower elastic modulus and tensile yield strength, but higher elongation-at-break than compression-moulded items. The FDM-printed specimens from PLA-dried distillers grain with soluble (DDGS) showed lower tensile strength than neat PLA due to poor interfacial bonding between PLA and DDGS, whereas the samples had comparable Young's modulus and elongation-at-break to neat PLA [96]. PLA/beech wood filament exhibited an increase in tensile strength from 55 MPa to 57 MPa with the addition of 10 wt.% wood, then decrease to 30 MPa with 50 wt.% wood addition [72]. The addition of raw sugarcane bagasse (SCB) to PLA reduced the tensile strength and bending strength but improved the flexural modulus of FDM-printed samples [98]. The inclusion of 10 wt.% poplar powder decreased the impact strength of FDM-printed parts from 14 kJ/m^2 for PLA to 11 kJ/m^2 for PLA/poplar powder 10% [12] (**Figure 2-17**). The decrease in mechanical properties could affect the end-user application. The key limitation is the deteriorated toughness, which could not only affect the application of the material, but also decrease the processability and printability of the material.

The mechanical properties could be optimized by the printing parameters. The samples printed in parallel orientation had superior tensile strength than those printed in the cross and vertical direction [98]. Ayrilmis *et al.* [99] observed that the tensile strength, tensile modulus, flexural strength, and flexural modulus of 3D-printed

specimens from a commercial wood/PLA (30 wt.%/70 wt.%) composite filament all decreased with the increasing printing layer thickness (0.05 mm, 0.10 mm, 0.20 mm, and 0.30 mm) due to the increased porosity. To improve the toughness, Xie *et al.* [94] investigated glycerol and tributyl citrate as plasticizers for PLA/poplar wood flour filament, the filament with 4% tributyl citrate exhibited optimum tensile strength and breaking elongation. The incorporation of POE in PLA/poplar powder composites as a toughening agent improved the impact strength of FDM parts (**Figure 2-17**).

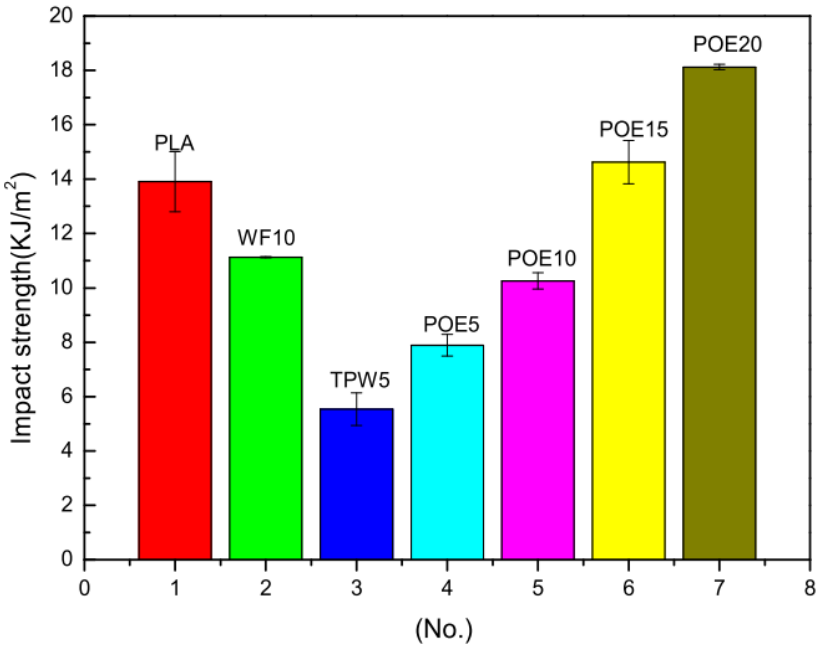

Figure 2-17 Impact strength of 3D printing PLA/poplar wood powder composites [12].

2.3.3.3 FDM-printed products: Surface finish

The addition of biomass filler affected the density and finish quality of FDM-printed items. The density of filament and FDM-printed parts decreased from 1.27 g/cm^3 and 0.63 g/cm^3 for neat PLA to 1.16 g/cm^3 and 0.48 g/cm^3 for PLA/50 wt.% beech wood powder, respectively, attributed to the relatively lower density of beech wood and poor melt flow at the nozzle with wood addition, resulting in unevenly filling in the FDM-printed parts [72]. The surface of FDM-printed items became rougher and uneven, more pores and voids were observed on the fracture surface with increasing biomass content [22, 70, 72], as shown in **Figure 2-18**, due to the decreased melt

flow. The pores acted as stress concentration points and affected the strength of printed parts. It is observed that the increasing printing layer thickness (0.05 mm, 0.1 mm, 0.2 mm, and 0.3 mm) resulted in increased surface roughness of the 3D-printed specimens using commercial wood/PLA (30 wt.%/70 wt.%) composite filament [100]. Pop *et al.*[101] compared PLA/PHA/Bamboo Fill filament from ColorFabb with PLA and ABS filaments on the structural changes and found that the materials underwent reorientations related to both tactility increase and crystallinity decrease during 3D printing extrusion, whereas ABS only undertook crosslinking due to butadiene segment. PLA/PHA/Bamboo Fill filament has the lowest density, the printed specimens have highest defects, whereas PLA printed samples have fewest defects. Both the filament and FDM-printed parts showed the highest water absorption and lowest thermal stability due to the presence of bamboo filler.

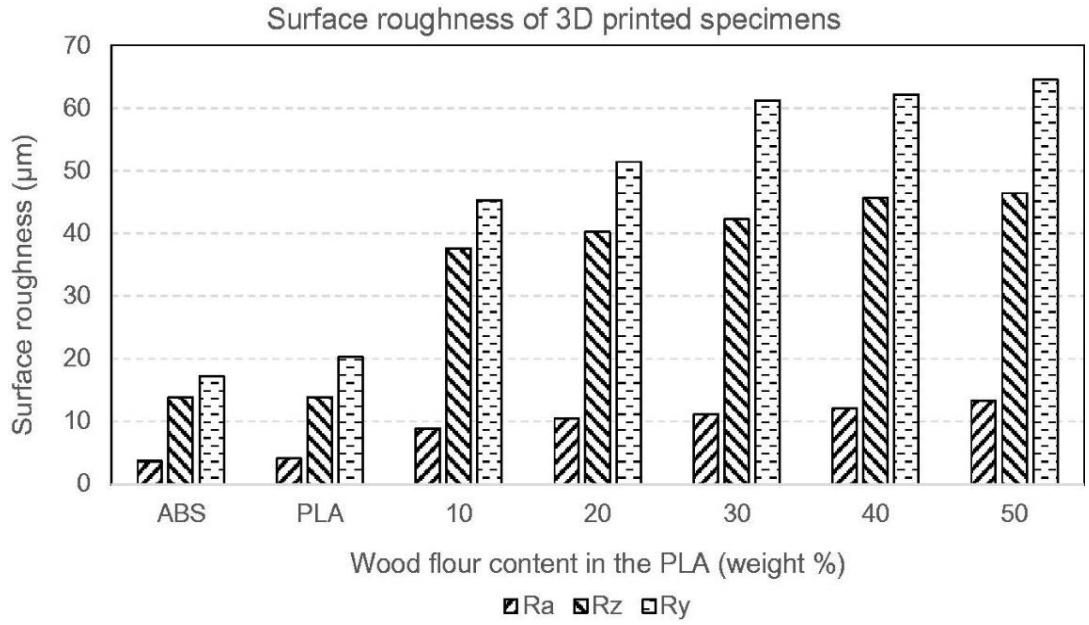

Figure 2-18 Surface roughness perpendicular to the printing direction of the FDM-printed specimens [22]. $\boldsymbol{R_a}$, the average arithmetic deviation of the profile, $\boldsymbol{R_z}$, the average peak to valley height and $\boldsymbol{R_y}$, the maximum peak-to-valley height.

2.4 PLA biocomposites: Improve toughness

As summarized in the previous sections, the increasing biomass loading and decreasing biomass particle size generally decreased toughness, including elongation-at-break and impact strength. The addition of biomass materials such as BP to PLA causes decreased impact strength [15, 102]. PLA/15 wt.% BP decreased

impact strength by approx. 44%, compared with neat PLA [15]. However, the printability and end-user application of FDM feedstock depend on the properties of feedstock, especially the toughness of the feedstock. Low-impact-strength biocomposite often breaks during filament extrusion and 3D printing. It is necessary to improve the toughness of PLA/biomass biocomposites for FDM application [8]. There are various strategies to enhance the toughness of PLA biocomposites, the toughening modification of PLA biocomposites have been conducted as summarized in **Table 2-7.** These strategies are focused on:

i) Surface treatment of biomass filler using alkalis [17, 65, 70]

ii) Compatibility improvement using coupling agents [11, 16, 64, 65, 71, 77], including lysine-based diisocyante (LDI), methylene diphenyl diisocyanate (MDI), PLA-g-MAH, and silane

iii) Improvement in elongation-at-break using plasticizers, such as PEG [11, 14, 103], it was observed that the melt flow was also improved with the inclusion of plasticizers

iv) Enhancing impact strength using toughening agents, such as poly (butylene adipate-co-terephthalate) (PBAT) [16, 17, 21, 104], an acrylic core–shell impact modifier BPM520 [20], polyolefin elastomer (POE) [9, 12], poly(ethylene–acrylic acid) copolymer (PEAA) [77], thermoplastic polyurethane (TPU) [71] and PCL [9, 71] as flexible elastomers

2.4.1 Surface treatment of biomass filler

The mechanical properties, including the tensile properties and impact strength, were improved with the alkali treatment of biomass filler [14, 17], as highlighted in **Figure 2-19** due to the enhanced interfacial adhesion.

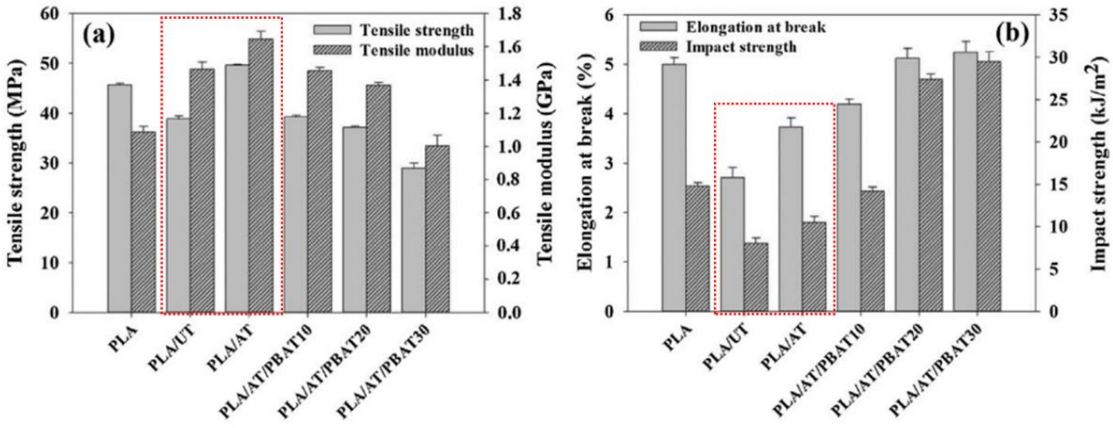

Figure 2-19 Mechanical properties of PLA and PLA/ironwood sawdust composites (a) tensile strength and tensile modulus and (b) elongation-at-break and impact strength [17].

Table 2-7 A summary of the modification of PLA biocomposites

Biomass species	Modifiers	Properties	Reference
Iron wood sawdust	Alkali treated, PBAT (10, 20, 30 wt.%)	Alkali treatment improved the mechanical properties of the PLA/Iron wood sawdust composites. The increasing PBAT content led to an increase in elongation-at-break and impact strength of PLA/sawdust composites, whereas decreased tensile strength and tensile modulus.	[17]
Poplar wood powder	NaOH treated, PLA-g-MAH	Tensile strength increased for PLA-g-MAH/WF, compared with PLA/WF.	[65]
Bamboo fibre	LDI	LDI improved the tensile properties and interfacial adhesion of PLA/BF.	[64]
American wood fibres	MDI, PEAA	MDI increased tensile strength and modulus. PEAA decreased tensile strength and increased impact strength.	[77]
Poplar wood flour	PCL, POE, TPU, GMA	TPU (28 MPa, 52 MPa, 10 kJ/m^2 for tensile, flexural, and impact strength, respectively) showed better mechanical properties improvement than PCL (4 kJ/m^2) and POE and exhibited higher complex viscosity, lower crystallinity. GMA is efficient to improve the tensile strength and impact strength.	[9]
Hemp hurd	GMA-g-PLA	GMA-g-PLA improved mechanical properties.	[68]
Jute fibre	PCL, trimethoxy (methyl) silane	Surface modification improved tensile strength and modulus, reduced impact strength. The addition of PCL recovered the impact toughness, without much sacrifice in stiffness and strength. Hybrid biocomposite with 10 wt.% PCL attained an optimum balance between stiffness and toughness.	[71]
Kenaf fibre	PBAT, (3-aminopropyl) trimethoxy silane (APTMS)	Tensile strength and modulus, flexural properties decreased, whereas impact strength increased with PBAT content, 2% (3-aminopropyl) trimethoxy silane obtained the best mechanical properties.	[16]
Micro/Nanocellulose (MNC)	Silane coupling agent KH-550, PEG	PEG improved MFR. 1% KH550 obtained best mechanical, 5% PEG6000 improve elongation-at-break, the other mechanical properties decreased with increasing PEG content.	[11]
Rubber wood sawdust	0.5-10% BPM520	Impact strength improved by BPM520.	[20]
Poplar powder	Lubricant (TPW604), POE	TPW604 improved the fluidity and impact strength of 3D printing materials. POE improved the fluidity and impact strength of 3D printing materials.	[12]

2.4.2 Coupling agents improve the interfacial compatibility

The effect of LDI and APTMS silane as coupling agents on the mechanical properties is shown in **Figure 2-20**, LDI improved the tensile properties of PLA/bamboo fibre composites with the increasing NCO content due to the enhanced interfacial adhesion [64], 2 wt.% (3-aminopropyl) trimethoxy silane obtained the optimum mechanical properties for PLA/PBAT/Kenaf fibre composites [16]. The addition of MDI also improved tensile strength, tensile modulus, and elongation-at-break of PLA/WF biocomposites due to the enhanced interfacial adhesion between wood flour particles and PLA matrix, the impact strength increased when the wood flour content increased to greater than 20 wt.% [77].

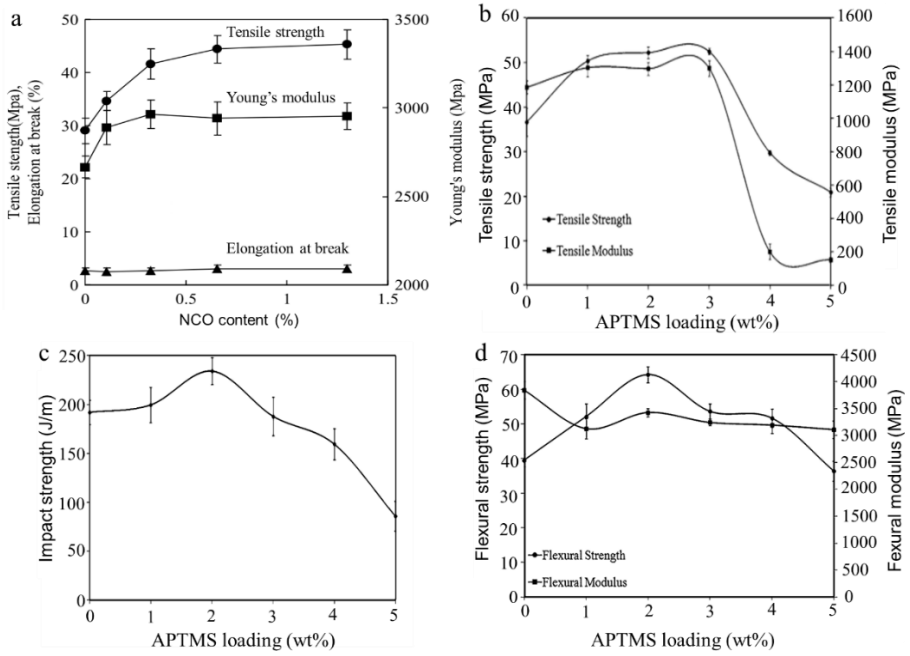

Figure 2-20 (a) Tensile properties of PLA/BF composites as a function of NCO content [64], (b) tensile properties, (c) impact strength, and (d) flexural properties of PLA/PBAT/Kenaf fibre as a function of APTMS loading [16].

2.4.3 Plasticization of PLA

The addition of plasticizers, such as PEG improved elongation-at-break [11, 14], as shown in **Figure 2-21**, it is observed that with the inclusion of 5 wt.% PEG6000, the elongation-at-break reached maximum from 8.9% of micro/nanocellulose-PLA (MNC/PLA) without PEG to 11.9%, the melt flow was also improved from 0.17 g/10 min to 0.57 g/10 min [11]. Between the PEG6000, PEG10000 and PEG20000,

PEG20000 was the best plasticizer. 10 wt.% PEG20000 increased the elongation-at-break by 56%, it is also observed that 5 wt.% PEG20000 improved MFR of PLA/bamboo fibre composites [14].

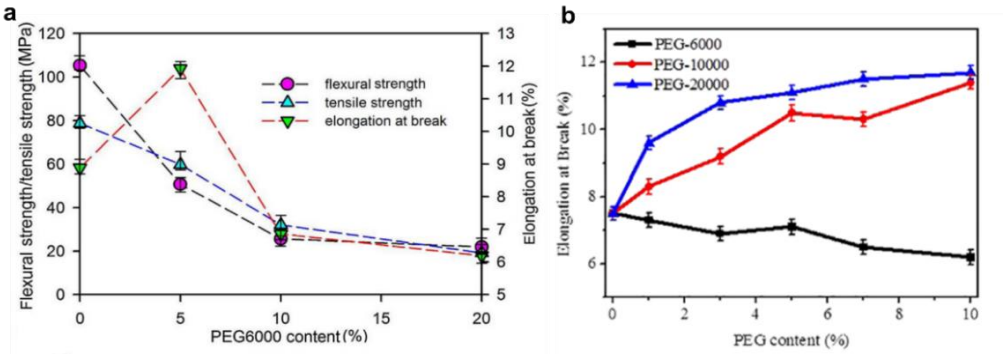

Figure 2-21 The effect of PEG content on elongation-at-break of (a) MNC/PLA composite [11] and (b) PLA/bamboo fibre composites [14].

2.4.4 Toughening agents

To address the toughness loss of PLA caused by the incorporation of biomass filler, melt blending with flexible polymers [20, 77, 104-110], which act as stress concentration sites, is a common technique to improve the brittleness resistance of biocomposites, and to produce continuous and constant-diameter filaments. Flexible polymers, such as PEAA [77], TPU [9, 71], POE [9, 12], acrylic impact modifiers (ACR) [20, 105, 111], PBAT [16, 17, 21, 104], ethylene glycidyl methacrylate (EGMA) [107], PCL [9, 71], and polyhydroxyalkanoates (PHAs) [83] , have been applied to improve the toughness of PLA biocomposites, as summarized in **Table 2-7**.

The addition of toughening agents to PLA biocomposites increased the elongation-at-break and impact strength, while decreased tensile strength and modulus, together with decreased flexural strength and modulus. PEAA increased the elongation-at-break and impact strength of PLA/WF composites, although decreased tensile strength and tensile modulus, however, when the wood flour content increased to and above 30 wt.%, the tensile modulus was higher than PLA/WF composites without PEAA [77]. TPU was a more efficient toughening agent for PLA/wood flour biocomposites than PCL and POE, with 51.3% increase in impact strength [9]. However, increasing POE content led to improved impact strength for PLA/poplar

powder 3D printed materials [12]. The addition of ACR (core−shell ratio = 79.2/20.8) to PLA (PLA/ACR = 80/20) achieved a notched Izod impact strength of 77 kJ/m^2 [111]. The addition of 5 wt.% acrylic core-shell impact modifier (BPM520) led to a five-fold increase in the impact strength of PLA, and further enhanced the impact strength (**Figure 2-10d**) and elongation-at-break (**Figure 2-7a**) of PLA/rubber wood sawdust composites [20].

The incorporation of biodegradable polymers to PLA biocomposites is an efficient way to improve toughness without sacrificing its biodegradability. PBAT is a candidate for toughening PLA based lignocellulosic filler biocomposites. The increasing PBAT content increased elongation-at-break and impact strength of PLA/PBAT blend [16, 112]. The addition of PBAT in PLA also increased melt elasticity and viscosity of PLA/PBAT, together with improved processability [112]. The evidence of PBAT toughness enhancement was also observed in PLA/sawdust (**Figure 2-19**) [17], PLA/ramie composites (**Figure 2-22a**, **b**) [104] and PLA/bark flour of plane tree biocomposites (**Figure 2-22c**) [21]. The combination of EGMA, with functional glycidyl methacrylate (GMA) end groups, was effective for improving the interfacial adhesion and impact strength of PLA/PBAT blend [108, 109], and PLA/PBAT biocomposites [68, 69, 107, 113, 114]. EGMA is an efficient compatibilizer for PLA/sisal fibre, where EGMA enhanced the interfacial interaction between PLA and sisal fibre, improved the toughness (impact strength) of PLA/sisal biocomposites without significant reduction in stiffness. The impact strength of PLA/sisal biocomposites with 10 wt.% EGMA was more than three times higher than the biocomposites without EGMA, due to effective energy dissipation [107].

Melt blending of PLA with PCL is an economic way to gain toughness while maintaining biodegradability, compared to plasticization and copolymerization. PCL is a flexible and biodegradable aliphatic polyester [115] synthesized by ring-opening polymerization of caprolactone and has elongation-at-break of about 600% [116], which is widely used for toughening PLA [117-120]. The addition of PCL also resulted in increased melt flow rate (MFR) for the biocomposites [120, 121], which is favourable for forming a more stable flow pattern at the nozzle when used for 3D printing [122]. PCL increased the impact strength of PLA/jute fibre composites, 10 wt.% PCL obtained the optimal balance between stiffness and toughness (**Figure 2-22d**) [71]. Nevertheless, the addition of PCL to PLA/WF biocomposites decreased

the impact strength due to the poor interfacial compatibility [9]. PLA and PCL, however, are immiscible polymers, the obtained phase-separation blends exhibited limited enhancement in toughness [123, 124].

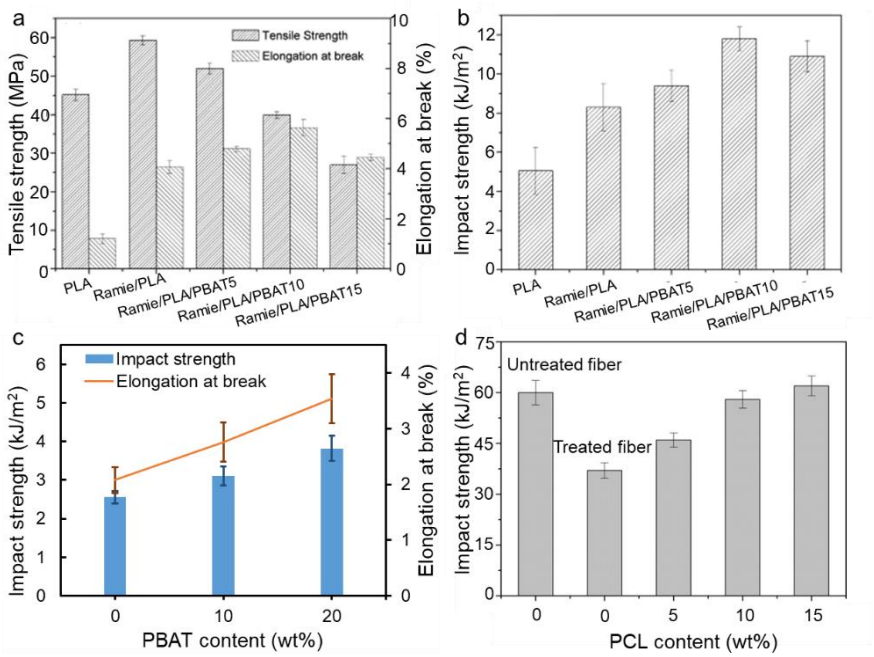

Figure 2-22 (a) Tensile properties and (b) impact strength of PLA/ramie composites [104], impact strength of (c) PLA/bark flour of plane tree composites [21] toughened by PBAT and (d) PLA/jute fibre composites toughened by PCL [71].

To address this phase-separation and concomitantly achieve the desirable toughness, lactide/caprolactone copolymers with segments identical to PLA and PCL are used for compatibilization [117, 125-128]. A summary of the literature on lactide/caprolactone copolymer compatibilization is presented in **Table 2-8**. The copolymer compatibilizer segments tend to interact with their blend counterparts while residing at the interface and interpenetrating to PLA and PCL phases, concurrently enhancing the interfacial adhesion and therefore, improved impact strength and ductility [117]. Stereocomplexation between the PLLA (industrialized PLA) and PDLA enantiomers is also deemed to be beneficial to achieve the enhanced interfacial adhesion and mutual interaction between components and contributed to the toughness of PLA [129, 130]. The core-shell structure of P[CL-co-LA] as core and PDLA as shell [129], Poly(butyl acrylate) grafted PDLA [130], four-armed PCL-b-PDLA [131] and PDLA-PEG-PDLA tri-block copolymer [132]

improved mechanical properties of PLA due to the stereocomplexation between PLA and PDLA.

Table 2-8 A summary of the previous work in compatibilization of PLLA/PCL by lactide/caprolactone copolymers

Ref	Method	Performance
[125]	4 wt.% of triblock PLLA-PCL-PLLA copolymer blended with PLA and PCL (70/30) by melt mixing	● Enhanced toughness of PLA/PCL blend ● Elongation-at-break increased from 2% to 53% ● Impact strength increased from 1.1 to 3.7 kJ/m^2
[117]	PLA/PCL (80/20) toughened with l-lactide/caprolactone (LACL) copolymer via solution mixing, casting, and conditioning compression	● LACL enhanced dispersion of PCL in PLA increased crystallinity of PLA ● 5 wt.% LACL increased elongation-at-break by >100% ● Decreased tensile strength and modulus
[126]	Random copolymer P(LLA-co-εCL) and diblock copolymer P(LLA-b-εCL) (0, 5, 10, and 15 phr) as compatibilizers for PLLA/PCL (70/30) via solution casting	● Both copolymers enhanced compatibility between PCL and PLLA ● P(LLA-co-εCL) caused more pronounced reduction in domain size of PCL and molecular weight of PLLA/PCL films during hydrolysis
[127]	Lactide-Caprolactone copolymer (LACL) mixed with PLA/PCL blend using solution mixing and fabricated via solution casting	● LACL exhibited compatibilization effect on the immiscible PLA/PCL blend by promoting the nucleation of PLA with higher nuclei density
[128]	Poly(l,l-lactide-co-ε-caprolactone) [P(lLA-co-εCL)] (0, 5, 10, and 20 phr) mixed with PLLA/ PCL (50/50) via solution-casting method	● Enhanced compatibility in PLLA/PCL blend ● Lower recrystallization temperature after the inclusion of P(LLA-co-εCL)
[133]	PLLA/PCL films blended with and without 10 wt.% poly(l-lactide-co-εcaprolactone) via solution casting	● Poly(l-lactide-co-ε-caprolactone) increased compatibility and elongation-at-break of PLLA/PCL blends
[129]	PLLA toughened using Poly(*ε*-caprolactone-*co*-lactide)-*b*-PDLA core−shell rubber particles (0, 5, 10, 15, and 20 wt.%) via solution blending	● PDLA shell facilitated core−shell rubber particle/PLLA interaction via stereocomplexation ● Over 10-fold increase in elongation-at-break ● Young's modulus and tensile strength retained

2.5 Literature review: Synopsis

Summing up, 3D printing technology is gaining importance because of its rapid-prototyping, freedom in design, the ability to produce complex geometries, and

reduced wastage and cost in comparison with conventional processes. The limitations of 3D printing technologies are:

i) High cost because of the use of laser for SLA and SLS
ii) Limited accessibility of the materials for SLA and SLS, the feedstock for SLA is a cytotoxic UV resin
iii) Insufficient strength and low printing resolution for 3DP parts

3D printing technologies are mainly utilised in: i) prototyping, ii) product design and iii) innovation areas, iv) also well utilized in industrial and business machines, and v) aerospace industries and medical fields. A majority of the 3DP products are still used as conceptual prototypes rather than functional components because of the insufficient strength and functionality of the products 3D printed by pure polymer products.

FDM technology, using thermoplastic as feedstock, is widely applied due to its simplicity, cost-effectiveness, and feedstock accessibility. PLA is the most common feedstock for FDM. PLA/biomass biocomposites are gaining increasing interest due to their reduced cost, sustainability, and retaining the biodegradability of materials, compared with PLA. The effect of biomass addition, including the biomass content and particle size on the properties, including melt flow and mechanical properties of PLA biocomposites was reviewed. The printability, mechanical properties, and surface quality of FDM-printed parts were summarized for biocomposites applied in FDM. The addition of biomass filler decreased the melt flow and the toughness of PLA biocomposites, whereas the effect of particle size of biomass on PLA biocomposites has rarely been investigated. Due to the decrease in the toughness of PLA biocomposites filled with biomass, the toughening of PLA biocomposites is necessary for the application in FDM [8] to address the brittleness which may cause challenges during filament manufacturing and FDM printing. The effect of toughening on PLA biocomposites as FDM feedstock has not been reported. For improving the compatibility between PLA and PCL, and further improving the toughness of PLA/PCL/biomass biocomposites, lactide/caprolactone copolymers were applied as compatibilizers. Whether lactide/caprolactone copolymer compromises in miscibility or compatibility while modifying toughness in PLA/PCL blends, and the formation of stereocomplex crystallites between PDLA segment in the copolymer and PLLA in the matrix, require further exploration.

Chapter 3: Research objectives

This chapter identifies the research gaps and presents the objectives of this research thesis.

3.1 Research gaps

The incorporation of biomass in PLA is favourable for achieving inexpensive, sustainable, and biodegradable biocomposites feedstock for FDM. To improve the utilization of biomass filler in FDM, the high loading level of biomass is expected to address the cost of feedstock because of cost-effective biomass in comparison to PLA baseline polymer, whereas the relationship between the biomass content, specifically the hemp hurd (HH) and bamboo powder (BP) content, and the comprehensive properties of PLA biocomposites as FDM feedstock has not been systematically investigated. The particle size of biomass is a factor in tailoring the surface roughness of FDM-printed items, and hence the mechanistic relationship between the particle size and properties of PLA biocomposites requires further investigation. Due to the decrease in toughness, which may cause the filament to break during manufacturing and FDM printing, the toughening of PLA biocomposites is necessary. Although there are various methods to improve the toughness of PLA/biomass, the investigation on the effect of toughening agents on the printability of biocomposites as FDM feedstock and the mechanism have not been reported in the literature. There are still several research gaps that remain to be explored:

I. Effect of toughening on the printability and mechanical properties of PLA/biomass biocomposites as FDM feedstock and the mechanisms require investigation.

II. For PDLA-PCL-PDLA (PCDL) tri-block copolymers as compatibilizers for PLA biocomposite toughened by PCL, the efficacy of compatibilization and related mechanisms are not clear.

III. The relationship between the loading levels of HH and BP and the comprehensive performance (printability, toughness, and surface finish) of PLA/biomass biocomposites as FDM feedstock and the mechanisms require investigation.

IV. The relationship between HH and BP particle sizes and comprehensive performance (printability, toughness, and surface finish) of PLA/biomass biocomposites as FDM feedstock and the mechanisms require further investigation.

3.2 Research objectives

The aims of this thesis are i) to facilitate the application of biomass filler (HH and BP) in PLA biocomposite to produce sustainable and cost-effective feedstock for FDM and ii) to disclose the underlying mechanisms of the influences of biomass powder (HH and BP) addition and toughening agents (PBAT, PCL/PCDL, and BPM520) on properties of PLA biocomposites feedstock. The main objectives of the thesis are:

i. Improve toughness of PLA biocomposites using PBAT/EGMA, BPM520, and PCL, investigate the compatibilization efficacy of PCDL tri-block copolymers on PLA/PCL blend and PLA/PCL/biomass biocomposites, inspect the melt flow, processability, filament quality, and mechanical properties of the FDM-printed specimens, and select the toughening agent for further study.

ii. Prepare toughened PLA/HH and PLA/BP biocomposites using melting-compounding and extrusion, which is a common way to manufacturing FDM feedstock and filament in industry. Examine the effects of biomass loading levels from 10 phr to 40 phr on the processability, printability, and thermal/mechanical properties of PLA biocomposites, filament quality, and finish quality of FDM-printed parts, aiding the understanding of mechanisms through the analysis of rheological behaviour, crystallization behaviour, interfacial adhesion, and interface morphology.

iii. Investigate the relationships between biomass particle sizes (100 mesh, 200 mesh, and 300 mesh) and the processability, printability, and thermal/mechanical properties of PLA biocomposite, filament quality, and finish quality of FDM-printed parts, and gain a greater understanding of mechanisms through the analysis of rheological behaviour, crystallization behaviour, particle distribution, and interface morphology.

3.3 Research workflow

An overview of the research workflow in this study is presented as a schematic in **Figure 3-1**, which summarizes the background experimental methods to be employed in this research for achieving the objectives. The first step details the preparation and characterization of biomass powder and PCDL. The biomass powder was prepared by jet milling and sorting using vibrating screens (100, 200, and 300 mesh). The particle size, morphology, moisture, chemical composition, thermal properties, and density were determined. PCDL was synthesized by ring-opening polymerization of D-lactide using HO-PCL-OH diol as a macroinitiator. The molecular weight, chemical structure, thermal properties, and chemical compositions were examined by gel permeation chromatography (GPC), H nuclear magnetic resonance (HNMR), differential scanning calorimetry (DSC), and Fourier transform infrared (FTIR), respectively.

The second step presents the preparation and characterization of PLA biocomposites pellets. Firstly, toughened PLA biocomposites (with 20-phr BP inclusion) by PBAT/EGMA, BPM520, and PCL were produced and compared. The investigation of PCDL as a compatibilizer in PLA/PCL and PLA/BP/PCL was also presented. Secondly, 0, 10, 20, 30, 40 phr of HH or BP with a volume-medium-diameter of 50 μm were incorporated in PLA/PBAT/EGMA matrix for examining the effect of the biomass loading levels on the comprehensive properties of PLA biocomposites. Thirdly, 20 phr HH or BP with various particle sizes were incorporated in PLA/PBAT/EGMA matrix for inspecting the effect of the biomass particle sizes on the comprehensive properties of PLA biocomposites. The melt flow, rheological properties, and thermal/mechanical properties were analysed.

In the third step, the biocomposite pellets were extruded to standard filament for quality evaluation and FDM-printed as ASTM-standard specimens for examination. The injection-moulded (IM) specimens were also fabricated for comparison. The filament quality, the finish quality of FDM-printed parts, the interface morphology and mechanical properties of both IM and FDM-printed items were investigated.

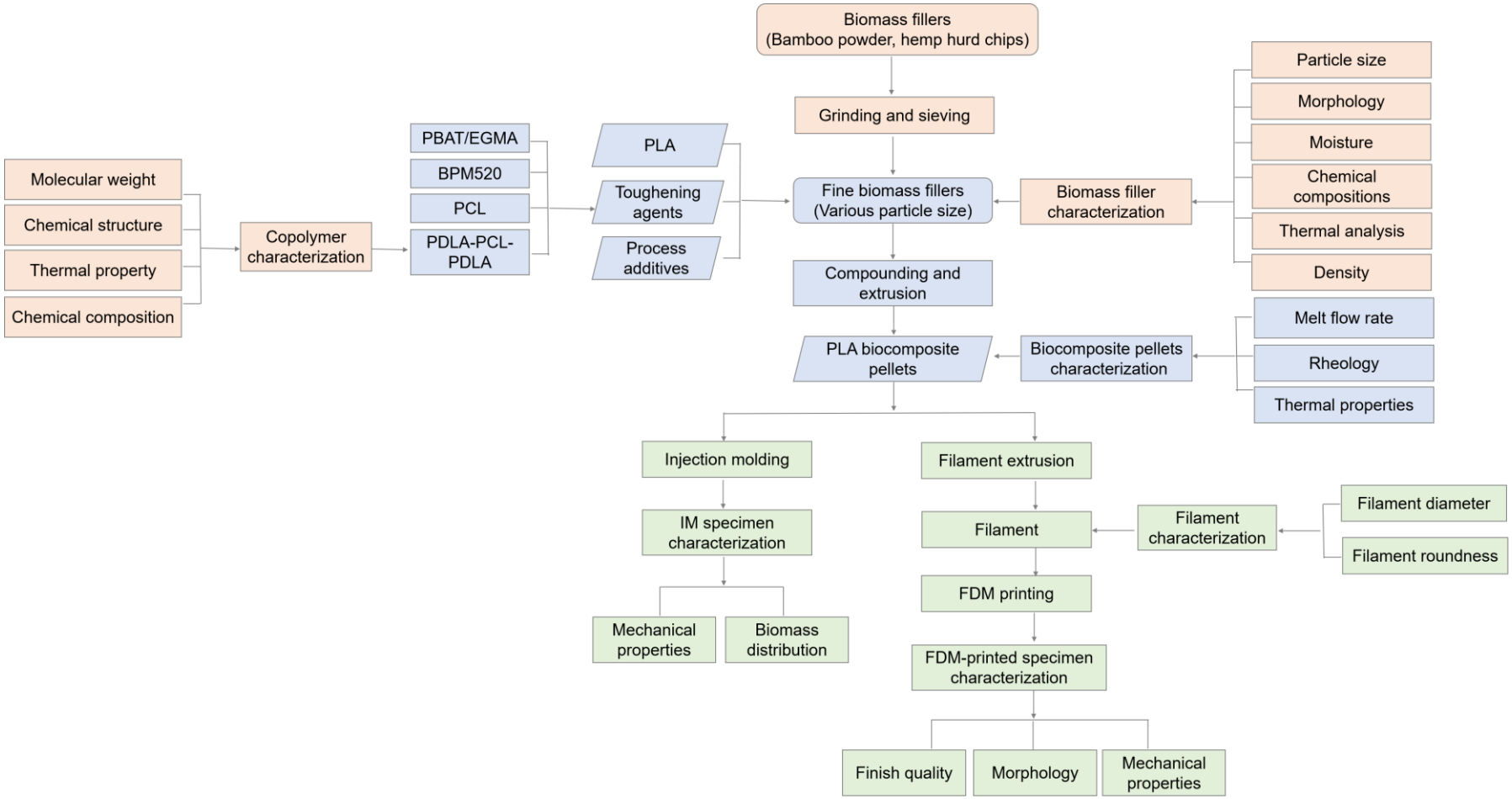

Figure 3-1 Schematic of experimental framework of this research work.

Chapter 4: Materials and Methods

This chapter presents the details of the constituent materials, the preparation procedures of PLA/biomass biocomposites and FDM filament, the fabrication of standard specimens for testing, and characterization methodologies used in this research. Subsequent chapters will reference materials and methods where appropriate.

4.1 Materials

The materials used in this research include PLA matrix, toughening agents, including PBAT combined with EGMA, BPM520, and PCL, biomass powder, including BP and HH, processing additives, including antioxidant, lubricant, and anti-hydrolysis agent, and PCDL tri-block copolymers as a compatibilizer for PLA/BP/PCL biocomposites.

PLA used in this work was grade 4032D (approx. 98.5% L-lactide, PLLA), which is purchased from NatureWorks LLC, USA and widely used as feedstock for 3D printing filament. PBAT includes various grades according to its end-user applications. Biocosafe 2003F (film grade, MFR = 4.2 g/10 min at 190°C/2.16 kg), procured from Xinfu Pharmaceutical Co., Ltd, China, was used as one of the toughening agents, together with random terpolymer EGMA (grade AX 8900, with 68 wt.% ethylene, 24 wt.% methyl acrylate and 8 wt.% glycidyl methacrylate, Arkema, Inc., France) as compatibilizer. The number-average molecular weight and polydispersity index of AX 8900 were 4.5×10^4 g/mol and 5.01, respectively. PLA and PBAT were dried to reduce moisture to below 0.5 wt.% before processing. A commercial core-shell acrylic impact modifier BPM520 (trade name, PARALOID) supplied by Dow Chemical Company was compared with PBAT. The shell component of BPM520 is poly(methyl methacrylate), and the core is poly (butyl acrylate). PCL (grade CAPA6500, MFR = 7 g/10 min at 160°C/2.16 kg) purchased from Perstorp UK Ltd. was used as a toughening agent as well. The molecular structure of the neat polymers is shown in **Figure 4-1**. The physical and melt properties of polymers are shown in **Table 4-1**. The commercial PLA (natural) filament from Shenzhen Esun Industrial Co., Ltd. (eSun) was used for comparison, as shown in **Figure 4-2**. Processing additives were applied to improve processability

and biocomposite stability during processing. Anti-hydrolysis agent (Carbodiimide, CARBODILITE HMV-15CA) was provided by Nissinbo Chemical Inc., antioxidants (1010 and 168) and lubricant (EBS) were also commercial products. These additives were used as received.

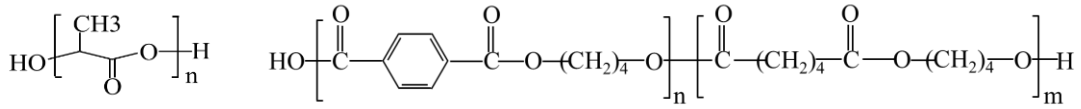

PLA **PBAT**

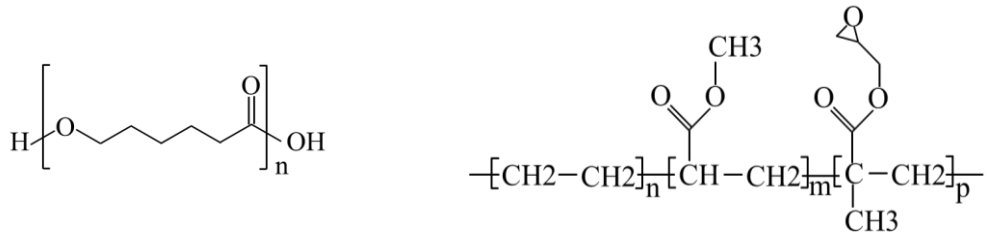

PCL **EGMA**

Figure 4-1 Molecular structure of PLA, PBAT [134], PCL and EGMA [107].

Table 4-1 Thermo-physical properties of the materials from commercial vendors

Grade	MFR (g/10 min)	Density (g/cm^3)	T_g (°C)	T_m (°C)
Ingeo® 4032D	7.0 (210°C, 2.16 kg)	1.24	65	167
Biocosafe® 2003F	4.2 (190°C, 2.16 kg)	1.23	-29	113
Lotader® AX8900	6.0 (190°C, 2.16 kg)	0.95	-	65
CAPA 6500	28 (190°C, 2.16 kg)	1.14	-60	60-62

* Melt flow rate (MFR) of 2003F was tested using melt flow indexer.

Figure 4-2 Commercial PLA filament from eSun.

HH and BP were investigated for producing the biocomposite feedstock for 3D printing in this research. Industrial HH is a lignocellulosic by-product of hemp bast fibre production with no major end application and constitutes 60 wt.% – 80 wt.% of the dry mass of the hemp (Cannabis sativa) stem [135]. HH contains 40%–48% cellulose, 18%–24% hemicellulose and 21%–24% lignin [136], which is a relatively higher fraction of cellulose and comparable lignin as wood, thus possessing a greater reinforcement potential [137] and emerging as a valuable substitute for wood in PLA-based composites. HH was provided in chips form (**Figure 4-3a**) by Yunnan Dama Co., Ltd, China, and milled by a jet grinder as HH powder with volume-median-diameter (d_{50}) of 90 µm (**Figure 4-3b**). The main components of BP are cellulose (60%), lignin (20%–30%) and hemicellulose (10%-20%) [138]. BP with indicative particle sizes of 300 mesh (d_{50} = 58 µm, **Figure 4-3c**) was purchased from Zhejiang Jinque bamboo powder factory, China. HH (90 µm) and BP (58 µm) were vibration-sieved and passed through screens of 100, 200 and 300 mesh sequentially. The particle size distribution of the obtained biomass powder is shown in **Table 4-2**. The volume-median-diameter is denoted as equivalent to the d_{50} size. Although HH and BP were sorted by the screens with the same sizes of 100, 200 and 300 mesh, the obtained HH showed higher particle size and particle size distribution (span) compared to BP. The only exception being the powder passed through 200 mesh, which showed a similar particle size distribution. All BP exhibited similar particle size distributions with a similar span around 2.04. HH exhibited increasing span with

increasing particle size from 2.12 for HH-1 to 2.34 for HH-4, HH-3 showed a higher span of 2.45 because it is not vibration-sieved. HH and BP were characterized in detail in Chapter 5 and dried to a moisture level below 0.5 wt.% before extrusion.

Figure 4-3 Digital images of as-received (a) HH chips, (b) HH powder, and (c) BP.

Table 4-2 Particle size distribution of HH and BP (d_{10}: 10th percentile, d_{50}: median size, d_{90}: 90th percentile)

Biomass powder	Specification	Particle Size (μm)			Span
		d_{10}	d_{50}	d_{90}	$((d_{90}- d_{10})/d_{50})$
HH-1/35 μm	300 mesh	9	34	81	2.12
HH-2/50 μm	200-300 mesh	12	48	115	2.15
HH-3/90 μm	Before sieving	16	91	239	2.45
HH-4/160 μm	100-200 mesh	49	163	430	2.34
BP-1/20 μm	300 mesh	5	21	48	2.05
BP-2/50 μm	200-300 mesh	14	51	118	2.04
BP-3/65 μm	100-200 mesh	15	67	152	2.04

PCDL tri-block copolymers employed as compatibilizers for PLA/PCL and PLA/BP/PCL biocomposite in this research were synthesized in the laboratory of eSun and characterized detailed in Chapter 5. The copolymers were synthesized by ring-opening polymerization of D-lactide using poly(ε-caprolactone) diol (HO-PCL-OH) as macro-initiator and Tin (II) bis(2-ethyl hexanoate) as the catalyst, as shown in **Figure 4-4**. The viscosity-averaged molecular weight ($\overline{M}_\eta$) of HO-PCL-OH initiator used in this research was 8k and 10k, determined according to the GB/T 37642-2019 standard. PLLA-PCL-PLLA using HO-PCL-OH with $\overline{M}_\eta$ of 10k as macro-initiator was also synthesized for comparison. The viscosity-average molecular weight of HO-PCL-OH and the ratios of feed compositions are listed in **Table 4-3**. The copolymers have tri-block architecture comprising of a central PCL block and two PDLA or PLLA blocks on two ends, respectively. The chemical structure and properties of copolymers are presented in **Table 4-4**.

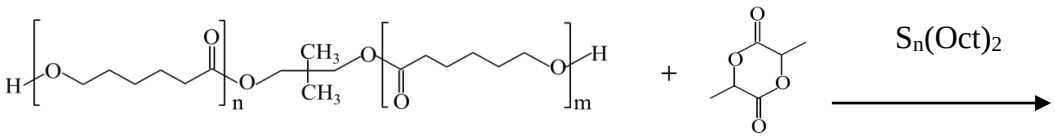

HO-PCL-OH **D-lactide**

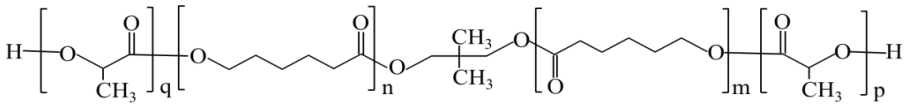

PDLA-PCL-PDLA (PCDL)

Figure 4-4 **S**ynthesis of PCDL.

Table 4-3 The compositions of PCDL tri-block copolymers

Sample	Macro initiator	$\overline{M}_\eta$ of macroinitiator [a]	Macro initiator/Lactide (w/w) [b]
PDLA-PCL_{8k}-PDLA/$PCDL_{8k}$	HO-PCL_{8k}-OH	7555	0.286
PDLA-PCL_{10k}-PDLA/$PCDL_{10k}$	HO-PCL_{10k}-OH	11231	0.400
PLLA-PCL_{10k}-PLLA/$PCLL_{10k}$	HO-PCL_{10k}-OH	11231	0.393

[a, c] The viscosity-average molecular weight of HO-PCL-OH and copolymers were obtained according to the internal analysis method of eSun.

[b] $PCLL_{10k}$ used L-lactide for polymerization, others used D-lactide.

Table 4-4 The characteristics of PCDL tri-block copolymers

Sample	$\bar{M}_n$ [a] (g/mol)	$\bar{M}_w$ [a] (g/mol)	PDI [a]	CL content [b] (mol%)	DLA content [b] (mol%)	T_{cc} (°C)	T_m [c] (°C)	*TS* [d] *(MPa)*	ε_b (%)
$PCDL_{8k}$	40062	55780	1.39	25.5	74.5	91.0	170.8	25.5	27.2
$PCDL_{10k}$	34218	47817	1.40	34.9	65.1	78.4	168.7	12.3	14.0
$PCLL_{10k}$	32004	45776	1.43	34.2	65.8	80.8	168.1	16.9	60.6

[a] Number-averaged molecular weight ($\bar{M}_n$), weight-averaged molecular weight ($\bar{M}_w$) and molecular weight distribution/polydispersity (PDI, $\bar{M}_w / \bar{M}_n$) were measured by GPC in THF using polystyrene standards.

[b] CL contents and DLA contents were calculated from H NMR results using the integration ratio of the bands due to PDLA blocks at 5.16 ppm and to PCL blocks at 4.07 ppm or 2.3 ppm.

[c] T_{cc} and T_m were measured by DSC (second heating).

[d] TS (tensile strength) and elongation-at-break (ε_b) were provided by eSun.

4.2 Preparation of PLA biocomposites and FDM filaments

The biocomposites FDM feedstock was produced using a two-step process as shown in **Figure 4-5**. Firstly, PLA biocomposites were produced by melt-compounding and melt-extrusion of PLA, toughening agent, additives, and biomass powder through a co-rotating twin-screw extruder (L/D = 44, D = 35 mm). PLA, PBAT, BPM520, PCL and PCDL were dehydrated to eliminate moisture to below 200 ppm. BP and HH powder were dried to a moisture level below 500 ppm prior to use. Additives were used as received. The extrusion temperature was controlled at nine contiguous zones along the extruder barrel, and a die to obtain an overall temperature profile in the range of 165°C – 175°C. The co-rotational speed of the screw was around 144 rpm. The biocomposites were pelletized after wind-cooling. Then tests on the melt flow rate, rheological properties, and thermal properties of the biocomposites pellets were conducted. Subsequently, the biocomposite pellets from the previous stage were extruded as filament using a 3D printing filament extrusion line with a single screw (L/D = 28, D = 35 mm). The temperature of the extrusion barrel zones was set at 170°C, 175°C, 175°C, 180°C and 175°C from the feeder to the die, with a screw rotational speed around 364 rpm. The filament was drawn and cooled through a

water bath maintained at 60°C using a drawing speed around 351 rpm, the filament with a designed diameter of 1.75 mm was collected on a spool for FDM printing.

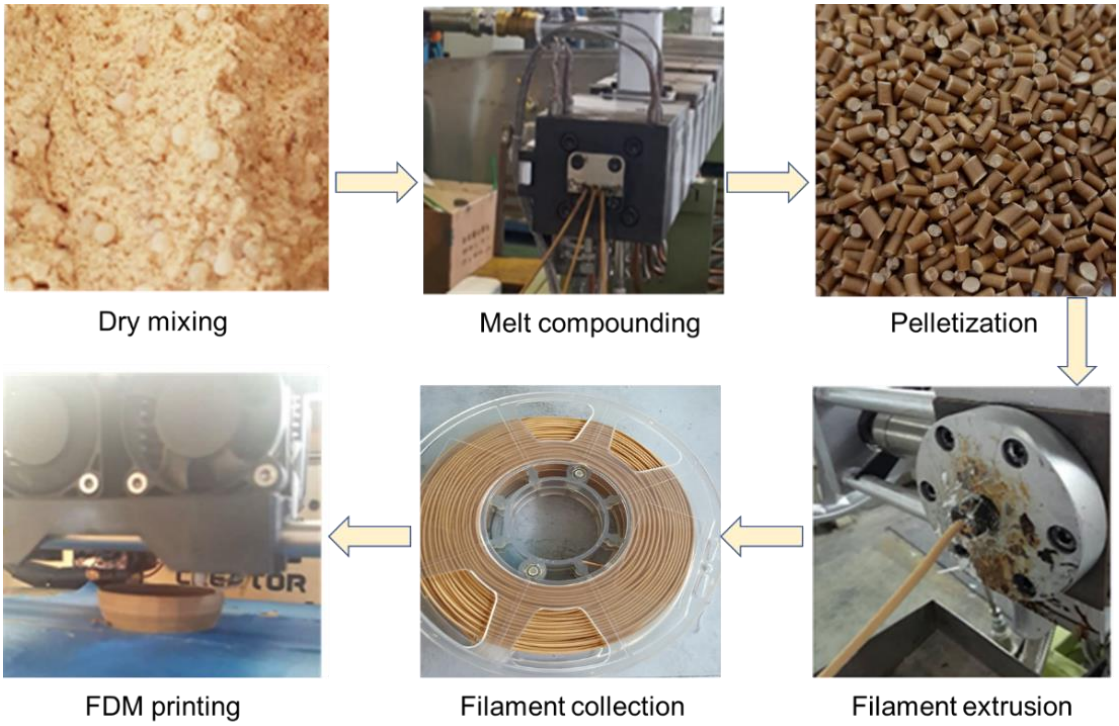

Figure 4-5 The manufacturing process of biocomposite filament.

4.3 Fabrication of test specimens

The biocomposite pellets from the first extrusion stage were also injection moulded to ASTM standard specimens, including tensile (166 mm × 19 mm × 4.2 mm, Type I, ASTM D 638), notched impact (63 mm × 12.7 mm × 4.2 mm, ASTM D 256), and flexural (100 mm × 12.7 mm × 4.2 mm, ASTM D 790) specimens, using an injection moulding machine (JT-350, Jintong Plastic Machinery Ltd., China) with barrel temperature set at 165°C, 175°C, 175°C, and 182°C and a mould temperature of 45°C. The 3D models of the specimens (**Figure 4-6**) were computer modelled and exported as a stereolithographic file (STL) and fabricated by a 3D da Vinci 1.0 professional printer (XYZ Printing, Inc., Thailand) (**Figure 4-7** left) in a flat orientation along the z-direction as shown in **Figure 4-6**, the build and print orientations of specimens are shown in **Figure 4-8**. The 3D printer had a nozzle diameter of 0.40 mm, the nozzle temperature, heat bed temperature, infill density, layer thickness, and print velocity were set at 200°C, 60°C, 100%, 0.15 mm, and 60 mm/s, respectively. The print temperature set at 200°C is better for tensile and

flexural properties [139]. The specimens with BP at different particle size were FDM-printed by Z-603S printer (JG AURORA, China) (**Figure 4-7** right**)** using an interwoven type of infill. This 3D printer also had a nozzle diameter of 0.40 mm, the nozzle temperature, heat bed temperature, infill density, layer thickness, and print velocity were set at 200°C, 60°C, 100%, 0.15 mm, and 30 mm/s, respectively. The print parameters are summarized in **Table 4-5**. Specimens were printed at room temperature and humidity conditions, with at least five specimens for each sample.

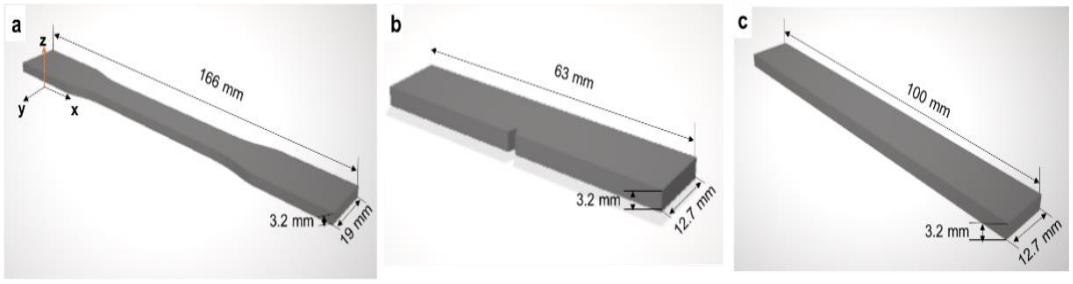

Figure 4-6 The computer-modelled standard (a) Tensile, (b) Impact, and (c) Flexural specimens.

Figure 4-7 3D da Vinci 1.0 professional printer (left) and Z-603S printer (right).

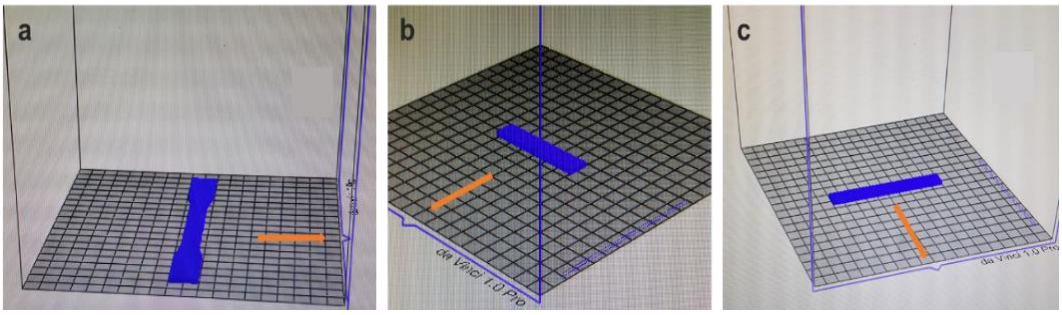

Figure 4-8 The build and print orientations of specimens: (a) tensile, (b) impact, and (c) flexural specimens.

Table 4-5 3D printing parameters on 3D da Vinci 1.0 professional printer and Z-603S printer

XYZ 3D da Vinci 1.0 professional printer		JG AURORA Z-603S printer	
Nozzle temperature	200°C	Printing temperature	200°C
Bed temperature	60°C	Bed temperature	60°C
Shell print speed	30 mm/s	Print speed	30 mm/s
Fill print speed	60 mm/s	Layer height	0.15 mm
Top shell fill print speed	30 mm/s	Shell thickness	1.2 mm
Bridge print speed	20 mm/s	Bottom/Top thickness	0.8 mm
Layer height	0.15 mm	Fill density	100%
Normal shell height	2 layers	Flow	100
Top/Bottom shell height	3 layers		
Fill density	100%		
Fill type	Interwoven		

4.4 Characterization

The following methods were used for the characterization and analysis of the constituent materials, biocomposites pellets, FDM filament, IM specimens and FDM-printed specimens to determine their thermo-physical and mechanical properties.

4.4.1 Physical properties of raw materials

4.4.1.1 Particle size distribution

The particle size and distribution of HH and BP were measured using a dynamic laser particle size analyser (Mastersizer 2000, Malvern Instruments Ltd.) with a size range resolution of 0.02 µm to 2000 µm. The intercepts for 10%, 50%, and 90% of the cumulative volume of the powder were calculated using the vendor software and translated as d_{10} (particle size at 10% undersize), d_{50} (particle size at 50% undersize), and d_{90} (particle size at 90% undersize). Water was used as the dispersant with a refractive index of 1.34.

4.4.1.2 Moisture content

The moisture content of HH and BP was analysed using SFY-20A Halogen Rapid Moisture Analyzer (Hangzhou Hengqing Technology Co. Ltd.) through heating to a temperature of 105°C for 40 s.

4.4.1.3 Bulk density

Bulk density of HH and BP powder was determined by calculating the weight of the powder in a 100 mL measurement column, the average value of three measurements was used for the calculation of bulk density (ρ_b) (**Equation 1**).

$$\rho_b = \frac{(m_1 + m_2 + m_3)/3}{v} \qquad (1)$$

where v is the volume of the powder, which is 100 mL, m_1, m_2, m_3 are the weight of the powder obtained by 3 measurements, respectively.

4.4.1.4 Average molecular weight and molecular weight distribution

The average molecular weight and molecular weight distribution of PCDL and PCLL copolymers were measured by GPC using a PL-GPC 50 system (Polymer Laboratories) equipped with a refractive index detector. Tetrahydrofuran (HPLC grade, Fisher Scientific, U.K.) was used as mobile phase at a flow rate of 1.0 ml/min, column temperature was 40°C, injection volume was 100 µl. Separations were performed with 2 PLgel 5 µm Mixed-C columns (Polymer Laboratories). Molecular weight analysis was performed using the Cirrus GPC Version 4.3 software, which

provided information on several different molecular weight parameters, i.e., $\bar{M}_n$, peak molecular weight (M_p), and $\bar{M}_w$.

4.4.2 Chemical analysis

4.4.2.1 Chemical composition

FTIR spectra of HH and BP, and PCDL tri-block copolymers were collected on a Bruker Vertex 70 spectrometer (Germany) in the transmittance mode from 400 cm^{-1} to 4000 cm^{-1}, the samples were homogenized and pressed on KBr powder. IRAffinity-1S FTIR spectrometer (Shimadzu, Japan) was used for the spectra collection of IM and FDM-printed specimens for PLA/HH in the transmittance mode with a resolution of 4 cm^{-1} in the range from 400 cm^{-1} to 4000 cm^{-1} using a GladiATR 10 accessory from Shimadzu. Each spectrum was the aggregate of over 40 scans, and the transmittance was recorded as a function of wavenumbers and transformed to absorbance.

4.4.2.2 Chemical structure

The chemical structure of PCDL tri-block polymers was determined by a Varian 400 MHz ^1H NMR at room temperature used chloroform-*d* ($CDCl_3$) as the solvent. Chemical shifts were reported in parts per million (ppm) downfield from TMS with the solvent resonance as the internal standard (δ = 7.26 ppm).

4.4.3 Thermal analysis

4.4.3.1 MFR

MFR is a measure of the rheological properties and processability of the polymer [140]. MFR measurement was carried out on a melt flow indexer (Taian Ontime Testing Machine Manufacturing Co., Ltd, XNR-400C) at condition E (190°C, 2.16 kg), according to ASTM D1238.

4.4.3.2 Rheological properties

Rheological properties provide information on the viscoelastic behaviour, interfacial interaction [141] and processability of components [142]. The rheology analysis was conducted on a DHR-2 (TA Instruments, USA) rheometer equipped with a parallel-plate diameter of 25 mm and a sample gap of 1 mm was used. Dynamic frequency sweep mode was carried out from 0.01 Hz to 100 Hz at 190°C with a strain

amplitude of 1%. The steady-state shear rheological properties were investigated on MCR502, Anton Paar, Austria, using parallel plates (25 mm diameter and 1 mm sample gap) at 190°C. Dynamic frequency sweep mode (0.01−100 Hz) was used at a strain of 1%.

4.4.3.3 Melt torque

Melt torque measurement was carried out in an XSS-300 torque rheometer (Shanghai Kechuang Rubber Plastic Mechanical Equipment Co., Ltd., China). The biocomposites pellets were melt-extruded through an LSJ 20 plastic extruder with a single-screw diameter at 20 mm and L/D of 25:1, the temperature was set at 150°C, 170°C, 175°C, 175°C from the feeder to the die, and the screw rotational speed was 60 rpm. The melt torque of PLA/PCL blend and PLA/BP/PCL biocomposite was recorded during melt mixing in the torque rheometer.

4.4.3.4 Thermal transition temperatures and melting characteristics

Thermal transition temperatures and melting characteristics of copolymers, HH, PLA/PCL blends, and PLA biocomposites were measured using Q20 differential scanning calorimeter (DSC, TA Instruments, Inc.) under nitrogen atmosphere (50 ml/min). A cycle of heating/cooling/heating (20°C, maintained 2 min to 200°C, maintained 5 min, cool to 20°C, maintained 2 min, then heat to 260°C, maintained 2 min) was used for copolymers, PLA/PCL blends and PLA biocomposites. A cycle of heating/cooling/heating (40°C, maintained 2 min to 180°C, maintained 2 min, cool to 20°C, maintained 2 min, then heat to 260°C, maintained 2 min) was used for HH. The temperature ramp rate was 10°C/min. The cold crystallization enthalpy (ΔH_{cc}) and melting enthalpy (ΔH_m) were derived from the second heating. The degree of crystallinity (X_c) of the PLA phase was calculated using **Equation 2** [68].

$$X_c\ (\%) = \frac{(\Delta H_m - \Delta H_{cc})}{\Delta H_m^{\circ} w} \times 100 \qquad (2)$$

where ΔH_m° is the melting enthalpy of 100% crystalline L-PLA (93 J/g) [68], and *w* is the weight fraction of PLA in the blends and biocomposites.

4.4.3.5 Thermal stability

The thermal stability of HH and BP powder, IM and FDM-printed specimens of PLA/HH biocomposites was evaluated by thermogravimetric analysis (TGA Q500, TA instruments) from room temperature (~25°C) to 700°C at a heating rate of 10°C/min under air atmosphere. TGA analysis of PLA/PCL blends and PLA biocomposites was performed on TA Q50 thermogravimetric analyser from 30°C to 500°C at a heating rate of 10°C/min under nitrogen atmosphere. The weight-loss rate was obtained from the first derivative thermogravimetric (DTG) curves. The onset degradation temperature (T_{onset}) was defined as the intersection of the baseline weight from the beginning of the experiment and the tangent of the weight dependence on the temperature curve as decomposition occurs. The temperatures of 5% (T_5) and 50% (T_{50}) weight loss were collected from the weight loss curves, and the maximum thermal degradation temperature (T_{max}, the point of the greatest rate of change on the weight loss curve) was also collected from the peaks on the DTG curves.

4.4.4 Crystalline analysis

X-ray diffraction (XRD) was used for phase identification of crystalline materials. XRD analysis of PLA, PLA/PCL blends, HH and PLA/HH biocomposites were conducted on a Bruker D8 Advance diffractometer with Cu-K_α radiation (λ = 1.54 Å) under room temperature. X-ray scan was operated at 40 kV and 30 mA over a 2θ range between 10° and 60° at a scan of 3°/min (0.4 sec/step) and step size or increment at 0.02°. The scan range of PLA/PCL/PCDL blends was between 5° and 40° at a scan speed of 2°/min.

4.4.5 Mechanical properties

Tensile and flexural properties were measured using a CMT 6104 universal testing machine (MTS Systems, China) equipped with a 10 kN load cell, according to ASTM D 638 and ASTM D 790 standard method, respectively. Tensile testing was performed at a crosshead speed of 5 mm/min. The tensile testing for type 5B specimens cut from the hot-pressing sheet was performed according to the standard of GB/T1040.1-2006 at a crosshead speed of 1 mm/min. Flexural properties testing was carried out at a loading speed of 1.27 mm/min.

Notched Izod impact testing was performed following the ASTM D 256 standard, using an XJJU 5.5 J pendulum (Chengde COTs Scientific Instruments Co., Ltd., China) at ambient temperature and humidity. The impact strength was calculated using the absorbed energy divided by the width of the specimen. At least five specimens for each sample were tested, the average value was reported. The specific mechanical properties were obtained by dividing the mechanical properties by their density, which in turn were calculated by dividing the mass of flexural specimens by its bulk volume [42].

4.4.6 Morphological observations

The morphologies of HH and BP powder and the cryo-fractured surfaces of IM specimens and hot-pressing specimens were observed and analysed on a SU3500 scanning electron microscope (SEM, Hitachi), at an accelerating voltage of 15 kV. The powder was pasted on the carbon-based conductive adhesive. The impact fractured surfaces of FDM-printed specimens were observed and analysed by a JEOL JCM6000 SEM operated at 5–15 kV to preclude sample charging. The surfaces of samples were sputter-coated with a gold layer prior to SEM observation to provide enhanced conductivity.

4.4.7 Printability and finish quality

4.4.7.1 Filament quality

Filament quality, including filament diameter and roundness, is critical for FDM printability. Inconsistent diameter and roundness potentially cause unsteady extrusion, resulting in jamming or clogging in a 3D printing job. Filament diameter was measured using a digital Vernier calliper, the measurement was taken at three locations for each position, and the average value was reported. The diameter tolerance was obtained by subtracting the formulated diameter (1.75 mm) from each average value. The roundness of filament was calculated by subtracting the minimum diameter from the maximum diameter obtained at the three locations at the same test point, according to the GB/T 37644-2019 standard.

4.4.7.2 Surface roughness of FDM-printed parts

The surface roughness of FDM-printed specimens was determined by the stylus method using a MarSurf M 400 unit. The tracing speed, stylus tip diameter, and tip

angle were 1.0 mm/s, 2 μm and 90°, respectively. A trace length of 17.5 mm was used. Four roughness parameters specified in ISO 4287 standard, including arithmetic mean roughness (R_a), root mean square roughness (R_q), mean peak-to-valley height (R_z), and maximum peak-to-valley height (R_{max}), were measured to evaluate the surface characteristics of the specimens, respectively. R_a is the average of the absolute values of the profile deviations from the mean line and is by far the most used parameter in surface finish measurement. R_{max} can be used as an indicator of the maximum defect height within the measured profile.

4.4.7.3 Porosity and density of FDM-printed parts

Porosity is an indicator of the defects in the microstructure and affects the mechanical properties as an initiator of a failure mechanism. The porosity was calculated by dividing the difference in density between IM and FDM-printed specimens by the density of IM specimen, using **Equation 3**, by assuming that the IM samples were of negligible porosity [143]. The density was obtained by dividing the weight of flexural specimens by its bulk volume [42] on five specimens; the average density was reported for the calculation. The porosity fields in the IM specimens were characterized using X-ray computer tomography (CT) technique.

$$\text{Porosity (\%)} = \frac{(\rho_{\text{Injection}} - \rho_{\text{FDM}})}{\rho_{\text{Injection}}} \times 100 \qquad (3)$$

The density was also determined using Archimedean immersion method. The density was determined using a balance with a precision of 0.1 mg at a condition of 25°C, 60 RH% and calculated using the following **Equation 4**.

$$\rho_{\text{sample}} = \rho_{water} \left(\frac{m_{air}}{m_{air} - m_{water}}\right) \qquad (4)$$

Where ρ_{water} was the density of water (1 g/cm^3) at the test condition, m_{air} was the weight weighed in the air, and m_{water} was the weight weighed in the water.

The porosity fields in the FDM specimens were also characterized via X-ray computed tomography (CT) using a General Electric Phoenix v|tome|x s instrument operating at the micro-level. Scans were performed at 50 kV and 90 μA with a voxel

size of 8.0 μm. Two-dimensional (2D) sectional images were extracted and used to identify microstructural features in the specimens. A 3D volumetric representation of the specimens was constructed by collating the image projections. The X-ray CT data used to characterize the microstructure and the porosity in the FDM specimens was determined using the Porosity/Inclusion Analysis Module in the VolMaxStudio 3.0 Program.

4.4.7.4 Shrinkage of FDM-printed parts

Shrinkage indicates the dimensional accuracy or shape error of FDM-printed products. Besides aesthetics, thermo-physical properties of the finished products are key considerations for fit-and-form applications or products with intricate features [144]. Shrinkage was calculated by measuring the dimensional difference of FDM-printed flexural specimen against the intended specimens in length direction [145], according to ASTM D 955-08, using **Equation 5**.

$$S = \frac{L - L_0}{L_0} \times 100 \qquad (5)$$

Where L is the actual length of the FDM-printed specimen, L_0 is the intended length of the specimen, in this research, L_0 was constant at 100 mm. Measurements were conducted on 5 specimens and the results were arithmetically averaged.

Chapter 5: Characterization of raw materials

This chapter presents the characteristics of the constituent materials, including i) the thermal properties of PLA and PCL; ii) the particle size distribution, morphology, moisture, bulk density, chemical compositions, and thermal properties of HH and BP; and iii) the average molecular weight and polydispersity, chemical structure, chemical compositions, and thermal transition temperatures of PCDL triblock copolymers.

5.1 PLA and PCL

5.1.1 Thermal transition and crystallization behaviour

The thermal transition and crystallization behaviour of PLA and PCL determined by DSC (2^{nd} heating) are shown in **Figure 5-1**. Neat PLA had a glass transition temperature (T_g) = 61°C and melting temperature (T_m) = 168°C, with a small melting peak and degree of crystallinity = 3.1%, there was no cold crystallization peak observed. Neat PCL showed T_m at 56°C, overlapped with the glass transition temperature of PLA.

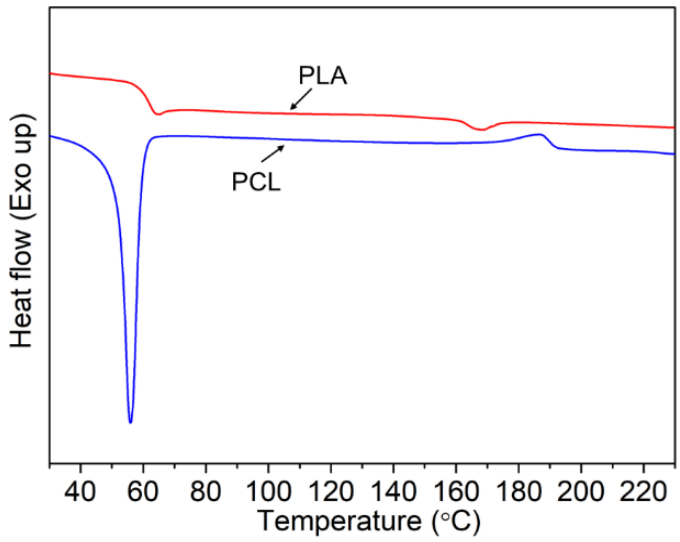

Figure 5-1 DSC curves of neat PLA and PCL.

5.1.2 Thermal stability

Thermal stability of PLA and PCL investigated by TGA is shown in **Figure 5-2**. PCL showed higher characteristic thermal decomposition temperatures than PLA,

indicating PCL has higher thermal stability than PLA. PCL exhibited lower residue than PLA. The data obtained from DSC and TGA are summarized in **Table 5-1**.

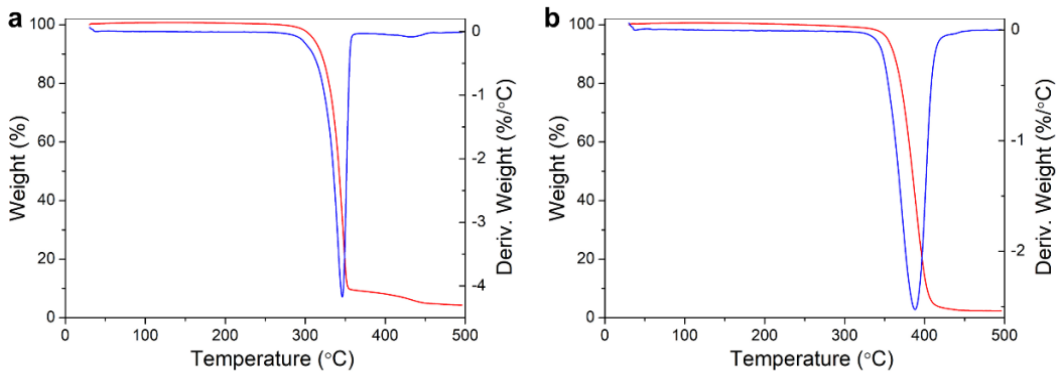

Figure 5-2 TGA and DTG curves of neat (a) PLA and (b) PCL.

Table 5-1 Thermal properties* of neat PLA and neat PCL

Sample	T_g (°C)	T_m (°C)	ΔH_m (J/g)	X_c (%)	T_{onset} (°C)	T_5 (°C)	T_{50} (°C)	T_{max} (°C)	Residue (@475°C)
PLA	62	168	2.90	3.1	331	310	342	347	4.53%
PCL	-	56	-	-	365	353	384	389	2.37%

* DSC data was obtained from the second heating cycle.

5.2 Hemp hurd and bamboo powder

5.2.1 Particle size and distribution

The particle size distribution graphs of HH and BP are shown in **Figure 5-3** and summarized in **Table 4-2**. Although HH and BP were sorted by the screens with the same sizes of 100, 200 and 300 mesh, the obtained HH showed higher particle sizes. Overall, the d_{50} of HH-1 (passed 300 mesh), HH-2 (200-300 mesh), and HH-4 (100-200 mesh) were 35, 50, and 160 µm, respectively, whereas the d_{50} of BP-1 (passed 300 mesh), BP-2 (200-300 mesh), BP-3 (100-200 mesh) were 20, 50, and 65 µm, respectively. Only the biomass powder passing through 200 mesh showed a similar particle size (d_{50} = 50 µm).

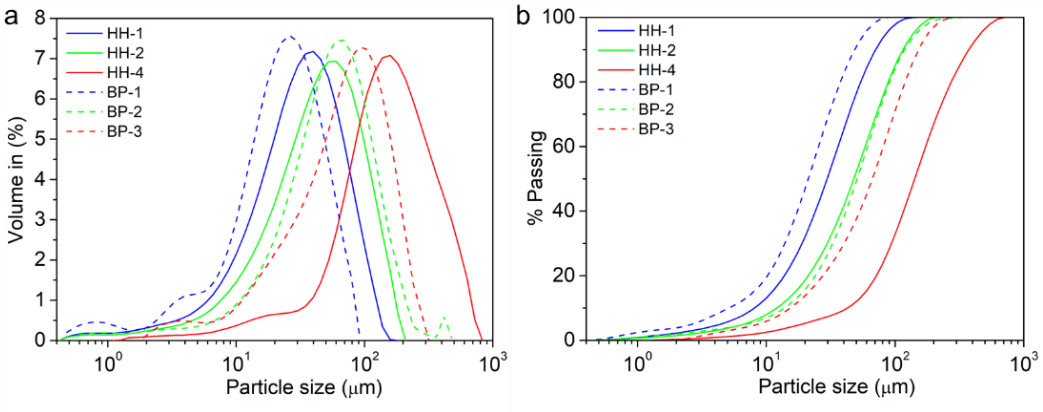

Figure 5-3 Particle size distribution comparison between HH and BP passed the screen with the same sizes: (a) volume in percentile and (b) passing percentile.

5.2.2 Morphology

The micro-morphology of HH and BP was observed by SEM. BP displayed particle shape with a few of fibrous structure under SEM (**Figure 5-4**), HH possessed fibrillary and channel structure (**Figure 5-5**) with a higher aspect ratio (*l*/*d*) than BP, and the length increased with an increasing particle size which supported the results of particle size distribution. The existence of a large particle size of HH could be explained by their higher aspect ratio that allowed them to pass through the mesh during the sieving step.

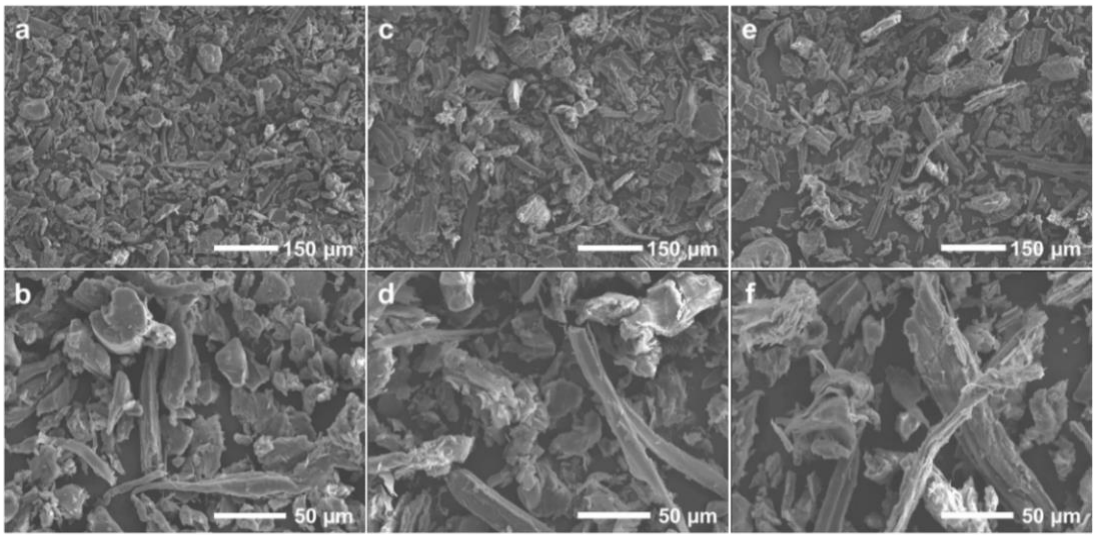

Figure 5-4 SEM images of (a, b) BP-1, (c, d) BP-2, and (e, f) BP-3 at magnifications of 150× and 500×.

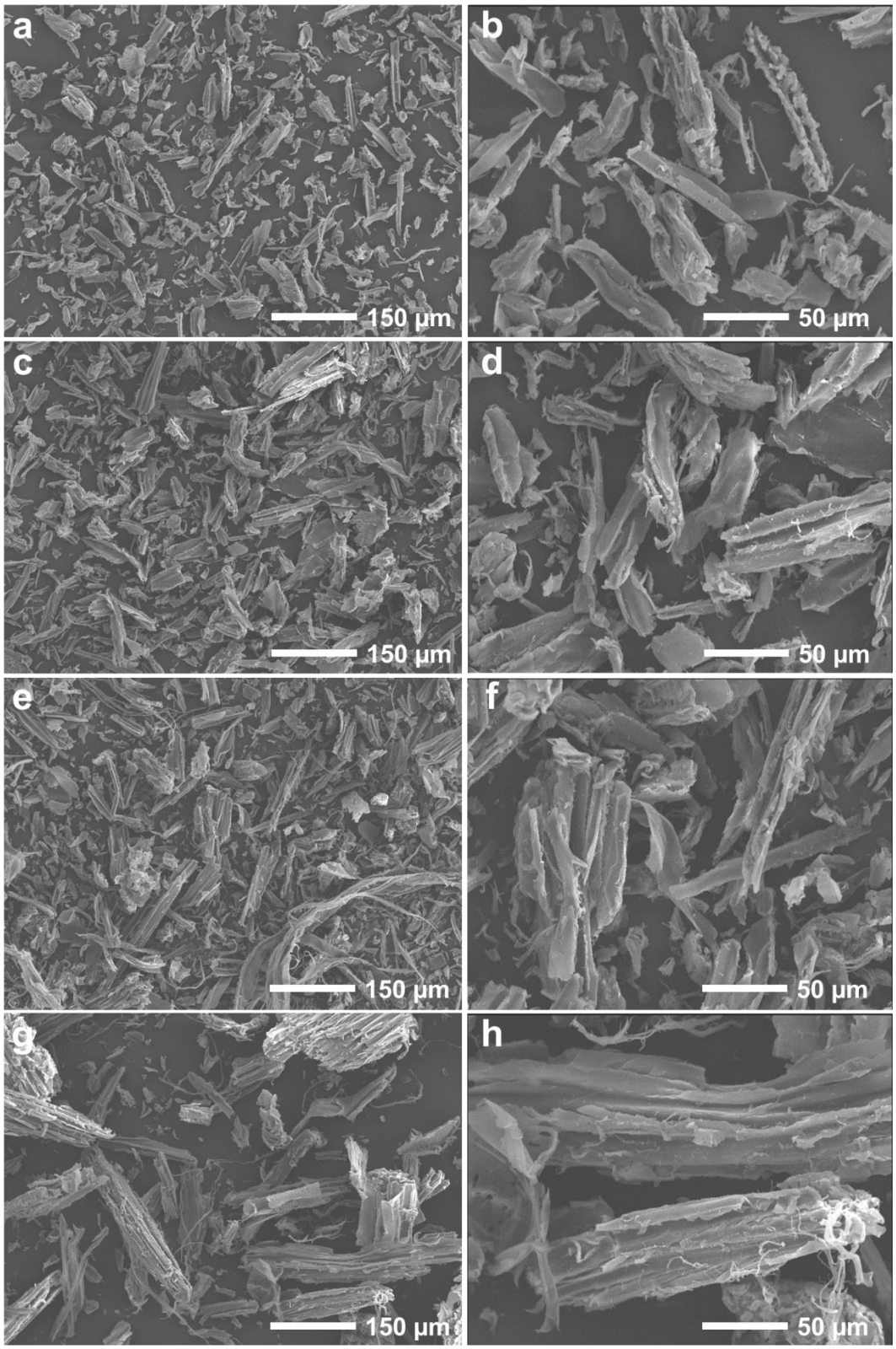

Figure 5-5 SEM images of (a, b) HH-1, (c, d) HH-2, (e, f) HH-3, and (g, h) HH-4 at magnifications of 150× and 500×.

5.2.3 Moisture and bulk density

The residual moisture in the biomass filler can interfere with the chemical and physical phenomenon at the polymer/filler interface. HH had higher original moisture than BP, as shown in **Table 5-2**. The moisture content reflects the natural tendency of biomass to absorb and adsorb moisture. Regardless of the initial condition, processing requires drying the fillers to remove the moisture to a level below 0.5 wt.% prior to use. Bulk density is shown in **Table 5-2**, close to the density of 0.118 g/cm^3 for HH [137, 146], and 0.300 g/cm^3 for BP [147]. HH exhibited a volume over double of BP with the same weight (**Figure 5-6**) due to the lower apparent density through the lesser packing efficacy of HH attributed to the particle size and morphological differences [148].

Table 5-2 Bulk density and moisture content of HH and BP

Source	Specification (mesh)	Bulk density (g/cm^3)	Moisture (%, 105°C, 40 s)	
			Average	Std. Dev.
HH-1	300	0.130±0.005	8.76	0.31
HH-2	200-300	0.128±0.001	9.05	0.01
HH-4	100-200	0.142±0.003	8.86	0.16
BP-1	300	0.277±0.005	6.53	0.31
BP-2	200-300	0.248±0.004	6.71	0.13
BP-3	100-200	0.246±0.005	7.26	0.68

Figure 5-6 Digital photos of (1) HH and (2) BP with the same weight showing the difference in bulk density between HH and BP.

5.2.4 Chemical compositions

The chemical compositions were determined using FTIR spectroscopy. HH and BP have similar FTIR spectra, as shown in **Figure 5-7**, indicating they were approximately equivalent qualitatively, except the carbonyl (C=O at 1728 cm^{-1}) and hydroxyl groups (O-H at 3323 cm^{-1}) were more pronounced in HH than BP, indicating that there is a higher ratio of polysaccharides and hemicellulose in HH than in BP, which is consistent with the literature [136, 138]. The main functional groups of biomass powder observed in FTIR spectra were identified referenced with Stevulova's work [136], as shown in **Table 5-3**, which supported that the main architectural components of HH and BP are cellulose, lignin, hemicelluloses [136, 138] and polysaccharides.

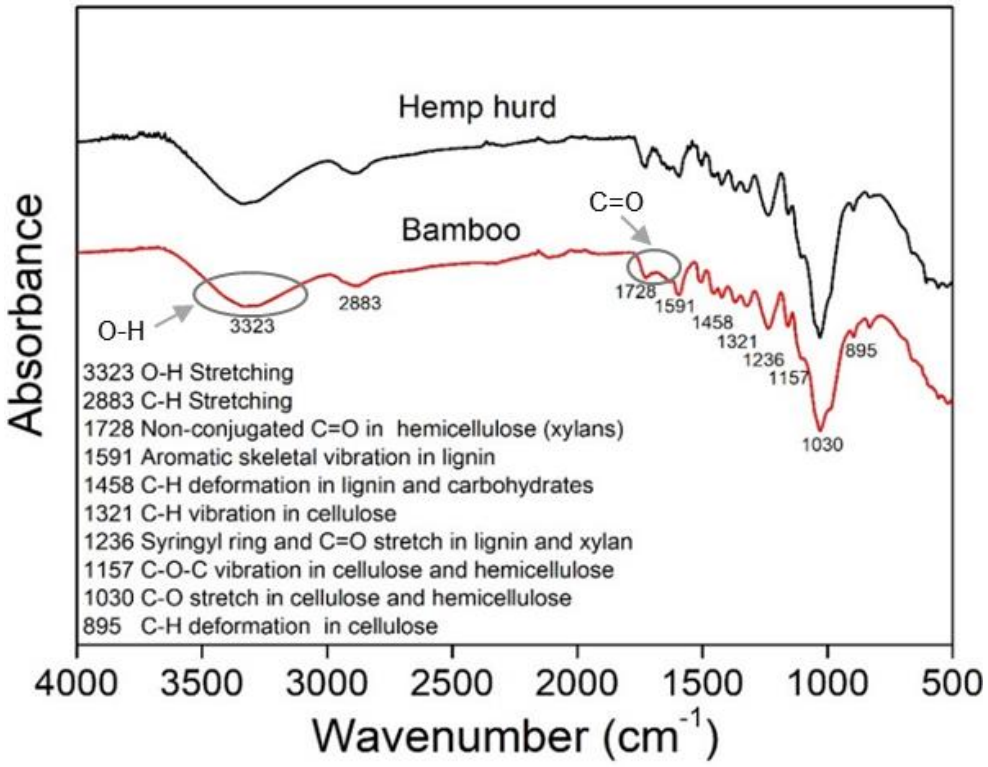

Figure 5-7 FTIR spectra of HH and BP.

Table 5-3 Main functional groups observed in FTIR spectra of HH (A: amorphous; C: crystalline) [136]

Wavenumber (cm^{-1})	Vibration of functional group	Source
3340	O-H stretching	polysaccharides
2897	C–H symmetrical stretching	polysaccharides
1733	C=O unconjugated stretching	hemicellulose
1636	OH (water)	cellulose
1507	C=C symmetrical stretching of the aromatic ring	lignin
1454	CH_2 bending	lignin
1422	CH_2 bending	cellulose
1373	CH bending	cellulose
1337	OH in-plane bending	cellulose (A)
1320	CH_2 wagging	cellulose (C)
1265	CO stretching	lignin
1157	C–O–C asymmetric bridge oxygen stretching	cellulose
1028	C–C, C–OH, C–H ring and side group vibrations	hemicellulose, pectin
896	Glycosidic bonds symmetric ring-stretching mode	polysaccharides

5.2.5 Thermal stability

The thermal stability of HH and BP was evaluated by TGA, as presented in **Figure 5-8**, the characteristic thermal temperatures are summarized in **Table 5-4**. HH had a lower onset temperature (296°C) and higher residual weight at 600°C (2.27%) than BP (300°C, 1.80%). HH exhibited a two-step degradation with two maximum decomposition peaks at 360°C and 461°C, with respect to 353°C and 454°C for BP, respectively, due to the decomposition of cellulose and lignin [62, 149].

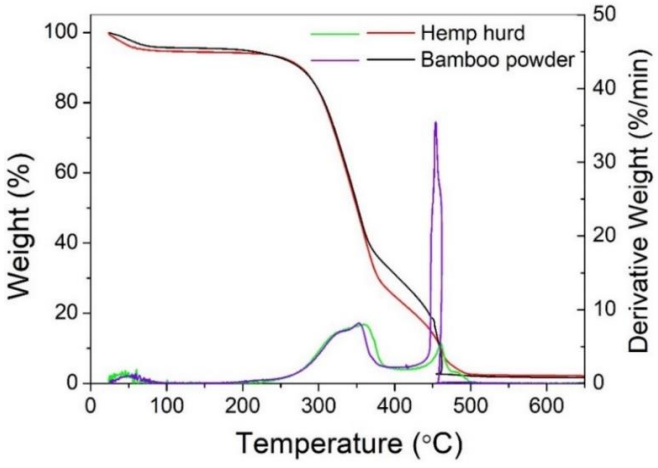

Figure 5-8 TGA and DTG curves of HH and BP (d_{50} = 50 μm for both).

Table 5-4 TGA characteristic parameters of HH and BP

Biomass	T_5 (°C)	T_{onset} (°C)	T_{50} (°C)	T_{max1} (°C)	T_{max2} (°C)	Residue (%) (@600°C)
HH	75	296	350	360	461	2.27
BP	193	300	351	353	454	1.80

5.2.6 Thermal transition and crystallization behaviour

DSC thermographs of HH are shown in **Figure 5-9**. There was no thermal transition during the second heating, indicating there is no crystallization occurred. The endothermic peak on the first heating curve was owing to the evaporation of water, which was also proved by TGA result. BP also exhibited an endothermic peak between 40 and 120°C on the DSC thermogram obtained from the first heating, which was not shown on the thermogram from the second heating [150].

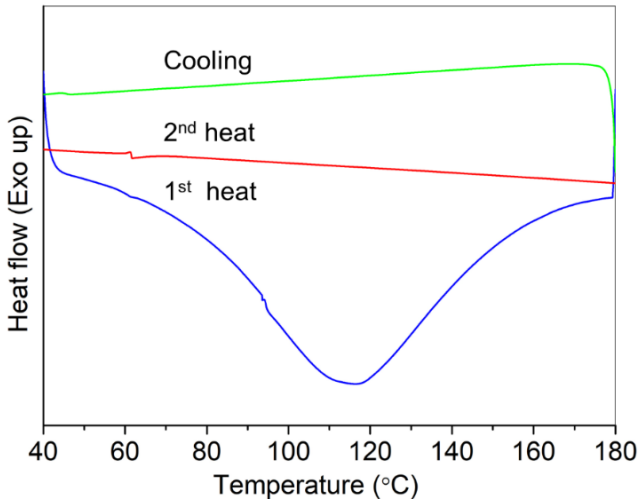

Figure 5-9 DSC thermograms showing that there was no crystallization during second heating and cooling for HH.

5.3 PCDL tri-block copolymers

5.3.1 Molecular weight and polydispersity

The average molecular weight and molecular weight distribution/polydispersity (PDI, $\bar{M}_w$ / $\bar{M}_n$) of PCDL and PCLL copolymers were measured by GPC and calculated, as shown in **Figure 5-10,** and summarized in **Table 4-4**. The copolymers had $\bar{M}_n$ in the range of 32000 ~ 40000, the PDI of each copolymer is similar and in a narrower range of 1.30 ~ 1.44, compared to 1.5 in the literature [151]. PDLA-

PCL_{10k}-PDLA ($PCDL_{10k}$) and PLA-PCL_{10k}-PLA ($PCLL_{10k}$) had similar molecular weight and PDI. $PCDL_{10k}$ had $\bar{M}_n$ value of 34218 g/mol, $\bar{M}_w$ value of 47817 g/mol and PDI of 1.40, $PCLL_{10k}$ had $\bar{M}_n$ value of 32004 g/mol, $\bar{M}_w$ value of 45776 g/mol and PDI of 1.43. PDLA-PCL_{8k}-PDLA ($PCDL_{8k}$) exhibited higher molecular weight than $PCDL_{10k}$ and $PCLL_{10k}$, whereas similar PDI at 1.39.

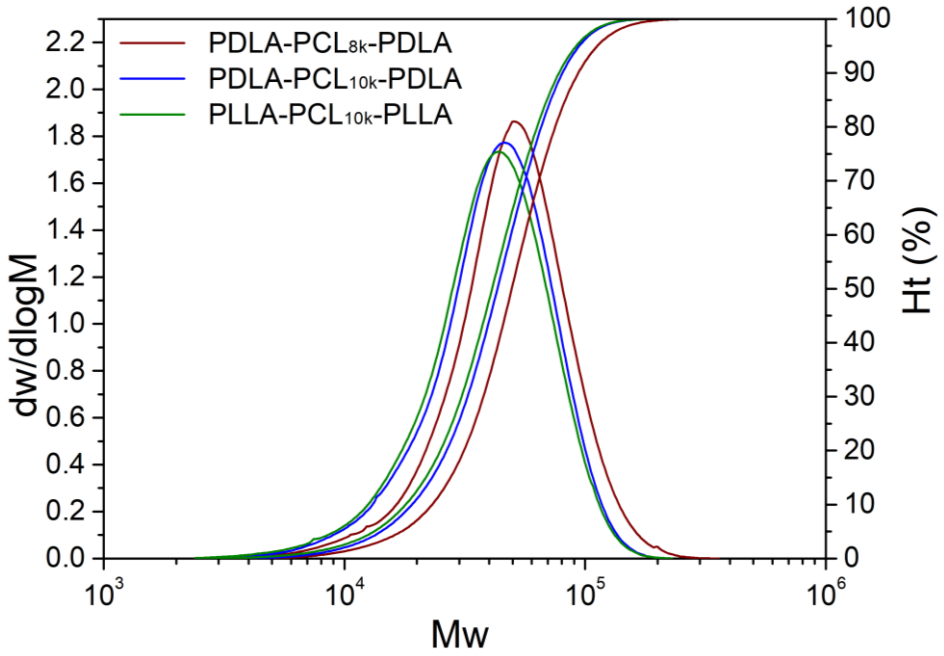

Figure 5-10 The molecular weight and distribution plots of copolymers.

5.3.2 Chemical structure

The chemical structure of PCDL tri-block polymers determined by ^1H NMR is shown in **Figure 5-11**. The molar ratio of caprolactone (CL) and lactide (D-LA and L-LA) was calculated based on the integration ratio of peaks due to methine proton (-CH-, 5.16 ppm) in D-LA and L-LA fraction and methylene proton (-CH_2-, 4.07 ppm or 2.3 ppm) in CL fraction [151] obtained from the HNMR spectra and summarized in **Table 4-4**. $PCDL_{8k}$ exhibited higher DLA/CL mole ratio (74.5/25.5), while $PCDL_{10k}$ and $PCLL_{10k}$ showed similar value around 65.5/34.5 in mole ratio.

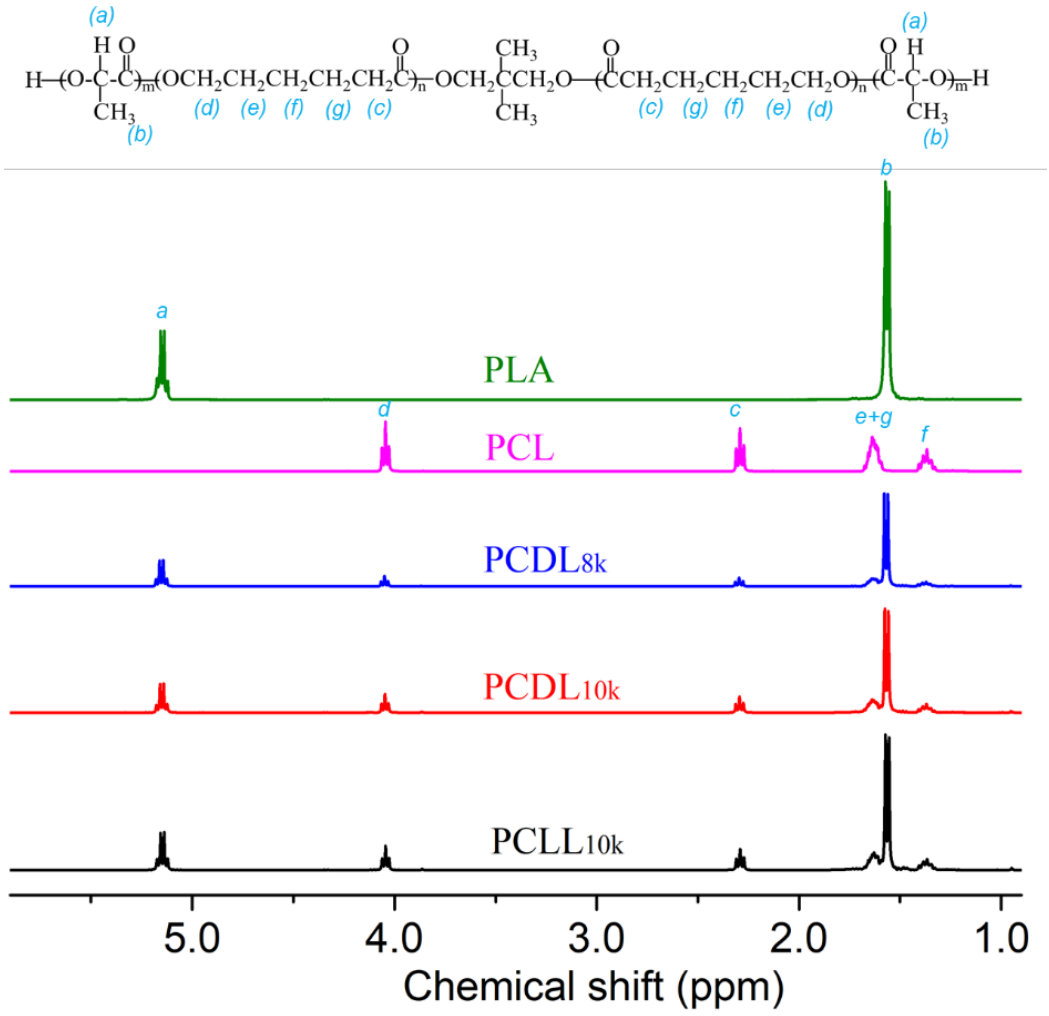

Figure 5-11 ^{1}H NMR spectra of neat PLA, PCL and copolymers.

5.3.3 Chemical compositions

FTIR spectra of PCDL tri-block copolymers (**Figure 5-12**) was collected to identify any changes in the chemical bonding between copolymers. FTIR spectra showed the copolymers have similar structures except for the stronger C=O peak at 1754 cm^{-1} and C-H peak at 2938 cm^{-1} in $PCDL_{8k}$ due to its higher intensity of DLA component.

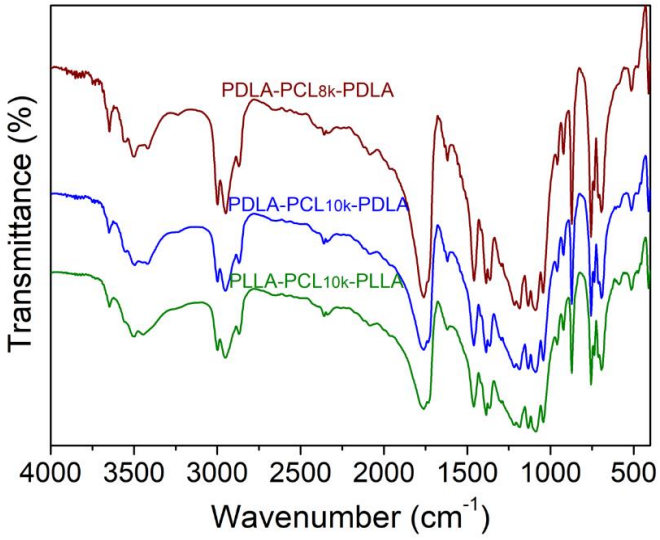

Figure 5-12 FTIR spectra of copolymers.

5.3.4 Thermal transition and crystallization behaviour

Thermal transition temperatures and melting characteristics of copolymers were measured by DSC. The typical thermographs are shown in **Figure 5-13**, the thermal transition temperatures are summarized in **Table 4-4**. $PCDL_{8k}$ exhibited endotherm melting peak (T_m) at 171°C and exothermal cold crystallization peak (T_{cc}) at 91°C. However, $PCDL_{10k}$ and $PCLL_{10k}$ showed lower T_{cc} (around 80°C) and T_m (around 168°C) than $PCDL_{8k}$ due to the lower content of DLA in the copolymers compared to $PCDL_{8k}$.

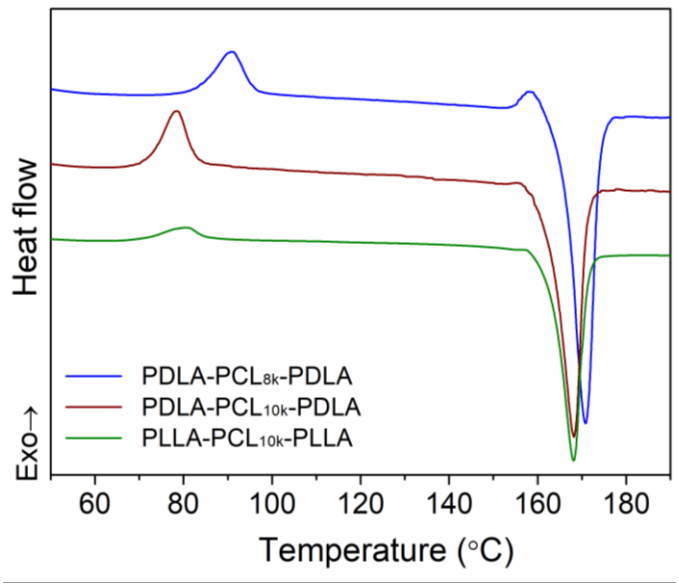

Figure 5-13 DSC thermograms of copolymers.

Chapter 6: Toughening of PLA biocomposites

3D printing biocomposite feedstock constituted by bio-based polymers and fillers are increasingly gaining prominence for FDM. Along with sustainability also emerges the trade-off of reduced toughness and increased brittleness often causing extrusion melt fracture and ensuing effects thereof. The addition of biomass materials such as BP to PLA causes decreased impact strength [15, 102]. Low-impact-strength biocomposite often breaks during extrusion and 3D printing. Toughness modification through blending with flexible polymers [20, 104-109] is a method to improve their resistance to brittleness. To that end, acrylic core-shell impact modifiers [20, 105], PBAT [104], and EGMA terpolymer [107] were investigated as toughening agents for PLA-based biocomposites, as summarized in section 2.4.4. It was found that 20 wt.% PBAT alone only improved the impact strength of PLA from 3.7 kJ/m^2 to 4.4 kJ/m^2 in our previous research. The reason is that the PLA/PBAT blend is a two-phase system, the final properties primarily depend on the level of compatibility. The combination of EGMA efficiently improved the interfacial adhesion and impact strength of PLA/PBAT blend [108, 109] and PLA/biomass biocomposites [68, 69, 107, 113, 114]. Polycaprolactone (PCL), a biodegradable flexible polyester, is also an efficient toughening agent for PLA based biocomposites [71].

The overall objective of this chapter was to select the toughening agent for PLA biocomposites for FDM application. In this chapter, PBAT/EGMA, BPM520 and PCL were compared on the toughening effect in PLA and PLA/BP biocomposites, the melt flow, mechanical properties, and surface roughness were discussed. Firstly, we investigated the toughening efficacy of PBAT/EGMA, BPM520, and PCL on the PLA matrix. Due to the limited improvement in toughness of PLA by PCL, PCDL triblock copolymers were then examined as compatibilizers to address the phase-separation of PLA/PCL blend and improve their toughness. Then, PBAT/EGMA, BPM520 and PCL were compared in PLA/BP biocomposites as toughening agents. Subsequently, PCDL triblock copolymers were used as compatibilizers in PLA/BP/PCL biocomposites to improve the toughness. Finally, PLA/BP/PBAT and PLA/BP/BPM biocomposites were fabricated into filaments and FDM-printed to standard specimens, due to the commercial availability of the toughening agents and

the minor enhancement in toughness achieved by using PCL/PCDL as toughening agent. The specimens were compared with IM specimens.

6.1 Toughening of PLA matrix

6.1.1 Toughening of PLA using PBAT, BPM520 and PCL

PLA was the matrix, and PBAT, EGMA (AX 8900), BPM520, and PCL were used as toughening agents in this research. According to the literature, the PLA/PBAT ratio of 90:10 was used in the studies. Sis et al. [16] used 90/10 (w/w) PLA/PBAT blends for kenaf fibre reinforced biocomposites, where higher PBAT improved impact strength, with a minor decrease in tensile strength and modulus. Li et al. [152] used a ratio of 87/13 (w/w) for PLA/PBAT blend, which was also investigated in our study. The addition of 5 wt.% BPM520 significantly improved the impact strength of PLA, the impact strength (**Figure 2-10d**) and elongation-at-break (**Figure 2-7a**) of PLA/rubber wood sawdust composites [20]. To further enhance the toughness, we investigated 8 phr BPM520 addition in this study. The formulations shown in **Table 6-1** were prepared by melt-compounding in a twin-screw extruder and granulated, and injection-moulded to standard specimens for the mechanical properties testing, according to the methods described in Chapter 4.

Table 6-1 Formulations of toughened PLA

Materials	PLA (phr)	PBAT (phr)	EGMA (phr)	BPM (phr)	PCL (phr)	Additives (phr)
PLA/PBAT	87	13	6.5			2.2
PLA/BPM	100			8		2.2
PLA/PCL	100				10	2.2

The toughening effect of i) PBAT/EGMA, ii) BPM520, and iii) PCL on PLA was investigated and compared, using neat PLA as control, as shown in **Table 6-2**. All toughening agents increased the elongation-at-break and impact strength of PLA, although decreased the tensile strength, flexural strength, and flexural modulus due to the low strength and modulus of toughening agents. PLA/PCL exhibited relatively lower elongation-at-break and impact strength, PLA/PBAT/EGMA presented superior toughening efficacy with higher elongation-at-break and impact strength

than PLA/BPM and PLA/PCL. The melt flow rate is similar for each blend, PBAT/EGMA slightly decreased MFR, whereas BPM520 and PCL increased MFR.

Table 6-2 Physical-mechanical properties of PLA and toughened PLA blend

Materials	MFR (g/10 min)	Tensile strength (MPa)	Elongation-at-break (%)	Impact strength (kJ/m^2)	Flexural strength (MPa)	Flexural modulus (GPa)
PLA	4.4	74.8±1.4	12±0.7	2.9±0.3	124±4.2	3.58±0.10
PLA/PBAT	3.7	50.5±2.1	34±7.5	7.0±0.4	62±1.2	2.39±0.21
PLA/BPM	4.9	54.4±1.4	32±11	5.4±0.9	87±0.8	3.27±0.06
PLA/PCL	4.9	62.8±1.0	18±5.0	4.3±0.4	99±3.8	3.13±0.06

6.1.2 Further enhancing toughness of PLA/PCL blend using PCDL

The work is published in the following journal:

X. Xiao, V. S. Chevali, P. Song, B. Yu, Y. Yang, H. Wang, 'Enhanced toughness of PLA/PCL blends using poly(d-lactide)-poly(ε-caprolactone)-poly(d-lactide) as compatibilizer', Composites communications. https://doi.org/10.1016/j.coco.2020.100385

PCL is an efficient toughening agent for PLA biocomposites [71]. The low melting temperature of PCL is expected to improve the melt flow of biocomposite [120, 121], enhancing the processability and printability of PLA biocomposite as 3D printing feedstock, also is expected to improve the surface smoothness, which was observed during our research, as shown in **Figure 6-1**. However, PLA/PCL is an immiscible blend, the obtained phase-separation blends exhibited limited enhancement in toughness [123, 124], as shown in **Table 6-2**. To improve the compatibility and concomitantly achieve the desirable toughness, PDLA-PCL$_{8k}$-PDLA tri-block copolymer was investigated as a compatibilizer for PLA/PCL blend.

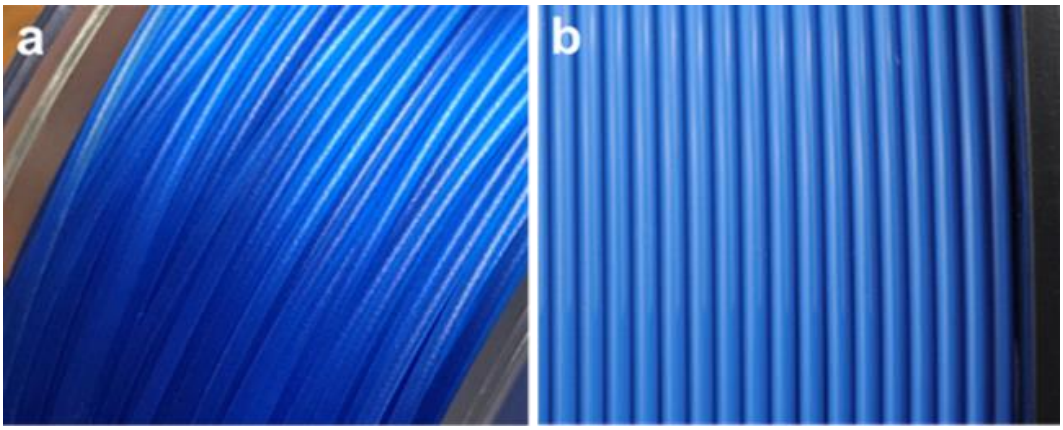

Figure 6-1 The visual appearance of (a) PLA and (b) PLA/PCL 3D printing filament.

This study examined the effect of PDLA-PCL_{8k}-PDLA ($PCDL_{8k}$) with PDLA and PCL blocks on the miscibility and compatibility of PLA/PCL (100/10 in w/w) blend, with (a) compatibilization effect through lactide/caprolactone copolymer and (b) interfacial interaction improvement between PLA matrix and PDLA through the formation of stereocomplex crystallites. PLA/PCL/PCDL blends with (a) 0.7 and (b) 3.5 phr loadings, and without PCDL were prepared by melt-compounding, to obtain PDLA ratios of 0, 0.5, and 2.5 phr in the blends, respectively. The PLA/PCL ratios in the blends were 100/10 (w/w), including the PCL fraction introduced by PCDL. The formulations of PLA/PCL blends are presented in **Table 6-3**. This work studied the compatibility improvement using a small amount of PCDL according to the literature, because 1 wt.% PLA-PBAT-PLA showed a 100% increase in elongation-at-break of PLA/PBAT blend [153] and 0.5 wt.% of two types of PLA-PBAT-PLA synergistically increased the elongation-at-break of PLA/PBAT blend [154]. PLA/PCL/PCDL blends were prepared by melt blending and extrusion at 170°C through a co-rotating twin-screw extruder (L/D = 44, D = 35mm), and injection-moulded to standard specimens at 175°C for mechanical testing. The effect of PCDL on the tensile properties and impact strength, morphologies, rheological properties, and thermal properties were analysed with respect to variable PCDL amounts.

Table 6-3 The experimental formulations of PLA/PCL/PCDL blends

Materials	PLA (phr)	PCL (phr)	$PCDL_{8k}$ (phr)
PLA	100	0	0
PLA/PCL	100	10	0
PLA/PCL/PCDL0.7	100	9.9	0.7
PLA/PCL/PCDL3.5	100	9.3	3.5

6.1.2.1 Mechanical properties

The effect of PDLA-PCL_{8k}-PDLA or $PCDL_{8k}$ compatibilizer on mechanical properties is presented in **Figure 6-2**. Tensile strength decreased with the addition of PCL because of the relatively lower tensile strength of PCL (12.5 MPa) [119] compared to PLA (74.8 MPa), and inadequate compatibility between PLA and PCL, which is in good agreement with the literature [119, 155]. Elongation-at-break (ε_b), on the other hand, increased from 12% for neat PLA to 18% for PLA/PCL. The tensile strength of PLA/PCL blends was unaffected with further PCDL addition, and retained at 62.0 ± 1.0 MPa, as shown in **Figure 6-2a**, **b**. Elongation, however, increased significantly with the PCDL addition, as shown in **Figure 6-2a**, **c**. PLA/PCL/PCDL3.5 exhibited ε_b of 43.3 ± 13 %, which was 140% higher than ε_b for PLA/PCL. The increase in ductility is indicative of compatibilization effect occurred between PLA and PCL components upon the incorporation of PCDL [117, 125]. Impact strength increased from 29.1 J/m of PLA to 44.0 ± 2.0 J/m of PLA/PCL blends with or without the incorporation of PCDL (**Figure 6-2d**), attributed to the addition of flexible PCL similar as an elastomer, the result is consistent with the reported literature [118, 125, 155].

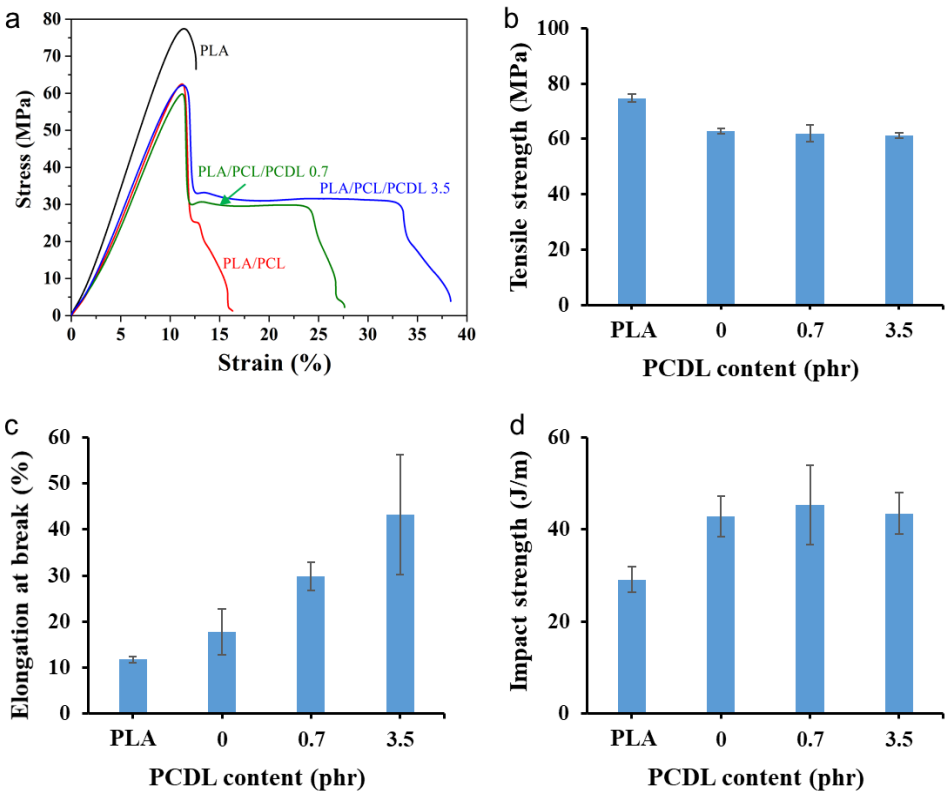

Figure 6-2 Mechanical properties of PLA and PLA/PCL/PCDL blends, showing: (a) tensile stress-strain curves, (b) tensile strength, (c) elongation-at-break (ε_b) and (d) impact strength as a function of PCDL tri-block copolymer content.

6.1.2.2 Morphology

The cryo-fractured surfaces of PLA control uncompatibilized PLA/PCL and compatibilized PLA/PCL blends by PCDL were observed by SEM, as shown in **Figure 6-3**. The SEM micrographs show the representation of a brittle fracture with smooth surfaces in neat PLA and PLA/PCL (**Figure 6-3a**, **b**) [122]. The dispersion of spherical PCL particle in PLA resembled a sea-island morphology, with a noticeable boundary between PLA and PCL, as observed in **Figure 6-3b**, indicating the immiscibility of PCL with PLA [117]. When PCDL was introduced, the fracture surface showed characteristics of higher ductility and impact resistance. PLA and PCL constituents were emulsified with the inclusion of PCDL, and the boundary between PLA and PCL phases was no longer noticeable, as shown in **Figure 6-3d**, as seen in compatibilized PLA/PCL blends [117, 156], which confirms improved mutual compatibility and interfacial adhesion [117].

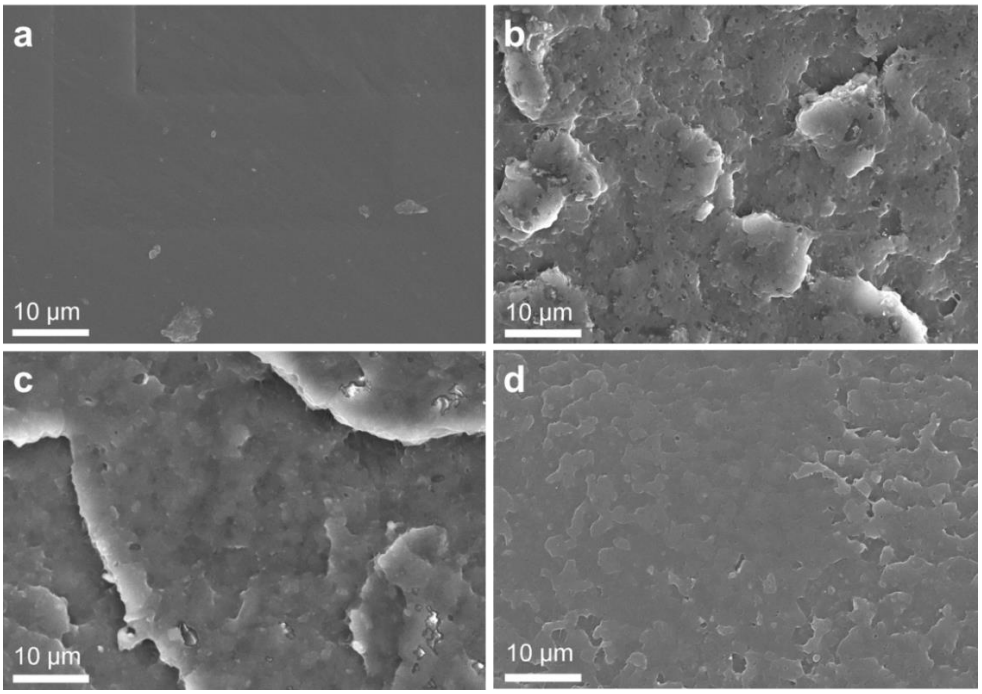

Figure 6-3 SEM micrographs of cryo-fractured surfaces of (a) PLA, (b) PLA/PCL, (c) PLA/PCL/PCDL0.7, and (d) PLA/PCL/PCDL3.5, all at a magnification of 2000×.

6.1.2.3 Rheological properties

The rheological analysis was used to elucidate the PLA/PCL interfacial interactions within the prepared blends (**Figure 6-4)**. The incorporation of PCL into PLA decreased the storage modulus (G'), loss modulus (G''), and complex viscosity ($|\eta^*|$), which resulted in a higher MFR value, leading to a smoother and smoothed surface appearance in the filament as shown in **Figure 6-1**. G' and G'' increased with increasing PCDL loading, with PLA/PCL/PCDL3.5 exhibiting higher G' and G'' than PLA, indicating the enhanced compatibility between PLA and PCL achieved through the incorporation of PCDL [155]. $|\eta^*|$ increased with PCDL loading, which is counter-intuitive of PCL-*b*-PLA diblock copolymer incorporation in PLA/PCL blend [157], MFR decreased with PCDL content as shown in **Figure 6-4d**, leading to a more stable flow of melt from at nozzle. This increase in $|\eta^*|$ could be attributed to the melt-reinforcement brought about by the underlying crosslinking effect of the stereocomplex crystallites as a rheological modifier [158]. This crosslinking effect enhances the interfacial adhesion between PLA and PCL, hence increasing the toughness of PLA/PCL blend [130].

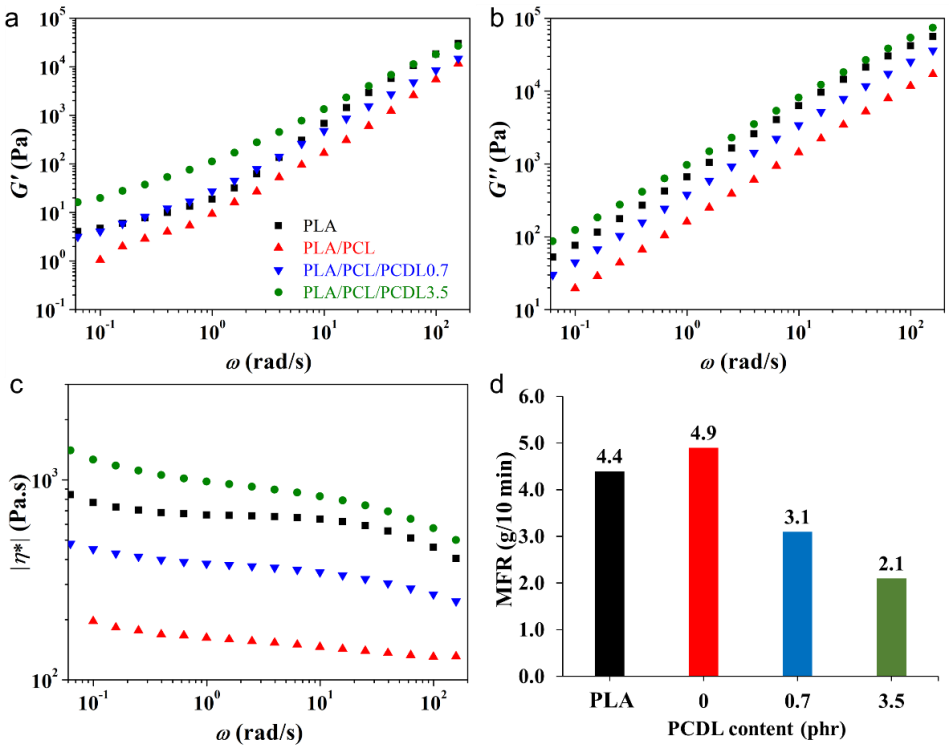

Figure 6-4 Rheological properties of PLA and PLA/PCL/PCDL blends, showing: (a) *G*', (b) *G*'', (c) $|\eta^*|$, and (d) MFR.

6.1.2.4 Thermal properties

Figure 6-5 shows the DSC thermograms of PLA, PCL and PLA/PCL/PCDL blends, the heat transition temperature and enthalpy are summarized in **Table 6-4**. The T_m of PCL and T_g of PLA are almost coincident (**Figure 6-5)**, thus it is difficult to identify the T_g of PLA in the blends directly from the thermograms due to an overlap, which causes a practical difficulty in analysing the effect of PCDL on T_g of PLA. T_m was 0.2°C and 0.6°C higher in PLA/PCL/PCDL0.7 and PLA/PCL/PCDL3.5, respectively compared to PLA (168.4°C). PLA/PCL/PCDL3.5 presented a melting peak at 212°C, demonstrating the formation of stereocomplex crystallites [159], which contribute to the toughness of PLA/PCL blend as aforementioned. The peak of the stereocomplex crystallite on PLA/PCL/PCDL0.7 curve was not discernible (**Figure 6-5)**, because the melting enthalpy of the stereocomplex crystallite is approx. 1.2 J/g theoretically, which is insignificant compared to the homocrystallite enthalpy (54.2 J/g).

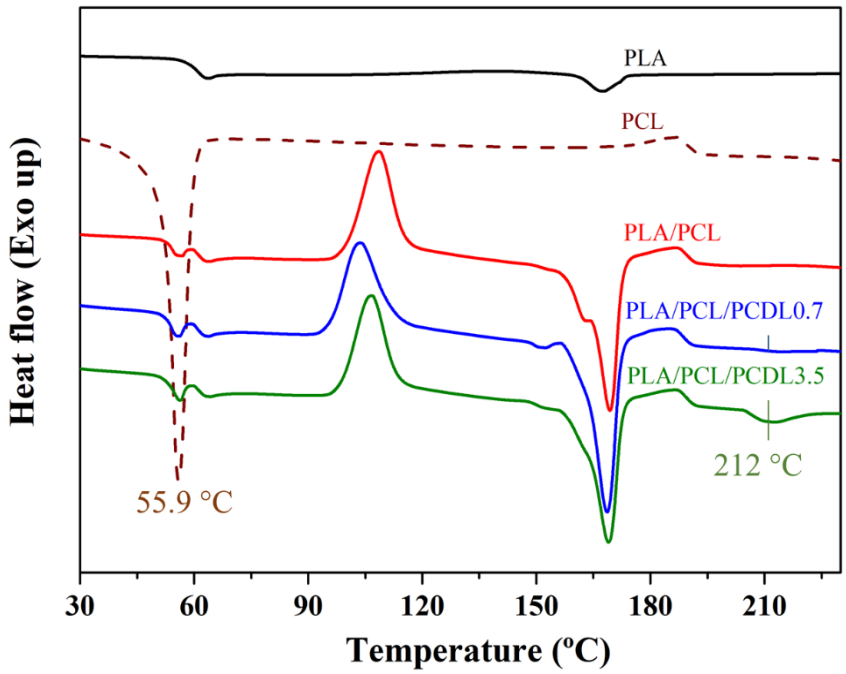

Figure 6-5 DSC thermograms of PLA, PCL and PLA/PCL/PCDL blends showing a stereocomplex crystallite peak.

Table 6-4 Crystallization and melting properties of PLA/PCL/PCDL blends

Materials	T_{m1} (°C)	T_g (°C)	T_{cc} (°C)	ΔH_{cc} (J/g)	T_{m2} (°C)	ΔH_{m2} (J/g)	X_c (%)	T_{m3} (°C)	ΔH_{m3} (J/g)
PLA	-	62.1	-	-	168.4	2.90	3.1	-	-
PLA/PCL	55.5	54.3	108.6	51.6	169.4	55.4	4.4	-	-
PLA/PCL/PCDL0.7	55.4	54.2	103.7	48.8	168.6	54.2	6.4	-	-
PLA/PCL/PCDL3.5	56.1	54.9	106.6	47.9	169.0	56.2	10.0	212.4	6.0

Cold crystallization was not observed on the thermogram of neat PLA, however, was observed on PLA/PCL thermogram at 108.6°C, demonstrating PCL facilitated the cold crystallization of PLA during heating because of the provision of nucleation sites. The degree of crystallinity (X_c) increased from 3.1% to 4.4%, which is attributed to the higher degree of PLA crystallization [160]. With the addition of PCDL, the cold crystallization temperature (T_{cc}) decreased to 103.7°C in PLA/PCL/PCDL0.7, suggesting the inclusion of PCDL enhanced the chain mobility of PLA [117], thereby improving its cold crystallization. This enhanced chain

mobility in PLA caused by PCDL leads to higher compatibility of PLA/PCL blend [128].

PLA in PLA/PCL/PCDL3.5 recrystallized at 106.6°C, which is a lower T_{cc} than that of neat PLA, albeit a relatively higher temperature than in PLA/PCL/PCDL0.7. This behaviour is consistent with the literature [112, 120], where the increase in l-lactide/caprolactone copolymer loading in PLA/PCL blends hinders the initiation of PLA cold crystallization because of the increase in lactide segments introduced by the copolymer. X_c increased to 10% for PLA/PCL/PCDL3.5, which demonstrated the inclusion of copolymer facilitated the crystallization ability of PLA due to the compatibilization effect of PCDL between PLA and PCL [117]. Higher crystallinity resulted in lower elongation-at-break [161], which however was improved in PLA/PCL/PCDL3.5 with higher crystallinity, confirming the enhanced compatibility between PLA and PCL through the addition of PCDL.

The addition of PCDL of 0.7 phr and 3.5 phr brought about lower cold crystallization temperature and higher crystallinity due to the improved compatibility. The addition of PCDL also facilitated the formation of stereocomplex crystallites, which improved the melt viscosity and decreased the melt flow due to the underlying crosslinking effect, hence enhanced the interfacial adhesion, therefore improved the interfacial morphology, and the toughness of PLA/PCL blends. PLA/PCL/PCDL blends showed noticeable improvements in elongation-at-break with respect to the PLA control.

Overall, the toughness of PLA/PCL blend was enhanced by PCDL tri-block copolymer, as supported by the improved ductility, with more than 140% increase in elongation-at-break in PLA/PCL/PCDL3.5 over the baseline PLA/PCL blend. The increase in toughness was underpinned by enhanced mutual compatibility between PLA and PCL caused by PCDL, as demonstrated by the emulsified interface morphology and the formation of stereocomplex crystallites, confirmed through differential scanning calorimetry. The melting viscosity of PLA/PCL was enhanced by PCDL due to the stereocomplexation, which was confirmed by the melting peak at 212°C. Overall, the PCDL caused a multi-faceted improvement in toughness, ease of processing, and interfacial compatibility of PLA/PCL blends.

6.2 Toughening of PLA/BP biocomposites

The work has been partly published in the following conference proceeding:

X. Xiao, V. S. Chevali, H. Wang 2019, 'Toughening of polylactide/bamboo powder biocomposite for 3D printing', Paper ID: 2405-6, ICCM 22, Melbourne, Australia, Aug 11-16, 2019.

6.2.1 Toughening of PLA/BP biocomposites using PBAT, BPM520 and PCL

PBAT/EGMA, BPM520 and PCL were compared on the toughening effect in PLA/BP biocomposites using the formulations in **Table 6-5**, which were prepared by melt-compounding in a twin-screw extruder and granulated, and injection-moulded to standard specimens for the mechanical properties testing, according to the methods described in Chapter 4. PLA, PBAT and BP were dried to the moisture level below 0.5 wt.% prior to extrusion. BP with a volume-median-diameter (d_{50}) of 75 μm was used as the biomass filler in this research. The melt flow and mechanical properties were discussed.

Table 6-5 Formulations of toughened PLA/BP biocomposite

Materials	PLA (phr)	PBAT (phr)	EGMA (phr)	BPM (phr)	PCL (phr)	BP (phr)	Additives (phr)
PLA/BP/PBAT	87	13	6.5			20	2.2
PLA/BP/BPM	100			8		20	2.2
PLA/BP/PCL	100				10	20	2.2

6.2.1.1 Mechanical properties

As shown in **Table 6-6**, all the toughening agents achieved higher impact strength for PLA/BP biocomposites than PLA control, whereas only PLA/BP/PBAT exhibited comparable elongation-at-break to PLA control, PLA/BP/BPM and PLA/BP/PCL displayed lower elongation-at-break than PLA control. PLA/BP/PBAT presented superior toughness among all the biocomposites. The tensile strength, flexural strength and flexural modulus all decreased due to the addition of toughening agents with low strength and modulus and insufficient interfacial adhesion between polymer matrix and BP particles.

Table 6-6 Physical-mechanical properties of PLA and toughened PLA blend

Materials	MFR (g/10 min)	Tensile strength (MPa)	Elongation-at-break (%)	Impact strength (kJ/m^2)	Flexural strength (MPa)	Flexural modulus (GPa)
PLA	4.4	74.8±1.4	12±0.7	2.9±0.3	124±4.2	3.58±0.10
PLA/BP/PBAT	2.0	40.2±0.3	12±0.8	4.7±0.3	72±1.0	2.92±0.10
PLA/BP/BPM	1.6	51.9±0.3	9.6±0.4	3.4±0.2	85±2.4	3.51±0.13
PLA/BP/PCL	4.9	45.8±0.7	8.8±0.2	3.8±0.2	76±2.6	3.57±0.13

6.2.1.2 Rheological and melt flow behaviour

The addition of BP and PBAT/EGMA or BPM520 decreased the melt flow as shown in **Table 6-6**. The effect of PBAT and BPM520 on viscoelastic behaviour and processability of PLA/BP biocomposites was evaluated. The rheological properties of PLA/BP/PBAT and PLA/BP/BPM biocomposites are shown in **Figure 6-6**. The biocomposites showed shear-thinning behaviour (**Figure 6-6b**) and lower complex viscosity than PLA at a frequency between 0.4 rad/s and 25 rad/s. The shear-thinning behaviour can be utilized to reduce viscosity and obtain improved melt flow than PLA by adjusting the material throughput and the diameter of the 3D printer nozzle [162]. The higher complex viscosity at low frequency is desired for holding the form of filament during extrusion [162]. PLA/BP/PBAT showed increased complex viscosity in the molten state than PLA/BP/BPM, indicating higher melt strength, and the steadier extrusion during filament processing, which is advantageous for obtaining filament with consistent diameter and roundness [163]. The biocomposites showed higher storage modulus and loss modulus than neat PLA at low frequency due to the decreased mobility of polymer chains in melt state with the incorporation of BP. The difference in storage modulus and loss modulus at high frequency was insignificant, attributed to the disentanglement and reorientation of BP and polymer chains in the flow direction [164]. There was no significant difference in storage (elastic) modulus and loss (viscous) modulus between PLA/BP/PBAT and PLA/BP/BPM, indicating the similar viscoelastic behaviour and mobility of polymer chains in the two biocomposites. At frequency above 0.6 rad/s, both biocomposites displayed viscous behaviour ($G'' > G'$).

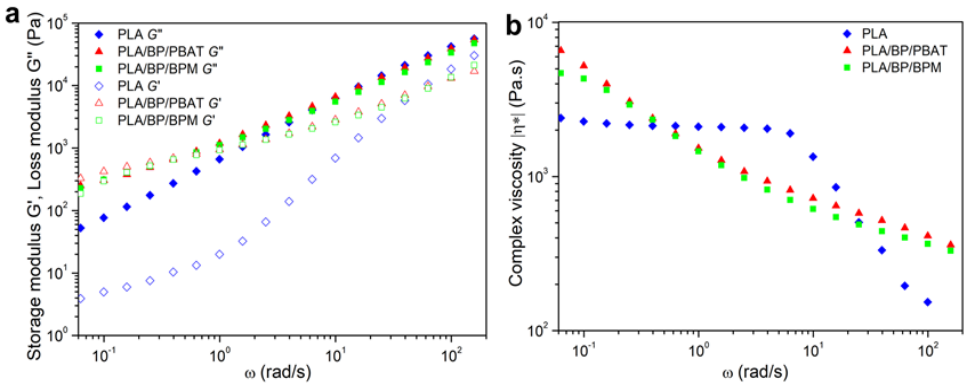

Figure 6-6 Dynamic frequency sweep plots for biocomposites: (a) *G*' and *G*", (b) $|\eta^*|$ as a function of angular frequency at 190°C.

The melt viscosity for a stabilized morphology was determined by the steady-state melt torque. **Figure 6-7** shows the torque-rheometer plots as a function of time. PLA/BP/PBAT showed a lower melt torque than PLA/BP/BPM, indicating that less energy was required [165] during the process and better processability for PLA/BP/PBAT. The result was following the MFR (190°C, 2.16 kg) of 2.0 g/10 min for PLA/BP/PBAT and 1.6 g/10 min for PLA/BP/BPM shown in **Table 6-6**.

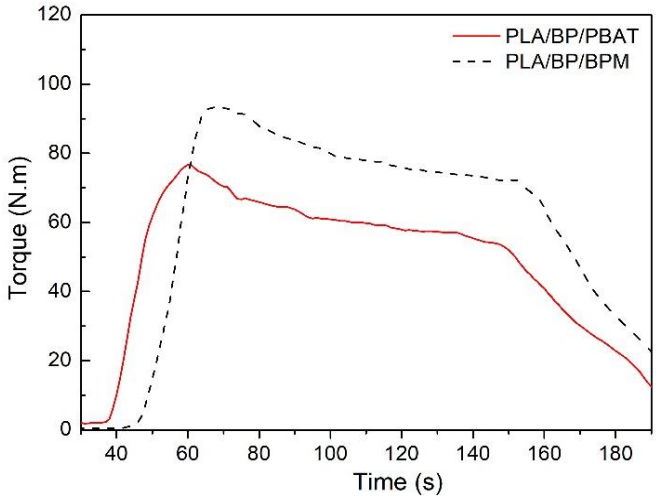

Figure 6-7 Melt torque versus time for processing toughened PLA/BP biocomposites.

6.2.2 Further enhancing toughness of PLA/BP/PCL biocomposite using PCDL

Due to the relatively lower impact strength and elongation-at-break of PLA/BP/PCL biocomposites and the enhancement in the toughness of PLA/PCL by $PCDL_{8k}$, PCDL and PCLL tri-block copolymers with varying HO-PCL-OH segment (8k and

10k) were examined as compatibilizers for PLA/BP/PCL biocomposite. The formulations are shown in **Table 6-7**. The weight fractions of PDLA introduced to the biocomposites were 2.5%, 5.0%, and 7.5% in weight percentage of total PLA (PLLA and PDLA), respectively. BP with d_{50} = 50 μm was used as biomass filler. PLA and PCL, in the form of pellets, PCDL in the form of powder, and BP were dried separately in vacuum ovens at 80°C, 60°C, 60°C, and 120°C for 8h, respectively. The ingredients were melting-blended in an XSS-300 torque rheometer (Shanghai Kechuang Rubber Plastic Mechanical Equipment Co., Ltd., China), with a rotational speed at 60 rpm for 6 min, the temperature was set at 180°C, 180°C, and 180°C, the melt torque as a function of compounding time was recorded. The compounds were then moulded into sheets with a dimension of 100 mm × 100 mm × 1 mm by hot-pressing at 200°C for preheating 10 min without pressure, then pressurize 5 min for forming the sheet using a press vulcanizer. The sheets were prepared for the characterization, including rheological properties, tensile properties, and DSC measurement. The specimens for the tensile test were cut from the sheet as Type 5B according to GB/T1040.2/ISO 527-2 standard, the cryo-fractured surfaces of tensile specimens were observed by SEM.

Table 6-7 Formulations of the PLA/BP/PCL biocomposites

Materials	PLA (phr)	PCL (phr)	$PCDL_{8k}$ (phr)	$PCDL_{10k}$ (phr)	$PCLL_{10k}$ (phr)	BP(phr)
PLA/BP/PCL	100	10.0	0	0	0	10
PLA/BP/PCL/$PCDL_{8k}$2.5	97.5	9.09	3.41			10
PLA/BP/PCL/$PCDL_{8k}$5.0	95.0	8.18	6.82			10
PLA/BP/PCL/$PCDL_{8k}$7.5	92.5	7.27	10.2			10
PLA/BP/PCL/$PCDL_{10k}$2.5	97.5	8.75		3.75		10
PLA/BP/PCL/$PCDL_{10k}$5.0	95.0	7.50		7.50		10
PLA/BP/PCL/$PCDL_{10k}$7.5	92.5	6.25		11.2		10
PLA/BP/PCL/$PCLL_{10k}$2.5	97.5	8.75			3.75	10
PLA/BP/PCL/$PCLL_{10k}$5.0	95.0	7.50			7.50	10
PLA/BP/PCL/$PCLL_{10k}$7.5	92.5	6.25			11.2	10

6.2.2.1 Melt torque

The torque-rheometer plots of PLA/BP/PCL biocomposites with PCDL and PCLL copolymers incorporation are presented in **Figure 6-8**. PLA/BP/PCL/$PCLL_{10k}$ biocomposites showed steady-state melt torque close to PLA/BP/PCL without

copolymer and exhibited a marginally decrease in steady-state melt torque with increasing $PCLL_{10k}$ content, ascribed to the $PCLL_{10k}$ with lower molecular weight than PLA and PCL acted as a plasticizer and inadequate interfacial interaction formation between PLA and PCL, resulting in improved processability. PLA/BP/PCL/$PCDL_{8k}$ and PLA/BP/PCL/$PCDL_{10k}$ displayed increased stabilized melt torque with increasing PCDL copolymer content and increasing $\overline{M}_\eta$ of HO-PCL-OH macro-initiator, due to the enhanced interfacial interaction between PLA and PCL as a result of the formation of stereocomplexation between PLA and PDLA in copolymers.

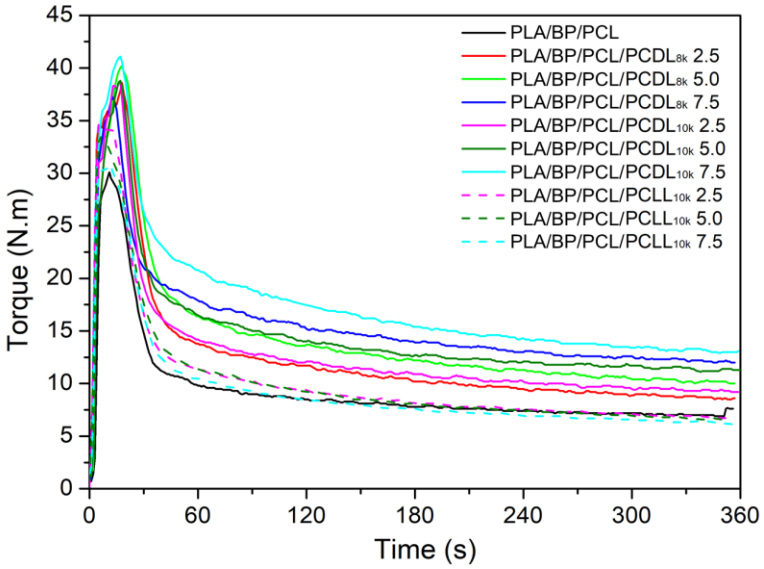

Figure 6-8 Melt torque versus time for processing compatibilized PLA/BP/PCL biocomposites.

6.2.2.2 Rheological properties

The dynamic frequency sweep graphs of biocomposites are shown in **Figure 6-9**. PLA/BP/PCL/$PCLL_{10k}$ biocomposites showed decreased G', G'' and $|\eta^*|$ as $PCLL_{10k}$ increased from 0 to 5.0 wt.%, indicating the decreased interfacial interaction between compositions. G', G'' and $|\eta^*|$ remained similar when $PCLL_{10k}$ content further increased to 7.5 wt.%. PLA/BP/PCL/$PCLL_{10k}$ with various $PCLL_{10k}$ content all showed higher Tan δ than PLA/BP/PCL biocomposite, indicating the pronounced viscous behaviour over elastic behaviour for PLA/BP/PCL/$PCLL_{10k}$. PLA/BP/PCL/PCDL biocomposites showed increased G', G'' and $|\eta^*|$ at low frequency with increasing PCDL content, indicating the increased interfacial

interaction and improved compatibility between compositions. When PCDL content reached 7.5 wt.%, the biocomposites could not melt at 190°C, the rheology of PLA/BP/PCL/PCDL$_{8k}$7.5 and PLA/BP/PCL/PCDL$_{10k}$7.5 was tested at 220°C. Both samples showed predominantly elastic behaviour (Tan δ < 1) even when the test temperature raised to 220°C from 190°C. PLA/BP/PCL/PCDL$_{10k}$ biocomposites showed higher *G'*, *G"*, |η*| and Tan δ than PLA/BP/PCL/PCDL$_{8k}$, attributed to the improved compatibility and enhanced mobility of copolymer chains.

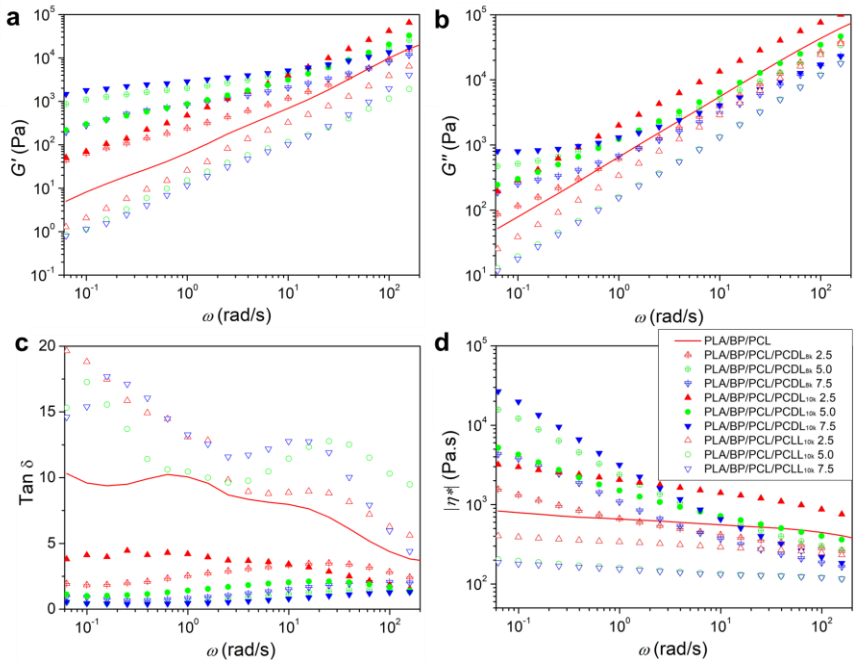

Figure 6-9 Dynamic rheological properties of PLA/BP/PCL/PCDL composites at 190°C. (a) *G'*, (b) *G"*, (c) tan δ, and (d) |η^*|. (PLA/BP/PCL/PCDL$_{8k}$7.5 and PLA/BP/PCL/PCDL$_{10k}$7.5 were tested at 220°C.)

6.2.2.3 Tensile properties

The tensile properties of biocomposites are compared and shown in **Figure 6-10**. With the addition of copolymers, the tensile strength decreased at first till the copolymer content increased to 5 wt.%, then increased when the content of copolymer increased to 7.5 wt.% for all the biocomposites, indicating a critical copolymer content (7.5 wt.%) for the compatibilization of PLA/BP/PCL biocomposites. Before the critical content, the compatibilization effect is insufficient to improve the tensile strength, on the contrary, the tensile strength decreased because of the further addition of copolymer, which bears a relatively lower tensile

strength than the base polymer. When the copolymer content reached 7.5 wt.%, the copolymer compatibilizer interact with their blend counterparts while residing at the interface and interpenetrating to PLA and PCL phases, concurrently enhancing the interfacial adhesion and therefore, improved the mechanical properties. The increase in stereocomplex crystals also benefits to achieve the enhanced interfacial adhesion and mutual interaction between components and contributed to the properties of PLA. The elongation-at-break showed a similar trend with tensile strength. When the copolymer content was 7.5 wt.%, PLA/BP/PCL/PCDL$_{10k}$ and PLA/BP/PCL/PCDL$_{8k}$ showed higher elongation-at-break, whereas PLA/BP/PCL/PCLL$_{10k}$ showed lower elongation-at-break than PLA/BP/PCL without copolymer. PLA/BP/PCL/PCDL$_{10k}$ showed higher tensile strength and elongation-at-break than PLA/BP/PCL/PCLL$_{10k}$ at all copolymer loadings, indicating the formation of stereocomplex crystalline enhanced the compatibility between PLA and PCL. PLA/BP/PCL/PCDL$_{10k}$7.5 displayed the highest ductility (ε_b = 11%) among all the samples due to the highest compatibility improvement. However, the increment in elongation-at-break was insignificant, compared with PLA/BP/PCL (ε_b = 10%) without compatibilizer.

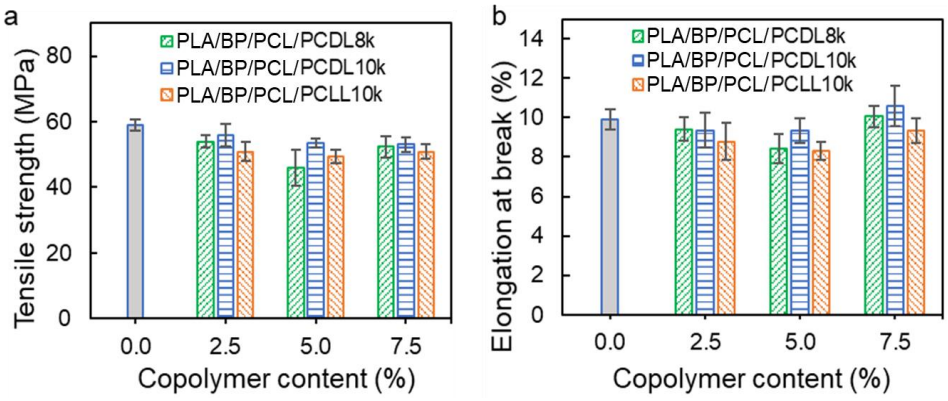

Figure 6-10 Tensile properties of biocomposites: (a) tensile strength, (b) elongation-at-break.

6.2.2.4 Morphology

The cryo-fractured surfaces of PLA/BP/PCL/PCDL specimens were observed by SEM, as shown in **Figure 6-11**. BP combined tightly and encapsulated in the polymer matrix for both PLA/BP/PCL/PCDL2.5 biocomposites (**Figure 6-11c**, **e**). BP filler also showed good interfacial bonding with polymer matrix for PLA/BP/PCL/PCDL7.5 biocomposites (**Figure 6-11d**, **f**). The gap between polymer

matrix and BP and BP exposure from polymer matrix were observed on the surface for PLA/BP/PCL biocomposites (**Figure 6-11a, b**) and PLA/BP/PCL/PCLL (**Figure 6-11g**, **h**), demonstrating the relatively lower interfacial bonding compared with PLA/BP/PCL/PCDL biocomposites.

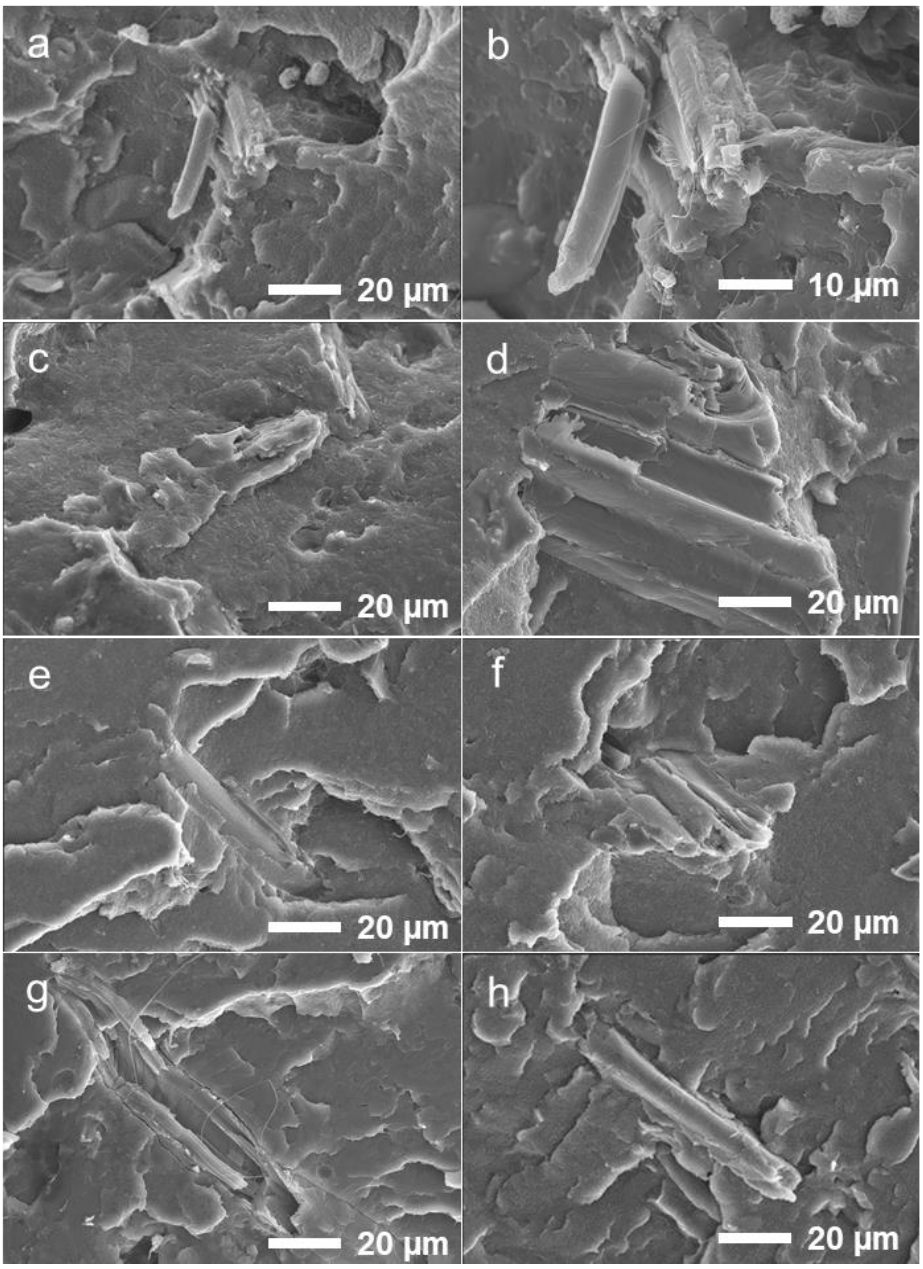

Figure 6-11 SEM micrographs of cryo-fractured surfaces of (a, b) PLA/BP/PCL, (c) PLA/BP/PCL/$PCDL_{8k}$2.5, (d) PLA/BP/PCL/$PCDL_{8k}$7.5, (e) PLA/BP/PCL/$PCDL_{10k}$2.5, (f) PLA/BP/PCL/$PCDL_{10k}$7.5, (g) PLA/BP/PCL/$PCLL_{10k}$2.5, and (h) PLA/BP/PCL/$PCLL_{10k}$7.5.

6.2.2.5 Thermal properties

DSC thermograms of biocomposites obtained at second heating scan are shown in **Figure 6-12**, the thermal transition temperatures and enthalpy are summarized in **Table 6-8**. The biocomposites exhibited enhanced crystallization ability for PLA, resulting in improved crystallinity, The addition of BP and PCL did not affect the melting transition of PLA, whereas the inclusion of PCDL copolymers reduced the T_m of PLA by 2 degrees, the incorporation of PCLL copolymers lowered the T_m of PLA by around 0.5 degree. The increasing content of $PCLL_{10k}$ decreased the cold crystallization temperature of PLA/BP/PCL biocomposite from 101°C to the range between 91°C and 94°C, indicating the addition of $PCLL_{10k}$ facilitated the cold crystallization of PLA/BP/PCL biocomposite. The cold crystallization peak disappeared with the addition of PCDL copolymers, indicating the formation of stereocomplex crystallite facilitated the crystallization of PLA homocrystallite, which was finished during the cooling cycle. The PLA homocrystallinity in PLA/BP/PCL/PCDL biocomposites decreased with increasing PCDL content, contrary to PLA/BP/PCL/PCLL biocomposites, because of the increase in stereocomplex crystallite with melting temperature between 213°C and 220°C. Both the melting temperature and melt enthalpy of stereocomplex crystallite increased with increasing PCDL content. Compared with PLA/BP/PCL, the addition of PCDL and PCLL both improved the homocrystallinity of PLA. The melting temperature of biocomposites was lowered by the incorporation of PCDL, whereas remained at around 168°C by the inclusion of PCLL.

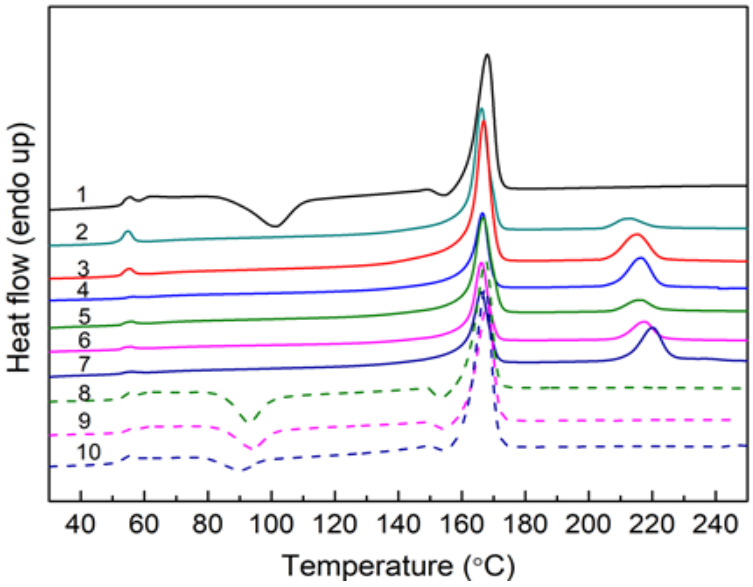

Figure 6-12 DSC thermograms of biocomposites: 1) PLA/BP/PCL, 2). PLA/BP/PCL/$PCDL_{8k}$2.5, 3. PLA/BP/PCL/$PCDL_{8k}$5.0, 4. PLA/BP/PCL/$PCDL_{8k}$7.5, 5. PLA/BP/PCL/$PCDL_{10k}$2.5, 6. PLA/BP/PCL/$PCDL_{10k}$5.0, 7. PLA/BP/PCL/$PCDL_{10k}$7.5, 8. PLA/BP/PCL/$PCLL_{10k}$2.5, 9. PLA/BP/PCL/$PCLL_{10k}$5.0, 10. PLA/BP/PCL/$PCLL_{10k}$7.5.

Table 6-8 Crystallization and melt phase properties of PLA/BP/PCL biocomposites

Materials	T_{m1} (°C)	ΔH_{m1} (J/g)	T_{cc} (°C)	ΔH_{cc} (J/g)	T_{m2} (°C)	ΔH_{m2} (J/g)	T_{m3} (°C)	ΔH_{m3} (J/g)	X_c (%)
PLA (4032D)					168.0	2.90			3.1
PLA/BP/PCL	58.6	0.53	101.3	17.2	168.0	40.8			30.5
PLA/BP/PCL/$PCDL_{8k}$2.5	54.8	2.04	-	-	166.2	41.4	213.1	4.5	54.8
PLA/BP/PCL/$PCDL_{8k}$5.0	55.0	0.85	-	-	166.9	37.2	215.5	8.8	50.5
PLA/BP/PCL/$PCDL_{8k}$7.5	-	-	-	-	166.5	28.4	216.5	12.7	39.6
PLA/BP/PCL/$PCDL_{10k}$2.5	55.4	0.57	-	-	166.7	37.9	216.3	4.4	50.2
PLA/BP/PCL/$PCDL_{10k}$5.0	54.8	0.52	-	-	166.2	31.6	217.6	8.5	42.9
PLA/BP/PCL/$PCDL_{10k}$7.5	55.6	0.36	-	-	166.1	29.7	220.1	13.5	41.4
PLA/BP/PCL/$PCLL_{10k}$2.5	55.1	0.41	93.0	11.9	167.5	40.7	-	-	38.1
PLA/BP/PCL/$PCLL_{10k}$5.0	-	-	94.2	11.5	168.0	42.2	-	-	41.7
PLA/BP/PCL/$PCLL_{10k}$7.5	55.2	0.50	91.1	5.15	167.4	40.7	-	-	49.6

Overall, the addition of PCDL improved the interfacial interaction between PLA and PCL, as evidenced by the increased melt torque and complex viscosity, storage modulus, loss modulus, and improved interfacial adhesion due to the improved compatibility and the formation of stereocomplex crystallite, which is confirmed by the DSC thermograms. However, the improvement in elongation-at-break is limited.

6.3 3D printing filament from toughened PLA/BP biocomposites

Due to the limited improvement in toughness of PLA/BP biocomposites by using PCL as a toughening agent and PCDL as a compatibilizer, PLA/BP/PBAT and PLA/BP/BPM were then extruded into FDM filament and examined. The filament diameter tolerance and roundness are represented by a box-and-whiskers chart, as shown in **Figure 6-13**. The box range cover from 25^{th} to 75^{th} percentile of the

dataset. Maximum value and minimum value were used to express the range of data distribution. PLA/BP/PBAT filament exhibited diameter tolerance and roundness at -0.05~0.04 mm and 0~0.02 mm respectively, demonstrating superior quality than corresponding -0.14~0.13 mm and 0~0.06 mm of PLA/BP/BPM filament, related with the relatively higher complex viscosity of PLA/BP/PBAT biocomposite [163], leading to a relatively higher melting strength and more stable melt flow.

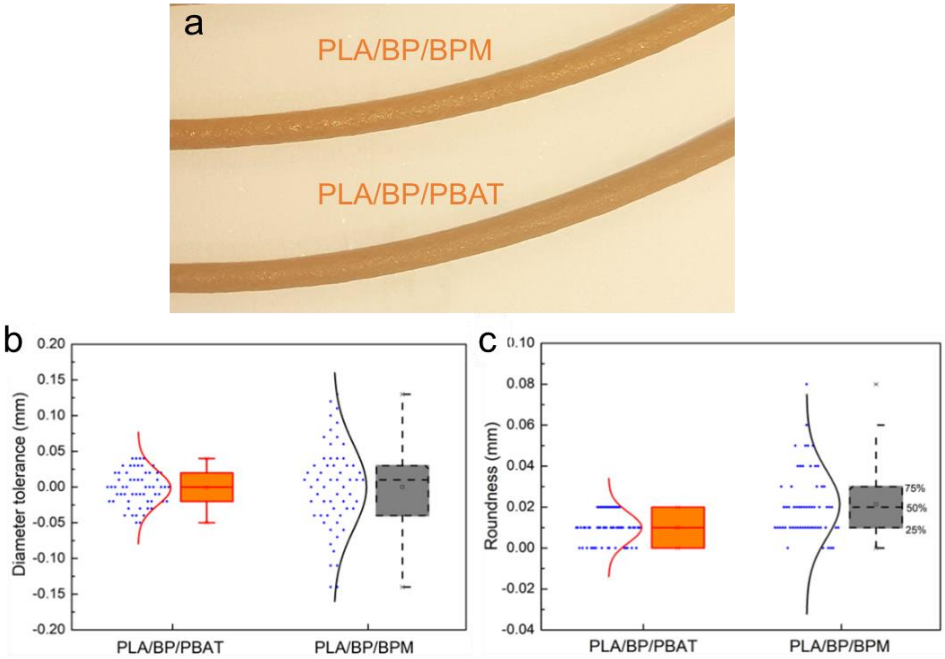

Figure 6-13 (a) Diameter tolerance and (b) roundness of PLA/BP biocomposite filament.

6.4 FDM-printed parts from toughened PLA/BP biocomposites

The biocomposite filaments were fabricated to standard specimens by FDM printing (using 3D da Vinci 1.0 Professional printer) shown in **Figure 6-14** and compared with the IM specimens.

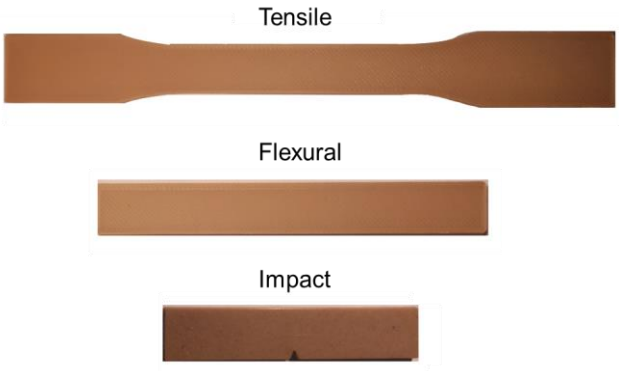

Figure 6-14 The FDM-printed specimens for mechanical test.

6.4.1 Mechanical properties

The mechanical properties are presented in **Figure 6-15**. With the addition of toughening agents and BP, the tensile strength (**Figure 6-15a**) of both IM and FDM-printed specimens decreased as expected, because of the lower tensile strength of toughening agents and weakening effect with the introduction of BP [15]. PLA/BP/PBAT showed higher elongation-at-break (**Figure 6-15b**, **c**) than PLA for both IM and FDM-printed specimens, demonstrating greater ductility because of the incorporation of a toughening agent with high ductility [166]. On the other side, PLA/BP/BPM exhibited lower elongation-at-break than PLA for both IM and FDM-printed specimens.

The impact strength is shown in **Figure 6-15d**. Toughened biocomposites showed higher impact strength than PLA feedstock for both IM and FDM-printed specimens. PLA/BP/PBAT and PLA/BP/BPM IM specimens showed 47% and 15% greater impact strength, and FDM-printed specimens showed 37% and 7% greater impact strength than corresponding PLA feedstock. FDM-printed specimens showed higher impact strength than IM specimens. PLA/BP/PBAT showed an increase in impact strength compared with PLA/BP/BPM for both IM and FDM specimens, demonstrating the higher toughness of PLA/BP/PBAT, attributed to the synergistic effect of both PBAT and reactive EGMA.

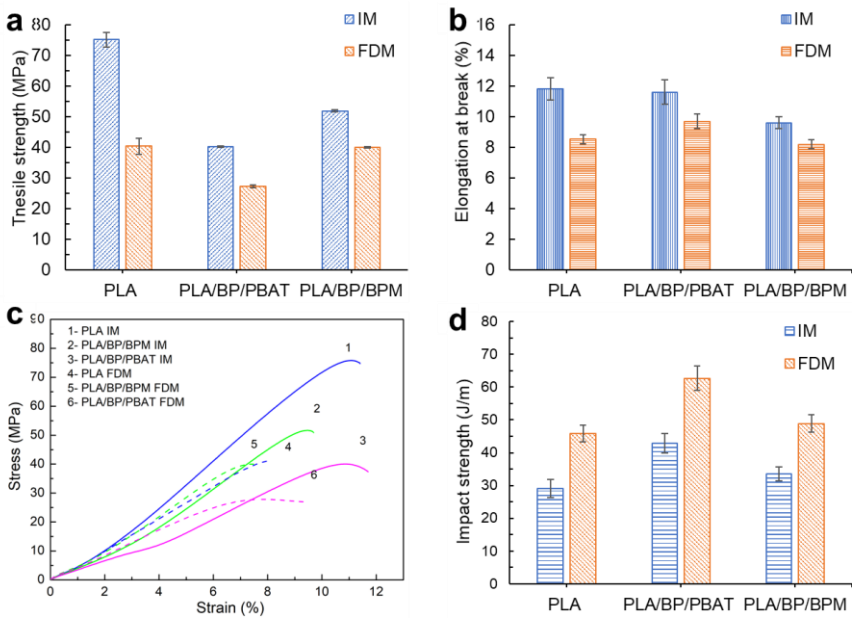

Figure 6-15 Mechanical properties of biocomposites: (a) tensile strength, (b) elongation-at-break, (c) representative tensile stress-strain curves, and (d) impact strength.

6.4.2 Fracture morphology

The SEM images for impact fracture surface of FDM specimens and cryo-fractured surfaces of IM specimens are shown in **Figure 6-15**. IM specimens showed smoother fracture surface than FDM-printed specimens, indicating higher brittleness of IM specimens, compared with FDM-printed sample, which contributed to the higher impact strength for FDM specimens against IM specimens. The biocomposites specimens showed ductile deformation as fibrils can be observed on the surfaces, contributing to the higher toughness of biocomposites against PLA. Fibre pull-out and debonding of BP filler from the matrix were observed on the fracture surfaces, indicating the interfacial bonding between BP and polymer matrix was lower than the internal strength of BP filler, the interfacial bonding was insufficient to provide satisfactory filler-matrix stress transfer [167].

Further BP filler pull-out and debonding from the polymer matrix on FDM specimen of PLA/BP/BPM were observed, compared to PLA/BP/PBAT, indicating enhanced interfacial adhesion between BP and PLA/PBAT matrix due to the existence of reactive GMA group, resulting in lower impact strength and elongation-at-break for PLA/BP/BPM than PLA/BP/PBAT. The PLA/BP/BPM IM specimen showed lower

filler-matrix adhesion because of discernible porosity between bamboo filler and matrix, leading to a lower impact strength than PLA/BP/PBAT [167].

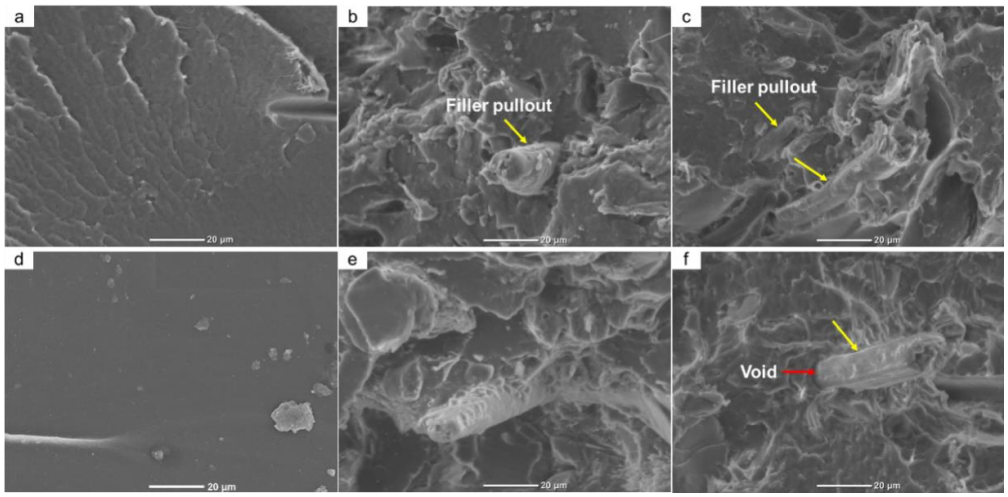

Figure 6-16 SEM images of the impact fracture surface of FDM-printed specimens: (a, b) PLA, (d, e) PLA/BP/PBAT and (g, h) PLA/BP/BPM, and cryo-fracture of IM specimens: (c) PLA, (f) PLA/BP/PBAT, and (i) PLA/BP/BPM specimens.

6.4.3 Surface roughness

The surface roughness of FDM-printed specimens was determined and compared in **Figure 6-16**. PLA/BP/BPM parts showed rougher surface and higher surface roughness with higher value in R_a, R_q, R_z, and R_{max} than PLA/BP/PBAT parts.

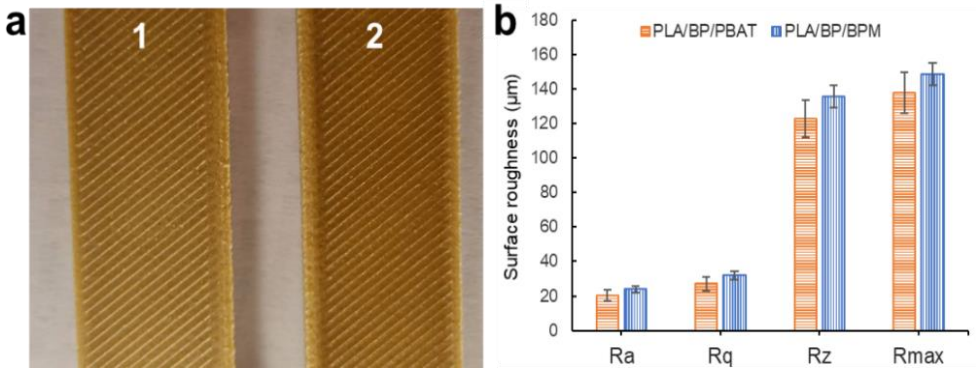

Figure 6-17 (a) FDM-printed specimens (1-PLA/BP/PBAT, 2-PLA/BP/BPM), and (d) surface roughness.

Overall, PBAT/EGMA, BPM520 and PCL improved the toughness of PLA/BP biocomposites for FDM application. PBAT/EGMA showed the maximum

toughening effect on both PLA and PLA/BP biocomposites. PCDL triblock copolymers were investigated as compatibilizers for PLA/PCL blend and PLA/BP/PCL biocomposites, the elongation-at-break of PLA/PCL blend was increased, whereas the improvement in impact strength was negligible. The increment in elongation-at-break of PLA/BP biocomposites brought by PCDL was also negligible. Based on the commercial accessibility, PLA/BP/PBAT and PLA/BP/BPM biocomposites were further examined as FDM feedstock. PLA/BP/PBAT possessed higher filament quality and showed higher ductility and impact strength for both IM and FDM products, smoother surface for FDM-printed parts, and better processability than PLA/BP/BPM. The results showed that PBAT/EGMA was an optimal toughening agent for PLA/BP biocomposites as FDM feedstock and was used as a toughening agent for the following research. This research provides fundamental data on the effect of toughness modification on the biocomposite feedstock, which facilitates the further application in FDM.

Chapter 7: Effect of biomass loading on properties of PLA biocomposites

The object of this chapter was investigating the effect of HH and BP loading on the comprehensive properties of PLA biocomposites for FDM application. HH and BP with the same particle size distributions (d_{50} = 50 μm) were studied in this study. PLA/HH biocomposite was enhanced by the increasing HH loading, the loading of 40 phr obtained the highest tensile strength, flexural strength, and flexural modulus. Whereas the mechanical properties of FDM-printed parts decreased as HH loading increased. The incorporation of BP decreased the mechanical properties for both IM and FDM-printed parts. Fortunately, the FDM-printed parts with HH loading and BP loading under 30 phr exhibited improved impact toughness than commercial PLA filament control, and the FDM-printed samples exhibited enhanced impact strength compared to IM parts. The flexural modulus of both IM and FDM-printed specimens increased when the HH and BP content increased up to 30 phr.

7.1 Effect of HH loading on PLA/HH biocomposites

Part of the work has been published in the following journal:

X. Xiao, V. S. Chevali, P. Song, D. He, H. Wang, Polylactide/hemp hurd bio-composites as sustainable 3D printing feedstock, Composites Science and Technology, p.107887, 2019.

Industrial HH is emerging as a bio-based filler in thermoplastic biocomposites. HH was utilized by Khan et al. [68, 69] in PLA/HH biocomposites with GMA compatibilizer, resulting in increased flexural modulus and mechanical performance at 20 wt.% comparable to neat PLA. However, PLA/HH biocomposite was not explored as FDM feedstock to the knowledge of the authors. In this study, HH/PLA biocomposites were developed as FDM feedstock through parametric analysis of the effects of HH loading in melt flow, rheology, physical, thermo-mechanical, and mechanical properties of the biocomposites using the formulations in **Table 7-1**. This work aimed to produce PLA/HH FDM filament comparable to neat PLA feedstock through systematic analysis of HH loading and associated filler effects. The central objectives of this work were to (a) investigate the thermal and crystallization response to analyse feedstock properties and explain underlying mechanisms of

microstructure development, and (b) parametrically investigate rheological behaviour, melt flow, filament quality, surface finish, and mechanical properties of FDM-printed samples, with respect to injection-moulded specimens of similar composition.

Table 7-1 The experimental formulations of PLA/HH biocomposites

Materials	PLA/PBAT (87 wt.%: 13 wt.%) (phr)	EGMA (phr)	HH (phr)	Additives (phr)
PLA-HH-0	100	6.5	0	2.2
PLA-HH-10	100	6.5	10	2.2
PLA-HH-20	100	6.5	20	2.2
PLA-HH-30	100	6.5	30	2.2
PLA-HH-40	100	6.5	40	2.2

* The compositions of additives are antioxidant (1010 and 168, 1:2, 0.75 phr), anti-hydrolysis stabilizer (0.25 phr), and lubricant (EBS 1.3 phr). The calculation of HH volume% used 0.128 g/cm^3 for HH density.

7.1.1 The properties of biocomposites materials

7.1.1.1 Chemical structure

The FTIR analysis of neat PLA, HH powder, and PLA/HH biocomposites with and without HH was conducted to investigate the chemical linkage of HH and PBAT to PLA through EGMA. The FTIR spectra in the range of 4000 to 500 cm^{-1} are shown in **Figure 7-1**. HH has main functional groups at 3323 cm^{-1} and 2883 cm^{-1}, corresponding to O-H stretching and C-H symmetrical stretching from polysaccharides, 1728 cm^{-1} corresponding to C=O unconjugated stretching from hemicellulose and 1030 cm^{-1} for C–C, C–OH, C–H ring and side group vibrations from hemicellulose and pectin [136]. Neat PLA has the main functional groups at 1750 cm^{-1}, attributed to C=O stretching of ester groups [168], 1452 cm^{-1} for CH_3 symmetrical bends [169], and 1037, 1085, 1128 and 1182 cm−1 with respect to C-C and C-O stretching [170]. The FTIR spectra of PLA-HH-0 (PLA/PBAT/EGMA) is similar to that of PLA, however, there is a new peak observed at 727 cm^{-1} and highlighted with an arrow in **Figure 7-1**, attributed to the bending vibration absorption of CH- plane of the benzene of PBAT [26]. Whereas the peak at 1163 cm^{-1}, representing the stretching vibration motion of C-O band in neat EGMA [171], was

not found, indicating the end group of PLA or/and PBAT might react with EGMA. The PLA/HH biocomposites exhibited FTIR spectra combined PLA-HH-0 with HH powder. The absorbance at 1750 cm^{-1} decreased with increasing HH loading, due to the decrease in the PLA portion. The peak at 3323 cm^{-1} represents OH groups from HH disappeared in the PLA/HH biocomposites, may because of the reaction between OH groups and GMA functional group in EGMA and an interaction between the carbonyl groups of PLA, PBAT and hydroxyl groups of HH through hydrogen bonding [81].

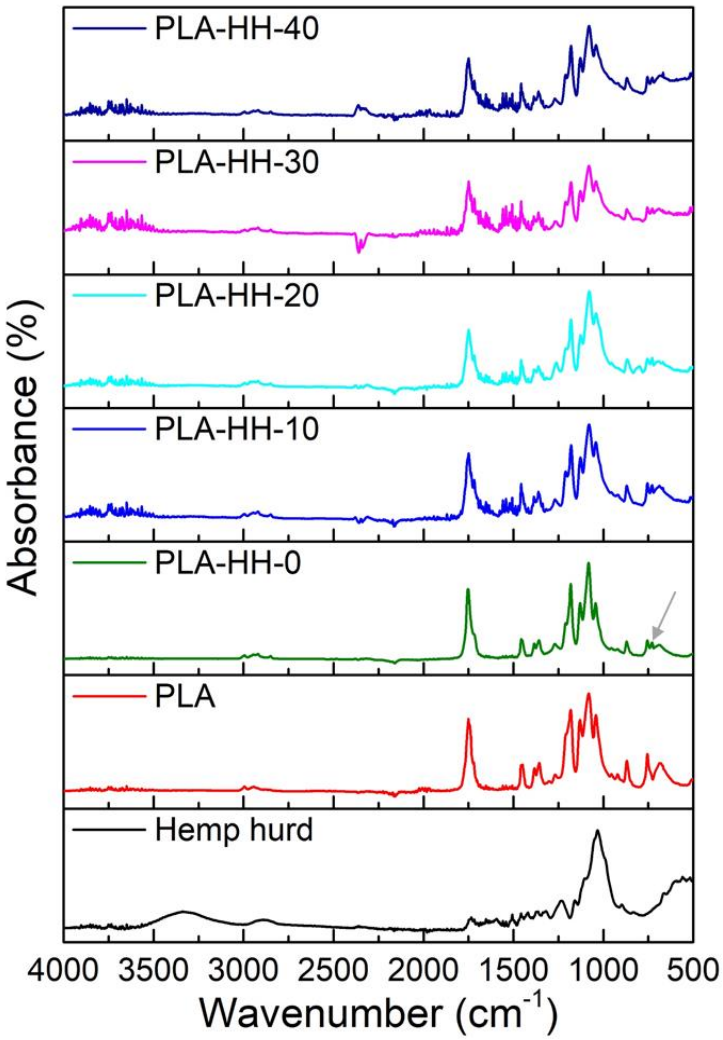

Figure 7-1 FTIR spectra of HH powder, PLA, and PLA/HH biocomposites.

7.1.1.2 Rheological properties

The melt rheological properties of biocomposites with and without HH were investigated by DHR-2 parallel-plate rotational rheometer, as presented in **Figure 7-2**. Complex viscosity increased with increasing HH loading at a low angular

frequency, indicating a decrease in melt flow and processability, proved by decreased melt flow index as shown in **Figure 7-2b.** MFR decreased from 3.30 g/10 min for PLA-HH-0 to 1.26 g/10 min for PLA-HH-40. The HH inclusion in particulate composite increased the viscosity in melt form and hindered the mobility of polymer chains as expected. Tian et al. [172] observed that an MFR lower than 2 g/10 min at processing caused challenge during extrusion. The biocomposites showed shear-thinning behaviour because of disentanglement, and reorientation of HH and polymer chains in the flow direction, weakening the viscous resistance [164], indicating particle-to-particle interaction in melt [173]. PLA-HH-10 showed a slighter shear-thinning behaviour (similar as PLA-HH-0) than other biocomposites, because of weak inter-particle interaction. The shear-thinning behaviour of biocomposites was enhanced with increasing HH loading, with minor differences in complex viscosity within the biocomposites at high angular frequency. This shear-thinning behaviour assists in lowering complex viscosity and obtaining improved melt flow and processability with enhancements in extrusion throughput during melt extrusion [162]. PLA-HH-40 showed the highest complex viscosity over the whole frequency range, leading to the lowest ease of printability and roughest surface within the biocomposites because of melt instability. Both storage modulus and loss modulus increased with increasing HH loading, mainly at low frequencies. This behaviour suggests the inhibited mobility of polymer chains in melt state due to the presence of HH [167, 174]. The highest values of G' and G'' were observed for PLA-HH-40, indicating the strongest interaction between the polymer matrix and HH filler. In addition, G' and G'' of all samples displayed deviation from linear viscoelastic relationships of $\log G'(\omega) \sim 2\log \omega$ and $\log G''(\omega) \sim \log \omega$ in the terminal region ($\omega < 0.1$ rad/s). The slopes of G' and G'' in the terminal region deviated from 2 and 1, respectively, as presented in **Table 7-2**, suggesting phase-separation in the biocomposites, where the addition of HH increased the tendency of phase-separation. Tan δ decreased and the dependency on angular frequency decreased with increasing HH loading, because of increased elasticity [112]. PLA-HH-0 showed a decrease in tan δ with increasing angular frequency, exhibiting a fluid-like rheological behaviour [107]. PLA-HH-10 showed characteristic viscous behaviour over the whole frequency range, and PLA-HH-20 showed viscous behaviour below 200 rad/s. PLA-HH-30 displayed viscous behaviour above 2 rad/s. PLA-HH-40 showed a tan δ value

less than 1 ($G' > G''$) over the whole oscillation frequency range, the solid-like behaviour indicates the elastic fraction being predominant over the viscous fraction, causing a decrease in interfacial energy dissipation [175], as PLA-HH-40 displayed lower melt flow and lower ease of processability than other biocomposite blends.

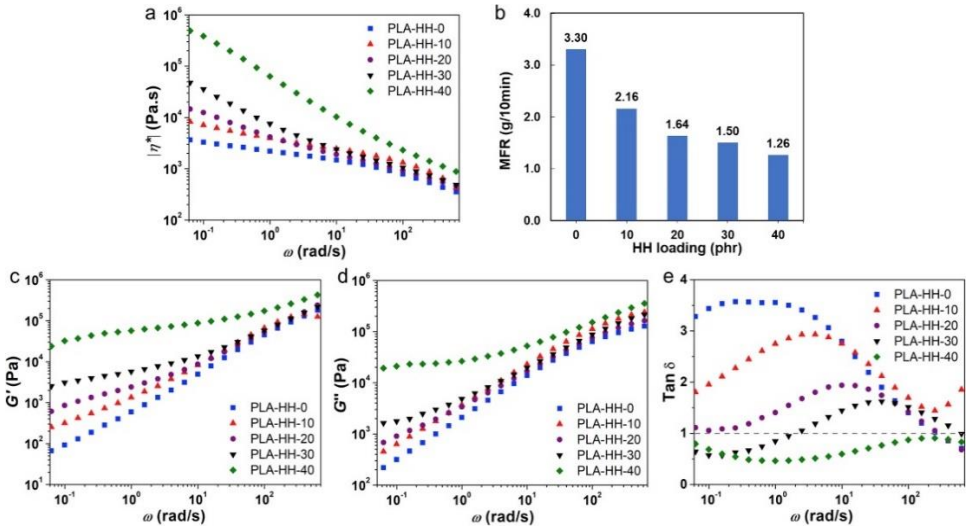

Figure 7-2 Rheological and melt behaviour of PLA/HH biocomposites: (a) $|\eta^*|$, (b) MFR versus HH loading, (c) G', (d) G'', and (e) tan δ.

Table 7-2 The slope of G' and G'' in the terminal region

Terminal slope	PLA-HH-0	PLA-HH-10	PLA-HH-20	PLA-HH-30	PLA-HH-40
G'	0.72	0.51	0.73	0.43	0.66
G''	0.79	0.73	0.61	0.18	0.19

The steady-state shear rheological properties at the same temperature (190°C) were determined on MCR502 (Anton Paar, Austria). Shear rate ranging from 0.01 to 10 000 s^{-1} was employed. Two specimens for each material were tested and the average value was used for the graphs in **Figure 7-3**. Zero-shear viscosity increased with increasing HH loading as summarized in the right table. The biocomposites with higher HH loading yielded at a lower shear rate, the materials showed smaller Newtonian region. The materials reached similar viscosity when the shear rate increased to around 6.8 s^{-1}.

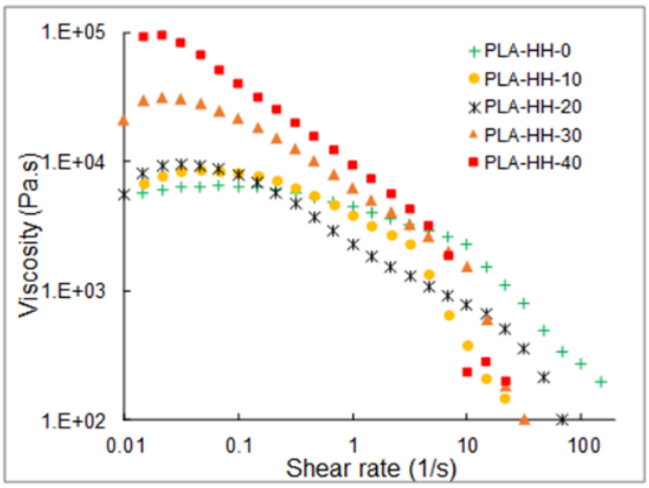

Materials	η_0 (Pa.s)
PLA-HH-0	6,430
PLA-HH-10	7,835
PLA-HH-20	9,315
PLA-HH-30	30,650
PLA-HH-40	94,900

Figure 7-3 Steady-shear viscosity vs shear rate plots and zero-shear viscosity of PLA/HH biocomposites determined by Anton Paar modular compact MCR502.

7.1.1.3 Thermal transition and crystalline properties

DSC characterizes transition temperatures and degree of crystallinity, which dictate the processing temperature and the mechanical properties. The second heating thermograms are presented in **Figure 7-4**, and the corresponding transition temperatures and enthalpy are listed in **Table 7-3**. Commercial PLA (4032D grade) was used as a control. T_g and T_m showed marginal changes with increasing HH loading, indicating the incorporation of HH did not affect the thermal transition of biocomposites. T_{cc} increased upon the inclusion of HH (PLA-HH-10), indicating HH inclusion impeded the crystallization of PLA, and resulted in decreased crystallization enthalpy correspondingly. Further increases in HH loading, i.e., PLA-HH-20 to PLA-HH-40 showed associated decreases in T_{cc}. This behaviour can be surmised as being driven by the increased availability of nucleation sites and heterogeneous nucleation, facilitating the secondary crystallization [32,33] and thereby causing increased crystallization enthalpy. Nevertheless, the crystallinity (X_c) increased from 3.1% to 33.6% after the addition of PBAT/EGMA, and furtherly increased to 43.2% after the incorporation of HH, indicating HH enhanced the crystallinity of the biocomposites. However, the crystallinity showed marginal changes (retained at 42.5±1 %) with additional HH loading, which can be attributed to a concomitant reduction in the availability of free volume [68, 84] with increasing occupancy of HH in the biocomposites.

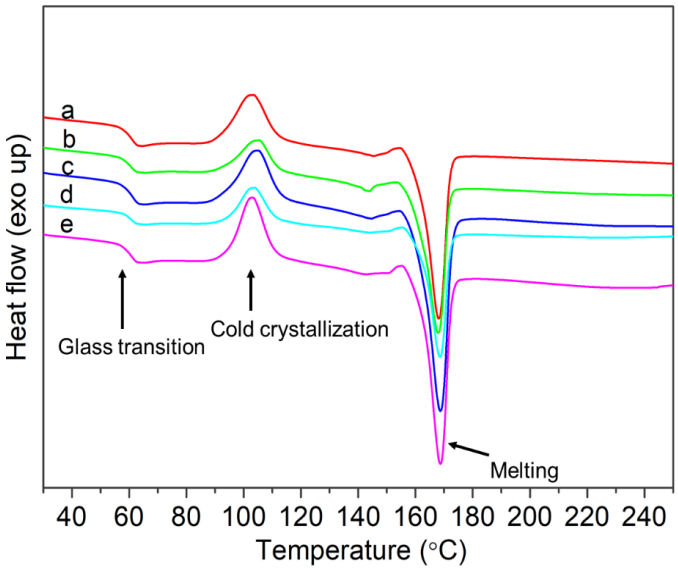

Figure 7-4 DSC curves of PLA/HH biocomposites with varying HH loading levels, (a) PLA-HH-0, (b) PLA-HH-10, (c) PLA-HH-20, (d) PLA-HH-30, (e) PLA-HH-40.

Table 7-3 Crystallization and melt phase properties of PLA/HH biocomposites as a function of HH loading

Sample	T_g (°C)	T_{cc} (°C)	ΔH_{cc} (J/g)	T_m (°C)	ΔH_m (J/g)	X_c (%)
PLA[a]	62.1	-	-	168.4	2.90	3.1
PLA-HH-0	61.1	103.2	24.7	168.0	49.7	33.6
PLA-HH-10	60.6	105.4	15.8	167.9	45.2	43.2
PLA-HH-20	61.2	105.0	18.0	168.7	44.7	42.5
PLA-HH-30	61.0	103.7	18.8	168.5	43.7	42.7
PLA-HH-40	60.6	103.0	21.4	168.6	44.1	41.7

[a] Neat PLA, without PBAT/EGMA.

The crystalline structure of neat PLA, HH, and PLA-HH-0 (PLA/PBAT/EGMA without HH) was furtherly characterized by XRD, and the XRD patterns are shown in **Figure 7-5**. HH has two diffraction peaks at 2θ = 15.8° and 22.3°, in accordance with the data reported by Khan et al. [68]. The high-intensity peak of PLA is observed at 2θ of 16.5°. PLA-HH-0 exhibits a peak at a similar position with a similar shape as PLA. The XRD patterns of PLA, HH, and PLA/HH biocomposites with and without HH were compared in **Figure 7-6**. There was no peak observed on

the XRD pattern of HH, neat PLA, and PLA-HH-0, whereas PLA-HH-20 and PLA-HH-40 exhibited strong peaks at 2θ of 16.5° with high intensity, assigned to PLA, indicating the increase in crystallinity of PLA aided by HH. PLA-HH-40 showed lower intensity than PLA-HH-20 due to the lower PLA content in biocomposite and the inhibition of crystallization because of an excess of HH, agree with the DSC results during the first heating.

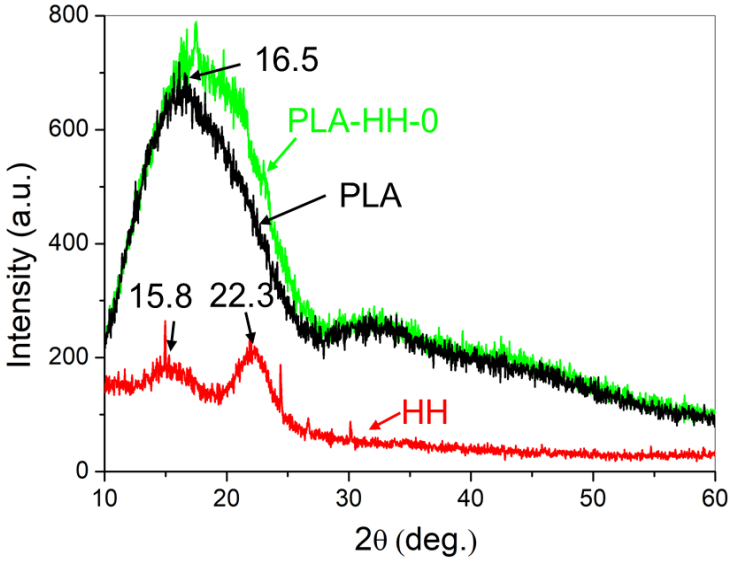

Figure 7-5 XRD patterns of neat PLA, HH and PLA-HH-0 (PLA/PBAT/EGMA without HH).

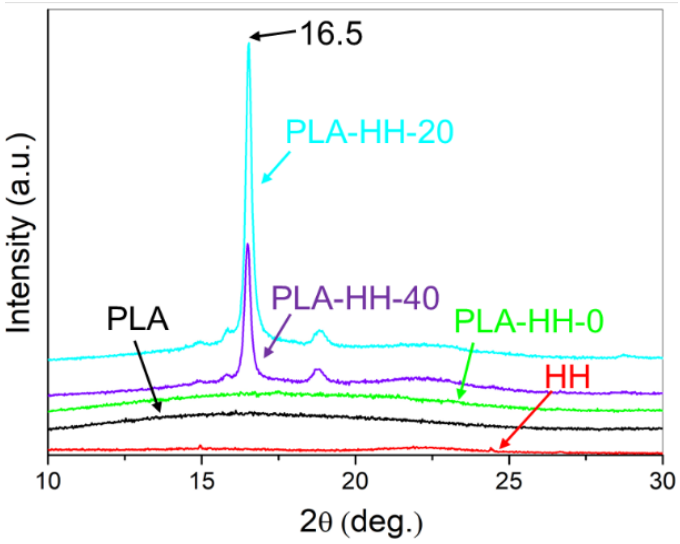

Figure 7-6 XRD patterns of neat PLA, HH, PLA-HH-0 and PLA/HH biocomposites.

7.1.1.4 Fracture morphology of HH and PLA interface

The cryo-fractured surfaces of IM specimens were observed by SEM, as shown in **Figure 7-7**. HH fillers dispersed in the polymer matrix in both parallel and perpendicular direction of the fracture surface and encapsulated in the matrix. The filler parallel to the surface retains its fibrillary structure with aspect ratio suggestive of a filler (**Figure 7-7c**, gold arrow). The filler perpendicular to the surface showed failure within the filler (**Figure 7-7b**, white arrows), demonstrating adequate interfacial adhesion, rather than pull-out from the matrix. As HH loading increased, HH filler debonding (**Figure 7-7d**, **d'**, red arrow) and pull-out (**Figure 7-7d**, **d'**, light blue arrow) from matrix occurred in PLA-HH-40, indicating the decrease in interfacial adhesion between HH and PLA/PBAT matrix. HH filler was agglomerated (**Figure 7-7d**, **d'**, yellow arrow) in PLA-HH-40, indicating a decreased filler dispersion and increased particle cohesion. The SEM images suggested brittle fracture in IM specimens, as shown in the smooth fracture surfaces without plastic deformation [176].

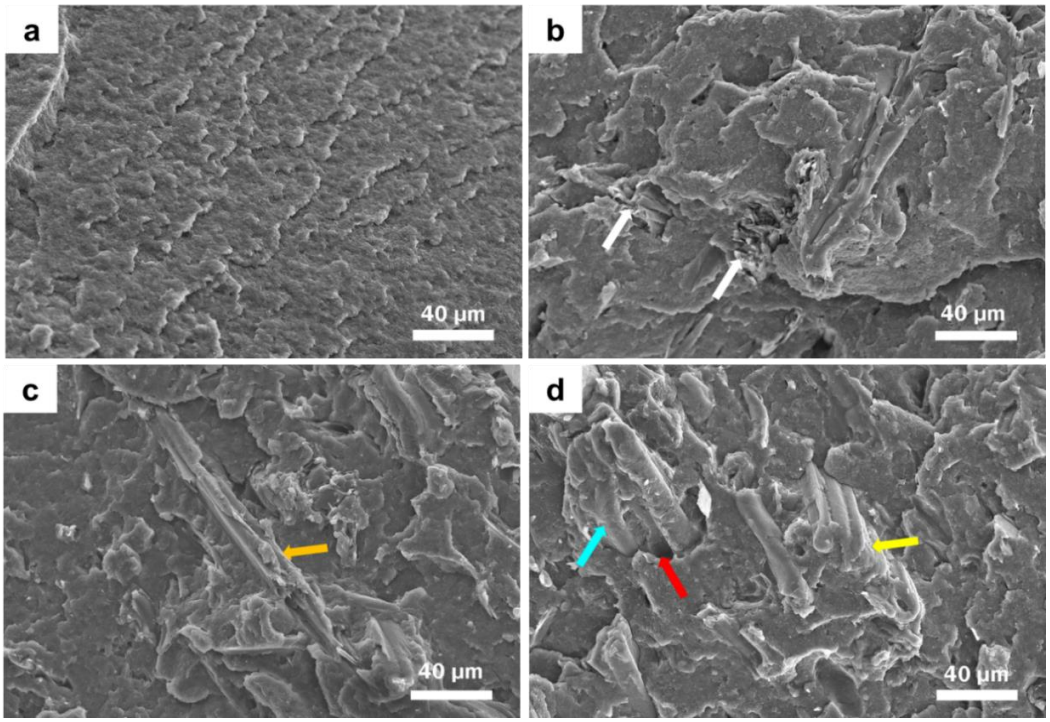

Figure 7-7 SEM images of cryo-fractured surfaces of specimens: (a) PLA-HH-0, (b) PLA-HH-10, (c) PLA-HH-20 and (d) PLA-HH-40 at a magnification of 500×.

7.1.1.5 Mechanical properties of IM specimens

Mechanical properties of IM specimens are shown in **Figure 7-8**. After a decrease from 51.9 to 47.5 MPa, the tensile strength increased to 57.5 MPa in injection moulded PLA-HH-40. Flexural strength also showed a similar increasing trend as tensile strength, increased from 75 MPa for PLA-HH-0 to 84 MPa for PLA-HH-40. The reinforcement effect of HH in the tensile and flexural strength can be attributed to the fibrillary structure and interaction between the PLA/PBAT matrix and HH, contributing to the enhanced filler-matrix stress transfer, as supported by SEM imagery showing fracture confined within the filler. Impact strength decreased as expected [64], from 69.8 J/m in PLA-HH-0 to 42.9 J/m in PLA-HH-40, as the dispersion of HH particles in the matrix created regions of stress concentration that yielded under stress [177]. SEM also supported the prevalence of brittle fracture, where a flat fracture surface was discernible. The flexural modulus increased from 2.4 GPa in PLA-HH-0 to 3.9 GPa in PLA-HH-40 as expected, because of the increased stiffness brought about by the inclusion of HH filler resembling an elongated filler [88]. The incorporation of HH to PLA/PBAT matrix slowed down the chain movements, and hence showed an increased stiffness. The stiffness and brittleness of the biocomposites were also enhanced by an increase in crystallinity of PLA because of the HH inclusion, as demonstrated through DSC analysis.

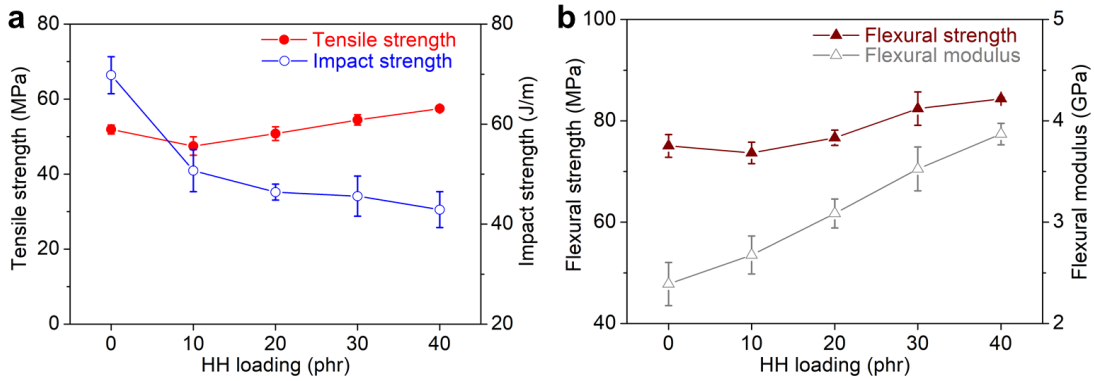

Figure 7-8 Mechanical properties of IM specimens: (a) tensile and impact strength, and (b) flexural properties, as a function of HH loading.

7.1.2 Filament quality

Biocomposite filaments extruded using biocomposite pellets through a sing-screw filament extruder (the process is shown in **Figure 7-9a**) were compared about the

diameter tolerance and roundness. The surface of the filaments discernibly becomes rougher with increasing HH loading (**Figure 7-9b**). The filament diameter tolerance and roundness are represented as box-and-whiskers charts (**Figure 7-9b**, **c)**. The box range cover from 25th to 75th percentile of the dataset. The maximum value and minimum value were used to express the range of data distribution. All HH-filled filaments exhibited acceptable diameter tolerances (±0.02 mm, **Figure 7-9b**), better than the PLA-HH-0 filament. PLA-HH-0 showed a relatively higher diameter tolerance of ±0.03 mm because of its lower viscosity during processing (~190°C), leading to a relatively lower melt strength and perturbed melt flow. The roundness was less than 0.03 mm. PLA-HH-20 showed a roundness in the range of 0.01 mm to 0.06 mm due to the insufficient melt observed at the die exit, in turn leading to insufficient melt strength.

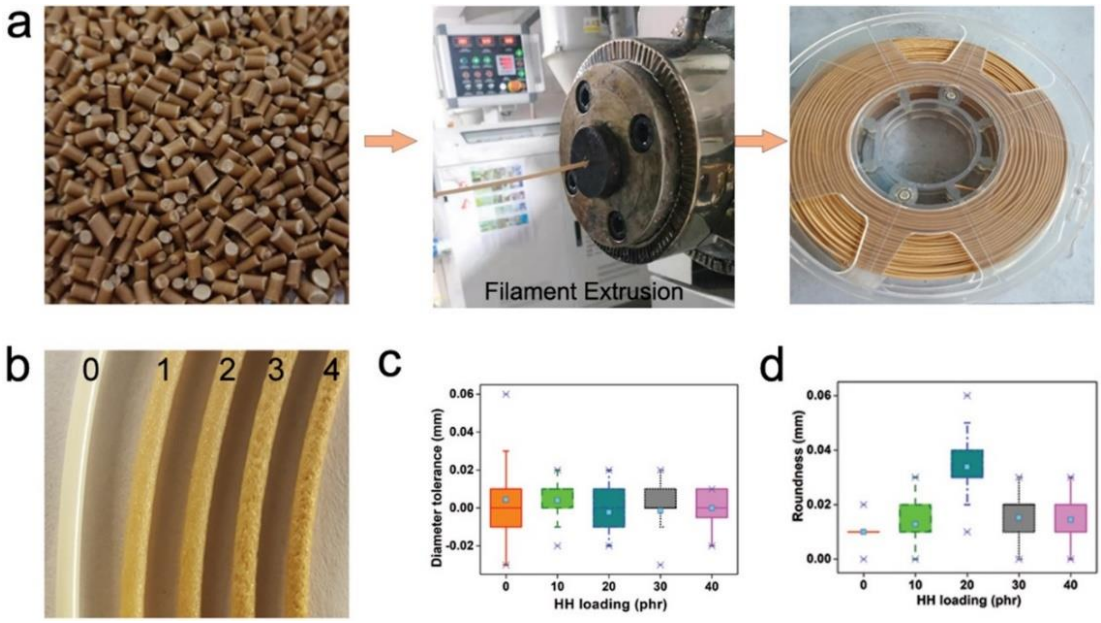

Figure 7-9 (a) PLA/HH pellets extruded as filaments, (b) PLA/HH filament, (c) diameter tolerance and (d) roundness of PLA/HH filament as a function of HH loading. The labels indicate (0) PLA–HH–0, (1) PLA–HH–10, (2) PLA–HH–20, (3) PLA–HH–30 and (4) PLA–HH–40.

7.1.3 The properties of FDM-printed specimens

7.1.3.1 Finish quality

FDM-printed specimens showed increasing surface roughness and darker colour with increasing HH loading (**Figure 7-10a**, **b**). The darker colour might be produced by the presence of a small number of aromatic residues in HH powder, which supposedly got oxidized during the heating process of filament extrusion and FDM printing [178]. Surface roughness data is presented in **Figure 7-10c**. With the addition of HH, R_a (arithmetic mean roughness) increased from 3.8 µm for PLA-HH-0 to 19.7 µm for PLA-HH-10 and maintained at 19.0±1.0 µm with increasing HH loading. R_q (root mean square roughness) remained unchanged at 26.0±1.0 µm after an increase from 4.5 µm of PLA-HH-0 to 27.0 µm for PLA-HH-10. The roughness values indicate that the surface smoothness decreased after the inclusion of HH, however, the average surface roughness value was not affected by increasing HH loading, attributed to an equivalent layer thickness (0.15 mm, and significantly larger than the average particle size of 50 µm). PLA-HH-10 and PLA-HH-20 showed nearly a similar value in mean peak-to-valley height, R_z (115.7 µm and 114.9 µm) and maximum peak-to-valley height, R_{max} (128.3 µm and 125.0 µm), and PLA-HH-30 and PLA-HH-40 showed higher R_z (122.7 µm and 124.0 µm) and R_{max} (149.4 µm and 145.5 µm), indicating PLA-HH-30 and PLA-HH-40 displayed a larger maximum defect height indicative of a rougher surface than PLA-HH-10 and PLA-HH-20, causing PLA-HH-30 and PLA-HH-40 to exhibit rougher surface than PLA-HH-10 and PLA-HH-20. The porosity and shrinkage data are presented in **Figure 7-10d**. The shrinkage of all samples is lower than that of PLA (0.33±0.04 %) and decreased from 0.30±0.06 % (PLA-HH-0) to 0.03±0.01 % (PLA-HH-40), indicating the dimensional accuracy improved with increasing HH loading. The shrinkage analysis demonstrated that increasing HH inclusion was advantageous for achieving dimensional constancy. The porosity increased from 5.8% of PLA-HH-0 to 17.9% of PLA-HH-40. The substantial fraction of porosity (~ 20%) in FDM samples was also reported by Le Duigou et al. [143] and is caused by increasing viscosity, resulting in decreasing melt flow from the nozzle and resultant inadequate adhesion between layers. The porosity and the corresponding bulk density (measured by dividing the mass of the flexural specimen by its bulk volume) of IM and FDM-printed specimens

were detailed in **Table 7-4**. The density of IM specimens increased with increasing HH loading, whereas FDM-printed specimens showed decreasing density with increasing HH loading. The porosity fields in the IM specimens were characterized using X-ray computer tomography (CT) technique. The analysis of porosity yielded a near-zero or zero porosity in the IM specimens as shown in **Figure 7-11**, demonstrating the homogeneous and low porosity structure of IM specimens, and hence support their usage as a basis for calculating the porosity in the FDM-printed specimens.

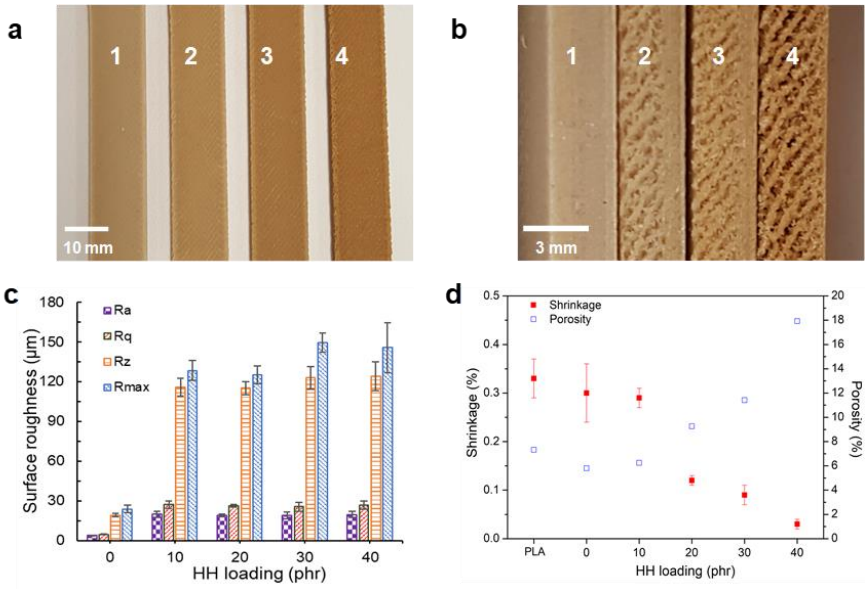

Figure 7-10 FDM-printed specimens in (a) top view, and (b) side view, (c) surface roughness, and (d) porosity and shrinkage as a function of HH loading. (1) PLA–HH–10, (2) PLA–HH–20, (3) PLA–HH–30 and (4) PLA–HH–40.

Table 7-4 Bulk density and porosity of processed specimens

Materials	Density (g/cm^3) FDM	Density (g/cm^3) IM	Porosity of FDM-printed specimens (vol. %)
PLA-HH-0	1.15±0.01	1.22±0.02	5.8
PLA-HH-10	1.16±0.01	1.24±0.01	6.2
PLA-HH-20	1.12±0.01	1.23±0.01	9.3
PLA-HH-30	1.13±0.01	1.28±0.01	11.4
PLA-HH-40	1.04±0.01	1.27±0.00	17.9

The density measured according to Archimedean immersion method (ASTM D 792/ISO 1183-1, method A) further proved that IM specimens had higher density and lower porosity than FDM-printed specimens, as shown in **Table 7-5**. PLA-HH-0 IM specimen exhibited lower density than FDM specimen because of the existence of voids in IM specimen as shown in **Figure 7-11**.

Table 7-5 Density and porosity of biocomposite specimens (Archimedean immersion method)

Materials	Density (g/cm^3) FDM	Density (g/cm^3) IM	Porosity (%) FDM
PLA-HH-0	1.237±0.001	1.221±0.002	-
PLA-HH-10	1.192±0.007	1.235±0.001	3.4
PLA-HH-20	1.164±0.013	1.246±0.001	6.6
PLA-HH-30	1.122±0.007	1.259±0.001	10.8
PLA-HH-40	1.053±0.012	1.274±0.002	17.3

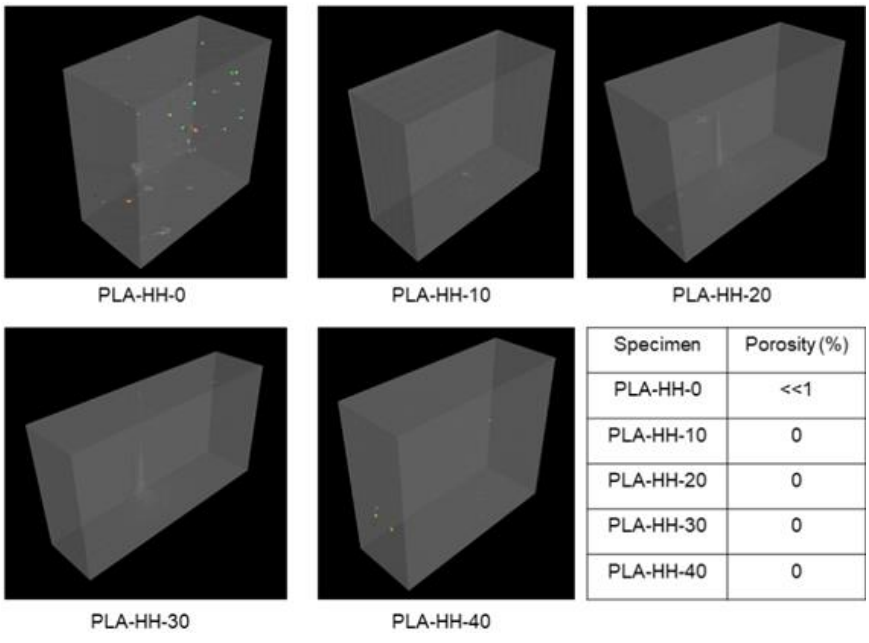

Figure 7-11 The X-ray CT imagery for the PLA-HH-0 to PLA-HH-40 IM specimens, showing zero or near-zero porosity.

7.1.3.2 Morphology

The impact fracture surfaces of FDM-printed specimens as observed by SEM are shown in **Figure 7-12**. The thickness of interlayer space between two deposited layers (yellow dotted rectangles in **Figure 7-12c** and **Figure 7-12e**) increased with increasing HH loading, resulting in decreased interfacial bonding and consequently decreased mechanical properties. PLA-HH-40 showed an indistinct boundary between layers (**Figure 7-12g**), because of highest viscosity and a predominant elastic fraction over a viscous fraction, resulting in inconsistent melt flow, thus deteriorating the interfacial bonding. The volume and count of voids on the fracture surface increased with increasing HH loading, because of the pull-out of HH filler from the polymer matrix or formed during FDM printing. Increased interlayer space and voids led to increased porosity and decreased mechanical properties. The HH filler pull-out indicates the insufficient interfacial bonding between HH and polymer matrix to provide satisfactory filler-matrix stress transfer, resulting in decreased mechanical properties as well. The FDM-printed specimens exhibited elasto-plastic deformation, with elongated fragments discernible on the surface, as shown in the SEM micrographs (**Figure 7-12b, d, f, h)**, which contributed to the enhanced impact strength compared with IM samples because of the energy dissipation.

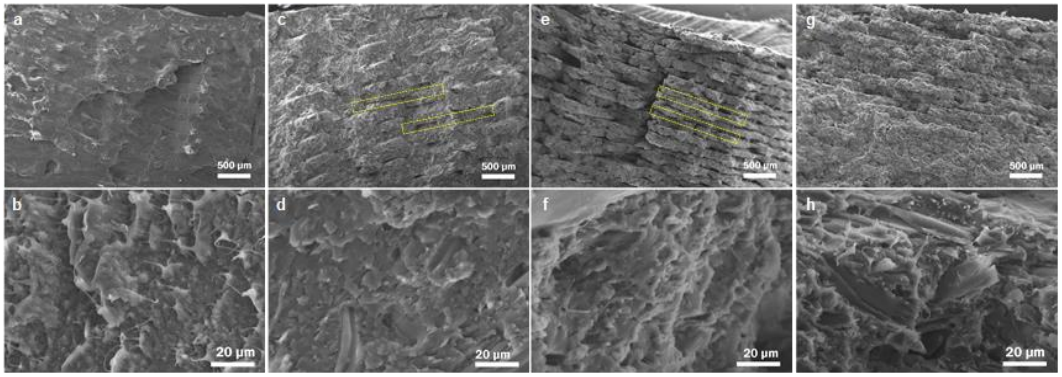

Figure 7-12 SEM images of impact fracture surfaces of FDM-printed specimens: (a, b) PLA-HH-0, (c, d) PLA-HH-10, (e, f) PLA-HH-20, and (g, h) PLA-HH-40. The layer boundary is shown using dotted rectangles in (c) and (e).

7.1.3.3 Mechanical properties

In contrast to IM specimens, both tensile strength and flexural strength decreased with increasing HH loading as shown in **Figure 7-13**, with PLA-HH-40 showing a decrease by 50% and 32% respectively, compared to PLA-HH-0. The decrease in mechanical properties is linked with insufficient interfacial bonding, resultant of voids and interlayer space produced at the interface between HH and polymers, and between layers during FDM process [26], because of the decreased melt flow. The impact strength decreased with increasing HH loading, like IM samples, and consistent with the literature [68]. Increased porosity and the addition of HH as stress raisers can be surmised to contribute to yielding [179], resulting in overall increased embrittlement in the FDM-printed specimens, affecting printability and subsequent application. Nevertheless, PLA-HH-30 exhibited impact strength comparable to commercial PLA FDM samples. Conversely, flexural modulus increased up to 30 phr HH loading. A decrease in flexural modulus at PLA-HH-40 can be attributed to an increase in porosity and the associated inadequate interfacial bonding, showing a critical loading level (30 phr) in terms of HH loading in the PLA/PBAT matrix.

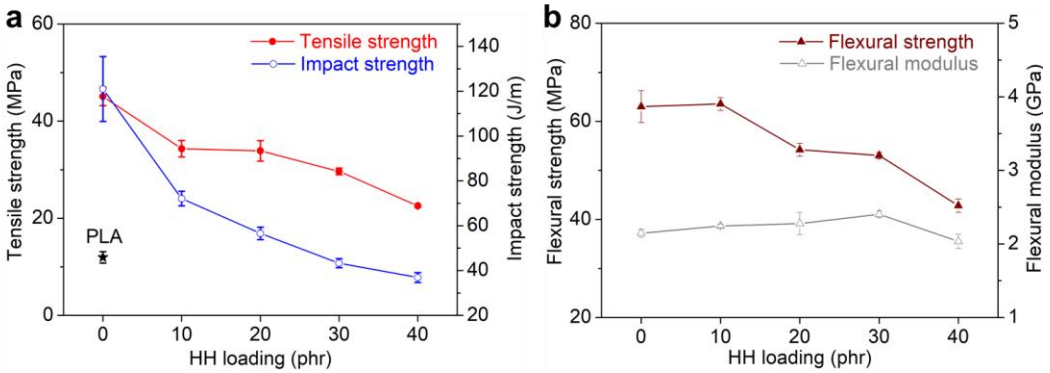

Figure 7-13 Mechanical properties of FDM-printed specimens: (a) tensile and impact strength and (b) flexural properties as a function of HH loading. The impact strength data of commercial PLA filament is shown using a (⋆) symbol.

Specific mechanical properties were calculated for commercial PLA filament and PLA/HH biocomposites produced using IM and FDM as illustrated in **Table 7-6**. The density normalization did not bear any effect on specific mechanical properties as they showed similar trends as the non-normalized values. The IM samples showed higher overall specific tensile and flexural properties than FDM-printed samples.

With increasing HH loading, the differences in specific tensile strength and flexural properties between FDM and IM samples were pronounced from unfilled to 40 phr grades. The higher specific tensile strength and flexural properties for IM samples are expected as a more homogenous, low-porosity structure (**Figure 7-14**, **Table 7-4**) was attained in the processing, in contrast to FDM-printed specimens. In the case of the FDM-printed specimens, porosity in the microstructure acted as stress raisers. A higher flexural modulus in the IM samples could also be attributed to higher-stiffness filler providing resistance to chain deformation, and the absence of major porosity. The specific impact strength values for FDM-printed samples were higher than IM samples. The increase in specific impact strength for FDM samples versus IM samples was diminished with increasing HH loading, which can be surmised as a combined effect of increased crystallinity from PLA-HH-0 (33.6%) to PLA-HH-40 (41.7%), and the increased porosity in the FDM-printed specimens (**Figure 7-10d**). In a particulate-filled thermoplastic composite, the impact toughness is dictated by the polymeric segments surrounding the contiguous particles, which assist in transforming the plane strain to plane stress [179]. The FDM-printed specimens can transfer the impact energy through the interface of each deposited PLA/HH layer, an effect that diminishes in higher HH loading in FDM sample because of the increased porosity and loss of effective interfacial bonding and dispersion of particles. Overall, the FDM process yielded higher impact strength parts over their IM counterparts.

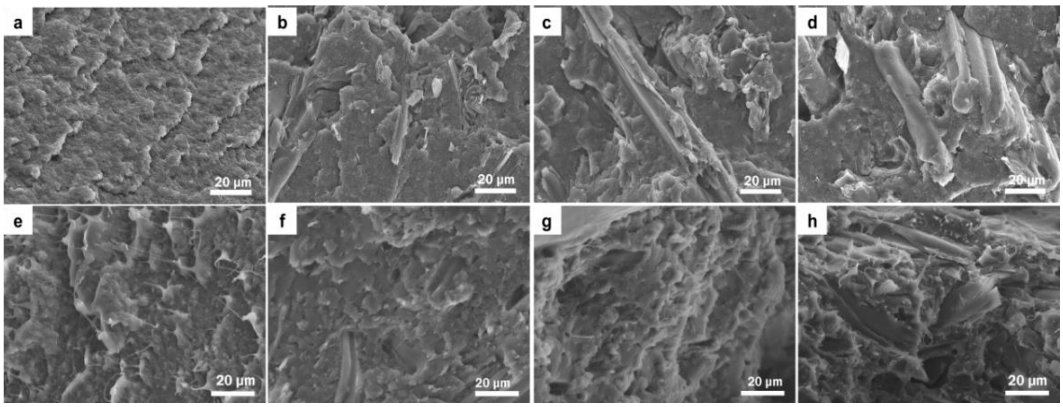

Figure 7-14 SEM images of surfaces of IM specimens: (a) PLA-HH-0, (b) PLA-HH-10, (c) PLA-HH-20 and (d) PLA-HH-40 and FDM specimens: (e) PLA-HH-0, (f) PLA-HH-10, (g) PLA-HH-20 and (h) PLA-HH-40.

Table 7-6 Specific mechanical properties of processed biocomposite feedstock and commercial PLA feedstock

Samples	Specific Tensile Strength (MPa.cm³/g)		Specific Impact Strength (J.cm³/g.m)		Specific Flexural Strength (MPa.cm³/g)		Specific Flexural Modulus (GPa.cm³/g)	
	FDM	IM	FDM	IM	FDM	IM	FDM	IM
PLA[§]	-	-	40±2.2	-	-	-	2.60±0.22	-
PLA-HH-0	39±1.6	42±1.0	105±13	57±3.0	55±2.8	62±1.8	1.87±0.05	1.96±0.17
PLA-HH-10	30±1.5	38±2.0	62±2.8	41±3.4	55±1.1	59±1.7	1.93±0.02	2.16±0.15
PLA-HH-20	30±1.9	41±1.5	50±2.5	38±1.3	48±1.2	62±1.2	2.03±0.14	2.51±0.12
PLA-HH-30	26±0.6	42±1.1	38±1.8	36±3.1	47±0.6	64±2.6	2.13±0.04	2.75±0.17
PLA-HH-40	22±0.3	45±0.3	36±2.1	34±2.8	41±1.3	66±0.2	1.96±0.09	3.05±0.08

[§] Commercial PLA FDM filament

7.1.3.4 Thermal stability

TGA determined the decomposition behaviour of materials. The TGA and DTG curves of FDM and IM specimens of PLA/HH biocomposites are shown in **Figure 7-15**, and the data are summarized in **Table 7-7**. All the characteristic temperatures decreased with increasing HH loading, indicating the increasing HH loading reduced the thermal stability of both FDM and IM specimens, due to the lower decomposition temperature of HH (T_{onset}: 296°C, T_{50}: 350°C, and T_{max}: 360°C as discussed in Chapter 4). FDM-printed specimens generally showed higher thermal temperatures than IM specimens, attributed to the lower pressure and shorter retention time in the nozzle with high temperature for FDM parts. The result demonstrates that the FDM process is advantageous for the thermal stability of products. PLA-HH-40 FDM sample showed significantly higher thermal temperatures than PLA-HH-40 IM specimen, because of the relatively higher injection pressure used due to its lowest melt flow.

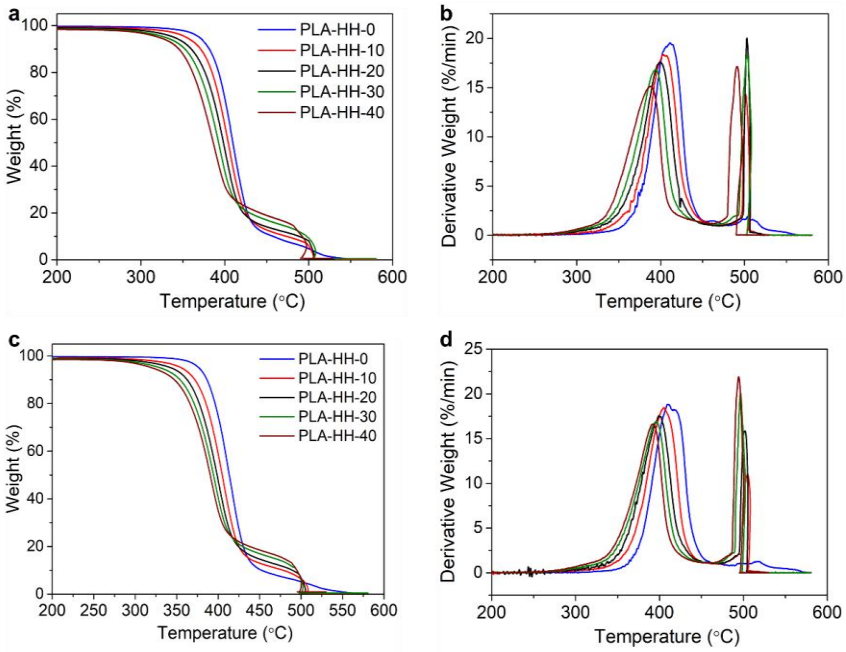

Figure 7-15 TGA and DTG curves of PLA/HH biocomposites specimens produced via (a, b) IM and (c, d) FDM printing.

Table 7-7 Thermal stability characteristics determined from TGA

Samples	T_{onset} (°C)		T_5 (°C)		T_{50} (°C)		T_{max} (°C)		Residue at 525°C (%)	
	IM	FDM	IM	FDM	IM	FDM	IM	FDM	IM	FDM
PLA-HH-0	381	382	369	377	410	413	411	411	0.1	2.4
PLA-HH-10	376	376	353	356	404	405	404	405	0.3	0.2
PLA-HH-20	371	370	340	342	398	399	402	397	0.3	0.3
PLA-HH-30	364	366	328	331	393	394	395	396	0.4	0.5
PLA-HH-40	354	361	322	321	386	390	388	392	0.6	1.0

Overall, HH inclusion in PLA is beneficial for achieving cost-effectiveness in PLA based FDM feedstock, the obtained FDM filament exhibited a diameter tolerance within ±0.02 mm, and roundness variability below 0.03 mm, and the FDM-printed parts with HH loading under 30 phr showed higher impact toughness than the commercial PLA filament control. The HH incorporation also aids in the secondary crystallization in the PLA/HH biocomposites. As a result, the flexural modulus increased with HH loading in both FDM-printed and IM samples. Furthermore, the

FDM-printed parts led to higher impact strength over the IM parts, both on an absolute and a specific impact strength basis, and higher thermal stability above IM specimens. The FDM-printed samples showed an increased dimensional accuracy with increasing HH loading. The parametric analysis of HH loading coupled with rheology, melt flow analysis, thermal analysis, and morphological analyses using SEM supported the mechanistic basis for the resultant thermo-mechanical performance. Roughness analysis and SEM analysis yielded information on the increasing roughness and corrugated appearance with increasing HH content. Shrinkage and porosity analyses provided support for analysis of damage initiation in FDM-printed specimens, which is divergent from the traditional IM biocomposite mechanical behaviour. The diverse microstructure and layer-wise structure necessitate further analysis of FDM printed components using tomography and other high-resolution imaging methods. Although FDM-printed components are quite different from IM parts, comprehensive mechanistic analyses on the processing-structure relationships are critical for further development and widespread utilization of the FDM processing method for industrial applications.

7.2 Effect of BP loading on PLA/BP biocomposites

Part of the work has been prepared to submit in the following journal:

X. Xiao, V. S. Chevali, P. Song, H. Wang, Polylactide/bamboo powder biocomposite for 3D printing: Effect of bamboo powder content and particle size, Polymer testing (**In submission**).

BP is an abundantly available and low-cost biomass waste produced from bamboo-pole slicing and bamboo-planks sanding. BP has been explored to fabricate PLA biocomposites, in which the efforts were to improve the compatibility between PLA and BP and enhance the toughness of the biocomposites using coupling agent, plasticizer and bamboo char [15, 47, 63, 64, 113]. There is limited research investigated BP/PLA as feedstock for 3D printing. Shin et al. [97] developed bamboo/PLA filament for 3D printing and found that bamboo flour (*Phyllostachys bambusoides)*/PLA (10/90) was the optimal material for 3D printing through the investigation of tensile properties of the biocomposites and the morphology of the fractured surface of the filaments. Depuydt et al. [88] observed that higher aspect ratio (l/d) of bamboo fibre achieved higher stiffness and rougher surface for the PLA

biocomposite filament. Zhao et al. [47] improved the printability and surface quality of 3D-printed items by the addition of polyethylene glycol as a plasticizer for PLA/BP composite.

To the knowledge of the authors, PLA/BP biocomposites have not been systematically investigated as FDM feedstock, and the relationship between the BP content and the mechanical properties, especially the toughness of the feedstock, which is critical for 3D printing materials during filament extrusion and printing, has not been reported yet. In addition, the relationship between the BP content and processability, including rheological behaviour and melt flow of the biocomposites, and the surface roughness of FDM-printed items need to be explored. This work aimed to utilize BP as biomass filler for the development of PLA/BP filament for FDM application through parametric analysis of BP loading following the formulations in **Table 7-8**. The main objectives of this study were to (i) investigate the rheological behaviours of the materials to examine the processability and printability of feedstock and explain the underlying mechanisms of microstructure development, (ii) parametrically investigate the mechanical properties of FDM-printed parts, with respect to IM specimens of varying BP content, and (iii) evaluate the impact strength of both FDM and IM specimens.

Table 7-8 The experimental formulations of PLA/BP biocomposites

Materials	PLA/PBAT (87 wt.%: 13 wt.%) (phr)	EGMA (phr)	BP (phr)	Additives (phr)
PLA-BP-0	100	6.5	0	2.2
PLA-BP-10	100	6.5	10	2.2
PLA-BP-20	100	6.5	20	2.2
PLA-BP-30	100	6.5	30	2.2
PLA-BP-40	100	6.5	40	2.2

7.2.1 The properties of biocomposites materials

7.2.1.1 Melt flow rate

MFR of PLA/BP biocomposites was shown in **Figure 7-16a**, which decreased from 3.30 g/10 min for PLA-BP-0 to 1.26 g/10 min for PLA-BP-40, indicating the reduced melt flow of the biocomposites with increasing BP loading. PLA-BP-30 and PLA-

BP-40 both exhibited low MFR less than 2 g/10 min, indicating the challenges in extrusion and processing [172]. The obtained PLA/BP filament exhibited decreased density (determined using glass density bottle) with increasing BP loading as shown in **Table 7-9**. Improving melt flowability could enhance the biomass powder dispersion in the polymer matrix, and improve the interlayer adhesion, hence increase the mechanical properties of biocomposites. PLA/BP biocomposites exhibited relatively higher MFR PLA/hemp hurd (PLA/HH) biocomposites as shown in **Figure 7-16b**, which is beneficial for improving the interfacial bonding between deposited layers in FDM parts. The higher MFR of PLA/BP biocomposites was ascribed to the particulate shape of BP against the fibrillary shape of HH.

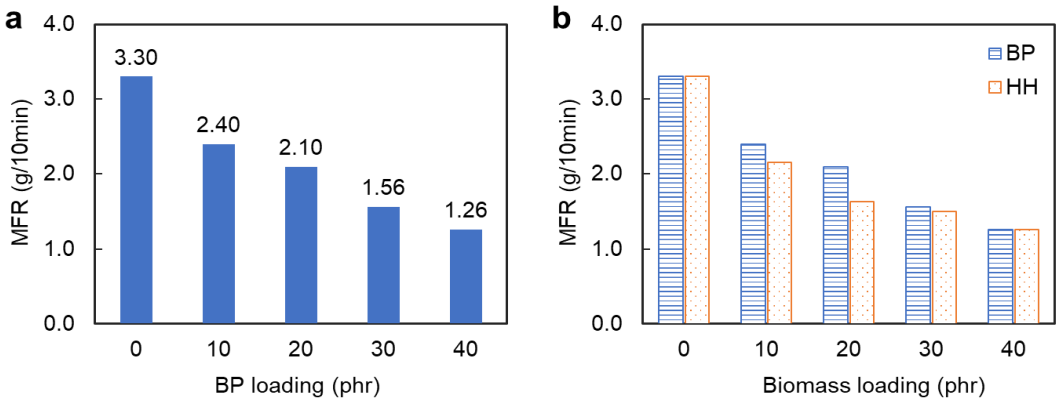

Figure 7-16 MFR of (a) PLA/BP biocomposites and (b) compared with PLA/HH biocomposites as a function of biomass loading.

Table 7-9 Density of PLA/BP biocomposite pellets

Materials	PLA-BP-0	PLA-BP-10	PLA-BP-20	PLA-BP-30	PLA-BP-40
Density (g/cm^3)	1.22	1.08	1.06	1.02	1.00

7.2.1.2 Rheological properties

The melt rheological properties of PLA/BP biocomposites are presented in **Figure 7-17**. At low angular frequency, the complex viscosity ($|\eta^*|$) increased with increasing BP loading, because the addition of rigid BP tended to decrease the melt flow [180]. The trend in $|\eta^*|$ agrees well with the results of PLA/HH biocomposites [122]. However, PLA/BP biocomposites exhibited relatively lower $|\eta^*|$ than PLA/HH

biocomposites (**Figure 7-18a**), consistent with the results in MFR, indicating improved processability for PLA/BP biocomposites [162]. PLA/BP biocomposites exhibited shear-thinning behaviour with increasing angular frequency, similar as PLA/HH biocomposites, the shear-thinning behaviour was enhanced by the increasing BP loading, and there was no significant difference in $|\eta^*|$ at high frequency, because of the reduced viscous resistance due to the disentanglement of polymer chains and reorientation of BP in the flow direction [164]. The shear-thinning behaviour aids in reducing $|\eta^*|$ and getting increased melt flow and processability, which enhances the output during melt extrusion [162]. PLA-BP-0 (without BP) displayed a rheological behaviour similar to Newtonian liquid, $|\eta^*|$ remained stable over the whole range of frequency. PLA-BP-10 exhibited lower $|\eta^*|$ than PLA-BP-0, due to slight inter-particle interaction [173]. Lower $|\eta^*|$ improved melt flow and processability during extrusion [162]. Tan δ defines the damping feature of materials. Tan δ decreased with increasing BP loading as shown in **Figure 7-17b**, because of increased elasticity and decreased viscous behaviour [112], due to particle-particle interaction with increasing BP loading, which retarded the interfacial energy dissipation [175]. PLA-BP-10 presented typical viscous behaviour (tan $\delta>1$, $G'<G''$) over the whole frequency range. PLA-BP-20 and PLA-BP-30 exhibited predominantly elastic behaviour over viscous behaviour (tan $\delta<1$) below an angular frequency of 2 rad/s and 30 rad/s, respectively. PLA-BP-40 showed elastic behaviour (tan $\delta<1$) over the frequency range. The predominant elastic behaviour resulted in poor melt flow and declined processability. Storage modulus (G') and loss modulus (G'') of PLA/BP biocomposites increased with the increase of BP loading at low frequency, as shown in **Figure 7-17c** and **d**, ascribed to the reduced mobility of polymer chains in melt state. The existence of BP led to the improved interfacial interaction between BP particles and polymers chains and enhanced inter-particle interaction [174]. PLA-BP-10 displayed lower G' and G'' than PLA-BP-0, like the change tendency of $|\eta^*|$, demonstrating that the inclusion of 10 phr BP lowered the interfacial interaction within polymer matrix. The cross over frequency ($G' = G''$) presents the transition from elastic to viscous behaviour. The cross over frequency of biocomposites increased with increasing BP content as summarized in **Table 7-10**. The biocomposites showed predominantly viscous behaviour when the loading of BP was below or at 10 phr. Compared with PLA/HH biocomposites (**Figure 7-18**),

PLA/BP biocomposites showed lower *G*' and *G*", indicating lower interfacial interaction and particle-to-particle interaction within PLA/BP biocomposites against PLA/HH biocomposites.

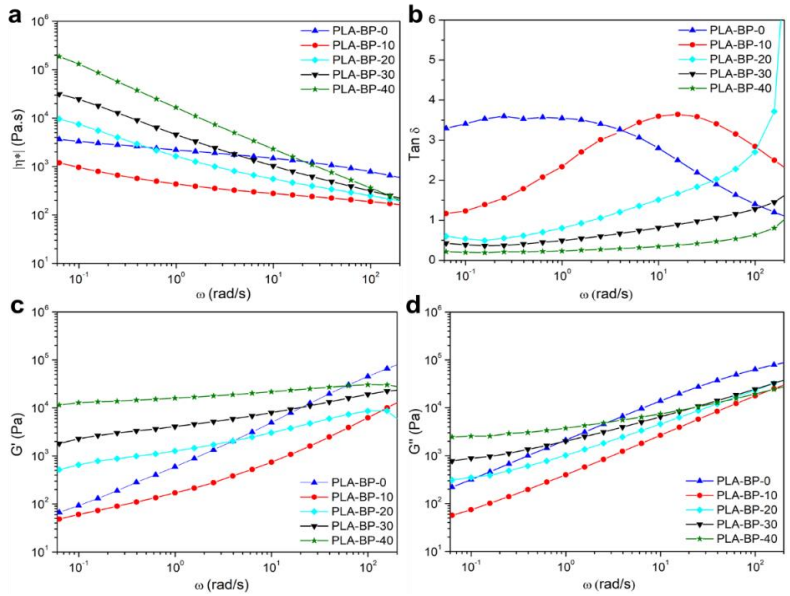

Figure 7-17 Rheological properties of PLA/BP biocomposites: (a) |η*|, (b) Tan δ, (c) *G*', and (d) *G*".

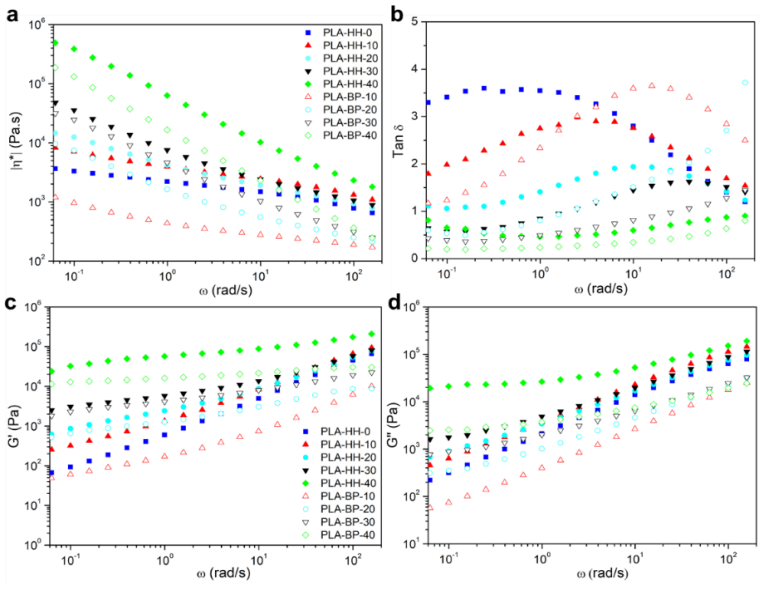

Figure 7-18 Rheological properties of PLA/BP biocomposites: (a) |η*|, (b) Tan δ, (c) *G*', and (d) *G*", compared with PLA/HH biocomposites.

Table 7-10 Cross over frequency (G'' = G') of PLA/BP biocomposites with increasing BP content.

Materials	PLA-BP-0	PLA-BP-10	PLA-BP-20	PLA-BP-30	PLA-BP-40
Cross over frequency (rad/s)	$G''> G'$	$G''> G'$	2.5	25	250

7.2.1.3 Thermal properties

The thermal properties of PLA/BP biocomposites were determined by DSC, the thermograms are presented in **Figure 7-19**, and the corresponding thermal transition temperatures and thermal enthalpy are recorded in **Table 7-11**. From the second heating thermograms (**Figure 7-19a**), PLA/BP biocomposites showed similar T_g at around 61°C and similar T_m at around 168°C as PLA-BP-0, indicating the addition of BP did not change the mobility of PLA chains. However, T_{cc} increased from 100.5°C of PLA-BP-0 to 103.0°C for PLA/BP biocomposites, indicating the incorporation of BP delayed the crystallization of PLA during heating, resulting in decreased cold crystallization enthalpy. Crystallinity decreased from 20.1% for PLA-BP-0 to 16.1% for PLA-BP-10, demonstrating that the addition of 10 phr BP hindered the crystallization of PLA. Then the crystallinity increased and maintained at around 23.0% with the further incorporation of BP, attributed to the combined effects of heterogeneous nucleation and the reduction of free volume [68, 181]. During first heating (**Figure 7-19b**), PLA crystallinity showed a similar trend as during the second heating, the addition of 10 phr BP decreased the crystallization ability of PLA, whereas 20 to 40 phr BP recovered the crystallization ability, the biocomposites showed higher crystallinity than the control. Compared the crystallinity obtained from the 1st heating and 2nd heating, insufficient crystallization at the cooling rate of 10°C/min is demonstrated, as supported by the crystallization behaviour observed during the cooling scan (**Figure 7-19c**).

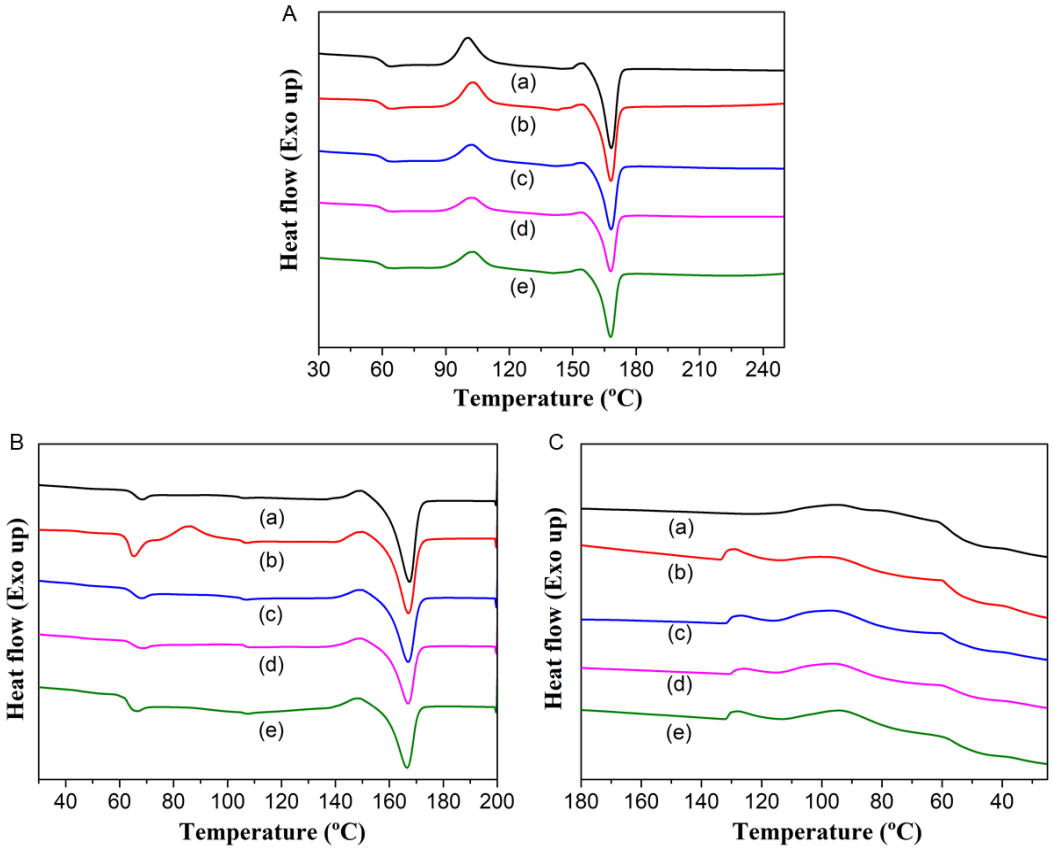

Figure 7-19 DSC curves of PLA/BP biocomposites: A) second heating, B) first heating, and C) cooling for (a) PLA-BP-0, (b) PLA-BP-10, (c) PLA-BP-20, (d) PLA-BP-30, and (e) PLA-BP-40.

Table 7-11 Crystallization and melt phase properties of PLA/BP biocomposites as a function of BP loading

Materials	First heating				Cooling		Second heating					
	T_g (°C)	T_m (°C)	ΔH_m (J/g)	X_c (%)	T_{c1} (°C)	T_{c2} (°C)	T_g (°C)	T_{cc} (°C)	ΔH_{cc} (J/g)	T_m (°C)	ΔH_m (J/g)	X_c (%)
PLA-BP-0	65.7	167.4	36.5	49.1	-	94.9	61.0	100.5	15.7	168.2	30.6	20.1
PLA-BP-10	63.7	166.9	29.3	31.0	129	96.0	60.7	103.1	14.0	168.1	24.9	16.1
PLA-BP-20	65.3	166.8	30.3	48.2	127	95.9	60.9	102.6	11.3	168.1	25.3	22.2
PLA-BP-30	64.9	166.8	28.3	48.6	126	95.2	60.6	102.8	9.8	168.0	23.4	23.4
PLA-BP-40	62.8	166.4	26.0	47.9	128	93.9	60.5	103.2	9.6	167.9	22.2	23.1

7.2.1.4 Fracture morphology of BP and PLA interface

Mechanical performance of biocomposites in service depends on the particle dispersion in the matrix and interfacial adhesion between biomass filler and polymer matrix [174, 182]. The cryo-fractured surfaces of IM specimens of PLA/BP biocomposites were observed by SEM, and the images are shown in **Figure 7-20**. BP particles distributed in the polymer matrix with orientation in both parallel and perpendicular directions. More BP fibres were observed on the fractured surface with increasing BP loading. The pull-out of BP fibre occurred on the surface of PLA-BP-10, as highlighted with a red arrow in **Figure 7-20c** and **d**. The debonding of BP from the matrix (highlighted with gold arrow) and the pores formed after BP pull-out (highlighted with white arrow) were detected on the surface of PLA-BP-20 and PLA-BP-40, as shown in **Figure 7-20e** to **h**. The results indicate the insufficient and decreased interfacial adhesion between BP and polymer matrix to enable the stress transfer from matrix to filler as BP content increased. The interface morphology of PLA/BP specimens is different from that of PLA/HH, which displayed higher interfacial adhesion between HH and polymer matrix.

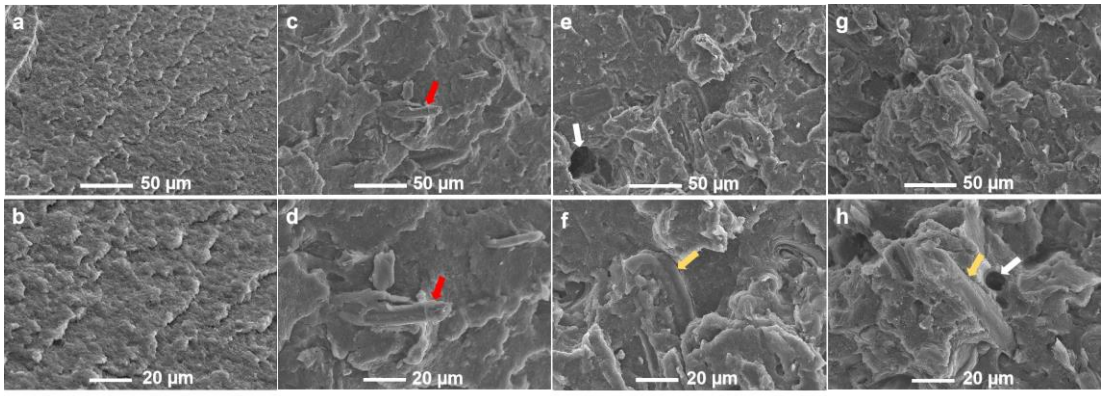

Figure 7-20 SEM images of cryo-fractured surface of IM specimens: (a, b) PLA-BP-0, (c, d) PLA-BP-10, (e, f) PLA-BP-20, and (g, h) PLA-BP-40 at two magnifications (500× and 1000×).

7.2.1.5 Mechanical properties of IM specimens

The mechanical properties of the IM specimens are shown in **Figure 7-21**. The tensile strength, impact strength and flexural strength all decreased with increasing BP loading, ascribed to the inadequate interfacial adhesion between BP and matrix [78], as shown in **Figure 7-20**. With the incorporation of more BP, more interfaces

between BP filler and matrix were created, which facilitated the crack initiation and propagation in the biocomposites [183]. BP particles also produced stress concentrations, which yield under a force application [177]. The dispersion of BP in the polymer matrix caused a discontinuity in the matrix phase [64], resulting in decreased strength as well. The flexural modulus increased with increasing BP loading due to the mobility confinement of polymer chains in the presence of BP particles, similar to PLA/HH biocomposites [122]. PLA/BP biocomposites showed lower mechanical properties than PLA/HH biocomposites and unexpected trends in tensile strength and flexural strength, compared to PLA/HH biocomposites as shown in **Figure 7-22**, although the formulations and process were the same, BP and HH had almost the same particle size distribution. The higher mechanical properties of PLA/HH was attributed to the reinforcement effect of HH due to its fibrillary and elongated structure shown in **Figure 5-5c** and **d**, and its higher interfacial adhesion between polymer matrix and HH [122], whereas the weakened interfacial adhesion between BP and PLA.

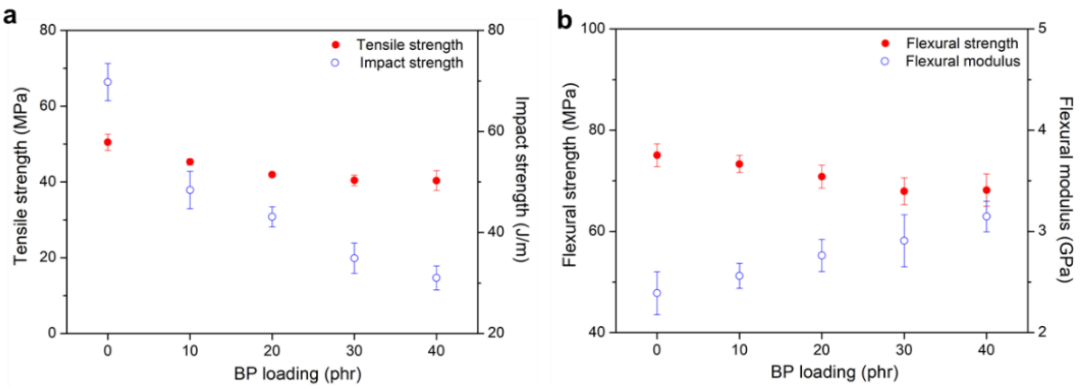

Figure 7-21 Mechanical properties of IM specimens: (a) tensile and impact strength, and (b) flexural properties as a function of BP loading.

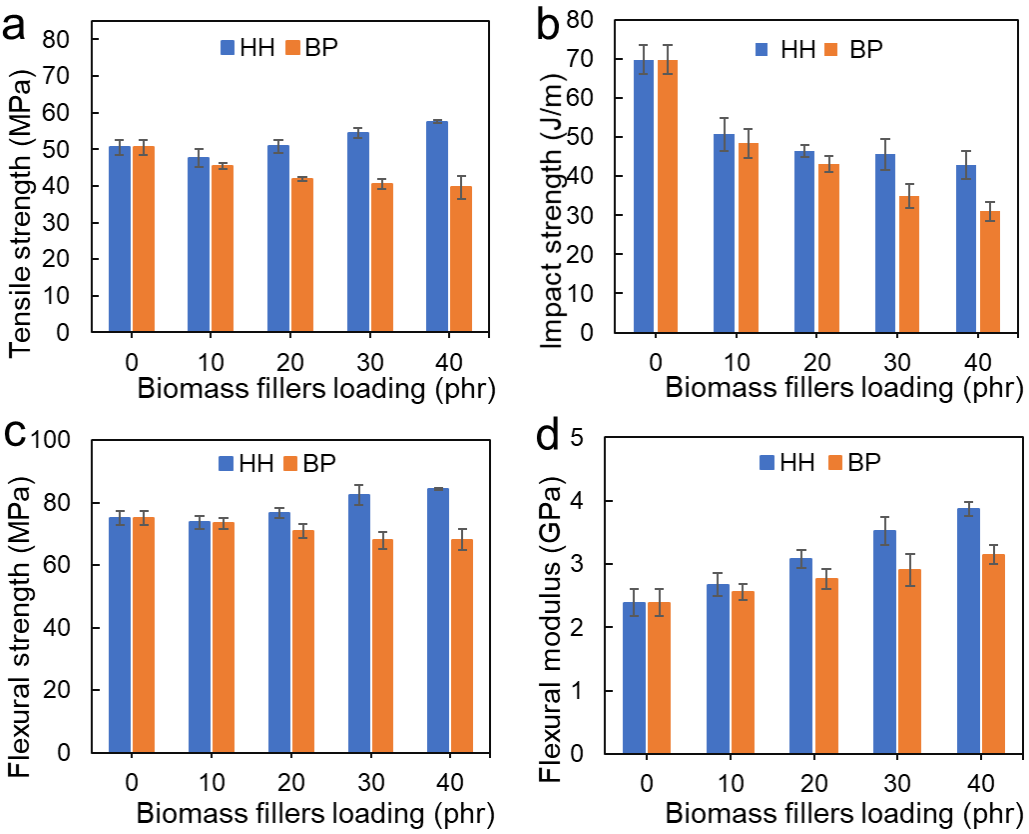

Figure 7-22 Mechanical properties of PLA/BP and PLA/HH IM specimens as a function of biomass loading.

7.2.2 Filament quality

The diameter tolerance and roundness of PLA/BP biocomposite filament were obtained using the method presented in Chapter 4 according to GB/T 37643-2019 standard, and the results are presented as a box-and-whiskers chart in **Figure 7-23**. The filament became darker and rougher with increasing BP loading. All PLA/BP biocomposite filaments exhibited acceptable diameter tolerance within the range of ±0.03 mm and roundness less than 0.04 mm, meet the requirement in the GB/T 37643-2019 standard. PLA-BP-0 showed a relatively higher diameter tolerance because of its low viscosity, leading to a relatively lower melt strength and unstable melt flow, causing unstable extrusion out of the extrusion die.

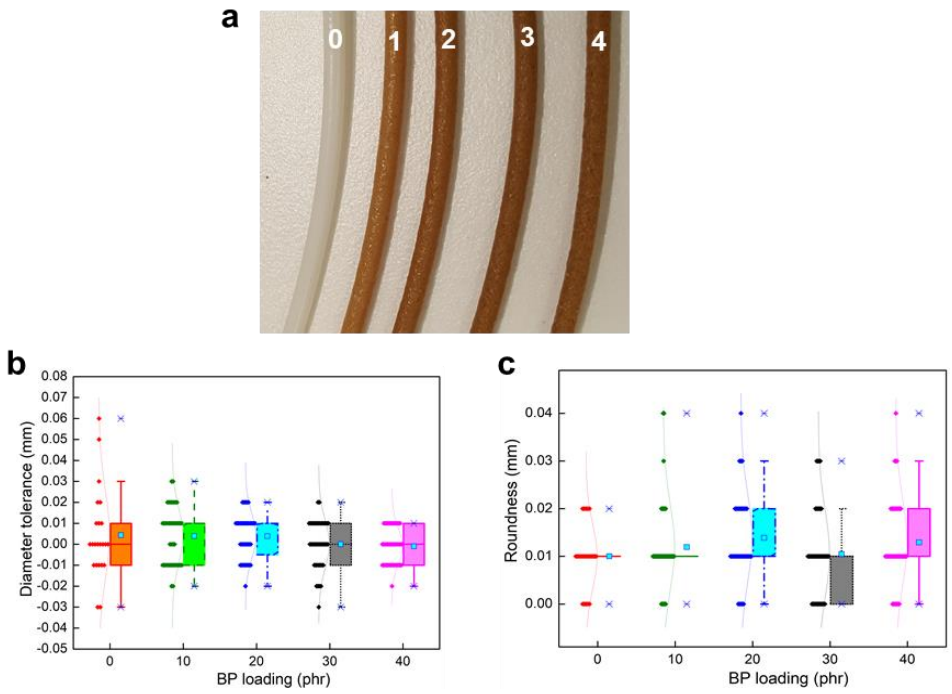

Figure 7-23 (a) PLA/BP filament, box plot of (b) filament diameter tolerance, and (c) filament roundness of PLA/BP biocomposites as a function of BP loading. (0) PLA-BP-0, (1) PLA-BP-10, (2) PLA-BP-20, (3) PLA-BP-30 and (4) PLA-BP-40.

7.2.3 The properties of FDM-printed specimens

7.2.3.1 Finish quality

The surface roughness and porosity of FDM-printed specimens with varying BP loading are presented in **Figure 7-24**. The specimens exhibited a darker colour and increased surface roughness with increasing BP loading (**Figure 7-24a**, **b**, and **c**). R_a increased from 3.8 µm (PLA-BP-0) to 17.7 µm (PLA-BP-10), and then remained at 18.5±1 µm with further increasing BP loading. R_q remained at 25.5±1.5 µm with an increase from 4.5 µm (PLA-BP-0) to 24.2 µm (PLA-BP-10). The increase in surface roughness indicates that the incorporation of BP produced rougher surface, which was slightly affected by further increasing BP loading, similar as PLA/HH biocomposite [122] because the average particle size (50 µm) of BP was smaller than the thickness (0.15 mm) of printing layer. R_z and R_{max} increased from 17.2 µm and 23.7 µm (PLA-BP-0) to 101 µm and 108 µm (PLA-BP-10), and then increased to 121 µm and 137 µm (PLA-BP-40), indicating that the increasing BP loading improved the maximum defect height, leading to a rougher surface for the FDM-printed parts in visual appearance. The porosity increased from 5.7% for PLA-BP-0

to 16.9% for PLA-BP-40 (**Figure 7-24d**) as a result of increased viscosity and decreased melt flow, which caused less melt output from the nozzle and lower interlayer adhesion.

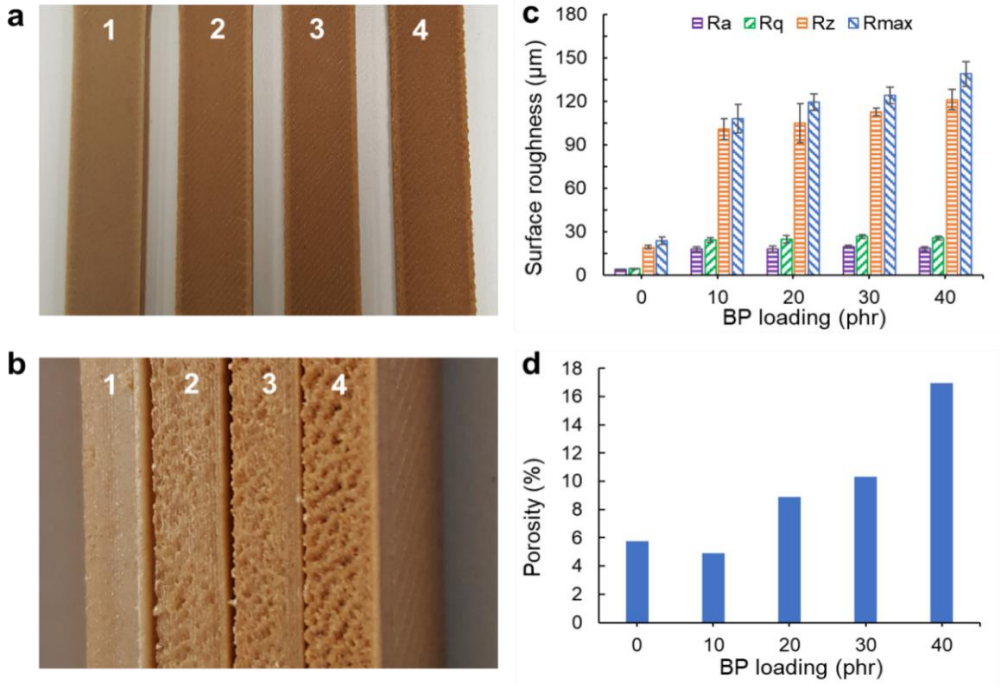

Figure 7-24 Finish quality of FDM specimens: (a) top view, (b) side view, (c) surface roughness, and (d) porosity for (1) PLA-BP-10, (2) PLA-BP-20, (3) PLA-BP-30 and (4) PLA-BP-40.

7.2.3.2 Morphology

The impact fracture surfaces of PLA/BP FDM-printed specimens were observed by SEM, as shown in **Figure 7-25**. Observed at low magnification of 30 (**Figure 7-25a**, **c**, **e**, and **g**), the voids and porous increased with increasing BP loading, the space and boundary between layers were detected. PLA-BP-10 presented fewer voids and indistinct boundary than other biocomposites, in accordance with its lower porosity and higher interlayer adhesion due to the lowest complex viscosity. Observed at a magnification of 1000× (**Figure 7-25b**, **d**, **f,** and **h**), the impact fractured surfaces of FDM-printed specimens showed elasto-plastic deformation. BP filler pull-out and debonding from polymer matrix were noticed, this phenomenon was pronounced as BP loading increased, suggesting weak interfacial bonding to enable the particle-matrix stress transfer. More voids and lower density were detected on the surfaces of FDM parts than IM specimens. Compared with PLA/HH FDM-printed parts,

PLA/BP specimens exhibited indistinct interlayer space and lower porosity, as shown in **Figure 7-26**, due to the improved melt flow and better interlayer adhesion.

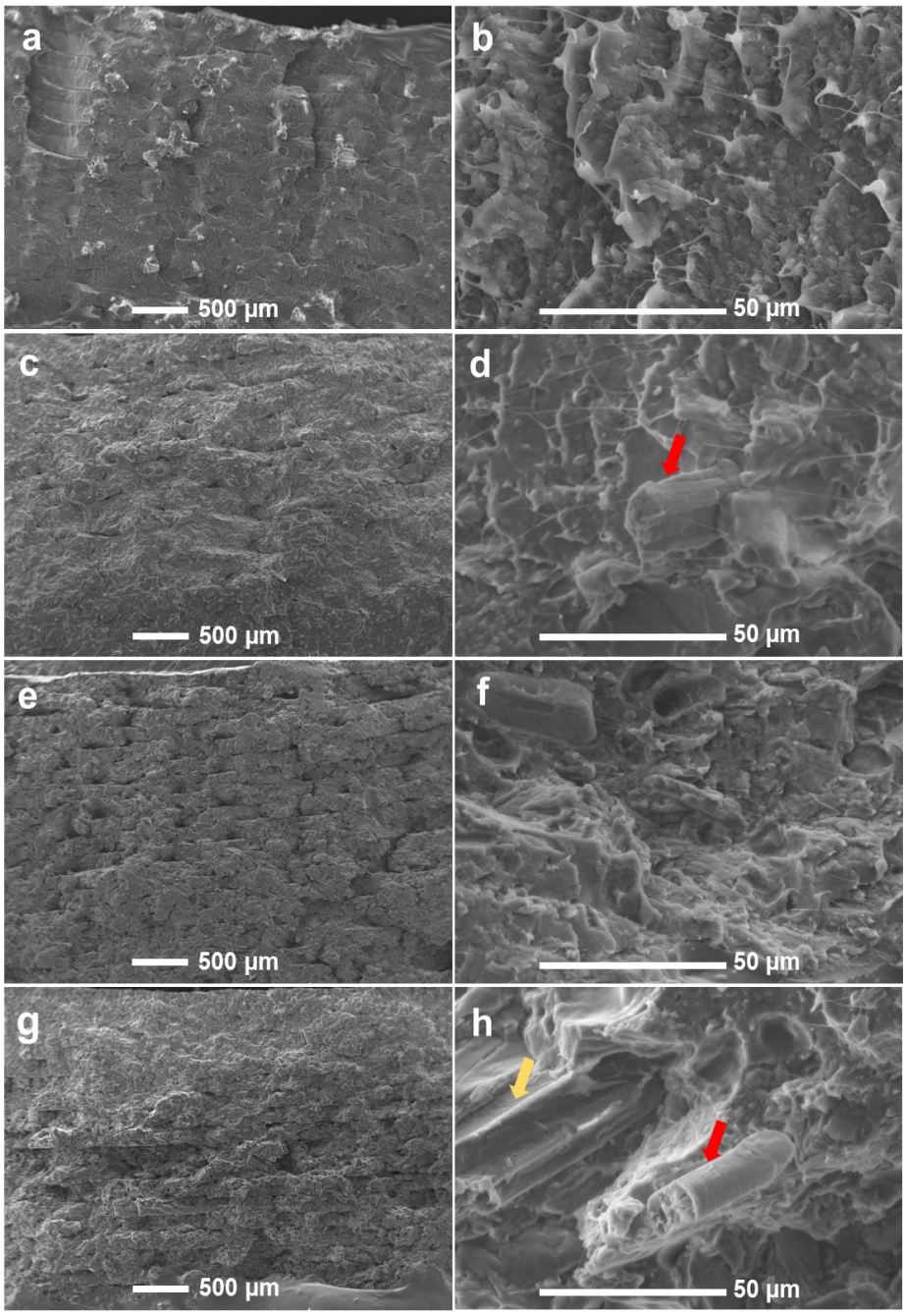

Figure 7-25 SEM images of impact fracture surfaces of FDM-printed specimens: (a, b) PLA-BP-0, (c, d) PLA-BP-10, (e, f) PLA-BP-20, and (g, h) PLA-BP-40 at magnifications of 30× and 1000×.

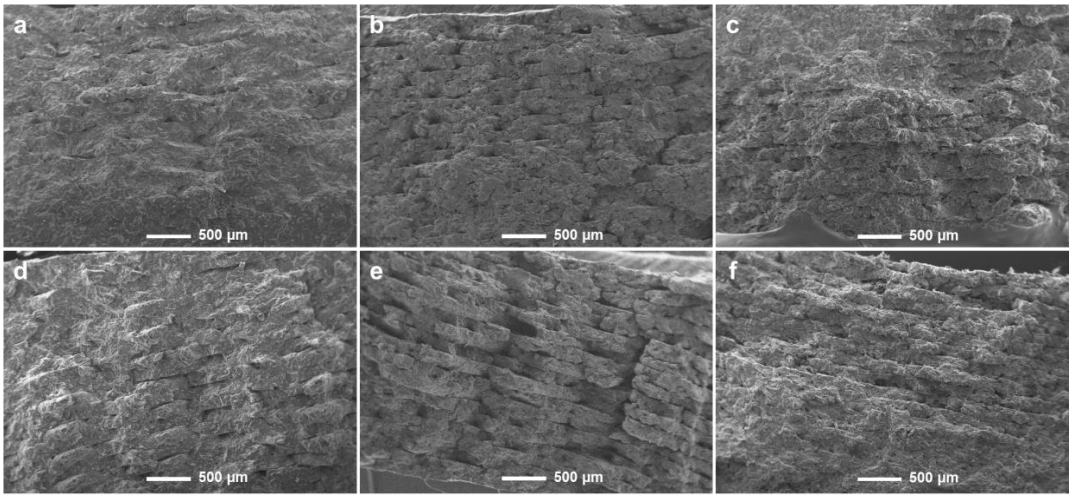

Figure 7-26 Morphology of impact fractured surfaces of FDM-printed specimens: (a) PLA-BP-10, (b) PLA-BP-20, (c) PLA-BP-40, and (d) PLA-HH-10, (e) PLA-HH-20, (f) PLA-HH-40.

7.2.3.3 Mechanical properties

The mechanical properties of FDM-printed specimens are shown in **Figure 7-27** and compared with IM specimens in **Table 7-12**. The tensile strength, impact strength and flexural strength of FDM-printed specimens all decreased with increasing BP loading, similar to the trends in IM specimens. These decreases are associated with the insufficient interfacial adhesion between BP and polymer matrix, together with the increased porosity [26], resulting in a marginal increase in flexural modulus whereas a pronounced decrease in other mechanical properties, compared to the IM samples shown in **Figure 7-21**. The major increase in porosity of PLA-BP-40 (**Figure 7-24d**) caused a decrease in flexural modulus as well. The incorporation of BP in the polymer matrix and acted as stress raisers, making the samples ease of yielding [179]. The decrease in mechanical properties, especially in impact strength deteriorated the printability and end-user application. Nevertheless, the specimen printed from PLA-BP-30 with 30 phr BP remained impact strength comparable with the items fabricated from commercial PLA feedstock (46±2.5 J/m) [122], as shown in **Table 7-12**. On the other side, flexural modulus increased with increasing BP loading due to the existence of BP filler, which impeded the mobility of polymer chains. The decrease in flexural modulus occurred at PLA-BP-40 is the resultant of a major decrease in density and the linked poor interfacial adhesion, illustrating an

upper limit of 30 phr (57% by volume ratio) BP loading level in the PLA/PBAT matrix.

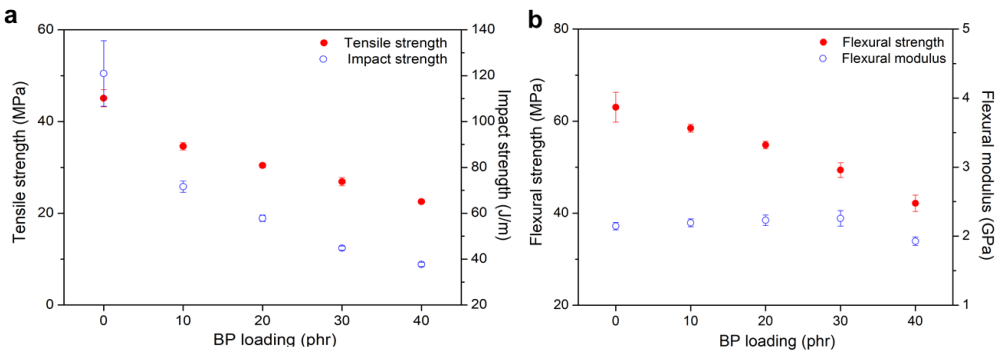

Figure 7-27 Mechanical properties of FDM-printed specimens as a function of BP loading.

FDM-printed specimens exhibited lower mechanical properties, including tensile strength, flexural strength, and flexural modulus than IM specimens (**Table 7-12**), attributed to the existence of porous and interlayer boundary, which weakened the interfacial adhesion, hence caused the decreasing mechanical properties for FDM-printed parts. However, FDM-printed parts presented a higher impact strength than IM parts, attributed to the elasto-plastic deformation during impact fracture, as convinced by the SEM images as shown in **Figure 7-25**, against the brittle fracture mode of IM specimens as evidenced by the SEM images in **Figure 7-20**.

Table 7-12 Mechanical properties of IM and FDM specimens as a function of BP loading

Samples	Tensile strength (MPa)		Impact strength (J/m)		Flexural strength (MPa)		Flexural modulus (MPa)	
	IM	FDM	IM	FDM	IM	FDM	IM	FDM
PLA*	75±1.4	40±2.5	29±2.8	46±2.5	124±4.2	89±1.3	3.58±0.10	2.97±0.25
PLA-BP-0	52±1.2	45±1.9	70±3.7	121±14	75±2.2	63±3.2	2.39±0.21	2.15±0.05
PLA-BP-10	45±0.8	35±0.8	48±3.7	72±2.5	73±1.7	58±0.9	2.56±0.12	2.19±0.06
PLA-BP-20	42±0.6	30±0.5	43±2.0	58±1.4	71±2.3	55±0.8	2.76±0.16	2.23±0.08
PLA-BP-30	40±1.4	27±0.9	35±3.0	45±0.9	68±2.7	49±1.6	2.91±0.26	2.26±0.11
PLA-BP-40	40±2.6	22±0.3	31±2.4	38±0.9	68±3.2	42±1.8	3.15±0.15	1.93±0.06

* PLA IM specimens were produced using neat PLA 4032D, PLA FDM-printed specimens were fabricated using commercial PLA filament.

The specific mechanical properties of IM and FDM-printed specimens are compared in **Table 7-13**. The density normalized mechanical properties exhibited similar trends as before density normalization. Normalized FDM-printed specimens also exhibited lower tensile strength, flexural strength, and flexural modulus than normalized IM specimens. On the other hand, the FDM-printed specimens still showed higher specific impact strength than IM specimens.

Table 7-13 Specific mechanical properties of IM and FDM specimens as a function of BP loading

Sample	Specific tensile strength ($MPa.cm^3/g$)		Specific impact strength ($J/m.cm^3/g$)		Specific flexural strength ($MPa.cm^3/g$)		Specific flexural modulus ($GPa.cm^3/g$)	
	IM	FDM	IM	FDM	IM	FDM	IM	FDM
PLA*	59±1.1	35±2.2	23±2.2	40±2.2	98±3.3	75±1.0	2.91±0.09	2.60±0.22
PLA-BP-0	42±1.0	39±1.6	57±3.0	105±13	62±1.8	55±2.8	1.96±0.17	1.87±0.05
PLA-BP-10	37±0.7	30±0.7	40±3.0	62±2.2	60±1.4	50±0.8	2.10±0.10	1.93±0.01
PLA-BP-20	34±0.4	27±0.4	35±1.6	51±1.2	57±1.8	48±0.7	2.23±0.13	1.93±0.02
PLA-BP-30	32±1.1	24±0.8	28±2.4	40±0.8	54±2.1	44±1.4	2.31±0.20	2.13±0.02
PLA-BP-40	32±2.1	22±0.3	25±1.9	37±0.9	54±2.5	41±1.7	2.54±0.12	1.97±0.05

* PLA IM specimens were produced using neat PLA (4032D), PLA FDM-printed specimens were fabricated using commercial PLA filament from eSun.

The mechanical properties of FDM-printed specimens of PLA/BP are compared with PLA/HH in **Figure 7-28**. PLA/BP FDM-printed specimens exhibited similar mechanical properties as PLA/HH specimens. The difference in mechanical properties between PLA/BP and PLA/HH specimens diminished in FDM-printed parts, compared with corresponding IM specimens, due to the higher melt flow and improved interfacial adhesion for PLA/BP biocomposites feedstock, leading to lower interlayer space and porosity for PLA/BP FDM parts (**Figure 7-24** to **Figure 7-26**).

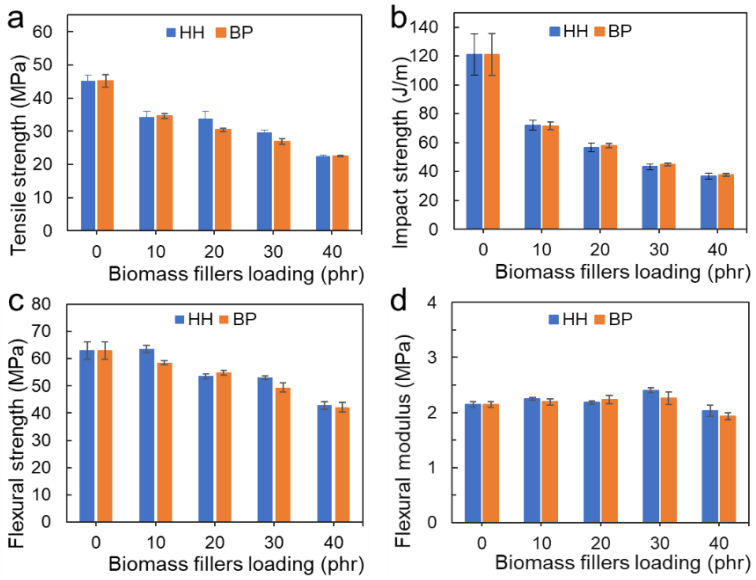

Figure 7-28 Mechanical properties of FDM-printed specimen of PLA/BP and PLA/HH biocomposites.

FDM-printed specimens displayed higher impact strength than IM parts for PLA/BP and PLA/HH biocomposite feedstock, controversy to the results in the literature [184, 185], related with the improved crystallinity of FDM parts induced by the heat from the 3D printer heat bed [186, 187]. PLA/HH IM specimens exhibited higher impact strength when HH content reached 30 phr, related with the stronger interfacial adhesion between HH and matrix than other samples.

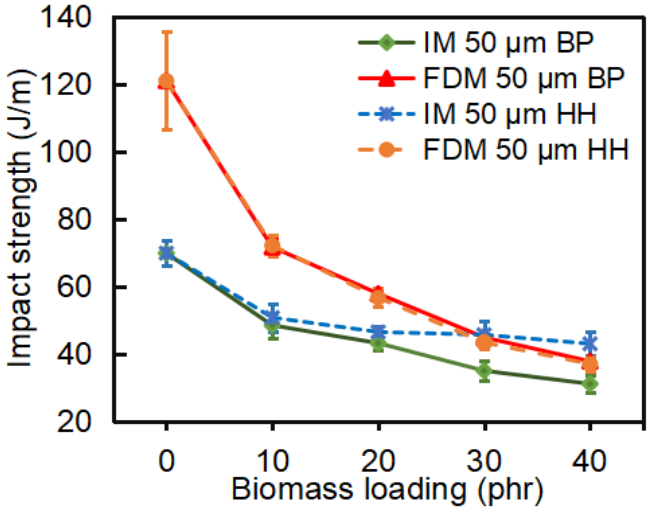

Figure 7-29 Impact strength of PLA/BP and PLA/HH IM and FDM specimens.

PLA/BP biocomposite exhibited decreased melt flow and increased complex viscosity, as BP content increased, however, there was no challenge in processing, and FDM printing the filament, but it became more difficult to process the materials with high BP content. The filaments extruded met the requirements in GB/T 37643-2019 standard. The FDM-printed items displayed increased porosity and surface roughness, whereas decreased mechanical properties with the increasing BP content. However, the FDM-printed items with up to 30 phr BP (~ 57 vol.%) exhibited comparable impact strength to commercial PLA and without problem in the 3D printing process. The FDM-printed samples exhibited a higher impact strength than IM parts. The flexural modulus of both IM and FDM-printed specimens increased when the BP content increased up to 30 phr.

Overall, PLA/HH and PLA/BP biocomposite filaments were developed and investigated through the analysis of the effects of HH and BP content on the melt flow, crystallization behaviour, filament quality, mechanical properties of both IM and FDM-printed products, and finish quality of FDM-printed parts. Although the melt flowability decreased with the addition of HH and BP, the filament quality all met the requirements in GB/T 37643-2019 standard. Although the decrease in mechanical properties, the FDM-printed specimens with up to 30 phr HH and BP incorporation showed comparable impact strength to commercial PLA control. PLA/BP biocomposites showed lower mechanical properties for both IM and FDM-printed specimens than PLA/HH biocomposites. However, the difference in mechanical properties between PLA/BP and PLA/HH biocomposites diminished in FDM-printed specimens, compared to the IM parts.

Chapter 8: Effect of biomass particle size on properties of PLA biocomposites

The surface of FDM parts shows higher roughness and unevenness with higher porosity observable in the fracture surface with the inclusion of biomass filler [22, 70, 72]. The surface quality is improved by changing printing parameters, including layer thickness [100, 188-190], printing orientation of the parts, model temperature, air gap and printing speed, whereas the layer thickness exhibits significant impact on the surface roughness than other process parameters [188, 191]. Chemical treatment using acetone [192] and other post-processing [193] have been used to improve the surface smoothness. The method of tailoring the surface finish of FDM components via particle size distributions of biomass has not been studied, according to the knowledge of the authors.

Tisserat *et al.* [67] reported that smaller particle size of Paulownia wood powder led to higher tensile strength and Young's modulus, while marginally affecting the elongation-at-break of PLA/paulownia wood powder biocomposite. Zhao *et al.* [66] found that the smallest particle size (<180 μm) of poplar fibre was the favourable particle size for PLA biocomposites to achieve a suitable viscosity and the highest tensile properties. The systematic investigation on the relationship between biomass particle size and rheological behaviour, mechanical properties, and surface quality of PLA biocomposites feedstock is conducive to the utilization of biomass in FDM.

The present work tends to adjust the surface roughness of FDM-printed parts through the particle size of biomass. In this chapter, we developed PLA/HH and PLA/BP biocomposite filaments using pristine HH and BP without treatment to obtain cost-effective feedstock for FDM application. HH with four different particle sizes and BP with three different particle sizes were used as the biomass filler in PLA biocomposite feedstock. HH and BP were melt-compounded and extruded with PLA/PBAT/EGMA matrix through the rotational twin-screw extruder and granulated, respectively. The biocomposite pellets were then manufactured to FDM filament using a single-screw filament extruder. The effect of HH and BP particle sizes on the melt flow and rheological properties of biocomposites, filament quality,

mechanical properties of both IM and FDM-printed specimens, and the finish quality of FDM-printed items, especially the surface roughness were examined.

8.1 Effect of HH particle size on PLA/HH biocomposites

Part of the work has been prepared to submit in the following journal:

X. Xiao, V. S. Chevali, P. Song, J. Feng, H. Wang, Rheological, mechanical, and surface properties of polylactide/hemp hurd biocomposite for 3D printing: hemp hurd particle size, Composites: Part A (**In submission**).

This work aimed to produce PLA/HH FDM feedstock with optimum surface quality, processability and mechanical properties. Pristine HH with d_{50} of 34 μm, 48 μm, 91 μm and 163 μm was used to modify the surface roughness of FDM-printed items. PLA/HH biocomposites (PLA-HH-1, PLA-HH-2, PLA-HH-3, and PLA-HH-4, corresponding to 34 μm, 48 μm, 91 μm and 163 μm HH respectively) and filaments were prepared using the methods present in Chapter 4 and the formulation in **Table 8-1**. The relationship between HH particle size and rheological, mechanical, and surface properties of PLA/HH feedstock was investigated. The IM specimens were prepared for comparison with FDM parts. The printability and finish quality of the FDM-printed samples were examined, the thermal and crystallization properties of the biocomposites and the microstructure of the specimens were analysed to explore the underlying mechanism.

Table 8-1 Formulations of PLA/HH biocomposites with HH of varying particle size

Constituent	PLA	PBAT	EGMA	Hemp hurd	Additives
phr	87	13	6.5	20	2.2

8.1.1 The properties of biocomposites materials

8.1.1 1 Rheological properties and melt flow rate

Rheological behaviour in melt state was determined to evaluate the internal structure and processability of PLA/HH biocomposites, as shown in **Figure 8-1**. PLA-HH-1 exhibited higher G', G'', and $|\eta^*|$ than other biocomposites (**Figure 8-1a** and **c**), whereas lower Tan δ than other biocomposites at low frequency (**Figure 8-1d**). $|\eta^*|$

and *G*' slightly decreased with increasing HH particle size at low frequency, in accordance with the trends in MFR (190°C/2.16 kg) (**Figure 8-2**), agrees with the result reported by Hristov et al. [194], indicating the small particles have a higher resistance to deformation, whereas the larger particles tend to flow, associated with the deteriorated wetting of particles by the polymers due to the smaller specific surface area of larger particles [85] and the improved mobility due to the looser packing, the smaller particle also facilitated the network formation within the polymer matrix [195]. PLA-HH-3 showed higher *G*', *G*'' and $|\eta^*|$ than PLA-HH-2 due to the impeded mobility of particles and polymers brought by the tighter packing of hemp hurd because of the broader particle size distribution. The rheological properties were of negligible difference between samples at high dynamic frequency. PLA-HH-1 and PLA-HH-3 exhibited predominant elastic behaviour (*G*' > *G*'', Tan δ<1) at frequency below 10 rad/s and 0.5 rad/s, respectively, whereas PLA-HH-2 and PLA-HH-4 showed viscous behaviour (*G*' < *G*'', Tan δ>1) in the whole frequency range (**Figure 8-1a** and **d**). The plot of log *G*'- log *G*'' was used to inspect the compatibility of components in the biocomposites in the melt state. It was demonstrated that if the biocomposite is a miscible or compatible system, the slope of the biocomposites would be the same as the polymer matrix [196]. The log *G*'- log *G*'' plots of PLA/HH biocomposites are compared with the composite without HH (PLA-HH-0) in **Figure 8-1b**. All the biocomposites showed a lower slope than PLA-HH-0, indicating the poor miscibility between HH and PLA. Tan δ increased with increasing HH particle size, indicating the pronounced viscous fraction predominant over elastic fraction with increasing HH particle size, in accordance with the trends in MFR (190°C/2.16 kg) (**Figure 8-2**). PLA-HH-3 showed lower MFR than PLA-HH-2 due to the broader particle size distribution of HH.

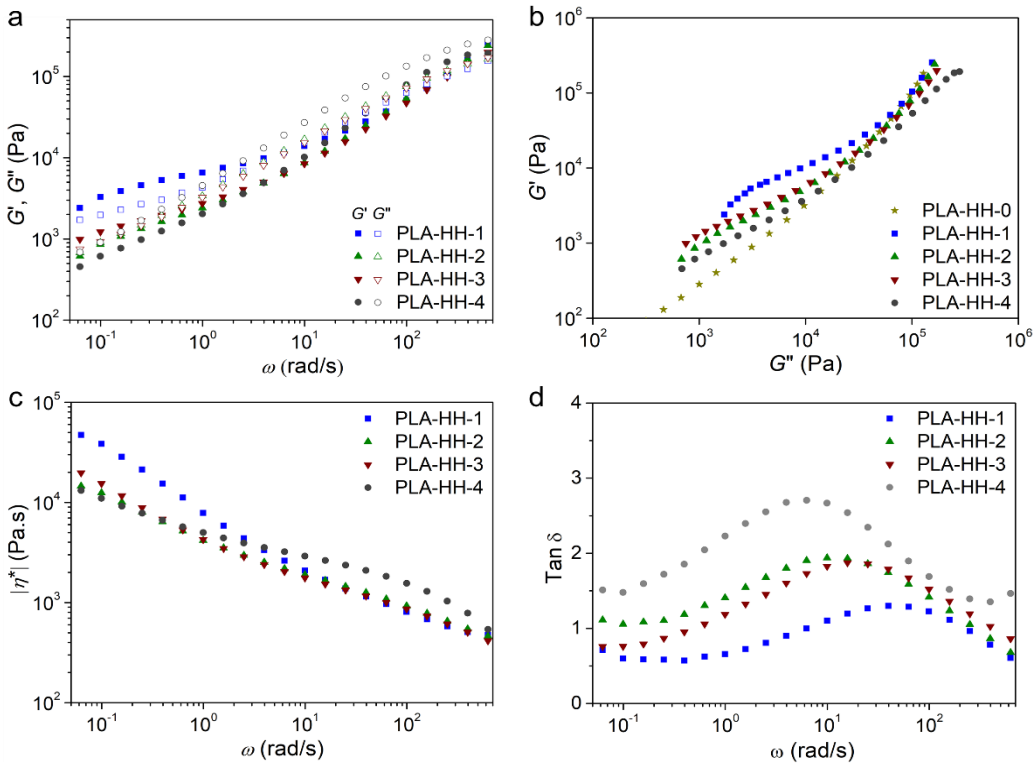

Figure 8-1 Rheological properties of PLA/HH biocomposites: (a) G', (b) G'', (c) $|\eta^*|$, and (d) tan δ.

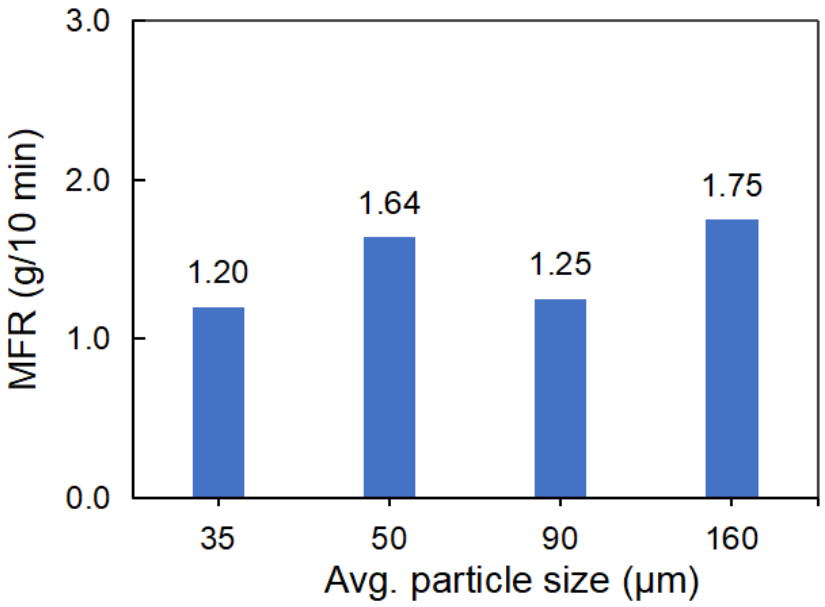

Figure 8-2 MFR of PLA/HH biocomposites as a function of HH particle size.

8.1.1.2 Thermal properties

The DSC thermograms of PLA/HH biocomposites with varying HH particle size are shown in **Figure 8-3**, the temperature and enthalpy transitions are summarized in **Table 8-2**. During the second heating after removing thermal history, the biocomposites showed similar T_g (61.2°C) and T_m (168.5°C). The melting enthalpy (ΔH_m) and the degree of crystallinity (X_c) were lower than the values obtained from the first heating (**Figure 8-3b**), indicating the crystallization of PLA was not complete during the cooling process at the cooling ramp rate of 10°C/min. ΔH_m and X_c decreased at PLA-HH-2 are related with the temperature ramp automatically during PLA/HH pellets preparation, which might cause the degradation of PLA, and are associated with the lower cooling temperature after extrusion from the twin-screw extruder [197]. PLA-HH-1 exhibited the highest X_c, attributed to the most availability of heterogeneous nucleating sites because of the existence of the highest amount of HH particles, which resulted in the enhanced nucleation and secondary crystallization [84, 181]. The cold crystallization was not witnessed during the first heating (**Figure 8-3b**), implying the completed crystallization after processing. ΔH_m and X_c decreased from PLA-HH-1 to PLA-HH-2, then increased with increasing HH particle size. During cooling, the crystallization initiated at decreasing temperature with increasing HH particle size, indicating that small particle size facilitated the crystallization during cooling.

Table 8-2 Crystallization and melt phase properties of PLA/HH biocomposites as a function of HH particle size

Materials	1st heating				Cooling		2nd heating					
	T_g (°C)	T_m (°C)	ΔH_m (J/g)	X_c (%)	T_{c1} (°C)	T_{c2} (°C)	T_g (°C)	T_{cc} (°C)	ΔH_{cc} (J/g)	T_m (°C)	ΔH_m (J/g)	X_c (%)
PLA-HH-1	67.5	167.4	29.8	47.4	123.6	97.9	61.5	104.6	9.4	168.6	24.4	23.8
PLA-HH-2	64.1	166.6	23.3	37.1	122.6	98.0	61.2	103.5	8.4	168.1	19.2	17.2
PLA-HH-3	66.2	167.7	28.5	45.4	120.4	98.3	61.2	105.1	10.9	168.9	23.6	20.2
PLA-HH-4	66.0	167.2	31.5	50.1	-	97.9	61.0	103.0	12.2	168.2	25.4	20.9

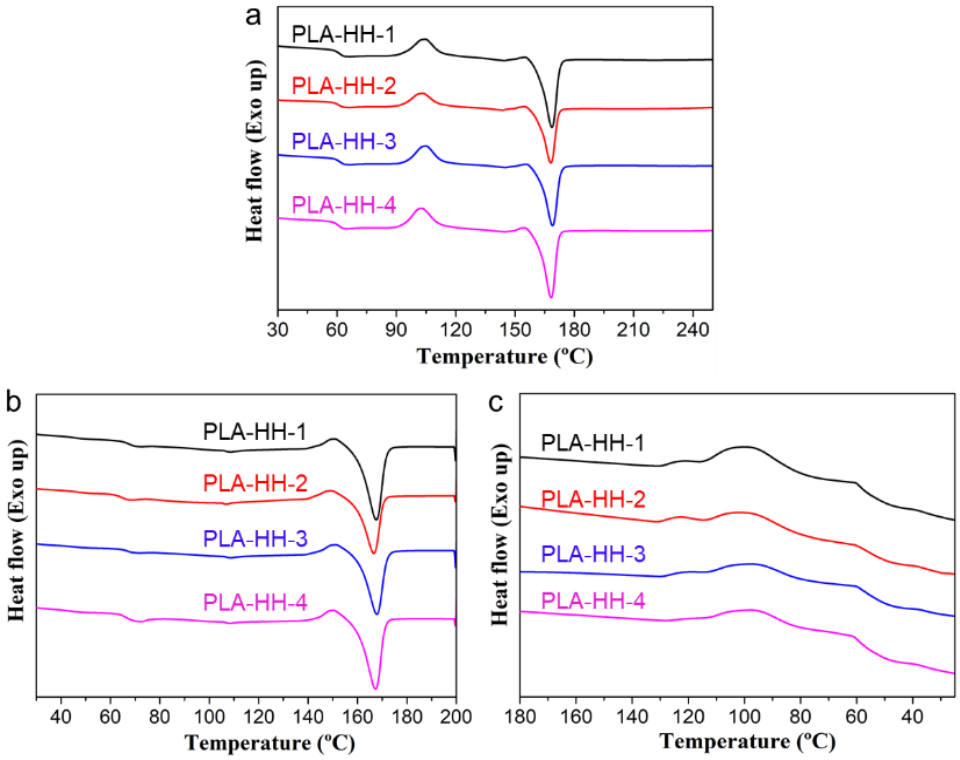

Figure 8-3 DSC curves of PLA/HH biocomposites: (a) second heating, (b) first heating, and (c) cooling.

8.1.1.3 Dispersion of HH and interface morphologies of IM specimens

The cryo-fractured surfaces of IM specimens were observed by SEM, as shown in **Figure 8-4.** HH dispersed in the polymer matrix evenly and retained their fibrillary structures. There are more HH fibres observed on the fractured surface of PLA-HH-1 filled with smallest HH particles. Cavities left by HH pull-out were detected on the fractured surface of PLA-HH-1. It seems that the interfacial adhesion was adequate between HH and matrix in PLA-HH-2 and PLA-HH-3, in which HH fibre showed a higher aspect ratio than in PLA-HH-1 due to the larger particle size. PLA-HH-4 showed failure within HH fibre, instead of pull-out and debonding from the matrix, demonstrating adequate interfacial adhesion between HH fibre and matrix to provide sufficient filler-matrix stress transfer. The SEM images showed that IM specimens had smooth fracture surfaces without obvious plastic deformation, demonstrating that the fracture manner was predominantly in brittle mode [176].

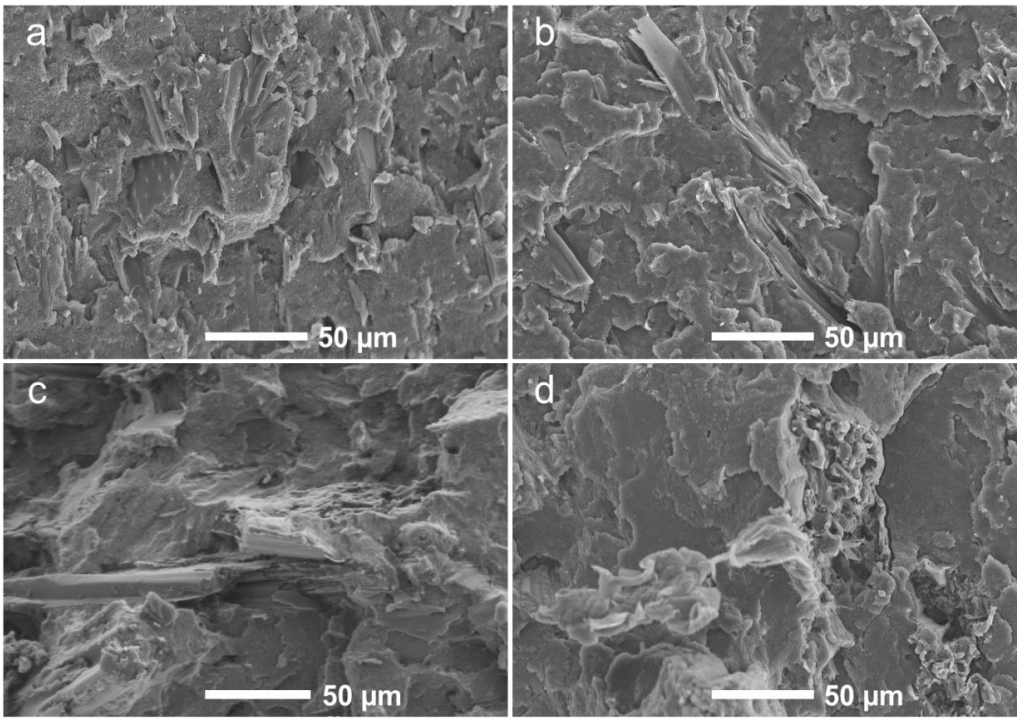

Figure 8-4 SEM images of cryo-fractured surfaces of IM specimens: (a) PLA-HH-1, (b) PLA-HH-2, (c) PLA-HH-3, and (d) PLA-HH-4.

8.1.1.4 Mechanical properties of IM specimens

The effect of HH particle size on the mechanical properties of PLA/HH IM specimens is shown in **Figure 8-5** and summarized in **Table 8-3**. PLA/HH biocomposites exhibited similar tensile strength and flexural strength, because of the uniform HH distribution in polymer matrix and adequate interfacial adhesion between polymer matrix and HH fibres. A lower tensile strength (47.2 MPa) occurred at PLA-HH-1 because of the highest interface area, which acted as the stress concentration sites, easily give in under pressure [177], as evidenced by more HH pull-out supported by SEM image (**Figure 8-4a**). The lower flexural strength (76.3 MPa) observed at PLA-HH-2 was related to the relative lower crystallinity [198]. An increment in impact strength was observed from 41.3 J/m to 54.4 J/m as the particle size increased from 35 to 160 μm, due to the improved filler-matrix stress transfer [86], as proved by SEM images shown in **Figure 8-4d**. The flexural modulus slightly decreased as the HH particle size increased, attributed to the reduced HH fibres dispersion of large-particle HH than small-particle ones.

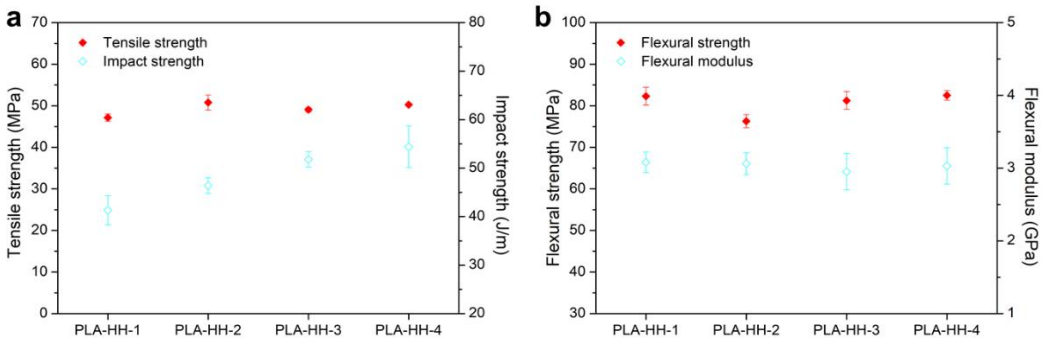

Figure 8-5 Mechanical properties of IM specimens with increasing HH particle size.

Table 8-3 Mechanical properties of IM specimens as a function of HH particle size

Materials	Tensile strength (MPa)	Impact strength (J/m)	Flexural strength (MPa)	Flexural modulus (GPa)
PLA-HH-1	47.2±0.9	41.3±3.0	82.3±2.2	3.08±0.1
PLA-HH-2	50.8±1.8	46.4±1.6	76.3±1.6	3.06±0.2
PLA-HH-3	49.1±0.5	51.8±1.6	81.3±2.2	2.95±0.3
PLA-HH-4	50.3±0.3	54.4±4.3	82.5±1.1	3.03±0.3

8.1.2 Filament quality

Filament diameter tolerance is an indicator of the variation in diameter, and filament roundness is an indicator of the filament ovality (or departure from non-circularity). Inconsistent diameter and roundness potentially produce unsteady extrusion, causing jamming, or clogging in 3D printing jobs. PLA/HH filament appearance is visually displayed in **Figure 8-6a**, the surface of filament clearly turned into coarser with increasing HH particle size. Box charts were used to demonstrate the distribution of filament diameter tolerance and roundness, as shown in **Figure 8-6b** and **c**. The filaments exhibited increasing diameter tolerances and roundness with increasing HH particle size. PLA-HH-1 and PLA-HH-2 exhibited diameter tolerance distribution within ±0.04 mm and roundness ⩽0.05 mm. PLA-HH-4 showed higher diameter tolerance (±0.06 mm) and roundness (⩽0.06 mm). PLA-HH-3 showed even broader distribution in filament diameter tolerance and roundness than PLA-HH-4, ascribed to its broader particle size distribution and lower melt flow. The requirement on the

diameter tolerance and the roundness of 1.75 mm filament is within ±0.03 mm and ⩽0.05 mm respectively, according to GB/T 37643-2019 standard. The filament quality could be improved by changing the diameter of the extrusion die during filament manufacturing. PLA-HH-2 showed a relatively higher filament quality because the filaments were manufactured using an extrusion die of 1.8 mm in diameter, whereas other filaments used 2.0 mm die. PLA-HH-3 and PLA-HH-2 produced using an extrusion die of 1.8 mm diameter (filament 2 and 4 in **Figure 8-7**) exhibited improved filament quality, compared with the filament produced using 2.0 mm extrusion die (filament 1 and 3 in **Figure 8-7**).

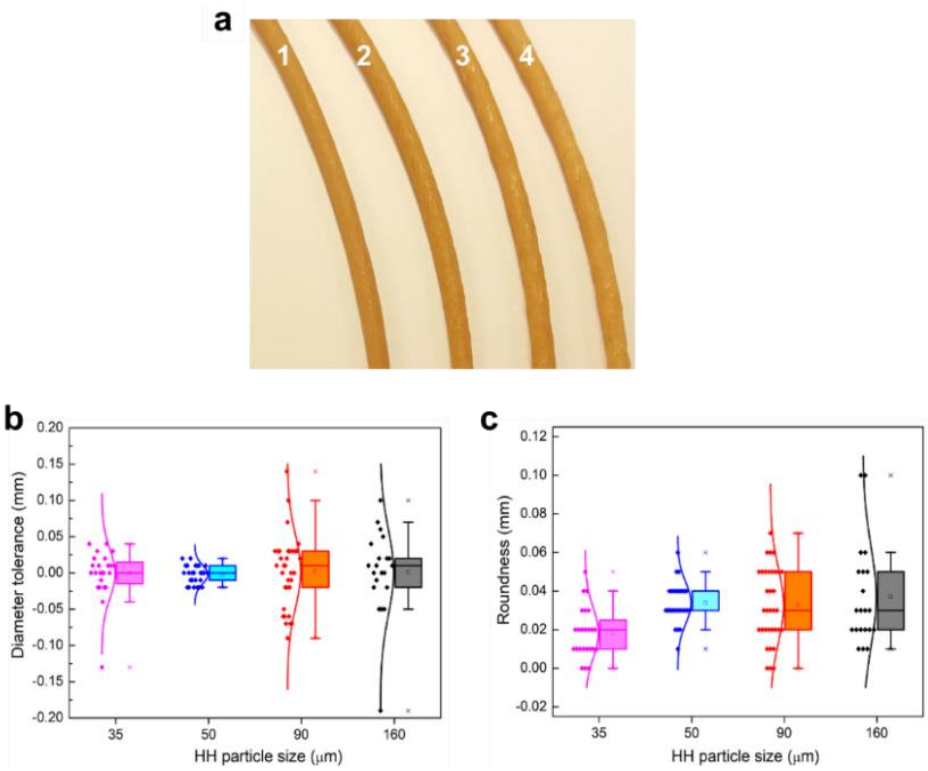

Figure 8-6 (a) PLA/HH filament of (1) PLA-HH-1, (2) PLA-HH-2, (3) PLA-HH-3, and (4) PLA-HH-4, (b) diameter tolerance and (c) roundness of filament as a function of HH particle size.

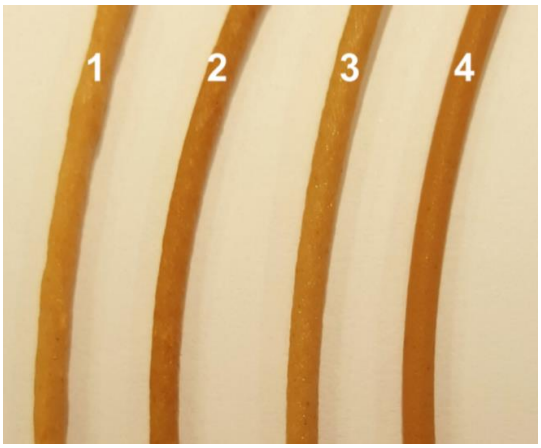

Figure 8-7 Filament of PLA-HH-3 produced using extrusion die of (1) 2.0 mm and (2) 1.8 mm and filament of PLA-HH-2 produced using extrusion die of (3) 2.0 mm and (4) 1.8 mm.

8.1.3 The properties of FDM-printed specimens

8.1.3.1 Surface roughness and porosity

Surface roughness describes the appearance and texture of the products, the porosity suggests the thermo-physical properties of the FDM-printed parts. **Figure 8-8** presents the visual appearance of FDM-printed specimens, which become rougher with increasing HH particle size. PLA-HH-3 showed the coarsest surface, associated with its lowest melt flow and the existence of large HH particles. The experimental value of surface roughness (**Figure 8-8b**) determined using the stylus method supports visual observation. The average roughness (R_a) is all around 20 µm, PLA-HH-1 and PLA-HH-2 showed similar roughness, because the particle sizes were both less than the printing layer thickness (0.15 mm). PLA-HH-3 and PLA-HH-4 showed relatively higher roughness due to the existence of larger particles over 150 µm (printing layer thickness). Nozzle jamming and clogging were observed during FDM printing of PLA-HH-3 and PLA-HH-4, causing interruption of the fabrication of FDM items. The results indicate that HH with large particle size impeded the melt flow throughout from the nozzle, and enhanced the surface roughness of the filament and FDM-printed parts although the biocomposites had higher MFR. PLA-HH-3 showed the highest roughness, due to the difficulty in the FDM process, the filament produced with extrusion die of 1.8 mm was employed to fabricate the test specimen.

The FDM-printed parts of PLA-HH-3 displayed rougher surface than PLA-HH-1 part as shown in **Figure 8-8c**.

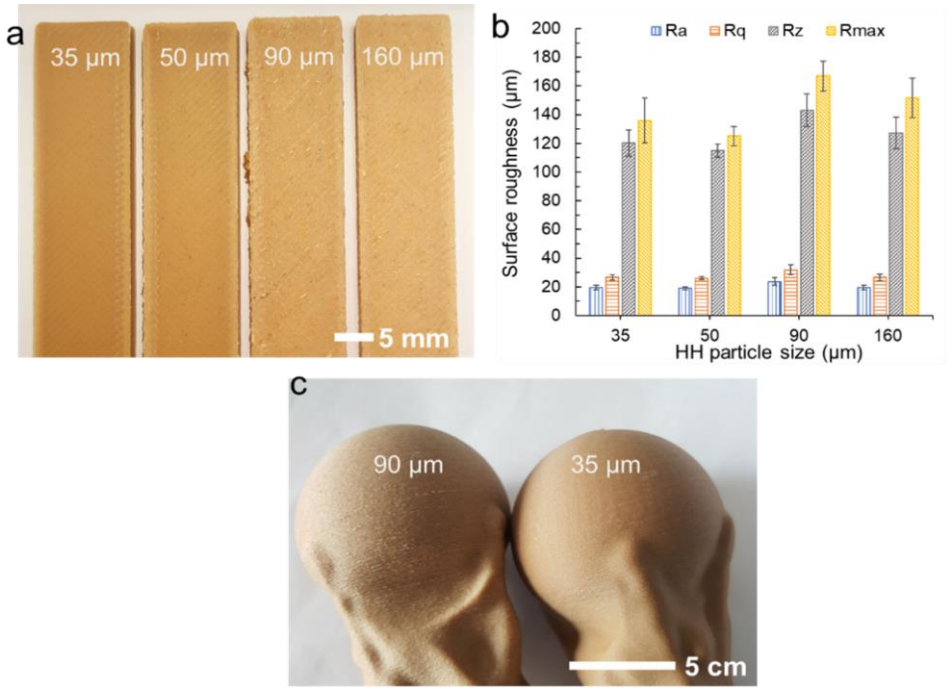

Figure 8-8 (a) FDM-printed specimens (top view) and (b) surface roughness, and (c) FDM parts.

The bulk density of FDM-printed specimens obtained by dividing the weight of flexural specimens by their bulk volume, and the porosity scanned by X-ray CT are summarized in **Table 8-4**. The bulk density slightly decreased, and the porosity increased with increasing HH particle size. The 3D porosity distributions in the FDM-printed specimens are shown in **Figure 8-9**. The coloured areas are ascribed to the distribution of voids of various size. The X-ray CT analysis revealed an increase in porosity volume fraction and average pore size with increasing HH particle size. This resulted from the incorporation of larger sized HH particles, which impeded the fusion bonding between printed layers and wires, thereby decreasing interfacial bonding and increasing porosity. The voids aligned with the adjacent print tracks demonstrated the inadequate melt fusion and the entrapment of vapours in voids [199]. Overall, X-ray CT results indicated the deteriorated melt fusion between the adjacent wires and layers with increasing HH particle size, as results of less melt output from the nozzle. PLA-HH-3 exhibited a structure with less large voids than other specimens did. The porosity increased from 4.86% for PLA-HH-1 to 9.85% for

PLA-HH-4, as plotted in **Fig. 8-9e**. PLA-HH-3 exhibited a lower porosity (5.99%) than PLA-HH-2 (6.34%), attributed to the higher effectiveness in filling the void space due to the broad particle size distribution of HH in PLA-HH-3.

Table 8-4 Bulk density and porosity of FDM-printed specimens

Materials	Bulk density (g/cm^3)	Porosity (%, by CT)
PLA-HH-1	1.14±0.01	4.86
PLA-HH-2	1.12±0.01	6.34
PLA-HH-3	1.13±0.00	5.99
PLA-HH-4	1.11±0.02	9.85

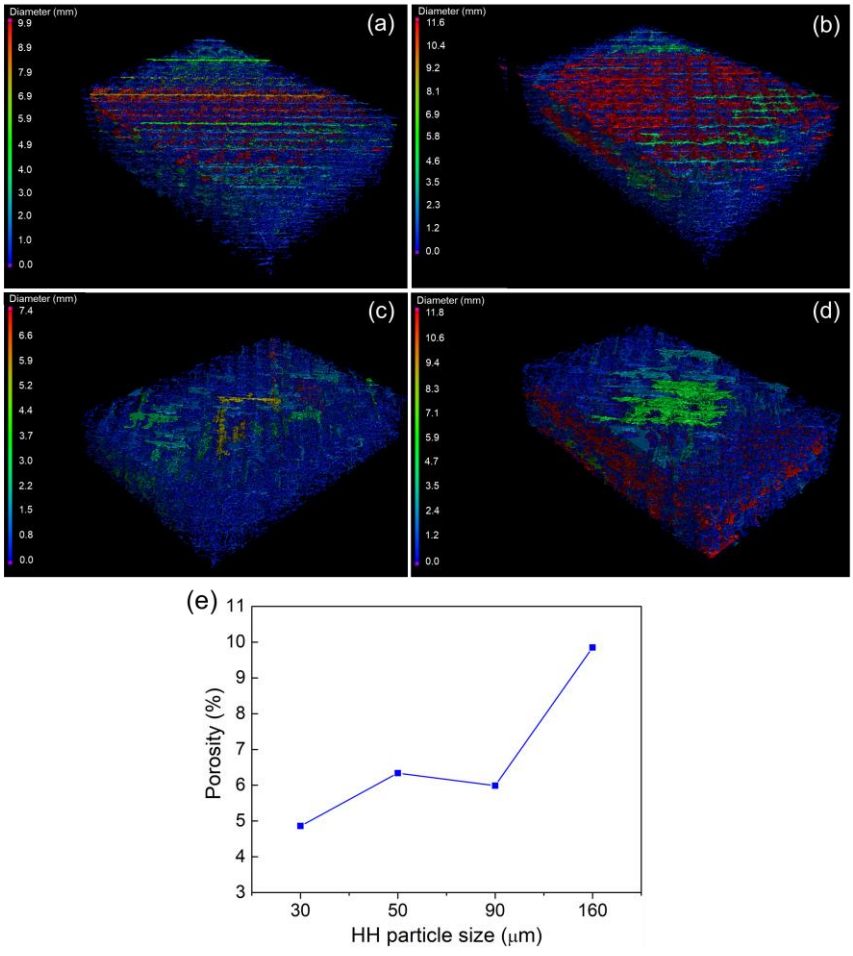

Figure 8-9 3D porosity distributions in FDM-printed specimens: (a) PLA-HH-1, (b) PLA-HH-2, (c) PLA-HH-3, (d) PLA-HH-4, and (e) the porosity values as a function of HH particle size.

8.1.3.2 Mechanical properties

The mechanical properties of FDM-printed specimens, especially the toughness, dictate the printability of filament and the application of the feedstock. The mechanical properties of FDM-printed specimens as a function of HH particle size are shown in **Figure 8-10** and summarized in **Table 8-5**. The tensile strength slightly increased with HH particle size, similar to the tendency in IM specimens, whereas decreased for PLA-HH-4, due to the major increase in porosity. All the specimens showed similar impact strength around 55 J/m, higher than the impact strength of IM specimens (**Table 8-3**), associated with the increased crystallinity after printing induced by the heated printer bed [187]. The increment in impact strength with increasing HH particle size in IM specimens was weakened by increased porosity in FDM specimens. The flexural strength of FDM specimens decreased with an increasing particle size of HH due to the increased porosity and decreased interfacial adhesion. The flexural modulus gradually decreased with increasing particle size, similar to that of IM specimens. PLA-HH-2 demonstrated higher comprehensive mechanical properties than other samples. The specific mechanical properties listed in **Table 8-6** exhibited a similar trend as the mechanical properties before density normalization.

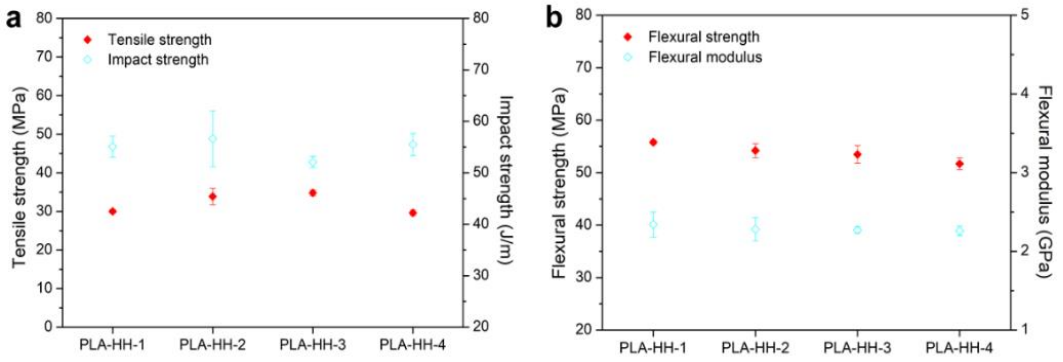

Figure 8-10 Mechanical properties of FDM-printed specimens: (a) tensile and impact strength and (b) flexural properties as a function of HH particle size.

Table 8-5 Mechanical properties of FDM-printed specimens as a function of HH particle size

Materials	Tensile strength (MPa)	Impact strength (J/m)	Flexural strength (MPa)	Flexural modulus (GPa)
PLA-HH-1	30.0±0.5	55.1±2.0	55.8±0.4	2.34±0.2
PLA-HH-2	33.9±2.1	56.6±5.4	54.2±1.3	2.28±0.2
PLA-HH-3	34.8±0.8	52.1±1.1	53.5±1.7	2.27±0.0
PLA-HH-4	29.6±0.7	55.5±2.2	51.7±1.2	2.26±0.1

Table 8-6 Specific mechanical properties of IM and FDM-printed specimens as a function of HH particle size

Materials	Specific tensile strength ($MPa.cm^3/g$)		Specific impact strength ($J/m.cm^3/g$)		Specific flexural strength ($MPa.cm^3/g$)		Specific flexural modulus ($GPa.cm^3/g$)	
	FDM	IM	FDM	IM	FDM	IM	FDM	IM
PLA-HH-1	26.3±0.4	38.0±0.7	48.3±1.8	33.3±2.4	48.9±0.4	66.4±1.7	2.05±0.1	2.48±0.1
PLA-HH-2	30.3±1.9	41.3±1.5	50.6±4.9	37.7±1.3	48.4±1.2	62.0±1.3	2.04±0.1	2.49±0.1
PLA-HH-3	30.8±0.7	40.2±0.4	46.1±1.0	42.5±1.3	47.3±1.5	66.6±1.8	2.01±0.0	2.42±0.2
PLA-HH-4	26.7±0.6	40.9±0.2	50.0±1.9	44.2±3.5	46.6±1.1	67.1±0.9	2.04±0.1	2.46±0.2

8.1.3.3 Morphology

The impact fracture surfaces of FDM-printed specimens were observed by SEM, as shown in **Figure 8-11** and **Figure 8-12**, to explore the effect of HH particle size on microstructure and interlayer morphology of PLA/HH specimens. The fracture surface became rougher with increasing HH particle size (**Figure 8-11**). More voids and improved interlayer space were observed as HH particle size increased, supporting the porosity obtained by X-ray CT scanning in **Figure 8-8d**. PLA-HH-1 and PLA-HH-2 exhibited elastoplastic deformation (**Figure 8-12**), contributed to the enhanced impact strength versus IM specimens shown in **Table 8-3**, whereas PLA-HH-3 and PLA-HH-4 displayed relatively smooth surface and lower wetting of HH particle by polymer matrix than PLA-HH-1 and PLA-HH-2, resulting in minor increase in impact strength. Large voids were detected on the surface of PLA-HH-3 parts, causing the low impact strength (**Table 8-5**).

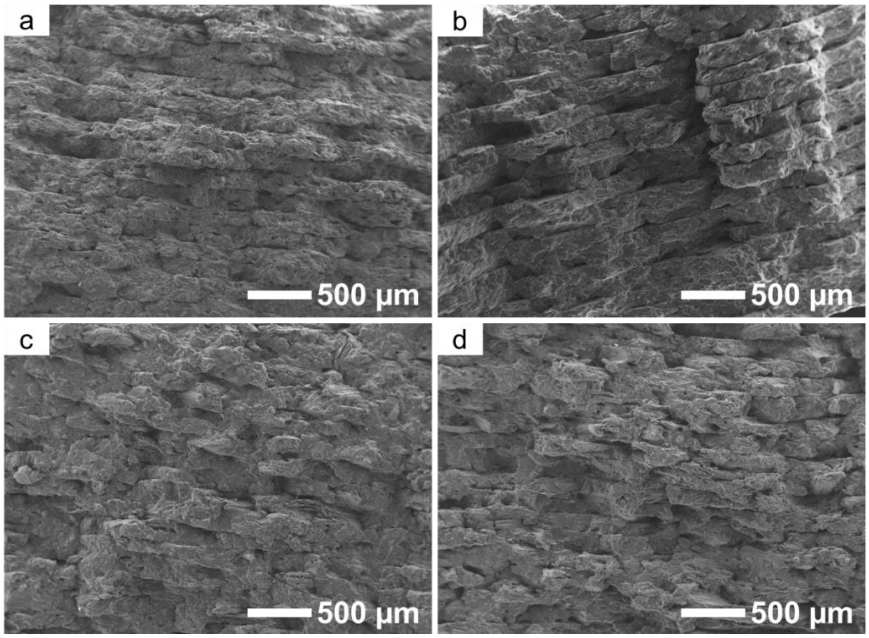

Figure 8-11 SEM images of impact fracture surfaces of FDM-printed specimens: (a) PLA-HH-1, (b) PLA-HH-2, (c) PLA-HH-3, and (d) PLA-HH-4, all at a magnification of 30×.

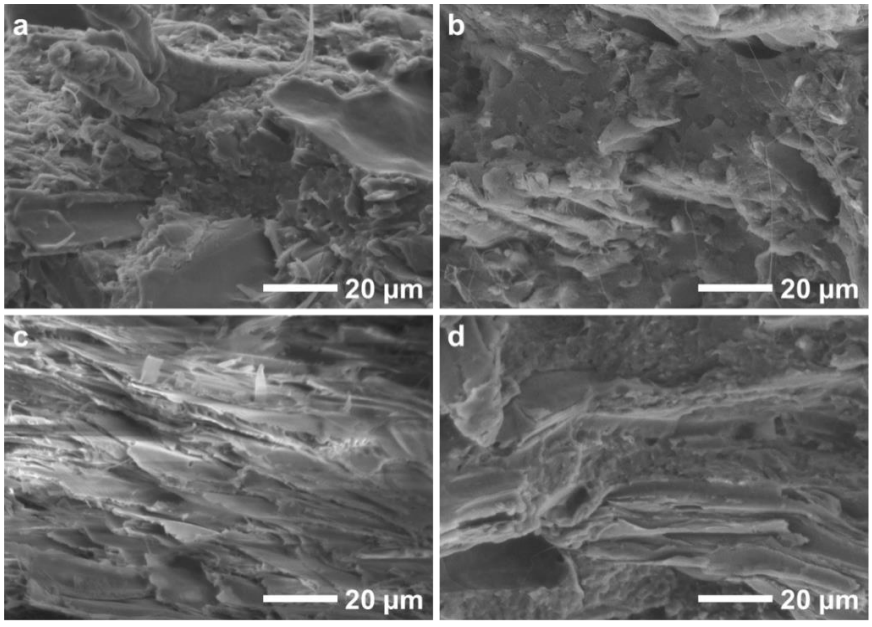

Figure 8-12 SEM images of impact fracture surfaces of FDM-printed specimens: (a) PLA-HH-1, (b) PLA-HH-2, (c) PLA-HH-3, and (d) PLA-HH-4, all at a magnification of 1000×.

In this study, HH of varying particle sizes was studied as biomass filler for PLA biocomposite as FDM feedstock using melt-compounding and extrusion. A systematic investigation in the printability, mechanical properties, and surface finish of the compounds with respect to the HH particle size was performed. The increase in HH particle size resulted in deteriorated printability, PLA-HH-3 and PLA-HH-4 filaments presented challenge in FDM printing. The surface roughness of FDM filament and printed parts increased with increasing HH particle size, although the melt flow increased. FDM specimens exhibited higher impact strength than IM samples. The IM specimens filled with HH of the larger particle size achieved higher impact strength, whereas the impact strength of FDM-printed specimens was marginally affected by HH particle size, as a combined result of increased porosity and deteriorated interfacial adhesion. The impact of HH particle size on other mechanical properties of IM specimens is negligible. However, HH with small particle size enhanced the comprehensive mechanical properties of FDM specimens.

Overall, the smaller particle size of HH is favourable for obtaining optimum properties for FDM parts. This research revealed the relationship between HH particle size and comprehensive properties of PLA/HH biocomposite feedstock.

8.2 Effect of BP particle size on PLA/BP biocomposites

Part of the work has been prepared to submit in the following journal:

X. Xiao, V. S. Chevali, P. Song, H. Wang, Polylactide/bamboo powder biocomposite for 3D printing: Effect of bamboo powder content and particle size, Polymer testing (**In submission**).

This study investigated bamboo power with varying particle sizes as biomass filler for PLA/BP biocomposites as FDM feedstock. The present work tended to tailor the surface roughness of FDM-printed items through the particle size of BP. The objective of this study was to explore the relationship between the particle size of BP and the processability of the biocomposites, mechanical properties and finish quality of the FDM-printed parts. Pristine BP with d_{50} of 20, 50, and 65 μm was melting compounded and extruded with PLA/PBAT/EGMA through a twin-screw and granulated to pellets, PLA/BP biocomposites (PLA-BP-1, PLA-BP-2, and PLA-BP-3) then were extruded to 1.75 mm filament for FDM 3D printing via a single-screw filament extruder. The compositions in the PLA/BP biocomposites are shown in

Table 8-7. The influence of BP particle size on melt flow, rheological properties of biocomposites, filament quality, mechanical properties of both IM and FDM-printed specimens, and the finish quality of FDM-printed items, especially the surface roughness were investigated.

Table 8-7 Formulations of PLA/BP biocomposites with BP of varying particle size

Constituent	PLA	PBAT	EGMA	Bamboo powder	Additives
phr	87	13	6.5	20	2.2

8.2.1 The properties of biocomposites materials

8.2.1.1 Rheological properties and melt flow rate

The dynamic rheology analysis provides information about the interfacial interaction [141] and processability of biocomposites in melt state [142]. **Figure 8-13** presented the dependence of rheological properties of PLA/BP biocomposites on the angular frequency at 190°C. The effect of particle size of BP on $|\eta^*|$ was insignificant (**Figure 8-13a**). PLA-BP-1 showed marginally lower $|\eta^*|$ than the other two samples, agrees well with the MFR results, which was higher for PLA-BP-1 than the other two samples (**Figure 8-14**). However, PLA/BP biocomposites exhibited relatively lower $|\eta^*|$ and higher MFR than PLA/HH biocomposites, indicating improved processability for PLA/BP biocomposites [162]. PLA/HH biocomposites exhibited increased MFR and decreased $|\eta^*|$ at low frequency with the increasing HH particle size. However, PLA/BP showed decreased MFR and increased $|\eta^*|$ at low frequency with increasing BP particle size. The biocomposites showed shear-thinning behaviour with increasing angular frequency, due to the disentanglement of BP particles and polymer chains in the flow direction [164]. The shear-thinning behaviour aids in reducing $|\eta^*|$ and getting increased melt flow and processability, which enhances the output during melt extrusion [162]. PLA-BP-1 showed Tan δ close to 1, whereas other two samples showed Tan δ above 1 at a low dynamic frequency, suggesting PLA-BP-1 was in a transition state from elastic to viscous at low frequency, while other two samples displayed viscous behaviour. PLA-BP-2 and PLA-BP-3 showed higher loss modulus (G'') than PLA-BP-1, and similar storage

modulus (*G'*) with PLA-BP-1, indicating larger BP particle size pronounced the viscous behaviour of biocomposites.

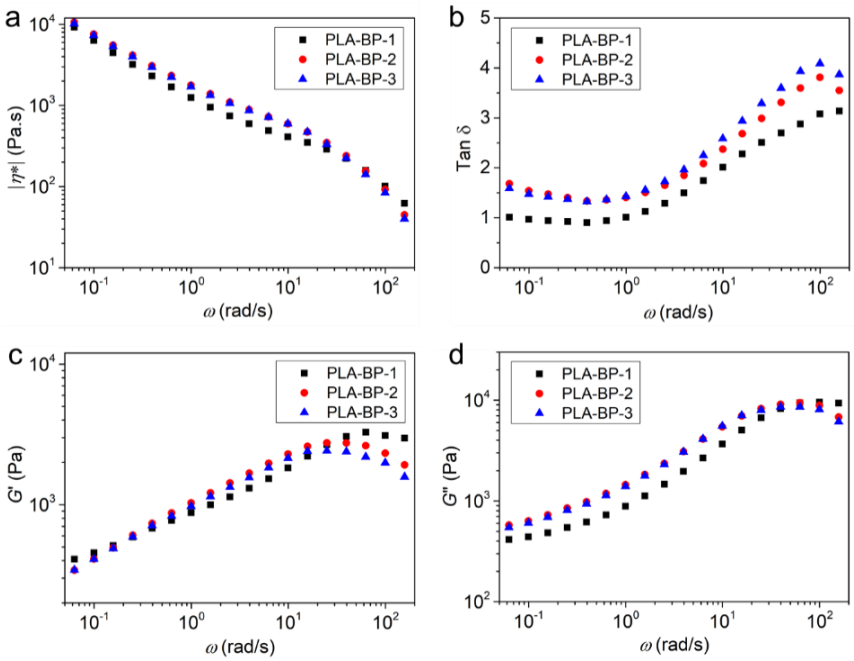

Figure 8-13 Melt rheological properties of PLA/BP biocomposites: (a) |η*|, (b) tan δ, (c) G', and (d) G'' as a function of angular frequency at 190°C.

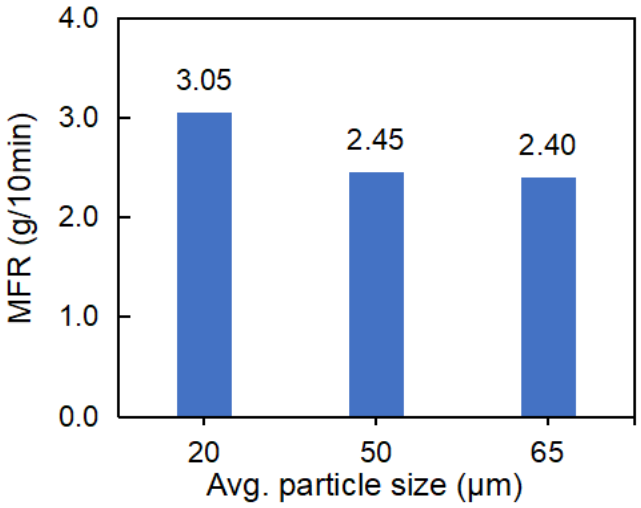

Figure 8-14 MFR of PLA/BP biocomposites at 190°C/2.16kg as function of BP particle size.

8.2.1.2 Thermal properties

The DSC thermograms of PLA/BP biocomposites of varying BP particle sizes are presented in **Figure 8-15**. The thermal transition temperatures and thermal enthalpy are recorded in **Table 8-8**. T_g slightly decreased from 66.7°C to 63.7°C with increasing BP particle size, associated with the presence of less crosslinking points because of less BP particles, and increased free volume, which improved the mobility of PLA polymer chains [200]. T_{cc} was higher than PLA-BP-0 without BP (100.5°C) for all samples, indicating that the incorporation of BP delayed the crystallization of PLA during heating, resulting in decreased cold crystallization enthalpy than PLA-BP-0 (15.7 J/g). T_m was similar for each sample. Crystallinity decreased with increasing BP particle size, due to the reduced nucleation sites. PLA-BP-1 and PLA-BP-2 exhibited similar X_c, which is a bit higher than PLA-BP-3. The crystallinity of PLA-BP-3 was even lower than that of PLA-BP-0. The crystallinity obtained from the second heating curves was only half of the value recorded from the first heating curve for all the counterparts, indicating incomplete crystallization at a cooling ramp rate of 10°C/min. From the first heating curves, it is witnessed that the PLA/BP biocomposites did not generate cold crystallization, indicating the complete crystallization, all the biocomposites exhibited lower crystallinity than PLA-BP-0 (49.1%), implying that the existence of BP impeded the crystallization of PLA after the process.

Table 8-8 Crystallization and melt phase properties of PLA/BP biocomposites as a function of BP particle size

Materials	First heating				Cooling		Second heating					
	T_g *(°C)*	T_m (°C)	ΔH_m (J/g)	X_c (%)	T_{c1} *(°C)*	T_{c2} (°C)	T_g *(°C)*	T_{cc} (°C)	ΔH_{cc} (J/g)	T_m (°C)	ΔH_m (J/g)	X_c (%)
PLA-BP-1	66.7	167.2	29.3	46.7	127.4	97.4	61.2	104.2	9.8	168.1	24.9	24.0
PLA-BP-2	65.3	166.8	30.3	48.2	127.1	95.9	60.9	102.6	11.3	168.1	25.3	22.2
PLA-BP-3	63.7	166.9	26.2	41.8	127.8	95.1	60.3	104.2	11.0	168.3	21.7	17.1

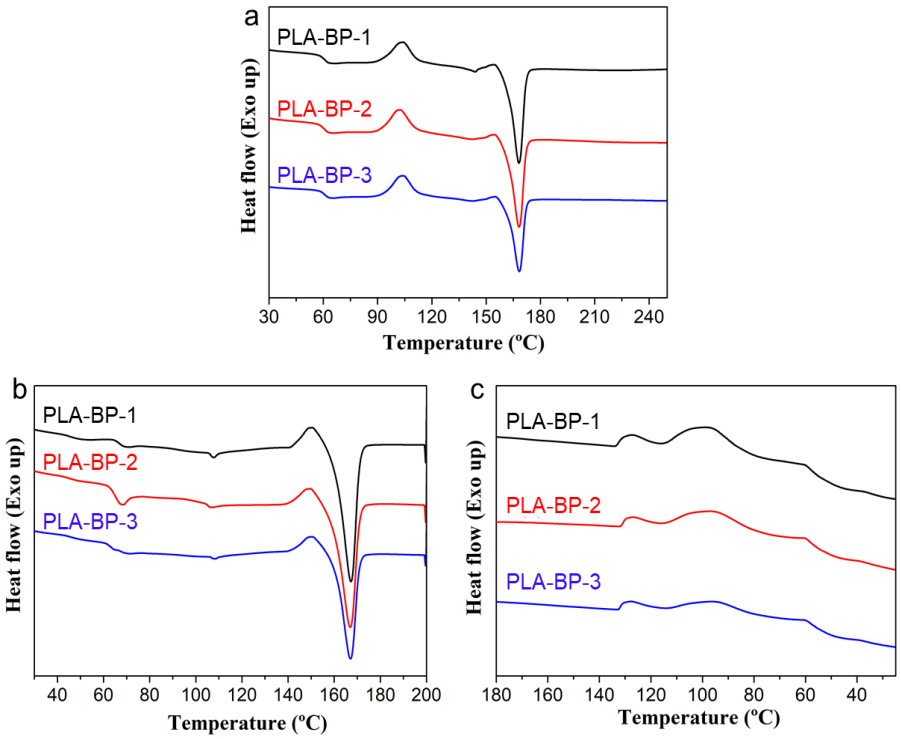

Figure 8-15 DSC curves of PLA/BP biocomposites: (a) second heating, (b) first heating, and (c) cooling.

8.2.1.3 Dispersion of BP and interface morphology of IM specimens

The cryo-fractured surfaces of IM specimens were observed by SEM, and the images are shown in **Figure 8-16**. With increasing BP particle size, the interfacial bonding between BP and polymer matrix decreased, BP was encapsulated in the matrix in PLA-BP-1 (**Figure 8-16a**, **b**, green arrow), there was no void or cavity observed on the surface, indicating good interfacial adhesion between BP and polymer matrix. As BP particle size increased, some of BP particles exhibited good interfacial adhesion with polymer matrix, whereas the boundary between BP and matrix (**Figure 8-16c**, **d**, gold arrow) and the cavity left by the BP pull-out (**Figure 8-16c**, white arrow) were detected on the surface of PLA-BP-2. The pull-out (**Figure 8-16e**, red arrow) and debonding (**Figure 8-16e**, **f**, gold arrow) of BP from the matrix were found on the surface of PLA-BP-3, indicating the reduced interfacial adhesion between the filler and matrix. The SEM images showed that IM specimens had smoother surfaces without obvious plastic deformation, demonstrating the fracture mode was predominantly in a brittle manner [176].

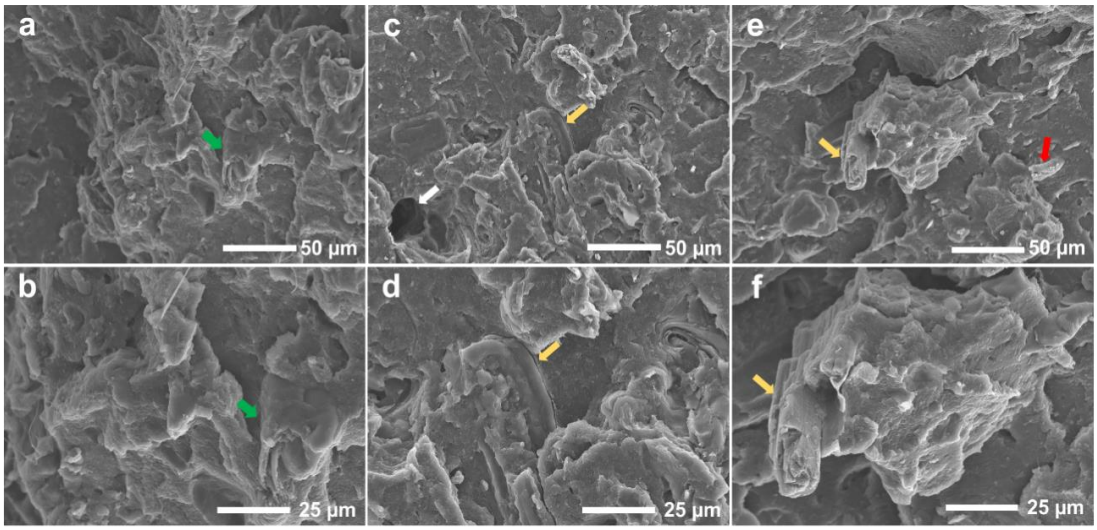

Figure 8-16 SEM images of cry-fractured surface of IM samples: (a, b) PLA-BP-1, (c, d) PLA-BP-2, and (e, f) PLA-BP-3 at magnifications of 500× and 1000×.

8.2.1.4 Mechanical properties of IM specimens

The mechanical properties of IM specimens with varying BP particle sizes are presented in **Figure 8-17** and compared with PLA/HH IM specimens in **Figure 8-18**. The tensile strength, flexural strength, and flexural modulus marginally decreased with increasing BP particle size, due to the deteriorated dispersion and reduced matrix-filler interfacial adhesion (**Figure 8-16**). However, the impact strength increased with increasing BP particle size, PLA-BP-3 exhibited an impact strength 13% higher than PLA-BP-1, further indicating the larger particle size favoured higher impact strength. Compared with the mechanical properties of PLA/HH biocomposites, PLA/BP displayed lower mechanical properties (**Figure 8-18**), attributed to the reinforcement of fibrillary HH filler and higher interfacial interaction between HH and polymer matrix, as evidenced by the higher value in rheological parameters and superior interfacial adhesion proved by SEM micrographs.

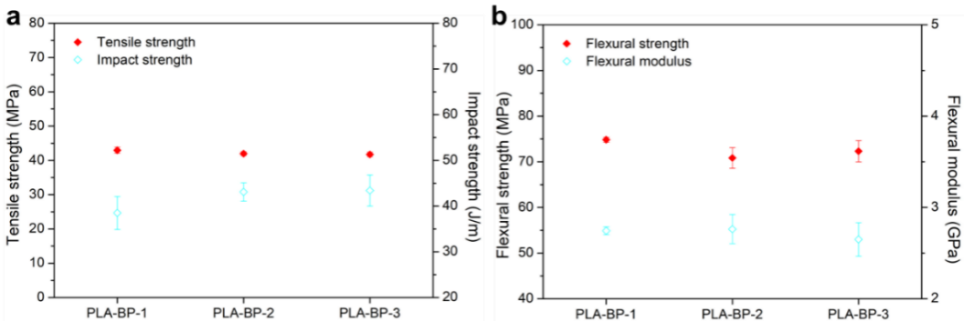

Figure 8-17 Mechanical properties of IM specimens as a function of BP particle size.

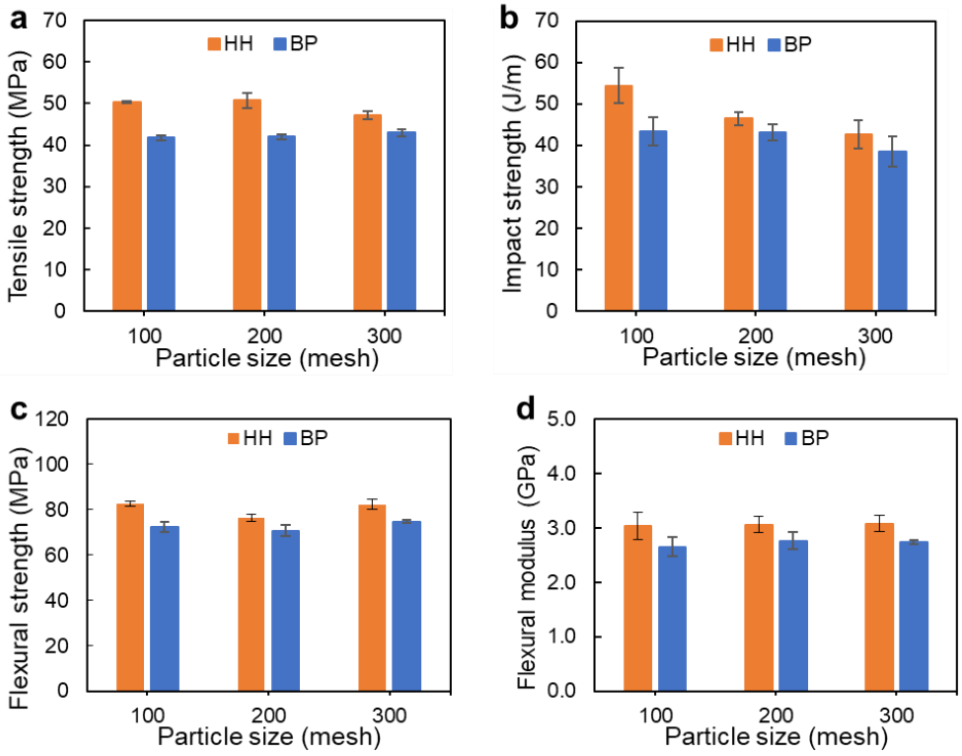

Figure 8-18 Mechanical properties comparison of IM specimens between the samples filled with HH and BP as a function of biomass particle size.

8.2.2 Filament quality

The visual appearance, diameter tolerance, and roundness of PLA/BP filament are shown in **Figure 8-19**. The surface of filament became coarser with increasing BP particle size, attributed to the decreased melt flow and increased BP particle size. PLA/BP filament showed increasing diameter tolerance and roundness with increasing BP particle size, in accordance with the visual surface appearance. PLA-

BP-1 and PLA-BP-3 exhibited diameter tolerance out of the specification of ±0.03 mm, which could be modified by using 1.8 mm die to replace 2.0 mm die for filament extrusion. PLA-BP-2 exhibited filament diameter tolerance within ±0.02 mm because of the utilization of 1.8 mm extrusion die during filament extrusion. The filament all exhibited roundness ⩽0.04 mm, met the requirement in GB/T 37643-2019 standard.

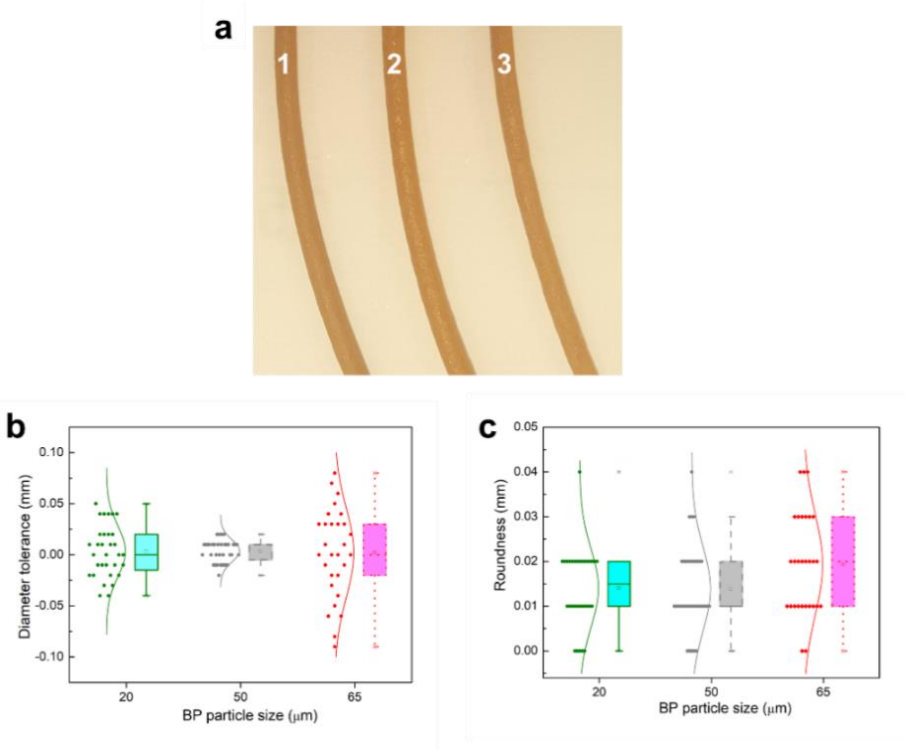

Figure 8-19 (a) Visual appearance, box plots of (b) diameter tolerance, and (c) roundness of PLA/BP filament as a function of BP particle size. (1) PLA-BP-1, (2) PLA-BP-2, and (3) PLA-BP-3.

8.2.3 The properties of FDM-printed specimens

8.2.3.1 Finish quality

Visual surface appearance and experimental surface roughness of FDM-printed specimens of varying BP particle size are presented in **Figure 8-20**. The specimens exhibited similar surface roughness visually, which was supported by the experimental data. The similar surface roughness is associated with the BP particle size were all smaller than the thickness (150 μm) of printing layer, the effect of particle size on the surface roughness was negligible. The bulk density and shrinkage

of FDM-printed specimens are presented in **Table 8-9**. FDM-printed specimens showed similar density and increased shrinkage with increasing BP particle size, implying that the smaller particle size is beneficial for the dimensional stability of FDM-printed specimens.

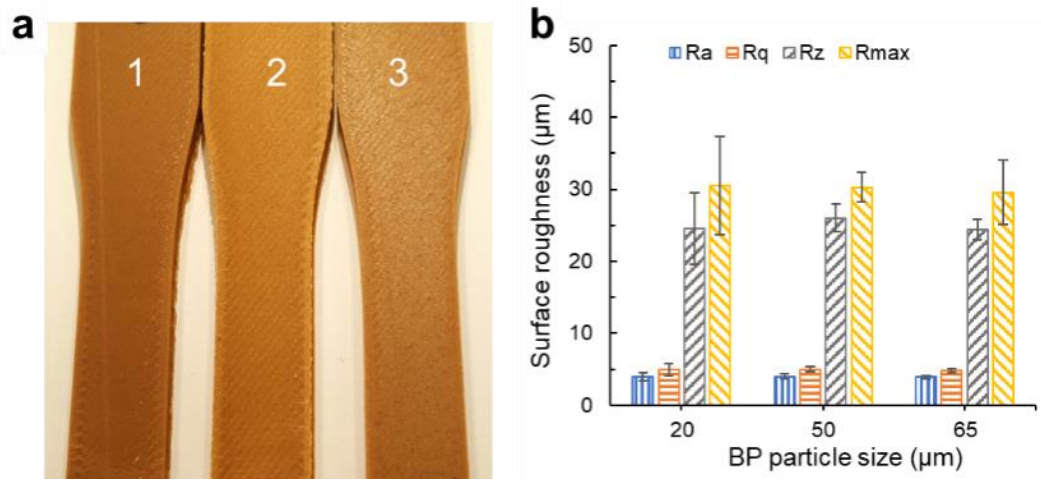

Figure 8-20 (a) Top view and (b) surface roughness of FDM-printed specimens. (1) PLA-BP-1, (2) PLA-BP-2, and (3) PLA-BP-3.

Table 8-9 Density and porosity of PLA/BP biocomposite specimens

Materials	Density (g/cm^3)	Shrinkage (%)
PLA-BP-1	1.17±0.02	0.01±0.10
PLA-BP-2	1.16±0.01	0.02±0.07
PLA-BP-3	1.17±0.02	0.26±0.05

8.2.3.2 Morphology

The interlayer morphologies of FDM-printed specimens are shown in **Figure 8-21**. Filler pull-out and voids were detected on the impact fracture surfaces of PLA-BP-1 and PLA-BP-2 (**Figure 8-21d** and **e**, yellow arrow), indicating insufficient interfacial adhesion between BP and polymer matrix. PLA-BP-2 showed a relatively lower density than PLA-BP-1 and PLA-BP-3, more voids and pores were perceived on the impact fracture surface (**Figure 8-21b**), the voids were more obvious at the magnification of 500× as shown in **Figure 8-21d**. PLA-BP-3 exhibited a surface without obvious voids, BP filler was well encapsulated in the polymer matrix

(**Figure 8-21f**, green arrow), the fracture surface was rougher than other samples, demonstrating improved interfacial adhesion between BP and matrix [201].

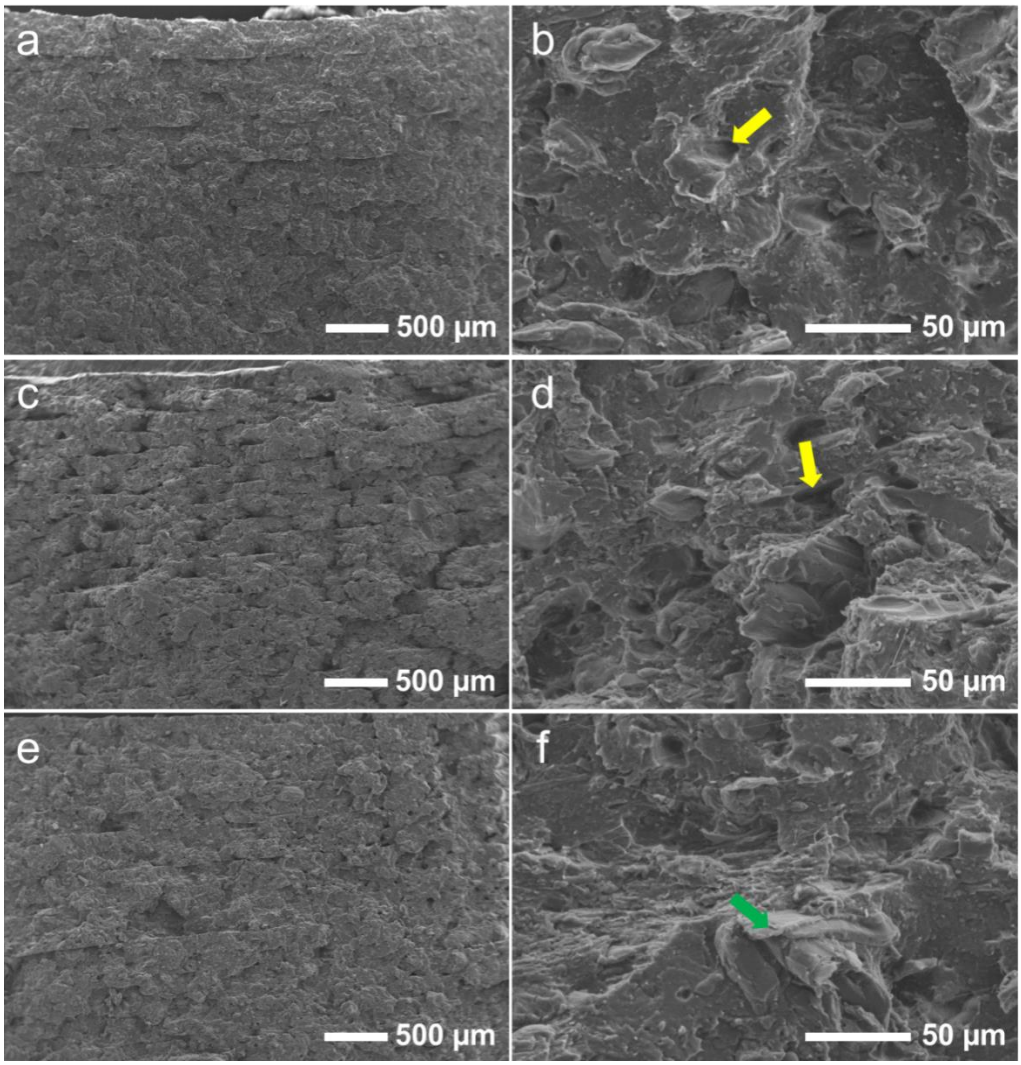

Figure 8-21 SEM images of impact fracture surfaces of FDM-printed specimens: (a, b) PLA-BP-1, (c, d) PLA-BP-2, and (e, f) PLA-BP-3 at magnifications of 30× and 500×.

8.2.3.3 Mechanical properties

The mechanical properties of FDM-printed specimens fabricated with PLA/BP biocomposites of varying BP particle sizes are shown in **Figure 8-22** and compared with IM specimens in **Table 8-10**. The specimens displayed a marginal decrease in tensile strength, whereas flexural strength and modulus, and impact strength all increased as BP particle size increased. The impact strength increased by 38% when the BP particle size increased from 20 μm to 65 μm due to the improved filler-matrix

stress transfer [86]. PLA-BP-2 showed relatively lower tensile strength than PLA-BP-3 because of the presence of more voids (**Figure 8-21b**, **d**). The FDM-printed specimens presented lower tensile strength, flexural strength, flexural modulus, whereas higher impact strength than IM specimens. The density normalized mechanical properties (**Table 8-11**) showed similar trends with the mechanical properties before density normalization. PLA/BP FDM-printed specimens exhibited different trend in mechanical properties with PLA/HH (**Figure 8-10**, **Table 8-5**), attributed to the higher melt flow, and resulted improved interfacial adhesion for PLA/BP samples.

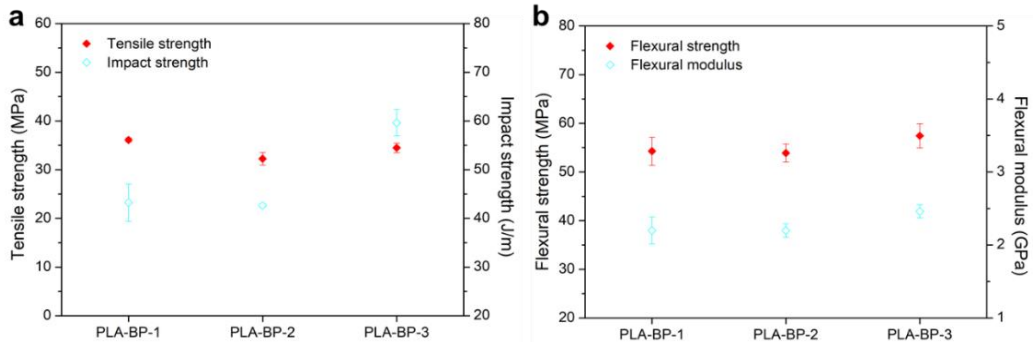

Figure 8-22 Mechanical properties of FDM-printed specimens of PLA/BP biocomposites.

Table 8-10 Mechanical properties comparison between IM and FDM-printed specimens of PLA/BP as a function of BP particle size

Materials	Tensile strength (MPa)		Impact strength (J/m)		Flexural strength (MPa)		Flexural modulus (GPa)	
	FDM	IM	FDM	IM	FDM	IM	FDM	IM
PLA-BP-1	36.1±0.4	43.0±0.9	43.2±3.8	38.5±3.6	54.3±2.9	74.8±0.6	2.20±0.2	2.75±0.0
PLA-BP-2	32.2±1.3	42.0±0.6	42.6±0.3	43.1±2.0	53.9±1.9	70.8±2.2	2.20±0.1	2.76±0.2
PLA-BP-3	34.5±1.0	41.7±0.6	59.7±2.7	43.4±3.4	57.4±2.5	72.3±2.3	2.46±0.1	2.65±0.2

Table 8-11 Specific mechanical properties comparison between IM and FDM-printed specimens as a function of BP particle size

Materials	Specific tensile strength ($MPa.cm^3/g$)		Specific impact strength ($J/m.cm^3/g$)		Specific flexural strength ($MPa.cm^3/g$)		Specific flexural modulus ($GPa.cm^3/g$)	
	FDM	IM	FDM	IM	FDM	IM	FDM	IM
PLA-BP-1	30.9±0.4	34.6±0.7	37.0±3.3	31.0±2.9	46.4±2.5	60.3±0.4	1.88±0.2	2.21±0.0
PLA-BP-2	28.5±1.2	34.1±0.4	37.7±0.3	35.0±1.6	47.7±1.6	57.6±1.8	1.95±0.1	2.25±0.1
PLA-BP-3	29.5±0.8	34.2±0.5	51.0±2.3	35.6±2.8	49.1±2.1	59.3±1.9	2.10±0.1	2.17±0.2

BP of various particle sizes was investigated as biomass filler for FDM feedstock. It was found that the influence of BP particle size on the surface roughness of FDM-printed specimens was negligible; however, smaller particle size obtained higher melt flow and crystallinity for PLA/BP biocomposite, improved interfacial adhesion and higher mechanical properties for IM specimens, and led to less shrinkage for FDM-printed items. Larger particle size as 65 μm acquired higher mechanical properties for FDM-printed specimens and higher impact strength for IM specimens. PLA-BP-3 with the largest particle size (65 μm) was the optimal candidate for FDM application from the points of both printability and mechanical properties. Overall, the influence of BP particle size on the melt flow of biocomposites, mechanical properties of IM specimens, and the finish quality of FDM-printed parts was insignificant. FDM-printed components showed a higher impact strength than IM parts.

In this chapter, HH and BP with various particle sizes were used to modify the surface roughness of FDM-printed parts. The relationship between the particle size and the comprehensive properties of the PLA-based feedstock was investigated. Surface roughness was a strong function of the setting of layer thickness. When the particle size was larger than the printing layer thickness, the surface roughness increased perceptibly with the increasing particle size of biomass. The particle size of HH and BP exhibited an opposite influence on the melt flow of PLA biocomposites. The larger particle size is advantageous for obtaining higher impact strength for both IM and FDM specimens of PLA/HH and PLA/BP biocomposites.

Chapter 9: Conclusions and recommendations

9.1 Conclusions

A comprehensive investigation on the development of PLA biocomposites feedstock for FDM 3D printing was performed through experimental and theoretical analysis. As the PLA biocomposites were used for FDM printing, the impact strength is an important parameter. The impact strength should not be lower than PLA control to guarantee the consistent filament manufacturing and 3D printing, so the toughening of PLA biocomposites was studied firstly. Based on the investigation, PBAT/EGMA was selected as the toughening agent for the systematic analysis of the relationships between HH loading, BP loading, HH particle size, BP particle size, and the comprehensive properties of PLA biocomposites for FDM 3D printing application. The major findings of this thesis are:

I. Using PBAT/EGMA as toughening agent provided improved properties than BPM520 and PCL/PCDL for PLA biocomposites, including improved filament quality, smoother surface for FDM parts, enhanced impact strength, and elongation-at-break for both IM and FDM parts.

II. PCDL tri-block copolymer efficiently enhanced the toughness of PLA/PCL blend due to the improved compatibility between PLA and PCL. PCDL exhibited higher efficiency in toughening PLA biocomposites compared to PLLA-PCL-PLLA due to the improved compatibility between PLA and PCL because of the formation of stereocomplexation.

III. The increasing biomass loading caused a decrease in melt flow and impact strength and increase in flexural modulus for both PLA/HH and PLA/BP biocomposites, increased tensile strength and flexural strength for PLA/HH whereas decreased corresponding properties for PLA/BP, attributed to the reinforcement by HH with fibrillary structure and enhanced interfacial adhesion between HH and polymer matrix.

IV. The increased biomass loading also caused increased surface roughness, porosity, and flexural modulus, decreased impact strength, tensile strength, and flexural strength for FDM parts. With up to 30 phr biomass filler (HH

and BP), there was no problem in filament extrusion and FDM printing, the FDM-printed specimens showed comparable impact strength to PLA control.

V. FDM specimens exhibited higher impact strength than IM specimens, attributed to the improved crystallinity induced by the heated bed of the 3D printer. FDM specimens also showed higher thermal stability than IM specimens. The addition of biomass improved the dimensional stability of the FDM parts.

VI. The surface roughness of FDM-printed items was negligibly affected by the particle size of biomass when it was less than the printing layer thickness. Only when the particle size was larger than the printing layer thickness, the surface roughness would increase.

VII. Biomass with larger particle size attained relatively lower filament quality and difficulty in FDM printing, and higher porosity for FDM parts. However, the larger particle size achieved higher impact strength for both IM and FDM specimens.

The thesis contributes to the understanding of the relationships between the toughening, the biomass content, and biomass particle size with the melt flow and mechanical properties of the biocomposite materials, filament quality, and finish quality of the FDM parts, hence facilitating the utilization of biomass in 3D printing.

9.2 Challenges

This research successfully developed sustainable PLA biocomposites feedstock using HH and BP biomass powder, possessing the comparable processability and impact strength as commercial PLA control. In this study, the major challenges resolved were:

i) Processability, including the decreased melt flow with the increasing HH and BP content, caused a challenge in the manufacturing and printing process of 3D filament when HH and BP content was above 30 phr. The higher extruding and lower drawing speed were used when produce filament with above 30 phr HH and BP. The nozzle of 3D printer needs to be cleaned more often when print the filament with HH and BP above 30 phr;

ii) Decreased consistency in filament diameter and roundness, increased porosity in FDM-printed products with increasing loading and particle size of biomass filler. The filament quality was optimized by the extrusion parameters, such as the size of the extrusion die.

9.3 Recommendations for future research

Based on the results and challenges in this study, there are a few areas that need further investigation, as recommend in the following section to promise the application of high biomass content as 3D printing feedstock.

9.3.1 Enhancement of melt flow

For PLA biocomposites with biomass content above 30 phr, the enhancement in melt flow is required for smooth melt flow from the extrusion die during filament manufacturing and from the nozzle during FDM printing, to obtain the qualified FDM filament and FDM-printed parts.

Overall,

I. Lubricants were used to improve the melt flow. However, the lubricants with low molecular weight would affect other properties of biocomposites, the relationship between the addition of lubricants and the comprehensive properties of the biocomposites, including printability, interfacial adhesion, filament quality, and mechanical properties, need to be investigated.
II. Process parameters can be used to improve the melt flow during extrusion and 3D printing, generally, high temperature improves the melt flow.
III. Using biodegradable flexible polymer with low melt temperature to improve the mobility of PLA chains and remain the biodegradability of the biocomposites, along with improved toughness.

9.3.2 Enhancement of impact strength

The decrease in mechanical properties, especially the impact strength decreased to the value below PLA control when the biomass content was above 30 phr, which hindered the application of PLA biocomposites in 3D printing, causing breakage during filament processing and printing, restrict the application in the fields requiring toughness. The decrease in mechanical properties is related to the decreased matrix-filler interfacial adhesion, which is affected by

I. The melt flow of biocomposites feedstock- low melt flow resulted in insufficient output from the nozzle, producing voids, decreasing the interlayer bonding and interfacial adhesion.
II. FDM printing parameters- the optimal FDM printing parameters should be investigated to make compact deposition and reduce the porosity.
III. Surface modification- improve the interfacial adhesion by surface treatment of the biomass filler using coupling-agent to improve the compatibility between biomass and polymer matrix.

9.3.3 Filament production

Manufacturing biocomposite filament in terms of quality (diameter and roundness, strength, and surface), production rate (melt flow, extrusion parameters), and cost analysis. Further improvements in the quality of the biocomposite filament through the process parameters and the optimization of the extrusion die.

9.3.4 FDM printing

FDM printing in terms of quality (strength and surface quality), printing parameters, and applications. Comprehensive mechanistic analyses on the processing-structure relationship are essential for widespread application of FDM-printed components for industrial products.

References

[1] Henke K, Treml S. Wood based bulk material in 3D printing processes for applications in construction. European Journal of Wood and Wood Products. 2012;71(1):139-41.

[2] Levy GN, Schindel R, Kruth JP. Rapid manufacturing and rapid tooling with layer manufacturing (LM) technologies, state of the art and future perspectives. CIRP Annals. 2003;52(2):589-609.

[3] Ngo TD, Kashani A, Imbalzano G, Nguyen KTQ, Hui D. Additive manufacturing (3D printing): A review of materials, methods, applications and challenges. Composites Part B: Engineering. 2018;143:172-96.

[4] Farahani RD, Dubé M, Therriault D. Three‐dimensional printing of multifunctional nanocomposites: Manufacturing techniques and applications. Advanced Materials. 2016;28(28):5794-821.

[5] Kumar S, Kruth JP. Composites by rapid prototyping technology. Materials and Design. 2010;31(2):850-6.

[6] Yamada A, Niikura F, Ikuta K. A three-dimensional microfabrication system for biodegradable polymers with high resolution and biocompatibility. Journal of Micromechanics and Microengineering. 2008;18(2):1-9.

[7] Mohan N, Senthil P, Vinodh S, Jayanth N. A review on composite materials and process parameters optimisation for the fused deposition modelling process. Virtual and Physical Prototyping. 2017;12(1):47-59.

[8] Xu M, Bi Y, Song Y. Preparation of poplar powder filled poly lactic acid composites material and application in 3D printing. Science & Technology Review. 2016;34(19):132-7.

[9] Guo R, Ren Z, Bi H, Song Y, Xu M. Effect of toughening agents on the properties of poplar wood flour/poly (lactic acid) composites fabricated with Fused Deposition Modeling. European Polymer Journal. 2018;107:34-45.

[10] Mittal V, Chaudhry AU, Matsko NB. “True” biocomposites with biopolyesters and date seed powder: Mechanical, thermal, and degradation properties. Journal of Applied Polymer Science. 2014;131(19):40816.

[11] Wang Z, Xu J, Lu Y, Hu L, Fan Y, Ma J, et al. Preparation of 3D printable micro/nanocellulose-polylactic acid (MNC/PLA) composite wire rods with high MNC constitution. Industrial Crops and Products. 2017;109:889-96.

[12] Zhang Q, Cai H, Zhang A, Lin X, Yi W, Zhang J. Effects of lubricant and toughening agent on the fluidity and toughness of poplar powder-reinforced polylactic acid 3D printing materials. Polymers. 2018;10(9):932.

[13] Wang Y, Qi R, Xiong C, Huang M. Effects of coupling agent and interfacial modifiers on mechanical properties of poly(lactic acid) and wood flour biocomposites. Iranian Polymer Journal. 2011;20(4):281-94.

[14] Long H, Wu Z, Dong Q, Shen Y, Zhou W, Luo Y, et al. Mechanical and thermal properties of bamboo fiber reinforced polypropylene/polylactic acid composites for 3D printing. Polymer Engineering & Science. 2019;59(s2):E247-E60.

[15] Song X, Wang M, Weng Y, Huang Z. Effect of bamboo flour grafted lactide on the interfacial compatibility of polylactic acid/bamboo flour composites. Polymers. 2017;9(12):323.

[16] Sis ALM, Ibrahim NA, Yunus WMZW. Effect of (3-aminopropyl) trimethoxysilane on mechanical properties of PLA/PBAT blend reinforced kenaf fiber. Iranian Polymer Journal. 2013;22(2):101-8.

[17] Nomai J, Jarapanyacheep R, Jarukumjorn K. Mechanical, thermal, and morphological properties of sawdust/poly(lactic acid) composites: Effects of alkali treatment and poly(butylene adipate-co-terephthalate) content. Macromolecular Symposia. 2015;354(1):244-50.

[18] Daver F, Lee KPM, Brandt M, Shanks R. Cork–PLA composite filaments for fused deposition modelling. Composites Science and Technology. 2018;168:230-7.

[19] Mimini V, Sykacek E, Syed Hashim SNA, Holzweber J, Hettegger H, Fackler K, et al. Compatibility of Kraft lignin, Organosolv lignin and Lignosulfonate with PLA in 3D printing. Journal of Wood Chemistry and Technology. 2019;39(1):14-30.

[20] Petchwattana N, Covavisaruch S. Mechanical and morphological properties of wood plastic biocomposites prepared from toughened poly (lactic acid) and

rubber wood sawdust (Hevea brasiliensis). Journal of Bionic Engineering. 2014;11(4):630-7.

[21] Dou Q, Cai J. Investigation on polylactide (PLA)/poly(butylene adipate-co-terephthalate) (PBAT)/bark flour of plane tree (PF) eco-composites. Materials. 2016;9(5):393.

[22] Ayrilmis N, Kariž M, Kitek Kuzman M. Effect of wood flour content on surface properties of 3D printed materials produced from wood flour/PLA filament. International Journal of Polymer Analysis and Characterization. 2019;24(7):659-66.

[23] Dimitrov D, Schreve K, de Beer N. Advances in three dimensional printing-state of the art and future perspectives. Rapid Prototyping Journal. 2006;12(3):136-47.

[24] Xu P, Hu M, Li N, Gao X. Magnetic controlled variable diameter nozzle for wood powder 3D printer. Revista Tecnica De La Facultad De Ingenieria Universidad Del Zulia. 2016;39(8):77-84.

[25] Wong KV, Hernandez A. A review of additive manufacturing. ISRN Mechanical Engineering. 2012;2012:1-10.

[26] Wang X, Jiang M, Zhou Z, Gou J, Hui D. 3D printing of polymer matrix composites: A review and prospective. Composites Part B: Engineering. 2017;110:442-58.

[27] Wei X, Li D, Jiang W, Gu Z, Wang X, Zhang Z, et al. 3D printable graphene composite. Sci Rep. 2015;5:11181.

[28] Chen Q, Mangadlao JD, Wallat J, De Leon A, Pokorski JK, Advincula RC. 3D printing biocompatible polyurethane/poly(lactic acid)/graphene oxide nanocomposites: Anisotropic properties. ACS Appl Mater Interfaces. 2017;9(4):4015-23.

[29] Zhou X, Nowicki M, Cui H, Zhu W, Fang X, Miao S, et al. 3D bioprinted graphene oxide-incorporated matrix for promoting chondrogenic differentiation of human bone marrow mesenchymal stem cells. Carbon. 2017;116:615-24.

[30] Wang L, Ni X. The effect of the inorganic nanomaterials on the UV-absorption, rheological and mechanical properties of the rapid prototyping epoxy-based composites. Polymer Bulletin. 2017;74(6):2063-79.

[31] Gallardo A, Pereyra Y, Martinez-Campos E, Garcia C, Salavagione HJ. Facile one-pot exfoliation and integration of 2D layered materials by dispersion in a photocurable polymer precursor. Nanoscale. 2017;9(30):10590.

[32] Shuai C, Feng P, Gao C, Shuai X, Xiao T, Peng S. Graphene oxide reinforced poly(vinyl alcohol): nanocomposite scaffolds for tissue engineering applications. RSC Advances. 2015;5(32):25416-23.

[33] Gaikwad S, Tate JS, Theodoropoulou N, Koo JH. Electrical and mechanical properties of PA11 blended with nanographene platelets using industrial twin-screw extruder for selective laser sintering. Journal of Composite Materials. 2013;47(23):2973-86.

[34] Utela B, Storti D, Anderson R, Ganter M. A review of process development steps for new material systems in three dimensional printing (3DP). Journal of Manufacturing Processes. 2008;10(2):96-104.

[35] Egham UK. Gartner survey reveals that high acquisition and start-up costs are delaying investment in 3D printers. Gartner; 2014.

[36] Kroll E, Artzi D. Enhancing aerospace engineering students' learning with 3D printing wind‐tunnel models. Rapid Prototyping Journal. 2011;17(5):393-402.

[37] Murphy SV, Atala A. 3D bioprinting of tissues and organs. Nat Biotechnol. 2014;32(8):773-85.

[38] Tao Y, Wang H, Li Z, Li P, Shi SQ. Development and application of wood flour-filled polylactic acid composite filament for 3D Printing. Materials. 2017;10(4):339.

[39] Tranchard S, Rojas V. Manufacturing our 3D future. 2015.

[40] Wohlers T. 3D printing and additive manufacturing state of the industry annual worldwide progress report Wohlers Report. 2019.

[41] Lipson H, Kurman M. Fabricated the new world of 3D printing: the promise and peril of a machine that can make (almost) anything. 2013.

[42] Yu WW, Zhang J, Wu JR, Wang XZ, Deng YH. Incorporation of graphitic nano‐filler and poly(lactic acid) in fused deposition modeling. Journal of Applied Polymer Science. 2017;134(15):1-11.

[43] Mello CHP, Martins RC, Parra BR, Pamplona ED, Salgado EG, Seguso RT. Systematic proposal to calculate price of prototypes manufactured through

rapid prototyping an FDM 3D printer in a university lab. Rapid Prototyping Journal. 2010;16(6):411-6.

[44] Liu XH, Li SP, Liu Z, Zheng XH, Chen XH, Wang ZB. An investigation on distortion of PLA thin-plate part in the FDM process. Int J Adv Manuf Technol. 2015;79(5-8):1117-26.

[45] Carneiro OS, Silva AF, Gomes R. Fused deposition modeling with polypropylene. Materials & Design. 2015;83:768-76.

[46] Yan YN, Zhang RJ, Hong GD, Yuan XM. Research on the bonding of material paths in melted extrusion modeling. Materials & Design. 2000;21(2):93-9.

[47] Zhao D, Cai X, Shou G, Gu Y, Wang P. Study on the preparation of bamboo plastic composite intend for additive manufacturing. Key Engineering Materials. 2016;667:250-8.

[48] Auras R, Lim L-T, Selke SEM, Tsuji H. Poly (lactic acid): synthesis, structures, properties, processing, and applications: John Wiley & Sons; 2011.

[49] Lim LT, Auras R, Rubino M. Processing technologies for poly(lactic acid). Progress in Polymer Science. 2008;33(8):820-52.

[50] Ray SS, Yamada K, Okamoto M, Ueda K. Polylactide-layered silicate nanocomposite: a novel biodegradable material. Nano letters. 2002;2(10):1093-6.

[51] Pang X, Zhuang X, Tang Z, Chen X. Polylactic acid (PLA): research, development and industrialization. Biotechnol J. 2010;5(11):1125-36.

[52] Pakkanen J, Manfredi D, Minetola P, Iuliano L. About the use of recycled or biodegradable filaments for sustainability of 3D printing. 2017;68:776-85.

[53] Tymrak BM, Kreiger M, Pearce JM. Mechanical properties of components fabricated with open-source 3-D printers under realistic environmental conditions. Materials & Design. 2014;58:242-6.

[54] Hsu SH, Yen HJ, Tseng CS, Cheng CS, Tsai CL. Evaluation of the growth of chondrocytes and osteoblasts seeded into precision scaffolds fabricated by fused deposition manufacturing. J Biomed Mater Res B Appl Biomater. 2007;80(2):519-27.

[55] Cohn D, Salomon AH. Designing biodegradable multiblock PCL/PLA thermoplastic elastomers. Biomaterials. 2005;26(15):2297-305.

[56] Ochi S. Mechanical properties of kenaf fibers and kenaf/PLA composites. Mechanics of Materials. 2008;40(4-5):446-52.

[57] Vatansever E, Arslan D, Nofar M. Polylactide cellulose-based nanocomposites. Int J Biol Macromol. 2019;137:912-38.

[58] Gardan J, Roucoules L. 3D printing device for numerical control machine and wood deposition. International Journal of Engineering Research and Applications. 2014;4(12):123-31.

[59] Oksman K, Skrifvars M, Selin JF. Natural fibres as reinforcement in polylactic acid (PLA) composites. Composites Science and Technology. 2003;63(9):1317-24.

[60] Akato K, Tran CD, Chen J, Naskar AK. Poly(ethylene oxide)-assisted macromolecular self-assembly of lignin in ABS matrix for sustainable composite applications. ACS Sustainable Chemistry & Engineering. 2015;3(12):3070-6.

[61] McKendry P. Energy production from biomass (part 1): overview of biomass. Bioresource Technology. 2002;83:37-46.

[62] Yang H, Yan R, Chen H, Zheng C, Lee DH, Liang DT. In-depth investigation of biomass pyrolysis based on three major components: hemicellulose, cellulose and lignin. Energy & Fuels. 2006;20(1):388-93.

[63] Qian S, Tao Y, Ruan Y, Fontanillo Lopez CA, Xu L. Ultrafine bamboo-char as a new reinforcement in poly(lactic acid)/bamboo particle biocomposites: the effects on mechanical, thermal, and morphological properties. Journal of Materials Research. 2018;33(22):3870-9.

[64] Lee S-H, Wang S. Biodegradable polymers/bamboo fiber biocomposite with bio-based coupling agent. Composites Part A: Applied Science and Manufacturing. 2006;37(1):80-91.

[65] Tsou C-Y, Wu C-L, Tsou C-H, Chiu S-H, Suen M-C, Hung W-S. Biodegradable composition of poly(lactic acid) from renewable wood flour. Polymer Science Series B. 2015;57(5):473-80.

[66] Zhao X, Tekinalp H, Meng X, Ker D, Benson B, Pu Y, et al. Poplar as biofiber reinforcement in composites for large-scale 3D printing. ACS Applied Bio Materials. 2019;2(10):4557-70.

[67] Tisserat B, Joshee N, Mahapatra AK, Selling GW, Finkenstadt VL. Physical and mechanical properties of extruded poly(lactic acid)-based Paulownia elongata biocomposites. Industrial Crops and Products. 2013;44:88-96.

[68] Khan BA, Na H, Chevali V, Warner P, Zhu J, Wang H. Glycidyl methacrylate-compatibilized poly(lactic acid)/hemp hurd biocomposites: Processing, crystallization, and thermo-mechanical response. Journal of Materials Science & Technology. 2018;34(2):387-97.

[69] Khan BA, Chevali VS, Na H, Zhu J, Warner P, Wang H. Processing and properties of antibacterial silver nanoparticle-loaded hemp hurd/poly(lactic acid) biocomposites. Composites Part B: Engineering. 2016;100:10-8.

[70] Stoof D, Pickering K, Zhang Y. Fused deposition modelling of natural fibre/polylactic acid composites. Journal of Composites Science. 2017;1(1):8.

[71] Goriparthi BK, Suman KNS, Nalluri MR. Processing and characterization of jute fiber reinforced hybrid biocomposites based on polylactide/polycaprolactone blends. Polymer Composites. 2012;33(2):237-44.

[72] Kariz M, Sernek M, Obućina M, Kuzman MK. Effect of wood content in FDM filament on properties of 3D printed parts. Materials Today Communications. 2018;14:135-40.

[73] Filgueira D, Holmen S, Melbø JK, Moldes D, Echtermeyer AT, Chinga-Carrasco G. Enzymatic-assisted modification of thermomechanical pulp fibers to improve the interfacial adhesion with poly(lactic acid) for 3D printing. ACS Sustainable Chemistry & Engineering. 2017;5(10):9338-46.

[74] Tanase-Opedal M, Espinosa E, Rodriguez A, Chinga-Carrasco G. Lignin: A biopolymer from forestry biomass for biocomposites and 3D printing. Materials. 2019;12(18):3006.

[75] Khan BA. Development of Antibacterial Hemp Hurd/Poly(Lactic Acid) Biocomposite for Food Packaging: University of Southern Queensland; 2017.

[76] Chun KS, Husseinsyah S, Osman H. Mechanical and thermal properties of coconut shell powder filled polylactic acid biocomposites: effects of the filler content and silane coupling agent. Journal of Polymer Research. 2012;19(5):9859.

[77] Petinakis E, Yu L, Edward G, Dean K, Liu H, Scully AD. Effect of matrix–particle interfacial adhesion on the mechanical properties of poly(lactic

acid)/wood-flour micro-composites. Journal of Polymers and the Environment. 2009;17(2):83-94.

[78] Orue A, Jauregi A, Unsuain U, Labidi J, Eceiza A, Arbelaiz A. The effect of alkaline and silane treatments on mechanical properties and breakage of sisal fibers and poly(lactic acid)/sisal fiber composites. Composites Part A: Applied Science and Manufacturing. 2016;84:186-95.

[79] Huda MS, Drzal LT, Misra M, Mohanty AK. Wood-fiber-reinforced poly(lactic acid) composites: Evaluation of the physicomechanical and morphological properties. Journal of Applied Polymer Science. 2006;102(5):4856-69.

[80] Pilla S, Gong S, O'Neill E, Rowell RM, Krzysik AM. Polylactide ‐ pine wood flour composites. Polymer Engineering & Science. 2008;48(3):578-87.

[81] Shah BL, Selke SE, Walters MB, Heiden PA. Effects of wood flour and chitosan on mechanical, chemical, and thermal properties of polylactide. Polymer Composites. 2008;29(6):655-63.

[82] Bax B, Müssig J. Impact and tensile properties of PLA/Cordenka and PLA/flax composites. Composites Science and Technology. 2008;68(7-8):1601-7.

[83] Qiang T, Yu DM, Gao HH. Wood flour/polylactide biocomposites toughened with polyhydroxyalkanoates. Journal of Applied Polymer Science. 2012;124(3):1831-9.

[84] Sawpan MA, Pickering KL, Fernyhough A. Improvement of mechanical performance of industrial hemp fibre reinforced polylactide biocomposites. Composites Part A: Applied Science and Manufacturing. 2011;42(3):310-9.

[85] Magalhães dS, Sara P., Lima PS, Oliveira JM. Rheological behaviour of cork-polymer composites for injection moulding. Composites Part B: Engineering. 2016;90:172-8.

[86] Petchwattana N, Covavisaruch S. Effects of rice hull particle size and content on the mechanical properties and visual appearance of wood plastic composites prepared from poly(vinyl chloride). Journal of Bionic Engineering. 2013;10(1):110-7.

[87] Luddee M, Pivsa-Art S, Sirisansaneeyakul S, Pechyen C. Particle size of ground bacterial cellulose affecting mechanical, thermal, and moisture barrier properties of PLA/BC biocomposites. Energy Procedia. 2014;56:211-8.

[88] Depuydt D, Balthazar M, Hendrickx K, Six W, Ferraris E, Desplentere F, et al. Production and characterization of bamboo and flax fiber reinforced polylactic acid filaments for fused deposition modeling (FDM). Polymer Composites. 2018:24971.

[89] Li L, Liu D, Chen Z. Effect of particle diameter of wood flour on the properties of wood-plastics composite. Modern plastics processing and applications. 2005;17(5):21-4.

[90] Stark NM, Rowlands RE. Effects of wood fiber characteristics on mechanical properties of wood/polypropylene composites. Wood and fiber science. 2003;35(2):167-74.

[91] Koronis G, Silva A, Fontul M. Green composites: A review of adequate materials for automotive applications. Composites Part B: Engineering. 2013;44(1):120-7.

[92] Mazzanti V, Malagutti L, Mollica F. FDM 3D printing of polymers containing natural fillers: A review of their mechanical properties. Polymers. 2019;11(7):1094.

[93] Jay ML. The 3-D Printing Boom. Composites manufacturing; 2017.

[94] Xie G, Zhang Y, Lin W. Plasticizer combinations and performance of wood flour–poly(lactic acid) 3D printing filaments. BioResources. 2017;12(3):6736-48.

[95] Wimmer R, Steyrer B, Woess J, Koddenberg T, Mundigler N. 3D printing and wood. International Conference “Wood Science and Engineering in the Third Millunnium”. 2015:145-50.

[96] Tisserat B, Liu Z, Finkenstadt V, Lewandowski B, Ott S, Reifschneider L. 3D printing bicomposites. Plastics Resarch Online. 2015:1-3.

[97] Shin YJ, Yun HJ, Lee EJ, Chung WY. A study on the development of bamboo/PLA bio-composites for 3D printer filament. J Korean Wood Sci Techno. 2018;46:107-13.

[98] Liu H, He H, Peng X, Huang B, Li J. Three-dimensional printing of poly(lactic acid) bio-based composites with sugarcane bagasse fiber: Effect of printing orientation on tensile performance. Polymers for Advanced Technologies. 2019;30(4):910-22.

[99] Ayrilmis N, Kariz M, Kwon JH, Kitek Kuzman M. Effect of printing layer thickness on water absorption and mechanical properties of 3D-printed wood/PLA composite materials. The International Journal of Advanced Manufacturing Technology. 2019;102(5-8):2195-200.

[100] Ayrilmis N. Effect of layer thickness on surface properties of 3D printed materials produced from wood flour/PLA filament. Polymer Testing. 2018;71:163-6.

[101] Pop MA, Croitoru C, Bedő T, Geamăn V, Radomir I, Cosnită M, et al. Structural changes during 3D printing of bioderived and synthetic thermoplastic materials. Journal of Applied Polymer Science. 2019;136(17):47382.

[102] Tokoro R, Vu DM, Okubo K, Tanaka T, Fujii T, Fujiura T. How to improve mechanical properties of polylactic acid with bamboo fibers. Journal of Materials Science. 2007;43(2):775-87.

[103] Rahman MA, De Santis D, Spagnoli G, Ramorino G, Penco M, Phuong VT, et al. Biocomposites based on lignin and plasticized poly(L-lactic acid). Journal of Applied Polymer Science. 2013;129(1):202-14.

[104] Yu T, Li Y. Influence of poly(butylenes adipate-co-terephthalate) on the properties of the biodegradable composites based on ramie/poly(lactic acid). Compos Pt A-Appl Sci Manuf. 2014;58:24-9.

[105] Xiao X. Study on mechanical properties of two kinds of impact modifiers toughening PLA. Plastics science and technology. 2014;42(8):88-90.

[106] Xiao X, Duan q. Study on toughening modification of PBC with PLA. Plastic Additives. 2016(3):63-6.

[107] Hao M, Wu H, Zhu Z. In situ reactive interfacial compatibilization of polylactide/sisal fiber biocomposites via melt-blending with an epoxy-functionalized terpolymer elastomer. RSC Adv. 2017;7(51):32399-412.

[108] Wu N, Zhang H. Mechanical properties and phase morphology of super-tough PLA/PBAT/EMA-GMA multicomponent blends. Materials Letters. 2017;192:17-20.

[109] Kumar M, Mohanty S, Nayak SK, Rahail Parvaiz M. Effect of glycidyl methacrylate (GMA) on the thermal, mechanical and morphological property

of biodegradable PLA/PBAT blend and its nanocomposites. Bioresour Technol. 2010;101(21):8406-15.

[110] Xiao X, Chevali VS, Wang H. Toughening of polylactide/bamboo powder biocomposite for 3D printing. ICCM22 proceedings. 2019.

[111] Li W, Zhang Y, Wu D, Li Z, Zhang H, Dong L, et al. The effect of core-shell ratio of acrylic impact modifier on toughening PLA. Advances in Polymer Technology. 2015:21632.

[112] Jiang L, Wolcott MP, Zhang J. Study of biodegradable polylactide/ poly(butylene adipate-co-terephthalate) blends. Biomacromolecules. 2006 (7):199-207.

[113] Wang Y-n, Weng Y-x, Wang L. Characterization of interfacial compatibility of polylactic acid and bamboo flour (PLA/BF) in biocomposites. Polymer Testing. 2014;36:119-25.

[114] Bin Y, Yang B, Wang H. The effect of a small amount of modified microfibrillated cellulose and ethylene–glycidyl methacrylate copolymer on the crystallization behaviors and mechanical properties of polylactic acid. Polymer Bulletin. 2017;75(8):3377-94.

[115] Ferri JM, Fenollar O, Jorda-Vilaplana A, García-Sanoguera D, Balart R. Effect of miscibility on mechanical and thermal properties of poly(lactic acid)/ polycaprolactone blends. Polymer International. 2016;65(4):453-63.

[116] Sarazin P, Li G, Orts WJ, Favis BD. Binary and ternary blends of polylactide, polycaprolactone and thermoplastic starch. Polymer. 2008;49(2):599-609.

[117] Zhang C, Zhai T, Turng L-S, Dan Y. Morphological, mechanical, and crystallization behavior of polylactide/polycaprolactone blends compatibilized by l-lactide/caprolactone copolymer. Industrial & Engineering Chemistry Research. 2015;54(38):9505-11.

[118] Bai H, Xiu H, Gao J, Deng H, Zhang Q, Yang M, et al. Tailoring Impact Toughness of Poly(l-lactide)/Poly(ε-caprolactone) (PLLA/PCL) Blends by Controlling Crystallization of PLLA Matrix. ACS Applied Materials & Interfaces. 2012;4(2):897-905.

[119] López-Rodríguez N, López-Arraiza A, Meaurio E, Sarasua JR. Crystallization, morphology, and mechanical behavior of polylactide/poly(ε-caprolactone) blends. Polymer Engineering & Science. 2006;46(9):1299-308.

[120] Harada M, Iida K, Okamoto K, Hayashi H, Hirano K. Reactive compatibilization of biodegradable poly(lactic acid)/poly(ε-caprolactone) blends with reactive processing agents. Polymer Engineering & Science. 2008;48(7):1359-68.

[121] Vilay V, Mariatti M, Ahmad Z, Pasomsouk K, Todo M. Characterization of the mechanical and thermal properties and morphological behavior of biodegradable poly(L-lactide)/poly(ε-caprolactone) and poly(L-lactide)/poly(butylene succinate-co-L-lactate) polymeric blends. Journal of Applied Polymer Science. 2009;114(3):1784-92.

[122] Xiao X, Chevali VS, Song P, He D, Wang H. Polylactide/hemp hurd biocomposites as sustainable 3D printing feedstock. Composites Science and Technology. 2019;184:107887.

[123] Wu D, Zhang Y, Zhang M, Zhou W. Phase behavior and its viscoelastic response of polylactide/poly(ε-caprolactone) blend. European Polymer Journal. 2008;44(7):2171-83.

[124] Simões CL, Viana JC, Cunha AM. Mechanical properties of poly(ε-caprolactone) and poly(lactic acid) blends. Journal of Applied Polymer Science. 2009;112(1):345-52.

[125] Maglio G, Migliozzi A, Palumbo R, Immirzi B, Volpe MG. Compatibilized poly (ϵ ‐ caprolactone)/poly (l ‐ lactide) blends for biomedical uses. Macromolecular rapid communications. 1999;20(4):236-8.

[126] Choi N-S, Kim C-H, Cho KY, Park J-K. Morphology and hydrolysis of PCL/PLLA blends compatibilized with P(LLA-co-ϵCL) or P(LLA-b-ϵCL). Journal of Applied Polymer Science. 2002;86(8):1892-8.

[127] Zhang C, Lan Q, Zhai T, Nie S, Luo J, Yan W. Melt crystallization behavior and crystalline morphology of polylactide/poly(epsilon-caprolactone) blends compatibilized by lactide-caprolactone copolymer. Polymers. 2018;10:1181.

[128] Choi N-S, Kim C-H, Cho KY, Park J-K. Effect of P(lLA-co-εCL) on the compatibility and crystallization behavior of PCL/PLLA Blends. Journal of Applied Polymer Science. 1999;77:226-31.

[129] Sun Y, He C. Biodegradable “Core–Shell” rubber nanoparticles and their toughening of poly(lactides). Macromolecules. 2013;46(24):9625-33.

[130] Ye S, Ting Lin T, Weei Tjiu W, Kwan Wong P, He C. Rubber toughening of poly(lactic acid): Effect of stereocomplex formation at the rubber-matrix interface. Journal of Applied Polymer Science. 2013;128(4):2541-7.

[131] Ning Z, Liu J, Jiang N, Gan Z. Enhanced crystallization rate and mechanical properties of poly(l-lactic acid) by stereocomplexation with four-armed poly(ϵ-caprolactone)-block-poly(d-lactic acid) diblock copolymer. Polymer International. 2017;66(6):968-76.

[132] Jing Z, Shi X, Zhang G, Lei R. Investigation of poly(lactide) stereocomplexation between linear poly(L-lactide) and PDLA-PEG-PDLA tri-block copolymer. Polymer International. 2015;64(10):1399-407.

[133] Tsuji H, Yamada T, Suzuki M, Itsuno S. Part 7. Effects of poly(L-lactide-co-ε-caprolactone) on morphology, structure, crystallization, and physical properties of blends of poly(L-lactide) and poly(ε-caprolactone). Polymer International. 2003;52(2):269-75.

[134] Wang X, Peng S, Chen H, Yu X, Zhao X. Mechanical properties, rheological behaviors, and phase morphologies of high-toughness PLA/PBAT blends by in-situ reactive compatibilization. Composites Part B: Engineering. 2019;173:107028.

[135] Liu S, Ge L, Gao S, Zhuang L, Zhu Z, Wang H. Activated carbon derived from bio-waste hemp hurd and retted hemp hurd for CO2 adsorption. Composites Communications. 2017;5:27-30.

[136] Stevulova N, Cigasova J, Estokova A, Terpakova E, Geffert A, Kacik F, et al. Properties characterization of chemically modified hemp hurds. Materials (Basel). 2014;7(12):8131-50.

[137] Li X, Xiao R, Morrell JJ, Zhou X, Du G. Improving the performance of hemp hurd/polypropylene composites using pectinase pre-treatments. Industrial Crops and Products. 2017;97:465-8.

[138] Jain S, Kumar R, Jindal UC. Mechanical behaviour of bamboo and bamboo composite. Journal of Materials Science. 1992;27(17):4598-604.

[139] Yang T-C. Effect of extrusion temperature on the physico-mechanical properties of unidirectional wood fiber-reinforced polylactic acid composite (WFRPC) components using fused deposition modeling. Polymers. 2018;10(9):976.

[140] Shenoy AV, Saini DR. Thermoplastic melt rheology and processing: CRC Press; 1996.

[141] Shi Y-D, Zhang K, Chen Y-F, Zeng J-B, Wang M. New approach to morphological control for polypropylene/polyethylene blends via magnetic self-organization. Materials & Design. 2017;117:24-36.

[142] Essabir H, Bensalah MO, Rodrigue D, Bouhfid R, Qaiss Ael K. Biocomposites based on Argan nut shell and a polymer matrix: Effect of filler content and coupling agent. Carbohydr Polym. 2016;143:70-83.

[143] Le Duigou A, Castro M, Bevan R, Martin N. 3D printing of wood fibre biocomposites: From mechanical to actuation functionality. Materials & Design. 2016;96:106-14.

[144] Turner BN, Gold SA. A review of melt extrusion additive manufacturing processes: II. Materials, dimensional accuracy, and surface roughness. Rapid Prototyping Journal. 2015;21(3):250-61.

[145] Choi Y-H, Kim C-M, Jeong H-S, Youn J-H. Influence of bed temperature on heat shrinkage shape error in FDM additive manufacturing of the ABS-engineering plastic. World Journal of Engineering and Technology. 2016;04(03):186-92.

[146] Stevulova N, Kidalova L, Cigasova J, Junak J, Sicakova A, Terpakova E. Lightweight composites containing hemp hurds. Procedia Engineering. 2013;65:69-74.

[147] Patience GS. Chapter 9 - Analysis of solids and powders. In: Patience GS, editor. Experimental Methods and Instrumentation for Chemical Engineers. Amsterdam: Elsevier; 2013. p. 307-51.

[148] Guen MJL, Hill S, Smith D, Theobald B, Gaugler E, Barakat A, et al. Influence of rice husk and wood biomass properties on the manufacture of filaments for fused deposition modeling. Front Chem. 2019;7:735.

[149] Stevulova N, Estokova A, Cigasova J, Schwarzova I, Kacik F, Geffert A. Thermal degradation of natural and treated hemp hurds under air and nitrogen atmosphere. Journal of Thermal Analysis and Calorimetry. 2017;128(3):1649-60.

[150] Bahari SA, Grigsby W, Krause A. Thermal stability of processed PVC/bamboo blends: effect of compounding procedures. European Journal of Wood and Wood Products. 2017;75(2):147-59.

[151] Huang M-H, Li S, Vert M. Synthesis and degradation of PLA–PCL–PLA triblock copolymer prepared by successive polymerization of ε-caprolactone and dl-lactide. Polymer. 2004;45(26):8675-81.

[152] Li C, He Z, Wu y, al e. Preparation and properties of PLA/PBAT blends modified with compatibilizer. China plastics industry. 2018;46(1):24-8, 70.

[153] Ding Y, Lu B, Wang P, Wang G, Ji J. PLA-PBAT-PLA tri-block copolymers: Effective compatibilizers for promotion of the mechanical and rheological properties of PLA/PBAT blends. Polymer Degradation and Stability. 2018;147:41-8.

[154] Sun Z, Zhang B, Bian X, Feng L, Zhang H, Duan R, et al. Synergistic effect of PLA–PBAT–PLA tri-block copolymers with two molecular weights as compatibilizers on the mechanical and rheological properties of PLA/PBAT blends. RSC Advances. 2015;5(90):73842-9.

[155] Jeon JS, Han DH, Shin BY. Improvements in the rheological properties, impact strength, and the biodegradability of PLA/PCL blend compatibilized by electron-beam irradiation in the presence of a reactive agent. Advances in Materials Science and Engineering. 2018;2018:1-8.

[156] Finotti PFM, Costa LC, Chinelatto MA. Effect of the chemical structure of compatibilizers on the thermal, mechanical and morphological properties of immiscible PLA/PCL blends. Macromolecular Symposia. 2016;368(1):24-9.

[157] Xiang S, Feng L, Bian X, Zhang B, Sun B, Liu Y, et al. Toughening modification of PLLA with PCL in the presence of PCL-b-PLLA diblock copolymers as compatibilizer. Polymers for Advanced Technologies. 2019;30(4):963-72.

[158] Liu Z, Luo Y, Bai H, Zhang Q, Fu Q. Remarkably enhanced impact toughness and heat resistance of poly(l -lactide)/thermoplastic polyurethane blends by constructing stereocomplex crystallites in the matrix. ACS Sustainable Chemistry and Engineering 2016;4(1):111-20.

[159] Liu Y, Shao J, Sun J, Bian X, Feng L, Xiang S, et al. Improved mechanical and thermal properties of PLLA by solvent blending with PDLA-b-PEG-b-PDLA. Polymer Degradation and Stability. 2014;101:10-7.

[160] Dell'Erba R, Groeninckx G, Maglio G, Malinconico M, Migliozzi A. Immiscible polymer blends of semicrystalline biocompatible components: thermal properties and phase morphology analysis of PLLA/PCL blends. Polymer. 2001;42(18):7831-40.

[161] Hu M, Deng C, Gu X, Fu Q, Zhang J. Manipulating the strength–toughness balance of poly(l-lactide) (PLLA) via introducing ductile poly(ε-caprolactone) (PCL) and strong shear flow. Industrial & Engineering Chemistry Research. 2020;59(2):1000-9.

[162] Nguyen NA, Barnes, S.H., Bowland, C.C., Meek, K.M., Littrell, K.C., Keum, J.K. and Naskar, A.K. A path for lignin valorization via additive manufacturing of high-performance sustainable composites with enhanced 3D printability. Science advances. 2018;4(12):eaat4967.

[163] Alzahrani M. Modification of recycled poly(ethylene terephthalate) for FDM 3D-printing applications: The University of Waterloo; 2017.

[164] Gupta A, Simmons W, Schueneman GT, Hylton D, Mintz EA. Rheological and thermo-mechanical properties of poly(lactic acid)/lignin-coated cellulose nanocrystal composites. ACS Sustainable Chemistry & Engineering. 2017;5(2):1711-20.

[165] Freire E, Bianchi O, Monteiro EEC, Reis Nunes RC, Forte MC. Processability of PVDF/PMMA blends studied by torque rheometry. Materials Science and Engineering: C. 2009;29(2):657-61.

[166] Krishnan S, Pandey P, Mohanty S, Nayak SK. Toughening of polylactic acid: An overview of research progress. Polymer-Plastics Technology and Engineering. 2015;55(15):1623-52.

[167] Feng J, Sun Y, Song P, Lei W, Wu Q, Liu L, et al. Fire-resistant, strong, and green polymer nanocomposites based on poly(lactic acid) and core–shell nanofibrous flame retardants. ACS Sustainable Chemistry & Engineering. 2017;5(9):7894-904.

[168] García NL, Lamanna M, D'Accorso N, Dufresne A, Aranguren M, Goyanes S. Biodegradable materials from grafting of modified PLA onto starch nanocrystals. Polymer Degradation and Stability. 2012;97(10):2021-6.

[169] Das O, Sarmah AK, Bhattacharyya D. Biocomposites from waste derived biochars: Mechanical, thermal, chemical, and morphological properties. Waste Manag. 2016;49:560-70.

[170] Nizamuddin S, Jadhav A, Qureshi SS, Baloch HA, Siddiqui MTH, Mubarak NM, et al. Synthesis and characterization of polylactide/rice husk hydrochar composite. Sci Rep. 2019;9(1):5445.

[171] Cao Z, Pan H, Chen Y, Han L, Bian J, Zhang H, et al. Ductile and biodegradable poly (lactic acid) matrix film with layered structure. Int J Biol Macromol. 2019;137:1141-52.

[172] Tian X, Liu T, Yang C, Wang Q, Li D. Interface and performance of 3D printed continuous carbon fiber reinforced PLA composites. Composites Part A: Applied Science and Manufacturing. 2016;88:198-205.

[173] Kamal MR, Khoshkava V. Effect of cellulose nanocrystals (CNC) on rheological and mechanical properties and crystallization behavior of PLA/CNC nanocomposites. Carbohydr Polym. 2015;123:105-14.

[174] Essabir H, Achaby MEI, Hilali EIM, Bouhfid R, Qaiss A. Morphological, structural, thermal and tensile properties of high density polyethylene composites reinforced with treated argan nut shell particles. Journal of Bionic Engineering. 2015;12(1):129-41.

[175] Shi Y, Cheng Y, Chen Y, Zhang K, Zeng J, Wang M. Morphology, rheological and crystallization behavior in thermoplastic polyurethane toughed poly(l-lactide) with stereocomplex crystallites. Polymer Testing. 2017;62:1-12.

[176] Zhang Y, Song Pa, Fu S, Chen F. Morphological structure and mechanical properties of epoxy/polysulfone/cellulose nanofiber ternary nanocomposites. Composites Science and Technology. 2015;115:66-71.

[177] Yakubu MK, Gumel MS, Umar A, Metelerkamp R. Physico-mechanical effects of surface-modified sorgum stalk powder on reinforced rubber. Journal of Reinforced Plastics and Composites. 2010;29(18):2855-68.

[178] Xu W, Pranovich A, Uppstu P, Wang X, Kronlund D, Hemming J, et al. Novel biorenewable composite of wood polysaccharide and polylactic acid for three dimensional printing. Carbohydr Polym. 2018;187:51-8.

[179] Chevali VS, Nerenz BA, Ulven CA. Acrylonitrile butadiene styrene (ABS)/lignocellulosic fiber biocomposite: Effect of artificial weathering on impact properties. Journal of Biobased Materials and Bioenergy. 2012;6(1):42-50.

[180] Sang L, Han S, Li Z, Yang X, Hou W. Development of short basalt fiber reinforced polylactide composites and their feasible evaluation for 3D printing applications. Composites Part B: Engineering. 2019;164:629-39.

[181] Gamon G, Evon P, Rigal L. Twin-screw extrusion impact on natural fibre morphology and material properties in poly(lactic acid) based biocomposites. Industrial Crops and Products. 2013;46:173-85.

[182] Essabir H, Bensalah M, Rodrigue D, Bouhfid R, Qaiss A. Structural, mechanical and thermal properties of bio-based hybrid composites from waste coir residues: Fibers and shell particles. Mechanics of Materials. 2016;93:134-44.

[183] Mansouri HR, Pizzi A. Recycled micronized polyurethane powders as active extenders of UF and PF wood panel adhesives. Holz als Roh- und Werkstoff. 2007;65(4):293-9.

[184] Li Y, Dong Q, Tai Q, Gao S, Guan H, Yan W. Mechanical properties of carbon fiber composite in fused deposition modeling of additive manufacturing. Journal of Plasticity Engineering. 2017;24(3):225-30.

[185] Xia X, Lin H, Yang S, Huang B, Qian Q, Chen Q, et al. Influence of fused deposition modeling processing parameters on impact properties of modified poly(lactic acid). Polymer Materials Science and Engineering. 2019;35(5):88-93.

[186] Benwood C, Anstey A, Andrzejewski J, Misra M, Mohanty AK. Improving the impact strength and heat resistance of 3D printed models: structure, property, and processing correlationships during fused deposition modeling (FDM) of poly(lactic acid). ACS Omega. 2018;3(4):4400-11

[187] Wang L, Gramlich WM, Gardner DJ. Improving the impact strength of poly(lactic acid) (PLA) in fused layer modeling (FLM). Polymer. 2017;114:242-8.

[188] Vasudevarao B, Natarajan DP, Henderson M, Razdan A. Sensitivity of RP surface finish to process parameter variation. Proceedings of solid free form fabrication. 2000:252-8.

[189] Hartcher-O'Brien J, Evers J, Tempelman E. Surface roughness of 3D printed materials: Comparing physical measurements and human perception. Materials Today Communications. 2019;19:300-5.

[190] Kang B, Hyeon J, So H. Facile microfabrication of 3-dimensional (3D) hydrophobic polymer surfaces using 3D printing technology. Applied Surface Science. 2020;499:143733.

[191] R. Anitha, S. Arunachalam, Radhakrishnan P. Critical parameters influencing the quality of prototypes in fused deposition modelling. Journal of Materials Processing Technology. 2001;118:385-8.

[192] Singh R, Singh S, Singh IP, Fabbrocino F, Fraternali F. Investigation for surface finish improvement of FDM parts by vapor smoothing process. Composites Part B: Engineering. 2017;111:228-34.

[193] Galantucci LM, Lavecchia F, Percoco G. Experimental study aiming to enhance the surface finish of fused deposition modeled parts. CIRP Annals - Manufacturing Technology. 2009;58(1):189-92.

[194] Hristov V, Vlachopoulos J. Effects of polymer molecular weight and filler particle size on flow behavior of wood polymer composites. Polymer Composites. 2008;29(8):831-9.

[195] Nagarajan V, Mohanty AK, Misra M. Biocomposites with size-fractionated biocarbon: Influence of the microstructure on macroscopic properties. ACS Omega. 2016;1(4):636-47.

[196] Han CD, Kim J. Rheological technique for determining the order–disorder transition of block copolymers. Journal of Polymer Science Part B: Polymer Physics. 1987;25(8):1741-64.

[197] Chaitanya S, Singh I, Song JI. Recyclability analysis of PLA/Sisal fiber biocomposites. Composites Part B: Engineering. 2019;173:106895.

[198] Scaffaro R, Lopresti F, Botta L. PLA based biocomposites reinforced with Posidonia oceanica leaves. Composites Part B: Engineering. 2018;139:1-11.

[199] Plessis Ad. Effects of process parameters on porosity in laser powder bed fusion revealed by X-ray tomography. Additive Manufacturing. 2019;30:100871.

[200] Pan Q, Yao Z, Zhou J, Zhou C, Zhang Y. Mechanical properties and crystall inity of wheat straw fiber/PLA composite. POLYMER MATERIALS SCIENCE AND ENGINEERING. 2012;28(8):101-4,9.

[201] Sang L, Han S, Peng X, Jian X, Wang J. Development of 3D-printed basalt fiber reinforced thermoplastic honeycombs with enhanced compressive mechanical properties. Composites Part A: Applied Science and Manufacturing. 2019;125:105518.

Appendix A

Composites Science and Technology 184 (2019) 107887

Contents lists available at ScienceDirect

Composites Science and Technology

journal homepage: http://www.elsevier.com/locate/compscitech

Polylactide/hemp hurd biocomposites as sustainable 3D printing feedstock

Xianglian Xiao [a,b,c], Venkata S. Chevali [a,*], Pingan Song [a], Dongning He [d], Hao Wang [a,b,**]

[a] Centre for Future Materials, University of Southern Queensland, Toowoomba, QLD, 4350, Australia
[b] China-Australia Institute for Advanced Materials and Manufacturing, Jiaxing University, Jiaxing, 314001, China
[c] Shenzhen Esun Industrial Co. Ltd, Shenzhen, 518057, China
[d] School of Chemistry and Chemical Engineering, Lingnan Normal University, Zhanjiang, 524048, China

ARTICLE INFO

Keywords:
Polymer-matrix composites (PMCs)
Impact behaviour
Elastic properties
Rheology
Injection moulding

ABSTRACT

Industrial hemp hurd (HH) is emerging as a bio-based filler in thermoplastic biocomposites. In this paper, HH/polylactide (PLA) biocomposites were developed as fused deposition modelling (FDM) feedstock through parametric analysis of the effects of HH loading with respect to melt flow, rheology, physical, thermo-mechanical, and mechanical properties of the biocomposites. Poly (butylene adipate-co-terephthalate) (PBAT) and ethylene-methyl acrylate-glycidyl methacrylate terpolymer (EGMA) were used as toughening and compatibilisation agents respectively in melt-compounding and extrusion to produce FDM filament. The FDM-printed standard samples were compared against corresponding injection-moulded biocomposites. The FDM filament exhibited a diameter tolerance within ±0.02 mm, and roundness variability below 0.03 mm, and the FDM-printed parts with HH loading under 30 phr showed higher impact toughness than the commercial PLA filament control. In addition, the FDM-printed samples exhibited greater dimensional accuracy with increasing HH loading.

1. Introduction

Poly (lactic acid) or polylactide (PLA) is a common filament feedstock material for fused deposition modelling (FDM) because of its environmental-friendliness, renewability, and biodegradability [1–5]. PLA melts at a relatively lower temperature, possesses higher tensile strength and elastic modulus for the printed parts over traditional petrochemical polymers [6], albeit with a lower cost-effectiveness. Biomass utilisation in FDM feedstock is potentially cost-effective and less hazardous compared to traditional plastics, and in combination with polymer can produce appearance alike wood. Wang et al. [7] developed 30 wt % micro/nanocellulose-PLA filament, with properties comparable as neat PLA. PLA filaments with 15 wt % bamboo and flax fibre [8], 5 wt % wood-flour-filled PLA [9,10], and impact-resistant cork-PLA FDM filaments [11] were also studied. Overall, a diverse range of biomass including bamboo, birch, cedar, coconut, ebony, olive, pine, and willow are utilised in commercial FDM filaments.

Industrial hemp hurd (HH) is a lignocellulosic by-product of hemp bast fibre production with no major end application, and constitutes 60 wt % – 80 wt % of the dry mass of the hemp (*Cannabis sativa*) stem [12]. Hemp hurd contains 40%–48% cellulose, 18%–24% hemicellulose and 21%–24% lignin [13], relatively higher fraction of cellulose and comparable lignin than wood, thus possessing a greater reinforcement potential [14], and emerging as a valuable substitute for wood in PLA-based blend. HH was utilised by Khan et al. [15,16] in PLA/HH biocomposites with glycidyl methacrylate (GMA) compatibilizer, resulting in increased stiffness at 20 wt % comparable to neat PLA. Overall, PLA/HH biocomposite was not explored for FDM feedstock to the knowledge of the authors.

This work aimed to produce a PLA/HH FDM filament comparable to a commercial neat PLA filament feedstock through systematic analysis of HH loading and associated filler effects. Poly (butylene adipate-co-terephthalate) (PBAT) was used as toughening agent [17–19], and ethylene-methyl acrylate-glycidyl methacrylate terpolymer (EGMA) was used as interfacial adhesion modifier [15,16,20,21]. The central objectives of this work were to (a) investigate the thermal and crystallization response to analyse feedstock properties and explain underlying mechanisms of microstructure development, and (b) parametrically investigate rheological behaviour, melt flow, filament quality, surface finish and mechanical properties of FDM-printed samples, with respect to

* Corresponding author.
** Corresponding author. University of Southern Queensland, 37 Sinnathamby Boulevard, Springfield Central, QLD, 4300, Australia.
E-mail addresses: xxlsony@hotmail.com (X. Xiao), Venkata.S.Chevali@gmail.com (V.S. Chevali), pingansong@gmail.com (P. Song), Hao.Wang@usq.edu.au (H. Wang).

https://doi.org/10.1016/j.compscitech.2019.107887
Received 2 April 2019; Received in revised form 5 September 2019; Accepted 18 October 2019
Available online 19 October 2019

injection-moulded specimens of similar composition.

2. Materials and methods

2.1. Materials

PLA (4032D) from Natureworks, LLC. (USA) was used as the base polymer along with PBAT (2003F) from Zhejiang Hangzhou Xinfu Pharm Co., Ltd. (China). EGMA (Lotader® AX 8900) from Arkema, Inc. (France) was used as the interfacial compatibilizer. Their physical and melt properties are shown in Table S1. HH chips were provided by Yunnan Dama Co., Ltd. (China), and were milled by a jet grinder and sorted using vibrating screens to obtain a volume-median-diameter of 50 μm. The physical properties of HH powder are shown in Fig. S1, which highlights the fibrillary structure of HH with an aspect ratio (l/d) of 1 to 7. An existing commercial unfilled PLA filament from Shenzhen Esun Industrial Co. Ltd, China was used as the baseline for comparison.

2.2. Preparation of biocomposite and FDM filament

The biocomposites were produced by melt-compounding and extruding PLA/PBAT (87 wt %: 13 wt %) matrices with EGMA as the compatibilizer, as (i) neat PLA/PBAT/EGMA, and (ii) PLA/PBAT/EGMA with HH loading from 10 phr to 40 phr (Table S2) on a parallel twin-screw extruder (L/D = 44, D = 35 mm). PLA, PBAT, and HH were dried for 24 h prior to processing to reduce moisture to below 0.5 wt %. The extrusion temperature was controlled at nine contiguous zones along the extruder barrel (rotational screw speed = 144 rpm) and the die, to obtain an overall temperature profile in the range of 165 °C to 175 °C. The biocomposite pellets from the aforementioned stage were extruded as filament using a 3D printing filament extrusion line with a single screw (L/D = 28, D = 35 mm). The temperatures of the five extrusion barrel zones were set at 170 °C, 175 °C, 175 °C, 180 °C and 175 °C, respectively, with a screw rotational speed of 347 rpm, through a water bath maintained at 60 °C. Using a drawing speed of 376 rpm, the FDM filaments with a formulated diameter of 1.75 mm were drawn and collected on spools. The processing steps to obtain the biocomposite filaments are shown in Fig. S2.

2.3. Test specimen preparation

The biocomposite pellets from the first extrusion stage were also injection moulded (IM) as standard specimens, i.e., tensile (166 mm × 19 mm × 3.2 mm, Type I, ASTM D 638), notched impact (63 mm × 12.7 mm × 3.2 mm, ASTM D 256), and flexural (100 mm × 12.7 mm × 3.2 mm, ASTM D 790), using an injection moulding machine (JT-350, Jintong Plastic Machinery Ltd., China). Barrel temperatures of 165 °C, 175 °C, 175 °C, and 182 °C were set for feed to die zones, and mould temperature of 45 °C was used. For FDM, 3D CAD models of the specimens were exported as stereolithographic file and fabricated on a 3D da Vinci 1.0 Professional Printer (XYZ Printing, Inc., Thailand) in a horizontal orientation, with deposition of layers in the z-direction using a nozzle diameter of 0.40 mm, as shown in Fig. S3. The nozzle temperature, heat bed temperature, infill density, layer thickness, and print velocity were set at 200 °C, 60 °C, 100%, 0.15 mm, and 60 mm/s, respectively.

2.4. Characterization

Rheological properties provide information on the viscoelastic behaviour, interfacial interaction [22] and processability of components. Shear-thinning and low viscosity are critical for enhancing flow characteristics during the 3D printing process [23]. Rheological measurements were conducted on a Discovery Hybrid Rheometer (DHR-2, TA Instruments, Inc.). Dynamic frequency sweep mode (0.01–100 Hz) was used for all samples at a strain of 1% at a constant temperature (190 °C) using a 25 mm (diameter) parallel plate geometry with 1 mm sample gap.

Thermal transition temperatures and melting characteristics of biocomposites were measured using a Q20 differential scanning calorimeter (TA Instruments, Inc.) under a nitrogen atmosphere. A cycle of heating, cooling and heating (from 20 °C to 260 °C) was used with a ramp rate of 10 °C/min. The second heating curve was used to determine the characteristic temperatures and enthalpy of the samples. The glass transition temperature (T_g), cold crystallization temperature (T_{cc}), and melting temperature (T_m) were recorded. The degree of crystallinity (X_c) of the PLA phase was calculated using Equation (1) from the second heating curve [15].

$$X_c\ (\%) = \frac{(\Delta H_m - \Delta H_{cc})}{\Delta H_m^{\circ} w} \times 100 \quad (1)$$

where ΔH_m is the enthalpy of melting, ΔH_{cc} is the cold crystallization enthalpy, and ΔH_m° is the melting enthalpy for a 100% crystalline PLA (93 J/g) [15], and w is the weight fraction of PLA in the biocomposites.

The morphologies of hemp hurd powder and the cryo-fractured surface of IM specimens were observed and analysed on an SU3500 scanning electron microscope (SEM, Hitachi), at an accelerating voltage of 15 kV. The impact fracture surfaces of FDM specimens were observed and analysed by a JCM6000 SEM (JEOL) operated at 5–15 kV to preclude sample charging. The fracture surfaces were sputter-coated with a gold layer prior to SEM observation, to provide enhanced conductivity.

Tensile and flexural tests were conducted on a universal testing machine, CMT 6104 (MTS Systems, China), according to ASTM D 638 and ASTM D 790 standard, respectively. Tensile testing was performed at a crosshead speed of 5 mm/min using a 10 kN load cell, and flexural testing was performed at 1.27 mm/min. Notched Izod impact testing was carried out according to ASTM D 256 standard, using an XJJU 5.5 J pendulum (Chengde COTs Scientific Instruments Co., Ltd., China) at ambient temperature and humidity. The impact strength was calculated using the absorbed energy divided by the width of the specimen. A minimum of five specimens were tested per sample. The specific mechanical properties were obtained by dividing the mechanical properties by their density, which in turn were calculated by dividing the mass of flexural specimens by its bulk volume [24].

Filament diameter tolerance is an indicator of the variation in diameter, and filament roundness is an indicator of the ovality (or departure from non-circularity) of the filament. Consistency in filament diameter and roundness is critical for FDM printability, as inconsistent diameter and roundness potentially cause unsteady extrusion, resulting in jamming or clogging in a 3D printing job. For a 1.75-mm filament, the acceptable diameter tolerance is ±0.03 mm, and the acceptable roundness tolerance is ≤ 0.05 mm, according to the GB/T 37643-2019 standard. Filament diameter was measured with a digital Vernier calliper, measured at three locations for each position and the average value was reported. The diameter tolerance was obtained by subtracting the formulated diameter (1.75 mm) from each average value, and the roundness was calculated by using the maximum diameter minus the minimum diameter sampled at 3 locations, according to the GB/T 37643-2019 standard.

Surface roughness, porosity, and shrinkage are critical indicators of process-induced microstructure of FDM-printed products. Surface finish is critical for the overall look and feel of the product, whereas the porosity and shrinkage are indicators of the thermo-physical properties of the printed product. The surface roughness of the FDM specimens was determined using a MarSurf M400 unit. Tracing speed, stylus tip diameter, and tip angle were 1.0 mm/s, 2 μm and 90°, respectively. A trace length of 17.5 mm was used. The roughness parameters specified in ISO 4287 standard, i.e., (i) arithmetic mean roughness (R_a), (ii) root mean square roughness (R_q), (iii) mean peak-to-valley height (R_z), and (iv) maximum peak-to-valley height (R_{max}), were measured to evaluate the surface characteristics. R_a is the average of the absolute values of the

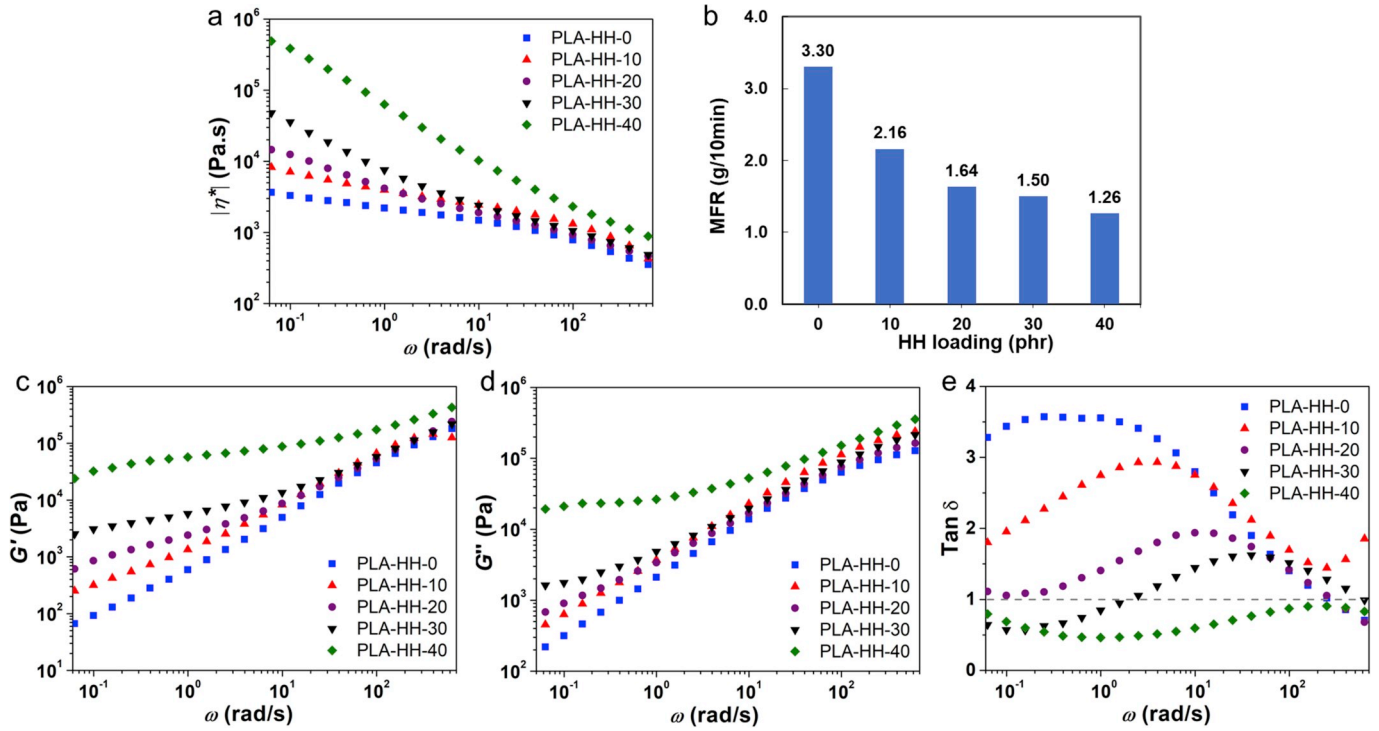

Fig. 1. Rheological and melt behaviour of PLA/HH biocomposites: (a) complex viscosity, $|\eta^*|$, (b) MFI (ASTM D 1238, Condition E) versus HH loading, (c) storage modulus, G', (d) loss modulus, G'', and (e) loss factor, tan δ.

profile deviations from the mean line and a common indicator showing the surface finish. R_{max} is an indicator of the maximum defect height within the measured profile. Porosity is an implicit measure of the microstructural defects and bears a major effect on mechanical properties as damage initiators. The porosity was calculated using Equation (2), by assuming that the IM samples were of negligible porosity [25], the average density was reported for the calculation (Table S3). Shrinkage indicates the dimensional accuracy of printed products. Besides aesthetics, thermo-physical properties of the finished products are key considerations for fit-and-form applications or products with intricate features [26]. Shrinkage data was calculated by measuring the dimensional change against the intended dimensions of FDM flexural specimens [27], according to ASTM D 955–08.

$$\text{Porosity}\ (\%) = \frac{(\rho_{\text{injection}} - \rho_{\text{FDM}})}{\rho_{\text{injection}}} \times 100 \quad (2)$$

3. Results and discussion

3.1. Rheological behaviour of biocomposites

The melt rheological properties of biocomposites with and without HH are presented in Fig. 1. Complex viscosity ($|\eta^*|$) were observed higher with increasing HH loading at low angular frequency (Fig. 1a), indicating a decrease in melt flow and processability, proved by decreased melt flow index as shown in Fig. 1b. The biocomposites showed shear-thinning behaviour, because of disentanglement, and reorientation of hemp hurd and polymer chains in the flow direction, weakening the viscous resistance [28], indicating particle-to-particle interaction in melt phase [29]. PLA–HH–10 showed a slighter shear-thinning behaviour (similar as PLA–HH–0) than other biocomposites, because of weak inter-particle interaction. The shear-thinning behaviour of biocomposites was enhanced with increasing HH loading, with minor differences in complex viscosity within the biocomposites at high angular frequency. This shear-thinning behaviour assists in lowering complex viscosity and obtaining improved melt flow and processability with enhancements in extrusion throughput during melt extrusion [23]. PLA–HH–40 showed the highest viscosity over the whole frequency range, leading to the lowest ease of printability and roughest surface within the biocomposites because of melt instability. Both storage modulus (G') and loss modulus (G'') increased with increasing HH loading, mainly at low frequencies (Fig. 1c and d). This behaviour suggests the inhibited mobility of polymer chains in melt state due to the presence of HH [30,31]. The highest values of G' and G'' were observed for PLA–HH–40, indicating the strongest interaction between the polymer matrix and HH filler. In addition, G' and G'' of all samples displayed deviation from linear viscoelastic relationships of log G' (ω) ~ 2 log ω and log G'' (ω) ~ log ω in the terminal region ($\omega < 0.1$ rad/s). The slopes of G' and G'' in the terminal region deviated from 2 to 1, respectively, as presented in Table 1, suggesting phase separation in the biocomposites, where the addition of HH increased the tendency of phase separation. Tan δ decreased and the dependency on angular frequency decreased with increasing HH loading (Fig. 1e), because of increased elasticity [17]. PLA–HH–0 showed a decrease in tan δ with increasing angular frequency, exhibiting a fluid-like rheological behaviour [20]. PLA–HH–10 showed characteristic viscous behaviour over the whole frequency range, and PLA–HH–20 showed viscous behaviour below 200 rad/s. PLA–HH–30 displayed viscous behaviour above 2 rad/s. PLA–HH–40 showed a tan δ value less than 1 ($G' > G''$) over the whole oscillation frequency range, with this solid-like

Table 1
The slope of G' and G'' in terminal region.

Terminal slope	PLA–HH–0	PLA–HH–10	PLA–HH–20	PLA–HH–30	PLA–HH–40
G′	0.72	0.51	0.73	0.43	0.66
G″	0.79	0.73	0.61	0.18	0.19

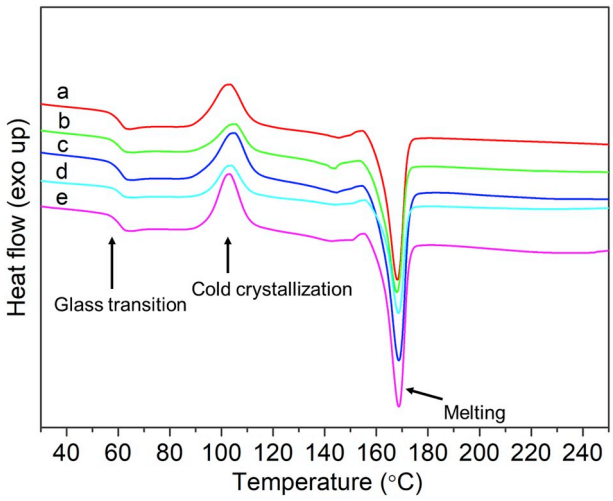

Fig. 2. DSC curves of PLA/HH biocomposites with varying loading levels of HH, (a) PLA–HH–0, (b) PLA–HH–10, (c) PLA–HH–20, (d) PLA–HH–30, and (e) PLA–HH–40.

behaviour indicating the elastic fraction being predominant over the viscous fraction, causing a decrease in interfacial energy dissipation [9], as PLA–HH–40 displayed lower melt flow and lower ease of processability than other biocomposite blends.

3.2. Thermal properties of biocomposites

Differential scanning calorimetry (DSC) characterises transition temperatures and degree of crystallinity, which dictate the processing temperature, and hence the mechanical properties. DSC thermograms are presented in Fig. 2, and the corresponding key values are listed in Table 2. Commercial grade PLA 4032D was used as a control for PLA cold crystallization and melt peaks. T_g and T_m showed marginal changes with increasing HH loading, indicating the incorporation of HH did not affect the thermal transition of biocomposites. T_{cc} increased upon the inclusion of HH (PLA–HH–10), indicating HH inclusion impeded the crystallization of PLA, and resulted in decreased crystallization enthalpy correspondingly. Further increases in HH loading, i.e., PLA–HH–20 to PLA–HH–40 showed concomitant decreases in T_{cc}. This behaviour can be surmised as being driven by the increased availability of nucleation sites and resultant nucleation, aiding the secondary crystallization [32,33] and thereby causing increased crystallization enthalpy. Nevertheless, the crystallinity (X_c) increased with increasing HH fraction, indicating the presence of HH enhanced the crystallinity of the biocomposites. However, the crystallinity showed marginal changes with further HH loading, which can be attributed to a concomitant reduction in the availability of free volume [16,33] with increasing occupancy of HH in the biocomposites.

Table 2
Crystallization and melt phase properties of biocomposites as a function of HH loading.

Sample	T_g (°C)	T_{cc} (°C)	ΔH_{cc} (J/g)	T_m (°C)	ΔH_m (J/g)	X_c (%)
PLA[a]	62.1	–	–	168.4	2.90	3.1
PLA–HH–0	61.1	103.2	24.7	168.0	49.7	33.6
PLA–HH–10	60.6	105.4	15.8	167.9	45.2	43.2
PLA–HH–20	61.2	105.0	18.0	168.7	44.7	42.5
PLA–HH–30	61.0	103.7	18.8	168.5	43.7	42.7
PLA–HH–40	60.6	103.0	21.4	168.6	44.1	41.7

[a] Without PBAT/EGMA.

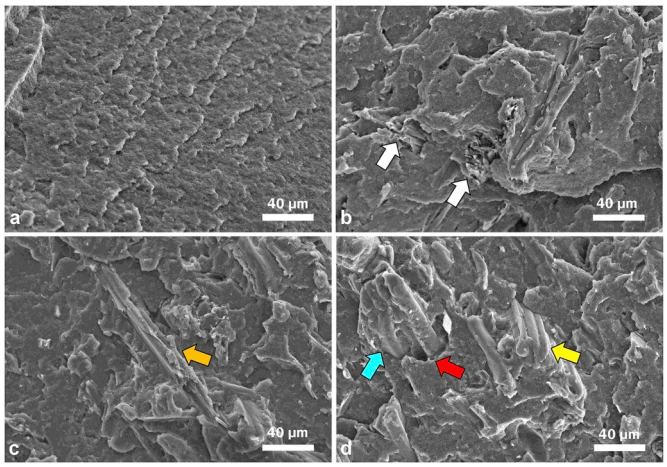

Fig. 3. SEM images of cryo-fractured surfaces of specimens: (a) PLA–HH–0, (b) PLA–HH–10, (c) PLA–HH–20, and (d) PLA–HH–40. The gold arrow shows the fibrillary structure retention, whereas the white arrows show filler failure perpendicular to the fracture surface. Debonding is shown using a red arrow, and pullout is shown using a blue arrow. (For interpretation of the references to colour in this figure legend, the reader is referred to the Web version of this article.)

3.3. Dispersion of hemp hurd and interface morphology of IM specimens

The cryo-fractured surfaces of IM specimens were observed by SEM, as shown in Fig. 3. The fracture surface of PLA–HH–0 showed a semi-brittle fracture (Fig. 3a). HH fillers showed near uniform dispersion with no particular preference for alignment. The filler parallel to the surface retained its fibrillary structure along with an aspect ratio suggestive of a filler (Fig. 3c, gold arrow). The filler perpendicular to the surface showed failure within the filler (Fig. 3b, white arrows), demonstrating adequate interfacial adhesion, rather than pull-out from the matrix. As HH loading increased, HH filler debonding (Fig. 3d, red arrow) and pull-out (Fig. 3d, light blue arrow) from matrix occurred in PLA–HH–40, indicating the decrease in interfacial adhesion between HH and PLA/PBAT matrix. HH filler was agglomerated (Fig. 3d, yellow arrow) in PLA–HH–40, indicating a decreased filler dispersion and increased particle cohesion. The SEM images suggested brittle fracture in IM specimens, as shown in the smooth fracture surfaces without plastic deformation [34].

3.4. Mechanical properties of IM samples

Mechanical properties of IM specimens are shown in Fig. 4. After a decrease from 51.9 MPa to 47.5 MPa, the tensile strength increased to 57.5 MPa in injection moulded PLA–HH–40. Flexural strength also showed a similar increasing trend as tensile strength. The reinforcement effect of HH in the tensile and flexural strength can be attributed to the fibrillary structure and an interaction between the PLA/PBAT matrix and HH, contributing to the enhanced filler-matrix stress transfer, as supported by SEM imagery showing fracture confined within the filler. Impact strength decreased as expected [35], from 69.8 J/m in PLA–HH–0 to 42.9 J/m in PLA–HH–40, as dispersion of HH particles in the matrix created regions of stress concentration that yielded under stress [36]. SEM also supported the prevalence of brittle fracture, where a flat fracture surface was discernible. The flexural modulus increased from 2.4 GPa in PLA–HH–0 to 3.9 GPa in PLA–HH–40 as expected, because of the increased stiffness brought about by the inclusion of HH filler resembling an elongated filler. The incorporation of HH to PLA/PBAT matrix slowed down the chain movements, and hence showed an increased stiffness. The stiffness and brittleness of the biocomposites were also enhanced by an increase in crystallinity of PLA because of the HH inclusion, as demonstrated through DSC analysis.

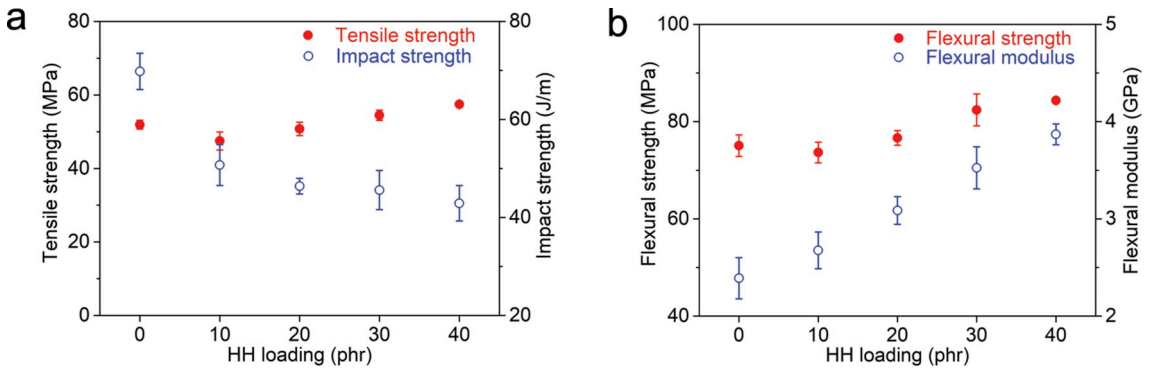

Fig. 4. Mechanical properties of the IM specimens: (a) tensile and impact strength, and (b) flexural properties, as a function of HH loading.

3.5. Diameter and roundness of filament

Biocomposite filaments extruded using biocomposite pellets through a single-screw filament extruder using the process as shown in Fig. 5a, and were compared with respect to their diameter tolerance and roundness. The surface of filaments discernibly becomes rougher with increasing HH loading (Fig. 5b). The filament diameter tolerance and roundness are represented as box-and-whiskers charts (Fig. 5c and 5d). All HH-filled filaments exhibited acceptable diameter tolerances (±0.02 mm, Fig. 5c), better than the PLA–HH–0 filament. PLA–HH–0 showed a relatively higher diameter range at ±0.03 mm because of its lower viscosity during processing (~190 °C), leading to a relatively lower melt strength and perturbed melt flow. The roundness (Fig. 5d) was less than 0.03 mm. PLA–HH–20 showed a roundness in the range of 0.01 mm to 0.06 mm due to the insufficient melt strength at the die exit.

3.6. Finish quality of FDM-printed specimens

FDM-printed specimens showed increasing surface roughness and darker colour with increasing HH loading (Fig. 6a and b). Surface roughness data is presented in Fig. 6c. With the addition of hemp hurd, R_a (arithmetic mean roughness) increased from 3.8 μm of PLA–HH–0 to 19.7 μm of PLA–HH–10, and was unchanged at 19.0 ± 1.0 μm with increasing HH loading. R_q (root mean square roughness) remained unchanged at 26.0 ± 1.0 μm after an increase from 4.5 μm of PLA–HH–0 to 27.0 μm for PLA–HH–10. The roughness values indicate that the surface smoothness decreased after the inclusion of hemp hurd, however, the average surface roughness value was not affected by increasing HH loading, attributed to an equivalent layer thickness (0.15 mm, and significantly larger than the average particle size of 50 μm). PLA–HH–10 and PLA–HH–20 showed nearly a similar value in mean peak-to-valley height, R_z (115.7 μm and 114.9 μm) and maximum peak-to-valley height, R_{max} (128.3 μm and 125.0 μm), and PLA–HH–30 and PLA–HH–40 showed higher R_z (122.7 μm and 124.0 μm) and R_{max} (149.4 μm and 145.5 μm), indicating PLA–HH–30 and PLA–HH–40 displayed a larger maximum defect height indicative of a rougher surface than PLA–HH–10 and PLA–HH–20, causing PLA–HH–30 and PLA–HH–40 to exhibit rougher surface than PLA–HH–10 and PLA–HH–20. The porosity and shrinkage data are presented in Fig. 6d. The porosity increased from 5.8% of PLA–HH–0 to 17.9% of PLA–HH–40. The substantial fraction of porosity (~20%) in FDM samples was also reported by Le Duigou et al. [25], and is caused by

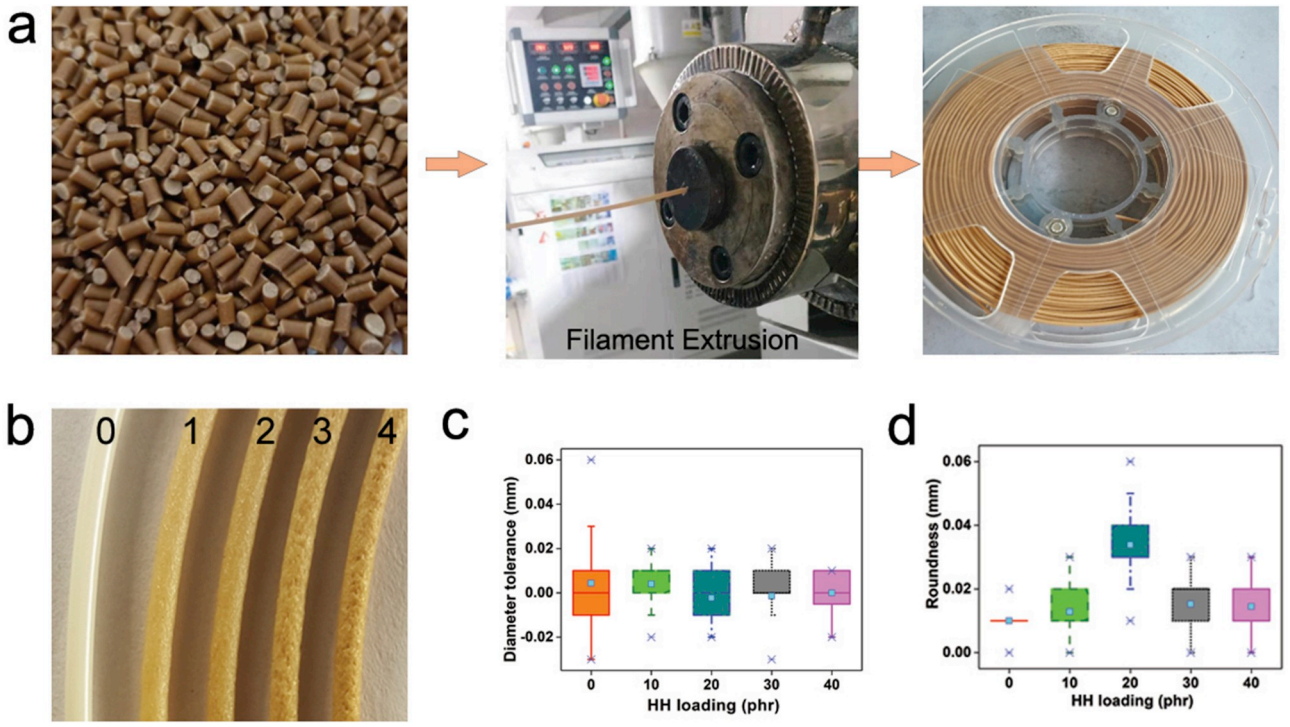

Fig. 5. (a) PLA/HH pellets extruded as filaments, (b) PLA/HH filament, (c) diameter tolerance, and (d) roundness of PLA/HH filament as a function of HH loading. The labels indicate (0) PLA–HH–0, (1) PLA–HH–10, (2) PLA–HH–20, (3) PLA–HH–30 and (4) PLA–HH–40.

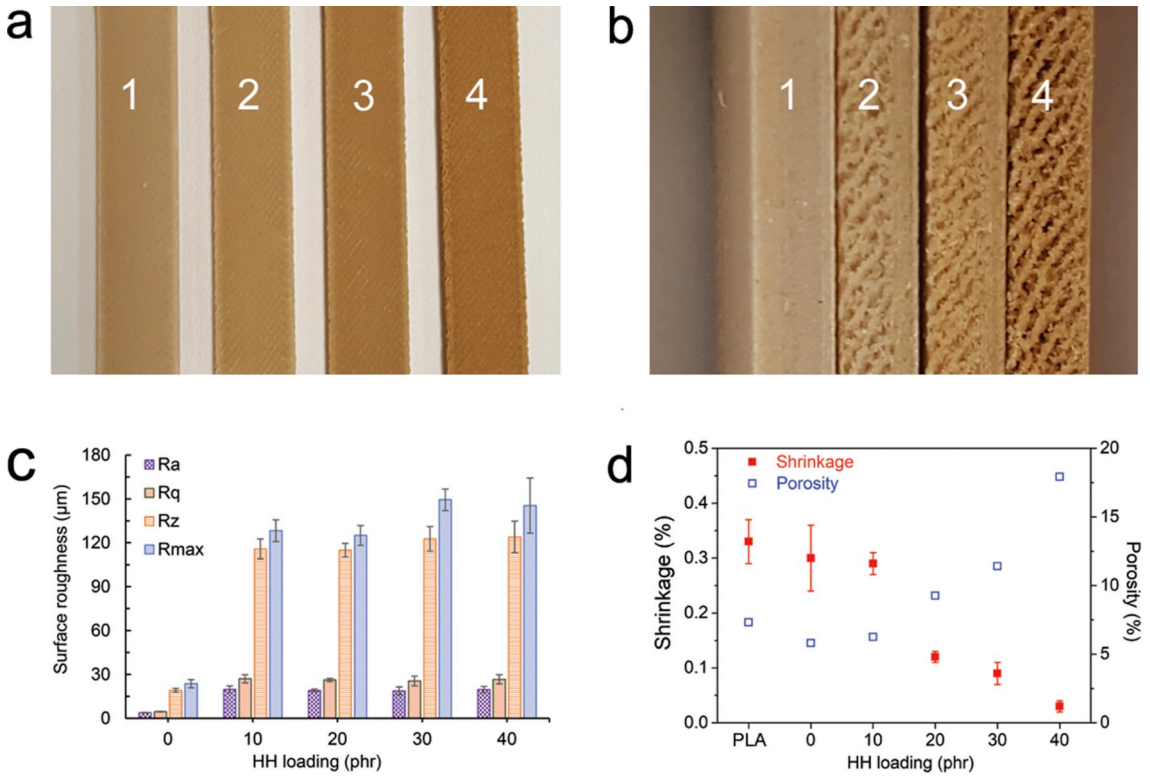

Fig. 6. FDM-printed specimens in (a) top view, and (b) side view, (c) surface roughness, and (d) porosity and shrinkage as a function of HH loading. Labels indicate: (1) PLA–HH–10, (2) PLA–HH–20, (3) PLA–HH–30 and (4) PLA–HH–40.

increasing viscosity, resulting in decreasing melt flow from the nozzle and resultant inadequate adhesion between layers. The shrinkage of all samples is lower than that of PLA ($0.33 \pm 0.04\%$) and decreased from $0.30 \pm 0.06\%$ (PLA–HH–0) to $0.03 \pm 0.01\%$ (PLA–HH–40), indicating an improvement in dimensional accuracy with increasing HH loading. The shrinkage analysis demonstrated that an increasing HH inclusion was advantageous for achieving dimensional constancy.

3.7. Morphology of FDM-printed specimens

The impact fracture surfaces of FDM-printed specimens as observed by SEM are shown in Fig. 7. The thickness of interlayer space between two deposited layers (yellow dotted rectangles in Fig. 7c and e) increased with increasing HH loading, resulting in decreased interfacial bonding and consequently decreased mechanical properties. PLA–HH–40 showed an indistinct boundary between layers (Fig. 7g), because of highest viscosity and a predominant elastic fraction over a viscous fraction, resulting in inconsistent melt flow, thus deteriorating the interfacial bonding. The volume and count of voids on the fracture surface increased with increasing HH loading, because of the pull-out of HH filler from the polymer matrix or being formed during FDM printing. Increased interlayer space and voids led to increased porosity and decreased mechanical properties. The HH filler pull-out indicates the insufficient interfacial bonding between HH and polymer matrix to provide satisfactory filler-matrix stress transfer, resulting in decreased mechanical properties as well. The FDM-printed specimens exhibited elasto-plastic deformation, with elongated fragments discernible on the surface, as shown in the SEM micrographs (Fig. 7b, d, f, h), which

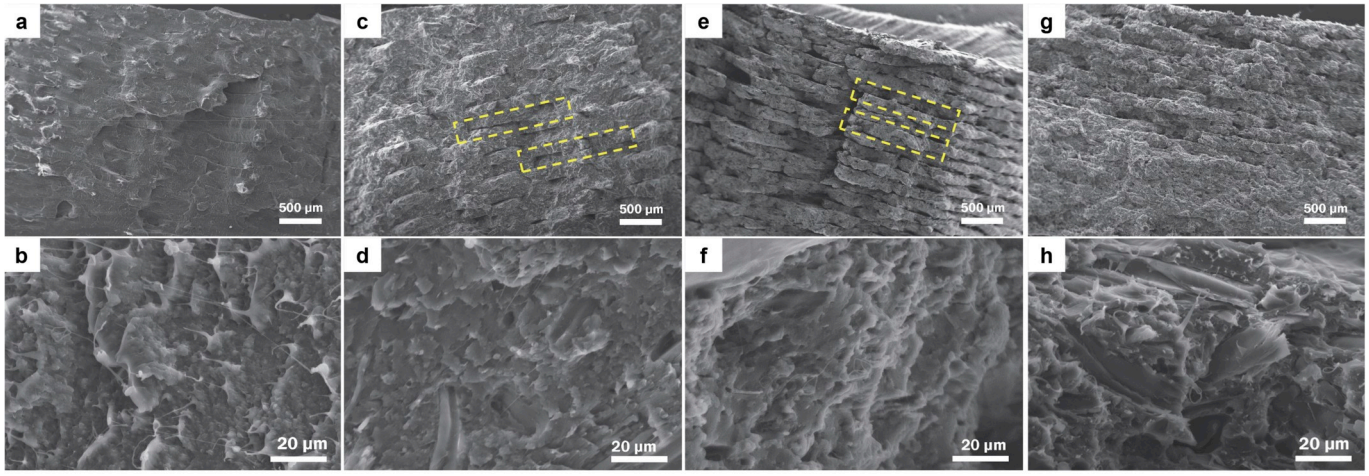

Fig. 7. SEM images of impact fracture surfaces of FDM specimens: (a, b) PLA–HH–0, (c, d) PLA–HH–10, (e, f) PLA–HH–20, and (g, h) PLA–HH–40. The layer boundary is shown using dotted rectangles in (c) and (e).

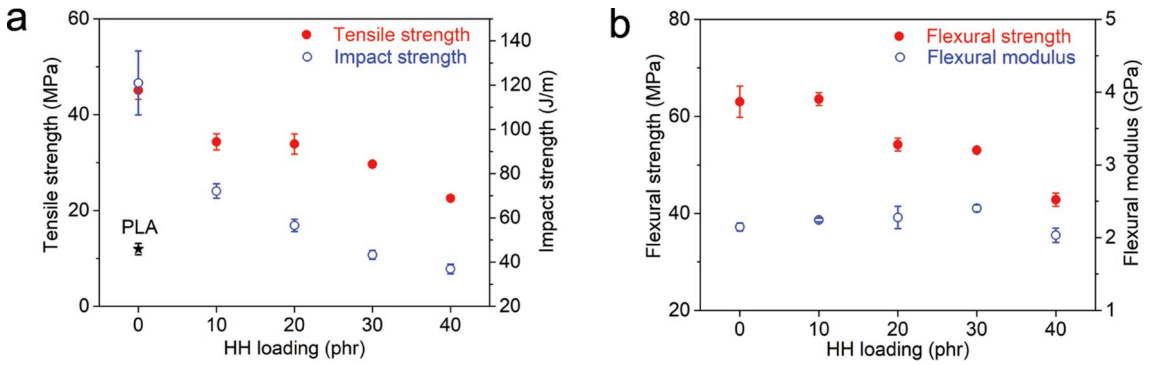

Fig. 8. Mechanical properties of FDM-printed specimens: (a) tensile and impact strength and (b) flexural properties as a function of HH loading. The impact strength data of commercial PLA filament is shown using a (★) symbol.

contributed to the enhanced impact strength compared with IM samples because of the energy dissipation.

3.8. Mechanical properties of FDM-printed specimens

In contrast to IM specimens, both tensile strength and flexural strength decreased with increasing HH loading as shown in Fig. 8, with PLA–HH–40 showing a decrease by 50% and 32% respectively, compared to PLA–HH–0. The decrease in mechanical properties is linked with insufficient interfacial bonding, resultant of voids and interlayer space produced at the interface between hemp hurd and polymers, and between layers during FDM process [26], because of the decreased melt flow. The impact strength decreased with increasing HH loading, like the IM samples, and consistent with the literature [15]. Increased porosity and the addition of HH as stress raisers can be surmised to contribute to yielding [36], resulting in overall increased embrittlement in the FDM specimens, affecting printability and subsequent application. Nevertheless, PLA–HH–30 exhibited impact strength comparable to commercial PLA FDM samples. Conversely, flexural modulus increased up to 30 phr of HH loading. A decrease in flexural modulus at PLA–HH–40 can be attributed to an increase in porosity and the associated inadequate interfacial bonding, showing a critical loading level (30 phr) in terms of HH loading in the PLA/PBAT matrix.

Specific mechanical properties were calculated for commercial PLA filament and PLA/HH biocomposites produced using IM and FDM as illustrated in Table 3. The density normalisation did not bear an effect on specific mechanical properties as they showed similar trends as the non-normalized values. The IM samples showed higher overall specific tensile and flexural properties than FDM-printed samples. With increasing HH loading, the differences in specific tensile strength and flexural properties between FDM and IM samples were pronounced from unfilled to 40 phr grades. The higher specific tensile strength and flexural properties for IM samples are expected as a more homogenous, low-porosity structure (Fig. S4, Table S3) was attained in the processing, in contrast to FDM specimens. In the case of the FDM specimens, porosity in the microstructure acted as stress raisers. A higher flexural modulus in the IM samples could also be attributed to higher-stiffness filler providing resistance to chain deformation, and the absence of major porosity. The specific impact strength values for FDM-printed samples were higher than IM samples. The increase in specific impact strength for FDM samples versus IM samples was diminished with increasing HH loading, which can be surmised as a combined effect of increased crystallinity from PLA–HH–0 (33.6%) to PLA–HH–40 (41.7%), and the increased porosity in the FDM-printed specimens (Fig. 6d). In a particulate-filled thermoplastic composite, the impact toughness is dictated by the polymeric segments surrounding the contiguous particles, which assist in transforming the plane strain to plane stress [36]. The FDM specimens can transfer the impact energy through the interface of each deposited PLA/HH layer, an effect that diminishes in higher HH loading in FDM sample because of the increasing porosity and loss of effective interfacial bonding and dispersion of particles. Overall, the FDM process yielded higher impact strength parts over their IM counterparts.

4. Conclusions

HH inclusion in PLA is beneficial for achieving cost-effectiveness in PLA based FDM feedstock, which also aids in the secondary crystallization in the PLA/HH biocomposites. As a result, the flexural modulus increased with HH loading in both FDM-printed and IM samples. Furthermore, the FDM-printed parts led to higher impact strength over the IM parts, both on an absolute and on a specific impact strength basis. The FDM-printed samples showed an increased dimensional accuracy with increasing HH loading. The parametric analysis of HH loading coupled with rheology, melt flow analysis, thermal analysis, and morphological analyses using SEM supported the mechanistic basis for the resultant thermo-mechanical performance. Roughness analysis and SEM analysis yielded information on the increasing roughness and corrugated appearance with increasing HH content. Shrinkage and porosity analyses provided support for analysis of damage initiation in FDM specimens, which is divergent from the traditional IM biocomposite mechanical behaviour. The diverse microstructure and layer-

Table 3
Specific mechanical properties of processed biocomposite feedstock and commercial PLA feedstock.

Sample	Specific Tensile Strength		Specific Flexural Strength		Specific Flexural Modulus		Specific Impact Strength	
	($MPa.cm^3/g$)		($MPa.cm^3/g$)		($GPa.cm^3/g$)		($J.cm^3/g.m$)	
	FDM	IM	FDM	IM	FDM	IM	FDM	IM
PLA[a]	–	–	–	–	2.60 ± 0.22	–	40 ± 2.2	–
PLA–HH–0	39 ± 1.6	42 ± 1.0	55 ± 2.8	62 ± 1.8	1.87 ± 0.05	1.96 ± 0.17	105 ± 13	57 ± 3.0
PLA–HH–10	30 ± 1.5	38 ± 2.0	55 ± 1.1	59 ± 1.7	1.93 ± 0.02	2.16 ± 0.15	62 ± 2.8	41 ± 3.4
PLA–HH–20	30 ± 1.9	41 ± 1.5	48 ± 1.2	62 ± 1.2	2.03 ± 0.14	2.51 ± 0.12	50 ± 2.5	38 ± 1.3
PLA–HH–30	26 ± 0.6	42 ± 1.1	47 ± 0.6	64 ± 2.6	2.13 ± 0.04	2.75 ± 0.17	38 ± 1.8	36 ± 3.1
PLA–HH–40	22 ± 0.3	45 ± 0.3	41 ± 1.3	66 ± 0.2	1.96 ± 0.09	3.05 ± 0.08	36 ± 2.1	34 ± 2.8

[a] Commercial PLA FDM filament.

wise structure necessitates further analysis of FDM printed components using tomography and other high-resolution imaging methods. Although FDM-printed components are quite different to IM parts, comprehensive mechanistic analyses on the processing-structure relationships is critical for further development and widespread utilisation of the FDM processing method for industrial applications.

Funding

The Forest and Wood Products Australia [Grant # PNA360-1516] and the USQ Postgraduate Research Scholarship for X. Xiao supported this work.

Acknowledgments

The authors acknowledge Ms Yanru Wang for providing technical assistance in SEM analysis.

Appendix A. Supplementary data

Supplementary data to this article can be found online at https://doi.org/10.1016/j.compscitech.2019.107887.

References

[1] J. Torres, J. Cotelo, J. Karl, A.P. Gordon, Mechanical property optimization of FDM PLA in shear with multiple objectives, JOM 67 (5) (2015) 1183–1193, https://doi.org/10.1007/s11837-015-1367-y.
[2] S. Bakrani Balani, F. Chabert, V. Nassiet, A. Cantarel, Influence of printing parameters on the stability of deposited beads in fused filament fabrication of poly (lactic) acid, Addit. Manuf. 25 (2019) 112–121, https://doi.org/10.1016/j.addma.2018.10.012.
[3] Y. Liu, W. Zhang, F. Zhang, J. Leng, S. Pei, L. Wang, X. Jia, C. Cotton, B. Sun, T. W. Chou, Microstructural design for enhanced shape memory behavior of 4D printed composites based on carbon nanotube/polylactic acid filament, Compos. Sci. Technol. 181 (2019) 107692, https://doi.org/10.1016/j.compscitech.2019.107692.
[4] P. Ravi, P.S. Shiakolas, T.R. Welch, Poly-L-lactic acid: pellets to fiber to fused filament fabricated scaffolds, and scaffold weight loss study, Addit. Manuf. 16 (2017) 167–176, https://doi.org/10.1016/j.addma.2017.06.002.
[5] J. Dong, C. Mei, J. Han, S. Lee, Q. Wu, 3D printed poly(lactic acid) composites with grafted cellulose nanofibers: effect of nanofiber and post-fabrication annealing treatment on composite flexural properties, Addit. Manuf. 28 (2019) 621–628, https://doi.org/10.1016/j.addma.2019.06.004.
[6] B.M. Tymrak, M. Kreiger, J.M. Pearce, Mechanical properties of components fabricated with open-source 3-D printers under realistic environmental conditions, Mater. Des. 58 (2014) 242–246, https://doi.org/10.1016/j.matdes.2014.02.038.
[7] Z. Wang, J. Xu, Y. Lu, L. Hu, Y. Fan, J. Ma, X. Zhou, Preparation of 3D printable micro/nanocellulose-polylactic acid (MNC/PLA) composite wire rods with high MNC constitution, Ind. Crops Prod. 109 (2017) 889–896, https://doi.org/10.1016/j.indcrop.2017.09.061.
[8] D. Depuydt, M. Balthazar, K. Hendrickx, W. Six, E. Ferraris, F. Desplentere, J. Ivens, A.W. Van Vuure, Production and characterization of bamboo and flax fiber reinforced polylactic acid filaments for fused deposition modeling (FDM), Polym. Compos. 40 (5) (2019) 1951–1963, https://doi.org/10.1002/pc.24971.
[9] Y. Tao, H. Wang, Z. Li, P. Li, S.Q. Shi, Development and application of wood flour-filled polylactic acid composite filament for 3D printing, Materials 10 (2017) 339, https://doi.org/10.3390/ma10040339.
[10] M. Kariz, M. Sernek, M. Obućina, M.K. Kuzman, Effect of wood content in FDM filament on properties of 3D printed parts, Mater, Today Commun. 14 (2018) 135–140, https://doi.org/10.1016/j.mtcomm.2017.12.016.
[11] F. Daver, K.P.M. Lee, M. Brandt, R. Shanks, Cork–PLA composite filaments for fused deposition modelling, Compos. Sci. Technol. 168 (2018) 230–237, https://doi.org/10.1016/j.compscitech.2018.10.008.
[12] S. Liu, L. Ge, S. Gao, L. Zhuang, Z. Zhu, H. Wang, Activated carbon derived from bio-waste hemp hurd and retted hemp hurd for CO 2 adsorption, Compos. Commun. 5 (2017) 27–30, https://doi.org/10.1016/j.coco.2017.06.002.
[13] N. Stevulova, J. Cigasova, A. Estokova, E. Terpakova, A. Geffert, F. Kacik, E. Singovszka, M. Holub, Properties characterization of chemically modified hemp hurds, Materials 7 (2014) 8131–8150, https://doi.org/10.3390/ma7128131.
[14] X. Li, R. Xiao, J.J. Morrell, X. Zhou, G. Du, Improving the performance of hemp hurd/polypropylene composites using pectinase pre-treatments, Ind. Crops Prod. 97 (2017) 465–468, https://doi.org/10.1016/j.indcrop.2016.12.061.
[15] B.A. Khan, H. Na, V. Chevali, P. Warner, J. Zhu, H. Wang, Glycidyl methacrylate-compatibilized poly (lactic acid)/hemp hurd biocomposites: processing, crystallization, and thermo-mechanical response, J. Mater. Sci. Technol. 34 (2018) 387–397, https://doi.org/10.1016/j.jmst.2017.03.004.
[16] B.A. Khan, V.S. Chevali, H. Na, J. Zhu, P. Warner, H. Wang, Processing and properties of antibacterial silver nanoparticle-loaded hemp hurd/poly(lactic acid) biocomposites, Compos. B Eng. 100 (2016) 10–18, https://doi.org/10.1016/j.compositesb.2016.06.022.
[17] L. Jiang, M.P. Wolcott, J. Zhang, Study of biodegradable polylactide/poly(butylene adipate-co-terephthalate) blends, Biomacromolecules 7 (2006) 199–207, https://doi.org/10.1021/bm050581q.
[18] J. Nomai, R. Jarapanyacheep, K. Jarukumjorn, Mechanical, thermal, and morphological properties of sawdust/poly(lactic acid) composites: effects of alkali treatment and poly(butylene adipate-co-terephthalate) content, Macromol. Symp. 354 (2015) 244–250, https://doi.org/10.1002/masy.201400120.
[19] T. Yu, Y. Li, Influence of poly(butylenes adipate-co-terephthalate) on the properties of the biodegradable composites based on ramie/poly(lactic acid), Compos. A Appl. Sci. Manuf. 58 (2014) 24–29, https://doi.org/10.1016/j.compositesa.2013.11.013.
[20] M. Hao, H. Wu, Z. Zhu, In situ reactive interfacial compatibilization of polylactide/sisal fiber biocomposites via melt-blending with an epoxy-functionalized terpolymer elastomer, RSC Adv. 7 (2017) 32399–32412, https://doi.org/10.1039/c7ra03513f.
[21] Y. Bin, B. Yang, H. Wang, The effect of a small amount of modified microfibrillated cellulose and ethylene–glycidyl methacrylate copolymer on the crystallization behaviors and mechanical properties of polylactic acid, Polym. Bull. 75 (2017) 3377–3394, https://doi.org/10.1007/s00289-017-2215-8.
[22] Y.-D. Shi, K. Zhang, Y.-F. Chen, J.-B. Zeng, M. Wang, New approach to morphological control for polypropylene/polyethylene blends via magnetic self-organization, Mater. Des. 117 (2017) 24–36, https://doi.org/10.1016/j.matdes.2016.12.035.
[23] N.A. Nguyen Barnes, H. S, C.C. Bowland, K.M. Meek, K.C. Littrell, J.K. Keum, A. K. Naskar, A path for lignin valorization via additive manufacturing of high-performance sustainable composites with enhanced 3D printability, Sci. Adv. 4 (2018), eaat4967, https://doi.org/10.1126/sciadv.aat4967.
[24] W.W. Yu, J. Zhang, J.R. Wu, X.Z. Wang, Y.H. Deng, Incorporation of graphitic nano-filler and poly(lactic acid) in fused deposition modeling, J. Appl. Polym. Sci. 134 (2017) 1–11, https://doi.org/10.1002/app.44703.
[25] A. Le Duigou, M. Castro, R. Bevan, N. Martin, 3D printing of wood fibre biocomposites: from mechanical to actuation functionality, Mater. Des. 96 (2016) 106–114, https://doi.org/10.1016/j.matdes.2016.02.018.
[26] B.N. Turner, S.A. Gold, A review of melt extrusion additive manufacturing processes: II. Materials, dimensional accuracy, and surface roughness, Rapid Prototyp. J. 21 (2015) 250–261, https://doi.org/10.1108/rpj-02-2013-0017.
[27] Y.-H. Choi, C.-M. Kim, H.-S. Jeong, J.-H. Youn, Influence of bed temperature on heat shrinkage shape error in FDM additive manufacturing of the ABS-engineering plastic, World J. Eng. Technol. 04 (2016) 186–192, https://doi.org/10.4236/wjet.2016.43D022.
[28] A. Gupta, W. Simmons, G.T. Schueneman, D. Hylton, E.A. Mintz, Rheological and thermo-mechanical properties of poly(lactic acid)/lignin-coated cellulose nanocrystal composites, ACS Sustain. Chem. Eng. 5 (2017) 1711–1720, https://doi.org/10.1021/acssuschemeng.6b02458.
[29] M.R. Kamal, V. Khoshkava, Effect of cellulose nanocrystals (CNC) on rheological and mechanical properties and crystallization behavior of PLA/CNC nanocomposites, Carbohydr. Polym. 123 (2015) 105–114, https://doi.org/10.1016/j.carbpol.2015.01.012.
[30] H. Essabir, M.E.I. Achaby, E.I.M. Hilali, R. Bouhfid, A. Qaiss, Morphological, structural, thermal and tensile properties of high density polyethylene composites reinforced with treated argan nut shell particles, J. Bionics Eng. 12 (2015) 129–141, https://doi.org/10.1016/s1672-6529(14)60107-4.
[31] J. Feng, Y. Sun, P. Song, W. Lei, Q. Wu, L. Liu, Y. Yu, H. Wang, Fire-resistant, strong, and green polymer nanocomposites based on poly(lactic acid) and core−shell nano fi brous flame retardants, ACS Sustain. Chem. Eng. 5 (2017) 7894–7904, https://doi.org/10.1021/acssuschemeng.7b01430.
[32] G. Gamon, P. Evon, L. Rigal, Twin-screw extrusion impact on natural fibre morphology and material properties in poly(lactic acid) based biocomposites, Ind. Crops Prod. 46 (2013) 173–185, https://doi.org/10.1016/j.indcrop.2013.01.026.
[33] N. Ayrilmis, A. Kaymakci, Fast growing biomass as reinforcing filler in thermoplastic composites: paulownia elongata wood, Ind. Crops Prod. 43 (2013) 457–464, https://doi.org/10.1016/j.indcrop.2012.07.050.
[34] Y. Zhang, P. Song, S. Fu, F. Chen, Morphological structure and mechanical properties of epoxy/polysulfone/cellulose nanofiber ternary nanocomposites, Compos. Sci. Technol. 115 (2015) 66–71, https://doi.org/10.1016/j.compscitech.2015.05.003.
[35] S.-H. Lee, S. Wang, Biodegradable polymers/bamboo fiber biocomposite with bio-based coupling agent, Composites Part A Appl. Sci. Manuf. 37 (2006) 80–91, https://doi.org/10.1016/j.compositesa.2005.04.015.
[36] V.S. Chevali, B.A. Nerenz, C.A. Ulven, Acrylonitrile butadiene styrene (ABS)/lignocellulosic fiber biocomposite: effect of artificial weathering on impact properties, J. Biobased Mater. Bioenergy 6 (2012) 42–50, https://doi.org/10.1166/jbmb.2012.1188.

Appendix B

Composites Communications 21 (2020) 100385

Contents lists available at ScienceDirect

Composites Communications

journal homepage: www.elsevier.com/locate/coco

Enhanced toughness of PLLA/PCL blends using poly(d-lactide)-poly (ε-caprolactone)-poly(d-lactide) as compatibilizer

Xianglian Xiao [a,b,c], Venkata S. Chevali [a], Pingan Song [a], Bin Yu [a], Yihu Yang [c], Hao Wang [a,b,*]

[a] Centre for Future Materials, University of Southern Queensland, Springfield Central QLD, 4300, Australia
[b] China-Australia Institute for Advanced Materials and Manufacturing, Jiaxing University, Jiaxing, 314001, China
[c] Shenzhen Esun Industrial Co., Ltd., Shenzhen, 518057, China

ARTICLE INFO

Keywords:
Poly(l-lactide)
Poly(ε-caprolactone)
PDLA-PCL-PDLA
Toughness
Stereocomplex
Compatibilization

ABSTRACT

Poly(l-lactide) (PLLA)/poly(ε-caprolactone) (PCL) blends traditionally show low ductility because of the immiscibility between PLLA and PCL. In this study, this ductility challenge was addressed by modifying the compatibility between PLLA and PCL using poly(d-lactide)-poly(ε-caprolactone)-poly(d-lactide) (PDLA-PCL-PDLA or PCDL) tri-block copolymer. PLLA/PCL and PLLA/PCL blends with 0.7 phr and 3.5 phr PCDL were prepared by melt-compounding and extrusion and analyzed. The compatibilized PLLA/PCL blend with 3.5 phr of PCDL exhibited an elongation-at-break of 43%, compared to 18% in uncompatibilized PLLA/PCL, although PLLA/PCL/PCDL3.5 showed the higher crystallinity of 10.0% compared to 3.1% in PLLA baseline. The stereocomplexation effect between PLLA and PDLA was confirmed with a melting peak of a stereocomplex crystallite at 212 °C through differential scanning calorimetry. PCDL compatibilization improved miscibility between PLLA and PCL as evidenced through the interfacial morphology analysis, and supported by the rheological analysis, which elucidated the enhanced melting viscosity and interfacial adhesion of PLLA/PCL. Overall, the compatibilization of PLLA/PCL blends with PCDL was effective in achieving an enhanced interfacial morphology and adhesion, and improved elongation-at-break.

1. Introduction

Poly(l-lactide, PLLA) is a bio-derived aliphatic polyester and an enantiomer of poly(lactic acid), which offers higher ease of processability and superior mechanical properties, comparable to traditional thermoplastics [1–5]. PLLA is often the first choice in biomedical applications [6] and 3D printing [1,7,8], albeit the inability of PLLA to crystallize during processing, leads to inadequate toughness and low thermal resistance that limit its extensive industrial applications [9,10].

The challenges in addressing toughness modification of PLLA is achieved through melt blending of PLLA with flexible and biodegradable polymers, such as poly(ε-caprolactone) (PCL) [10–13]. Melt blending of PLLA with PCL is an economic way to gain toughness while maintaining biodegradability, compared to plasticization and copolymerization. PCL with a low glass transition temperature (T_g =-60 °C) and melting temperature (T_m = 60 °C) is often melt-blended with PLLA to improve its toughness, causing increased melt flow rate (MFR) [13,14]. If used in 3D printing, such enhanced melt flow is favorable for achieving a more stable flow pattern at nozzle [1]. Toughness modification using PCL brings about additional challenges as PLLA/PCL blends are immiscible, and if phase-separated, these blends fail to achieve any enhancement in toughness [11,14].

To address this phase-separation and concomitantly achieve the desirable toughness, lactide/caprolactone copolymers with segments identical to PLLA and PCL were used for compatibilization [6,12,15–17]. A summary of the literature on lactide/caprolactone copolymer compatibilization is presented in Table 1. The copolymer compatibilizer segments tend to interact with their blend counterparts while residing at the interface and interpenetrating to PLLA and PCL phases, concurrently enhancing the interfacial adhesion and therefore, improved impact strength and ductility [12]. Stereocomplexation between the PLLA and PDLA enantiomers is also deemed to be beneficial to achieve the enhanced interfacial adhesion and mutual interaction between components and contribution to the toughness of PLLA [18,19]. WhetherPDLA-PCL-PDLA or PCDL tri-block copolymer compromises in miscibility or compatibility while modifying toughness in PLLA/PCL blends, and bears an effect on the formation of stereocomplexation between PDLA in the copolymer and PLLA in the matrix, require further

* Corresponding author. Centre for Future Materials, University of Southern Queensland, Brisbane, QLD, 4300, Australia.
E-mail addresses: xxlsony@hotmail.com (X. Xiao), Venkata.S.Chevali@gmail.com (V.S. Chevali), Hao.Wang@usq.edu.au (H. Wang).

https://doi.org/10.1016/j.coco.2020.100385
Received 4 December 2019; Received in revised form 30 April 2020; Accepted 2 June 2020
Available online 4 June 2020

Table 1
A summary of the previous work in compatibilization of PLLA/PCL by lactide/caprolactone copolymers.

Ref	Method	Performance
[6]	4wt% of triblock PLLA-PCL-PLLA copolymer blended with PLA and PCL (70/30) by melt mixing	• Enhanced toughness of PLA/PCL blend • Elongation-at-break increased from 2% to 53% • Impact strength increased from 1.1 to 3.7 kJ/m^2
[12]	PLA/PCL (80/20) toughened with l-lactide/caprolactone (LACL) copolymer via solution mixing, casting, and conditioning compression	• LACL enhanced dispersion of PCL in PLA, with increased crystallinity of PLA • 5 wt% LACL increased elongation-at-break by >100% • A decrease in tensile strength and modulus
[15]	Random copolymer P(LLA-co-εCL) and diblock copolymer P (LLA-b-εCL) (0, 5, 10, and 15 phr) as compatibilizers for PLLA/PCL (70/30) via solution casting	• Both copolymers enhanced compatibility between PCL and PLLA • P(LLA-co-εCL) caused more pronounced reduction in domain size of PCL and molecular weight of PLLA/PCL films during hydrolysis
[16]	Lactide-Caprolactone copolymer (LACL) mixed with PLA/PCL blend using solution mixing and fabricated via solution casting	• LACL exhibited compatibilization effect on the immiscible PLA/PCL blend by promoting the nucleation of PLA with higher nuclei density
[17]	Poly(l,l-lactide-co-ε-caprolactone) [P(lLA-co-εCL)] (0, 5, 10, and 20 phr) mixed with PLLA/PCL (50/50) via solution-casting method	• Enhanced compatibility in PLLA/PCL blend • Lower recrystallization temperature after the inclusion of P(lLA-co-εCL)
[20]	PLLA/PCL films blended with and without 10 wt% poly(l-lactide-co-ε-caprolactone) via solution casting	• Poly(l-lactide-co-ε-caprolactone) increased compatibility and elongation-at-break of PLLA/PCL blends
[18]	PLLA toughened using Poly (*ε*-caprolactone-*co*-lactide)-*b*-PDLA core−shell rubber particles (0, 5, 10, 15, and 20 wt%) via solution blending	• PDLA shell facilitated core−shell rubber particle/PLLA interaction via stereocomplexation • Over 10-fold increase in elongation-at-break • Young's modulus and tensile strength retained

exploration.

Specifically, this study examined the effect of PCDL on the toughness of PLLA/PCL blend, with (a) compatibilization effect through lactide/caprolactone copolymer and (b) interfacial interaction improvement between PLLA and PDLA through the formation of stereocomplex crystallites. PLLA/PCL/PCDL blends (a) without and with (b) 0.7 phr and (c) 3.5 phr PCDL were prepared to obtain PDLA ratios of 0, 0.5, and 2.5 phr in the blends, respectively. The effect of PCDL on the tensile properties and impact strength, morphologies, rheological properties, and thermal properties were analyzed with respect to variable PCDL loadings.

2. Experimental methods

2.1. Materials and processing

PLLA (Grade 4032D, 98.5% L-lactide) was obtained from Nature Works, LLC. PCL (Grade CAPA 6500) was purchased from Perstorp UK Ltd. PDLA-PCL-PDLA or PCDL was synthesized by ring-opening polymerization of D-lactide using poly(ε-caprolactone) diol (HO-PCL-OH, viscosity-average molecular weight = 7500) as macro-initiator, as shown in Scheme 1. The structure and properties of PCDL are provided in Table S1 and Fig. S1. The PLLA/PCL ratios in the blends were 100/10 (w/w), including the PCL fraction introduced by PCDL. The ratios of PCDL in the formulations were 0 phr, 0.7 phr, and 3.5 phr. The formulations of blends are shown in Table S2. The blends were prepared by melt blending and extruding at 170 °C through a co-rotating twin-screw extruder (L/D = 44, D = 35 mm), and injection-molding as mechanical testing standard specimens at 175 °C.

2.2. Materials characterization

Tensile testing was performed on a CMT 6104 universal testing machine (MTS Systems, China) at a crosshead speed of 5 mm/min, with a load cell of 10 kN capacity, according to ASTM D 638, using Type I specimens (166 mm × 19 mm × 3.65 mm). Notched Izod impact (63 mm × 12.7 mm × 3.65 mm) testing was conducted on an XJJU 5.5 J pendulum (Chengde COTs Scientific Instruments Co., Ltd.) at room temperature, according to ASTM D 256. The morphologies of the cryo-fractured surface were examined on a scanning electron microscope (SEM, SU3500, Hitachi) with an accelerating voltage of 15 kV. The fracture surfaces were sputter-coated with a gold layer before SEM observation. Rheological properties were determined on a Discovery Hybrid Rheometer (DHR-2, TA Instruments). Dynamic frequency sweep mode (0.0628–628 rad/s) was used at a strain of 1% at 190 °C using a parallel plate geometry with a diameter of 25 mm and a sample gap of 1 mm. Thermal properties were measured by differential scanning calorimetry (DSC, Q20, TA Instruments, USA) under a nitrogen atmosphere. A 3-step cycle of i) heating from 20 to 200 °C, ii) cooling to 20 °C, and iii) heating to 260 °C was used with a ramp rate of 10 °C/min. The degree of crystallinity (X_c) of the PLLA phase was calculated using Equation (1)

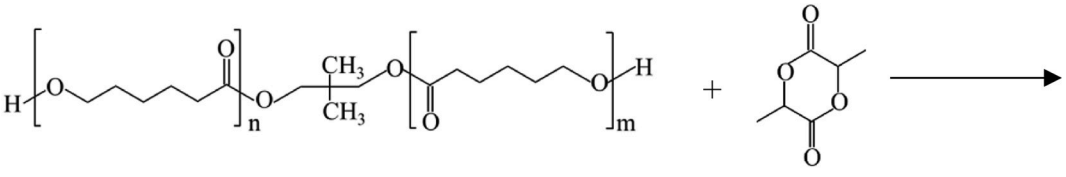

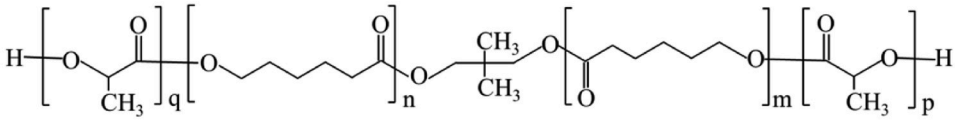

Scheme 1. Synthesis of PDLA-PCL-PDLA.

from the second heating curve.

$$X_c(\%) = \frac{(\Delta H_m - \Delta H_{cc})}{\Delta H_m^{\circ} w} \quad (1)$$

where ΔH_m is the enthalpy of melting, ΔH_{cc} is the cold crystallization enthalpy, and ΔH_m° is the melting enthalpy for a 100% crystalline PLLA (93 J/g) [1], and w is the weight fraction of PLLA in the blends.

3. Results and discussion

3.1. Mechanical properties

The effect of the PDLA-PCL-PDLA or PCDL compatibilizer on tensile properties and impact strength is presented in Fig. 1 and Table S3. Tensile strength decreased with the addition of PCL because of the relatively lower tensile strength of PCL (12.5 MPa) [11] compared to PLLA (74.8 MPa), and inadequate compatibility between PLLA and PCL, in accordance with the literature [11,12]. Elongation at break (ε_b), on the other hand, increased from 12% for neat PLLA to 18% for PLLA/PCL. The tensile strength of PLLA/PCL blends was unaffected with further PCDL addition, and retained at (62.0 ± 1.0) MPa, as shown in Fig. 1a and b. Elongation, however, increased significantly with the PCDL addition, as shown in Fig. 1a, c. PLLA/PCL/PCDL3.5 exhibited ε_b of (43.3 ± 13)%, which was 140% higher than ε_b for PLLA/PCL. The increase in ductility is indicative of compatibilization effect occurred between PLLA and PCL components upon the incorporation of PCDL [6,12]. Impact strength increased from 29.1 J/m in PLLA to (44.0 ± 2.0) J/m of PLLA/PCL blends with or without the incorporation of PCDL (Fig. 1d), attributed to the addition of flexible PCL that acted as an elastomer, consistent with the reported literature [6,10,21].

3.2. Morphology

The cryo-fractured surfaces of uncompatibilized and compatibilized PLLA/PCL blends and PLLA control were observed by SEM (Fig. 2). The SEM micrographs show the representation of a brittle fracture with smooth surfaces in neat PLLA and PLLA/PCL (Fig. 2a and b) [1]. The dispersion of spherical PCL particle in PLLA resembled a sea-island morphology, with a noticeable boundary between PLLA and PCL, as observed in Fig. 2b, indicating the immiscibility of PCL with PLLA [12]. When PCDL was introduced, the fracture surface showed characteristics of higher ductility and impact resistance. PLLA and PCL constituents were emulsified with the inclusion of PCDL, and the boundary between PLLA and PCL phases was no longer noticeable, as shown in Fig. 2c and d, as seen in compatibilized PLLA/PCL blends [12], which confirms improved mutual compatibility.

3.3. Rheological properties

Rheological analysis was used to elucidate the PLLA/PCL interfacial interactions within the prepared blends (Fig. 3). The incorporation of PCL into PLLA decreased the storage modulus (G'), loss modulus (G''), and complex viscosity ($|\eta^*|$), which resulted in a higher MFR value, leading to a smoothed surface appearance in the filament as shown in Fig. 4. G' and G'' increased with increasing PCDL loading, with PLLA/PCL/PCDL3.5 exhibiting higher G' and G'' than PLLA, indicating the enhanced compatibility between PLLA and PCL achieved through the

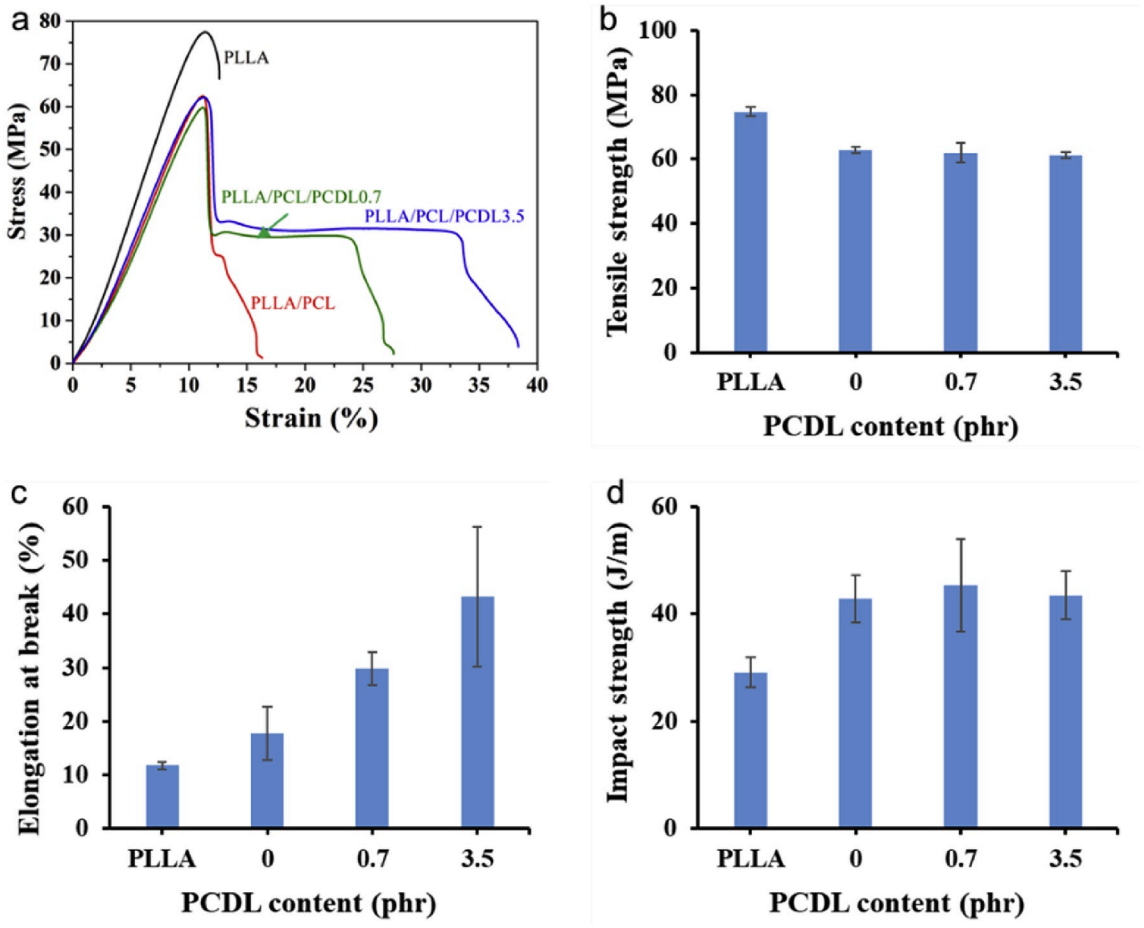

Fig. 1. Mechanical properties of PLLA and PLLA/PCL/PCDL blends, showing: (a) tensile stress-strain curves, (b) tensile strength, (c) elongation-at-break (ε_b) and (d) impact strength as a function of PCDL tri-block copolymer content.

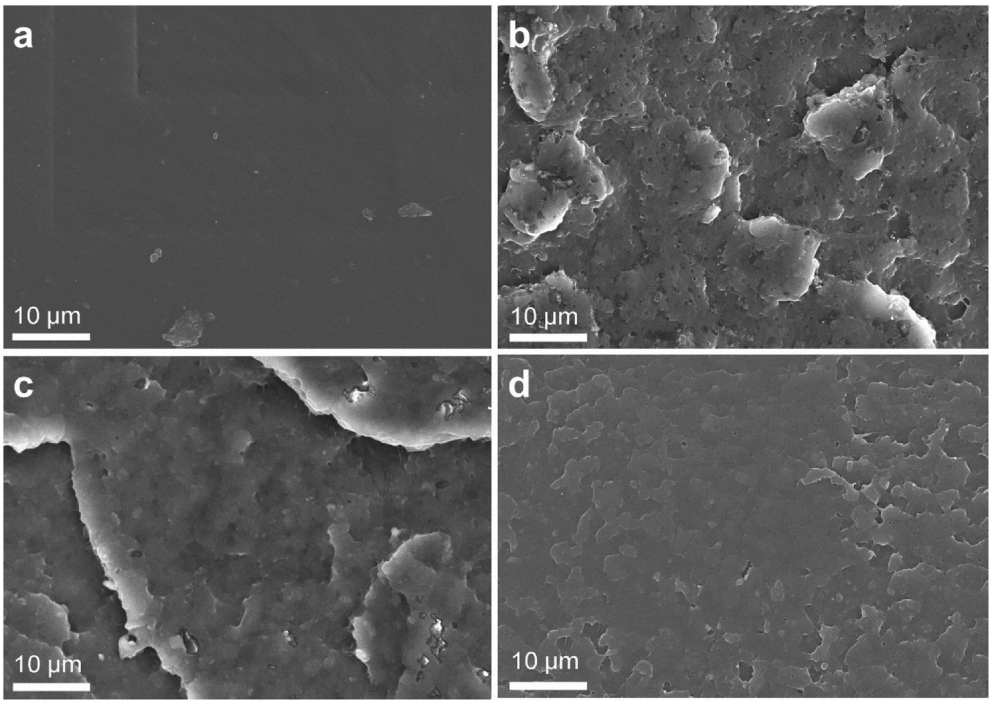

Fig. 2. SEM micrographs of cryo-fractured surfaces of (a) PLLA, (b) PLLA/PCL, (c) PLLA/PCL/PCDL0.7, and (d) PLLA/PCL/PCDL3.5 (all at a magnification of 2000×).

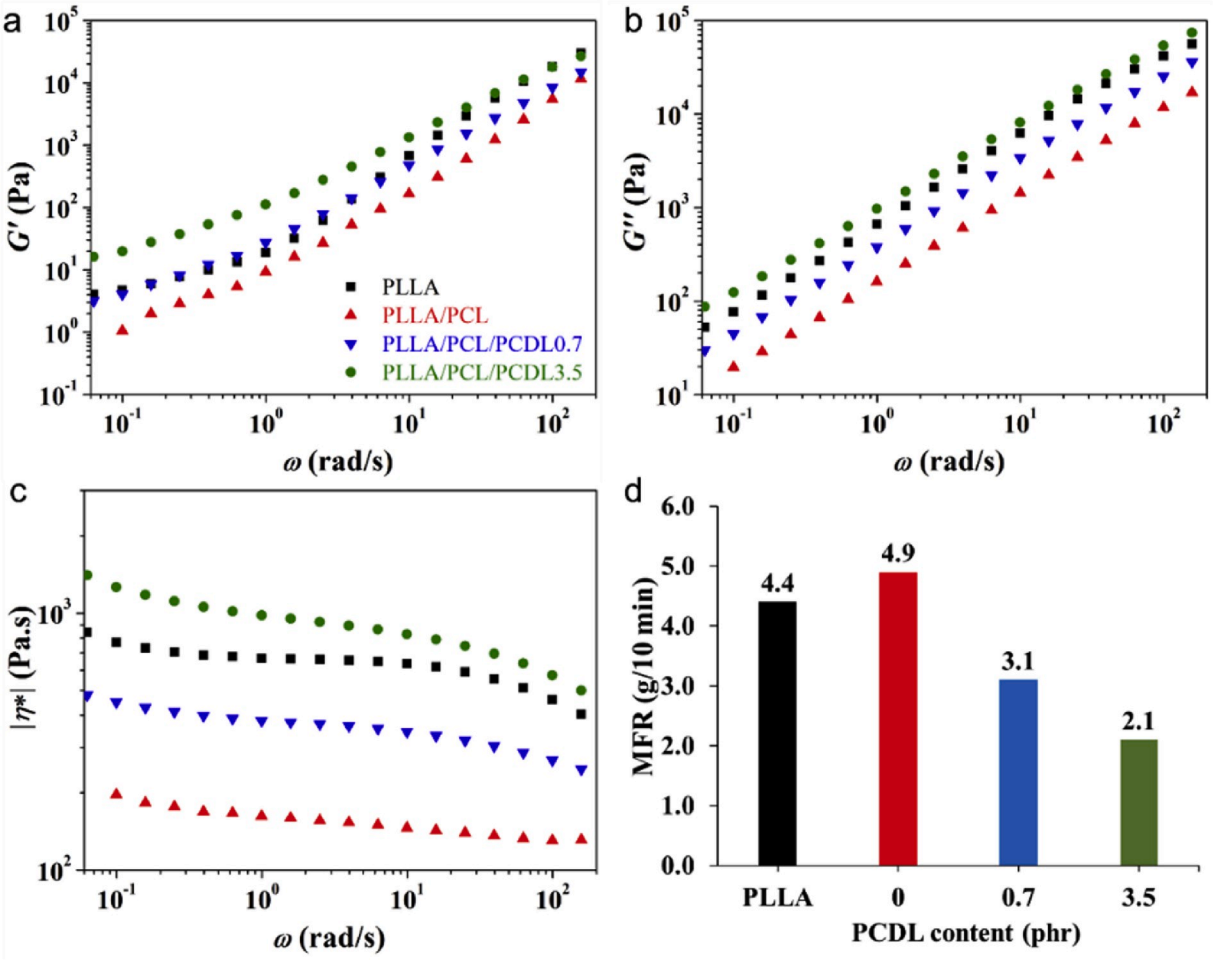

Fig. 3. Rheological behavior of PLLA and PLLA/PCL/PCDL blends, showing (a) G', (b) G'', (c) $|\eta^*|$, and (d) MFR (190°C/2.16 kg, ASTM D 1238, Condition E).

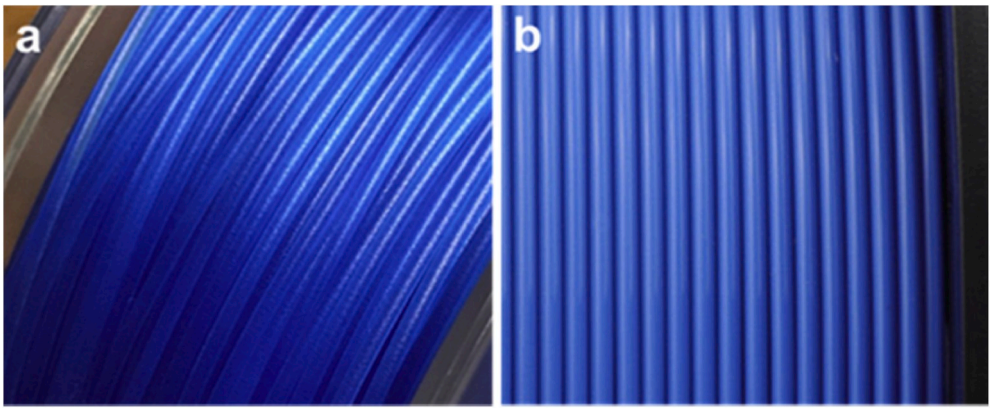

Fig. 4. The visual appearance of (a) PLLA and PLLA/PCL 3D printing filament with a diameter of 1.75 mm.

incorporation of PCDL [21]. $|\eta^*|$ increased with PCDL loading, which is counter-intuitive of PCL-*b*-PLLA diblock copolymer incorporation in PLLA/PCL blend [22], MFR decreased with PCDL content as shown in Fig. 3d, leading to a more stable flow of melt from at nozzle. This increase in $|\eta^*|$ could be attributed to the melt-reinforcement brought about by the underlying crosslinking effect of the stereocomplex crystallites as a rheological modifier [23]. This crosslinking effect enhances the interfacial adhesion between PLLA and PCL, hence increasing the toughness of the PLLA/PCL blend [19].

3.4. Thermal properties

Fig. 5 shows the DSC thermograms of PLLA, PCL and PLLA/PCL/PCDL blends. The T_m of PCL and T_g of PLLA are almost coincident (Fig. 5), thus it is difficult to identify the T_g of PLLA in the blends directly from the thermograms due to an overlap. This overlap causes a practical difficulty in analyzing the effect of PCDL on T_g of PLLA. T_m was 0.2°C and 0.6°C higher in PLLA/PCL/PCDL0.7 and PLLA/PCL/PCDL3.5, respectively compared to PLLA (168.4 °C). PLLA/PCL/PCDL3.5 presented a melting peak at 212°C, demonstrating the formation of stereocomplex crystallites [24], which contribute to the toughness of PLLA/PCL blend as aforementioned. The peak of the stereocomplex crystallite on PLLA/PCL/PCDL0.7 curve was not discernible (Fig. 5), because the melting enthalpy of the stereocomplex crystallite is approx. 1.2 J/g theoretically, which is insignificant compared to the homocrystallite enthalpy (54.2 J/g).

Cold crystallization was not observed on the thermogram of neat PLLA, however, was observed on PLLA/PCL thermogram at 108.6°C, demonstrating PCL facilitated the cold crystallization of PLLA during heating because of the provision of nucleation sites. The degree of crystallinity (X_c) increased from 3.1% to 4.4%, which is attributed to the higher degree of PLLA crystallization [25]. With the addition of PCDL, the cold crystallization temperature (T_{cc}) decreased to 103.7 °C in PLLA/PCL/PCDL0.7, suggesting the inclusion of PCDL enhanced the chain mobility of PLLA [12], thereby improving its cold crystallization. This enhanced chain mobility in PLLA caused by PCDL leads to higher compatibility of PLLA/PCL blend [17].

PLLA in PLLA/PCL/PCDL3.5 recrystallized at 106.6°C, a lower T_{cc} than that of neat PLLA, albeit a relatively higher temperature than in PLLA/PCL/PCDL0.7, consistent with the literature [12,17], where the increase in l-lactide/caprolactone copolymer loading in PLLA/PCL blends hindered the initiation of PLLA cold crystallization because of the increase in lactide segments introduced by the copolymer. X_c increased to 10% for PLLA/PCL/PCDL3.5, which demonstrated the inclusion of copolymer facilitated the crystallization ability of PLLA due to the compatibilization effect of PCDL between PLLA and PCL [12]. Higher crystallinity resulted in lower elongation-at-break [9], which however was improved in PLLA/PCL/PCDL3.5 with higher crystallinity,

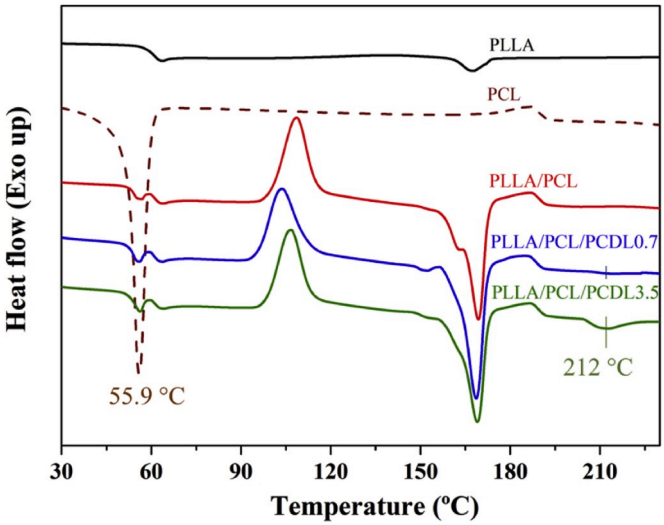

Fig. 5. DSC thermograms of PLLA, PCL, PLLA/PCL and PLLA/PCL/PCDL blends showing a stereocomplex crystallite peak.

confirming the enhanced compatibility between PLLA and PCL through the addition of PCDL.

Overall, the addition of PCDL at 0.7 phr and 3.5 phr brought about lower cold crystallization temperature and higher crystallinity due to the improved compatibility. The addition of PCDL also facilitated the formation of stereocomplex crystallites, which improved the melt viscosity and decreased the melt flow due to the underlying crosslinking effect, hence enhancing the interfacial adhesion, therefore improved the interfacial morphology, and the toughness of PLLA/PCL blends. PLA/PCL/PCDL blends showed noticeable improvements in elongation-at-break with respect to the PLLA control.

4. Conclusions

The toughness of PLLA/PCL blend was enhanced by PDLA-PCL-PDLA or PCDL tri-block copolymer, as supported by the improved ductility, with more than 140% increase in elongation-at-break in PLLA/PCL/PCDL3.5 over the baseline PLLA/PCL blend. The increase in toughness was underpinned by enhanced mutual compatibility between PLLA and PCL caused by PCDL, as demonstrated by the emulsified interface morphology and the formation of stereocomplex crystallites, confirmed through differential scanning calorimetry. The melting viscosity of PLLA/PCL was enhanced by PCDL due to the stereocomplexation, which was confirmed by the melting peak at 212°C. Overall, the PCDL caused a multi-faceted improvement in toughness, ease of processing, and

interfacial compatibility of PLLA/PCL blends.

Declaration of competing interest

The authors declare that they have no known competing financial interests or personal relationships that could have appeared to influence the work reported in this paper.

CRediT authorship contribution statement

Xianglian Xiao: Conceptualization, Methodology, Investigation, Visualization, Writing - original draft. **Venkata S. Chevali:** Visualization, Writing - review & editing. **Pingan Song:** Visualization, Writing - review & editing. **Bin Yu:** Visualization, Writing - review & editing. **Yihu Yang:** Resources. **Hao Wang:** Writing - review & editing, Funding acquisition, Supervision.

Acknowledgements

The Forest and Wood Products Australia [Grant No. PNA360-1516] and China-Australia Institute for Advanced Materials and Manufacturing in Jiaxing University [Grant No. 701170120] supported this work.

Appendix A. Supplementary data

Supplementary data to this article can be found online at https://doi.org/10.1016/j.coco.2020.100385.

References

[1] X. Xiao, V.S. Chevali, P. Song, D. He, H. Wang, Polylactide/hemp hurd biocomposites as sustainable 3D printing feedstock, Compos. Sci. Technol. 184 (2019) 107887.
[2] S. Ran, F. Fang, Z. Guo, P. Song, Y. Cai, Z. Fang, H. Wang, Synthesis of decorated graphene with P, N-containing compounds and its flame retardancy and smoke suppression effects on polylactic acid, Compos. B Eng. 170 (2019) 41–50.
[3] D.-F. Li, X. Zhao, Y.-W. Jia, X.-L. Wang, Y.-Z. Wang, Tough and flame- retardant poly(lactic acid) composites prepared via reactive blending with biobased ammonium phytate and in situ formed crosslinked polyurethane, Compos. Commun. 8 (2018) 52–57.
[4] X. Xiao, V.S. Chevali, H. Wang, Toughening of polylactide/bamboo powder biocomposite for 3D printing, in: ICCM22 2019, Engineers Australia, Melbourne, VIC, 2019, pp. 4927–4934.
[5] Z. Xiong, Y. Zhang, X. Du, P. Song, Z. Fang, Green and scalable fabrication of core–shell biobased flame retardants for reducing flammability of polylactic acid, ACS Sustain. Chem. Eng. 7 (2019) 8954–8963.
[6] G. Maglio, A. Migliozzi, R. Palumbo, B. Immirzi, M.G. Volpe, Compatibilized poly (ε-caprolactone)/poly (l-lactide) blends for biomedical uses, Macromol. Rapid Commun. 20 (1999) 236–238.
[7] M. Heidari-Rarani, M. Rafiee-Afarani, A.M. Zahedi, Mechanical characterization of FDM 3D printing of continuous carbon fiber reinforced PLA composites, Compos. B Eng. 175 (2019).
[8] G. Spinelli, P. Lamberti, V. Tucci, R. Ivanova, S. Tabakova, E. Ivanov, R. Kotsilkova, S. Cimmino, R. Di Maio, C. Silvestre, Rheological and electrical behaviour of nanocarbon/poly(lactic) acid for 3D printing applications, Compos. B Eng. 167 (2019) 467–476.
[9] M. Hu, C. Deng, X. Gu, Q. Fu, J. Zhang, Manipulating the strength–toughness balance of poly(l-lactide) (PLLA) via introducing ductile poly(ε-caprolactone) (PCL) and strong shear flow, Ind. Eng. Chem. Res. 59 (2) (2020) 1000–1009.
[10] H. Bai, H. Xiu, J. Gao, H. Deng, Q. Zhang, M. Yang, Q. Fu, Tailoring impact toughness of poly(L-lactide)/poly(epsilon-caprolactone) (PLLA/PCL) blends by controlling crystallization of PLLA matrix, ACS Appl. Mater. Interfaces 4 (2012) 897–905.
[11] N. López-Rodríguez, A. López-Arraiza, E. Meaurio, J.R. Sarasua, Crystallization, morphology, and mechanical behavior of polylactide/poly(ε-caprolactone) blends, Polym. Eng. Sci. 46 (2006) 1299–1308.
[12] C. Zhang, T. Zhai, L.S. Turng, Y. Dan, Morphological, mechanical, and crystallization behavior of polylactide/polycaprolactone blends compatibilized by l -Lactide/Caprolactone copolymer, Ind. Eng. Chem. Res. 54 (2015) 9505–9511.
[13] M. Harada, K. Iida, K. Okamoto, H. Hayashi, K. Hirano, Reactive compatibilization of biodegradable poly(lactic acid)/poly(ε-caprolactone) blends with reactive processing agents, Polym. Eng. Sci. 48 (2008) 1359–1368.
[14] V. Vilay, M. Mariatti, Z. Ahmad, K. Pasomsouk, M. Todo, Characterization of the mechanical and thermal properties and morphological behavior of biodegradable poly(L-lactide)/poly(ε-caprolactone) and poly(L-lactide)/poly(butylene succinate-co-L-lactate) polymeric blends, J. Appl. Polym. Sci. 114 (2009) 1784–1792.
[15] N.-S. Choi, C.-H. Kim, K.Y. Cho, J.-K. Park, Morphology and hydrolysis of PCL/PLLA blends compatibilized with P(LLA-co-εCL) or P(LLA-b-εCL), J. Appl. Polym. Sci. 86 (2002) 1892–1898.
[16] C. Zhang, Q. Lan, T. Zhai, S. Nie, J. Luo, W. Yan, Melt crystallization behavior and crystalline morphology of polylactide/poly(epsilon-caprolactone) blends compatibilized by lactide-caprolactone copolymer, Polym 10 (2018).
[17] N.-S. Choi, C.-H. Kim, K.Y. Cho, J.-K. Park, Effect of P(lLA-co-εCL) on the compatibility and crystallization behavior of PCL/PLLA blends, J. Appl. Polym. Sci. 77 (1999) 226–231.
[18] Y. Sun, C. He, Biodegradable "core–shell" rubber nanoparticles and their toughening of poly(lactides), Macromolecules 46 (2013) 9625–9633, https://doi.org/10.1021/ma4020615.
[19] S. Ye, T.T. Lin, W.W. Tjiu, P.K. Wong, C. He, Rubber Toughening of Poly (Lactic Acid): Effect of Stereocomplex Formation at the Rubber-Matrix Interface, 2013, pp. 2541–2547, https://doi.org/10.1002/app.38568.
[20] H. Tsuji, T. Yamada, M. Suzuki, S. Itsuno, Blends of aliphatic polyesters. Part 7. Effects of poly(L-lactide-co-ε-caprolactone) on morphology, structure, crystallization, and physical properties of blends of poly(L-lactide) and poly (ε-caprolactone), Polym. Int. 52 (2003) 269–275, https://doi.org/10.1002/pi.1093.
[21] J.S. Jeon, D.H. Han, B.Y. Shin, Improvements in the rheological properties, impact strength, and the biodegradability of PLA/PCL blend compatibilized by electron-beam irradiation in the presence of a reactive agent, Ann. Mater. Sci. Eng. 2018 (2018) 1–8.
[22] S. Xiang, L. Feng, X. Bian, B. Zhang, B. Sun, Y. Liu, G. Li, X. Chen, Toughening modification of PLLA with PCL in the presence of PCL-b-PLLA diblock copolymers as compatibilizer, Polym. Adv. Technol. 30 (2019) 963–972.
[23] Z. Liu, Y. Luo, H. Bai, Q. Zhang, Q. Fu, Remarkably enhanced impact toughness and heat resistance of poly(l -Lactide)/Thermoplastic polyurethane blends by constructing stereocomplex crystallites in the matrix, ACS Sustain. Chem. Eng. 4 (2016) 111–120.
[24] Y. Liu, J. Shao, J. Sun, X. Bian, L. Feng, S. Xiang, B. Sun, Z. Chen, G. Li, X. Chen, Improved mechanical and thermal properties of PLLA by solvent blending with PDLA-b-PEG-b-PDLA, Polym. Degrad. Stabil. 101 (2014) 10–17.
[25] R. Dell'Erba, G. Groeninckx, G. Maglio, M. Malinconico, A. Migliozzi, Immiscible polymer blends of semicrystalline biocompatible components: thermal properties and phase morphology analysis of PLLA/PCL blends, Polymer 42 (2001) 7831–7840, https://doi.org/10.1016/s0032-3861(01)00269-5.

TOUGHENING OF POLYLACTIDE/BAMBOO POWDER BIOCOMPOSITE FOR 3D PRINTING

Xianglian Xiao, Venkata. S Chevali, and Hao Wang

Centre for Future Materials, University of Southern Queensland, Toowoomba QLD 4350, Australia

Keywords: 3D printing, Fused deposition modelling, Polylactide, Bamboo, Toughness

ABSTRACT

3D printing biocomposite feedstock constituted by bio-based polymers and fillers are increasingly gaining prominence for fused deposition modelling. Along with sustainability also emerges the trade-off of reduced toughness and increased brittleness often causing extrusion melt fracture and ensuing effects thereof. Improving biocomposite toughness through impact modifiers is common, and the present work, we investigate a polylactide/bamboo powder system with two toughening agents: poly (butylene adipate-co-terephthalate) combined with ethylene-co-methyl acrylate glycidyl methacrylate terpolymer as the interfacial compatibiliser, and a commercially-available core/shell impact modifier. We melt compounded polylactide/bamboo powder biocomposites, and extruded as a filament, and utilised a commercially available PLA filament as the baseline. The extruded filament was used to print specimens using fused deposition modelling, and for injection moulding. We analysed the thermo-physical and thermo-mechanical properties of the biocomposite, and assessed the filament quality, surface roughness and processability. The polylactide/bamboo powder (20 phr) biocomposites show higher impact toughness than polylactide feedstock for both 3D printed and IM specimens. The poly (butylene adipate-co-terephthalate)-toughened feedstock exhibits higher impact strength and ductility, filament quality, processability, and lower surface roughness than core/shell-modifier-toughened feedstock.

1 INTRODUCTION

Polylactide (PLA)-based biocomposite feedstock for fused deposition modelling (FDM) has gained increasing attention in recent years because of its renewability and sustainability [1]. However, the addition of biomass materials such as bamboo powder (BP) to PLA causes decreased impact strength [2, 3]. PLA/15 wt.% BP decreased impact strength by approx. 44%, compared with neat PLA [3]. Low-impact-strength biocomposite often breaks during extrusion, and 3D printing. Toughness modification through blending with flexible polymers [4-10], which act as stress concentration sites, is a method to improve their resistance to brittleness, and for producing continuous and constant-diameter filaments.

To that end, an acrylic core–shell impact modifier [4, 5], poly (butylene adipate-co-terephthalate) (PBAT) [7], and ethylene-co-methyl acrylate glycidyl methacrylate (EGMA) terpolymer [8] were investigated as toughening agents for PLA-based biocomposites. The addition of 5 wt.% acrylic core–shell impact modifier led to a five-fold increase in the impact strength of PLA, and further enhanced the impact strength of PLA/wood sawdust biocomposites [4]. The evidence of PBAT impact strength enhancement was also observed in ramie/PLA biocomposite [7]. The combination of EGMA, with functional glycidyl methacrylate (GMA) end groups was effective in improving the interfacial adhesion and impact strength of PLA/PBAT blend [9, 10], PLA/BP biocomposite [11], and PLA/biomass biocomposites [8, 12-14].

In this study, PBAT/EGMA and core-shell acrylic impact modifier (BPM 520) were investigated as toughening agents for PLA/20-phr-BP biocomposites for FDM application. The biocomposite feedstock were prepared by melt extrusion and fabricated to standard specimens by both FDM printing and injection moulding. The toughness properties of biocomposites feedstock were compared with commercial PLA feedstock. The effect of toughness agents on viscoelastic behaviour and processability of biocomposites was evaluated. The filament quality and surface quality of 3D-printed

specimens were also assessed. An optimal toughening agent system for PLA/BP biocomposite was obtained through analysis of mechanical performance. This research provides fundamental data on the effect of toughness modification on the biocomposite feedstock, which facilitates the further application in FDM.

2 EXPERIMENTAL

2.1 Materials

PLA (4032D) was obtained from NatureWorks, LLC, USA, and PBAT (2003F, melt flow index (MFI): 4.2 g/10 min at 190 °C/2.16 kg) was supplied by Zhejiang Hangzhou Xinfu Pharm Co., Ltd, China. EGMA (Lotader® AX 8900) was purchased from Arkema, Inc., France. BPM 520 was purchased from Dow Chemical Company, USA. BP with a volume-median-diameter (d_{50}) of 75 μm was supplied by Zhejiang Jinque Bamboo Powder Factory, China. A commercial PLA filament (PLA natural) from Shenzhen Esun Industrial Co., Ltd was used as the baseline for comparison.

2.2 Feedstock preparation

The filament feedstock was obtained using a two-stage process. First, the biocomposites pellets were produced by melt-compounding of (a) PLA, (b) toughening agents, and (c) bamboo powder through a parallel twin-screw extruder with a screw diameter of 35 mm and L/D ratio of 44:1. PLA, PBAT, and bamboo powder (BP) was dried to a moisture level below 0.5 wt. % prior to extrusion. The formulations of the samples were 87 phr/13 phr/20 phr/6 phr for PLA/PBAT/BP/EGMA and 100 phr/20 phr/8 phr for PLA/BP/BPM. The combined PLA/PBAT/EGMA system, and PLA/BPM system were considered as a matrix for their corresponding biocomposites. The extrusion temperature was set to 165 °C – 175 °C along the extruder barrel, and the screw rotational speed was set to 146 rpm. Second, the biocomposite pellets were extruded to filament by a single-screw extruder with a screw diameter of 35 mm and L/D ratio of 28:1. The temperatures of the extrusion barrel zones were set to 170 °C, 175 °C, 175 °C, 180 °C and 180 °C, and the screw rotational speed was set to 364 rpm. The filament was drawn along a water bath maintained at 60 °C, at a drawing speed of 345 rpm (linear velocity was around 36.8 m/min), to achieve a filament diameter of 1.75 mm, which is a standard specification for FDM feedstock.

2.3 Specimen preparation

A 3D da Vinci 1.0 Professional printer (XYZ Printing, Inc., Thailand) with a nozzle diameter of 0.40 mm was used for the fabrication of specimens using 3D CAD models of standard tensile (166 mm × 19 mm × 3.2 mm, Type I, ASTM D 638) and notched impact (63 mm × 12.7 mm × 3.2 mm, ASTM D 256) test specimens. The specimens were printed in a horizontal orientation with the nozzle temperature, heat bed temperature, infill density, layer thickness, and print velocity set at 200 °C, 60 °C, 100 %, 0.15 mm, and 60 mm/s, respectively. IM specimens were prepared using an injection moulding machine (JT-350, Jintong Plastic Machinery Ltd., China) with barrel temperatures set at 165 °C, 175 °C, 175 °C, and 182 °C, and mould temperature set at 45 °C.

2.4 Characterization

Tensile properties of the biocomposites were measured using ASTM D 638 on a CMT 6104 (MTS Systems, China) universal tester at a crosshead speed of 5 mm/min under a 10 kN load cell. Notched Izod impact testing was conducted using ASTM D 256 on a XJJU 5.5 J pendulum (Chengde COTs Scientific Instruments Co., Ltd., China) at room temperature. The testing data are based on an average value of at least five tests. The morphologies of cryo-fractured surfaces of IM specimens and impact fracture surfaces of FDM specimens were examined using a JCM6000 scanning electron microscope

(SEM, JEOL, Japan) at an accelerating voltage of 10 kV. Prior to observation, the fracture surfaces were sputter-coated with a gold layer.

The rheological properties of the biocomposites were investigated using a DHR-2 rheometer (TA Instruments, USA). A parallel plate system with a diameter of 25 mm and a sample gap of 1 mm were used. Tests were conducted in the dynamic frequency sweep mode (0.0628−628 rad/s) with 1% strain, at 190 °C. Melt torque measurements were carried out in an XSS-300 torque rheometer (Shanghai Kechuang Rubber Plastic Mechanical Equipment Co., Ltd., China), the biocomposite pellets were melt extruded through an LSJ 20 plastic extruder with a diameter of 20 mm and L/D of 25:1, the temperatures were set at 150 °C, 170 °C, 175 °C, 175 °C from the feeder to the die, and the extrusion speed was set at 60 rpm.

Filament diameter measurements were performed using a digital Vernier calliper at 3 locations for each position, and the average value was reported. The diameter tolerance was calculated using the difference of the average value and the desired diameter (1.75 mm). Roundness was obtained by subtracting the minimum diameter from the maximum diameter obtained at 3 locations at the same position, based on an industry standard of Shenzhen Esun Industrial Co., Ltd. Stylus method was utilised to determine the surface roughness of the FDM specimens using a MarSurf M 400 unit with a stylus tip diameter of 2 µm, and a tip angle of 90°. The measurements were conducted at a tracing speed of 1.0 mm/s with a trace length of 17.5 mm. Four roughness parameters: arithmetic mean roughness (R_a), root mean square roughness (R_q), mean peak-to-valley height (R_z), and maximum peak-to-valley height (R_{max}), based on ISO 4287 standard.

3 RESULTS AND DISCUSSION

3.1 Mechanical properties

The mechanical properties are summarised in Figure 1. With the addition of toughening agents and bamboo powder, the tensile strength (Figure 1a) of biocomposites decreased compared to PLA as expected, because of the lower tensile strength of toughening agents and weakening effect of the introduction of BP [3]. PLA/BP/PBAT showed a higher elongation at break (Figure 1c) than PLA for both IM and FDM specimens, demonstrating greater ductility than PLA because of the incorporation of toughening agent with high ductility [15]. On the other side, PLA/BP/BPM exhibited lower elongation at break than PLA for both IM and FDM specimens.

The impact strength is shown in Figure 1d. FDM specimens showed higher impact strength than IM specimens. Toughened biocomposites showed higher impact strength than PLA feedstock for both IM and FDM specimens. PLA/BP/PBAT and PLA/BP/BPM IM specimens showed 47% and 15% greater impact strength, and FDM specimens showed 37% and 7% greater impact strength than corresponding PLA feedstock. PLA/BP/PBAT showed an increase in impact strength compared to PLA/BP/BPM for both IM and FDM specimens, demonstrating the higher toughness of PLA/BP/PBAT, compared with PLA/BP/BPM, attributed to the synergistic effect of both PBAT and reactive EGMA.

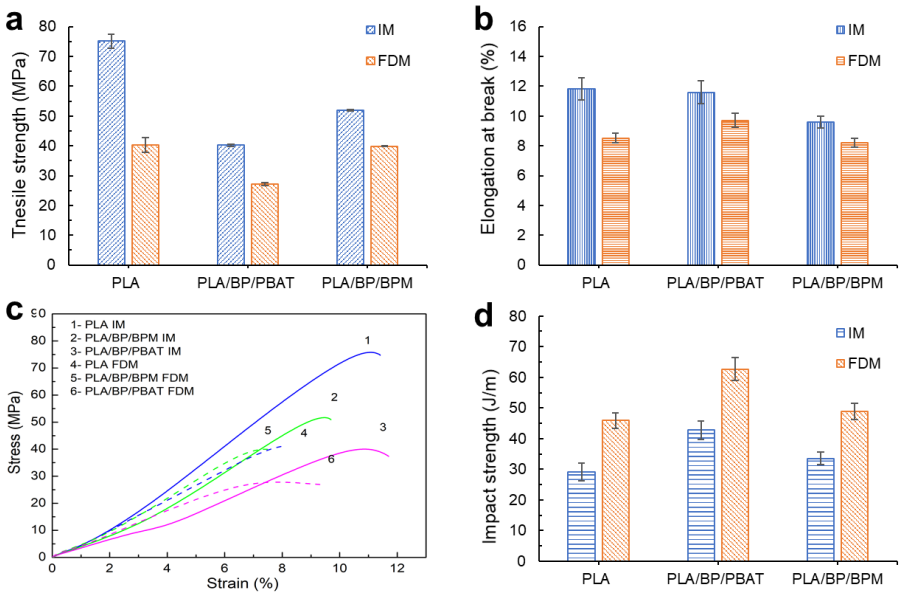

Figure 1: Mechanical properties of biocomposites: (a) tensile strength, (b) elongation at break, (c) representative tensile stress-strain curves, and (d) impact strength.

3.2 Fracture morphology

The SEM images for impact fracture surface of FDM specimens and cryo-fractured surfaces of IM specimens are shown in Figure 2. IM specimens showed smoother fracture surfaces than FDM specimen, indicating higher brittleness of IM specimens, compared with FDM sample, which attributed the higher impact strength for FDM specimens against IM specimens. The biocomposites specimens showed ductile deformation as fibrils can be observed on the surfaces, contributing to the higher toughness of biocomposites than PLA. Fibre pull-out and debonding of BP filler from the matrix were observed on the fracture surfaces, indicating the interfacial bonding between bamboo powder and polymer matrix was lower than the internal strength of BP filler, the interfacial bonding was insufficient to provide satisfactory filler-matrix stress transfer [16].

Further BP filler pull-out and debonding from the polymer matrix of PLA/BP/BPM FDM specimen than PLA/BP/PBAT were observed, indicating enhanced interfacial adhesion between BP and PLA/PBAT matrix due to the existence of reactive GMA group, resulting in lower impact strength and elongation at break for PLA/BP/BPM than PLA/BP/PBAT. The PLA/BP/BPM IM specimen showed a lower filler-matrix adhesion because of discernible porosity between bamboo filler and matrix, leading to the lower impact strength than PLA/BP/PBAT [16].

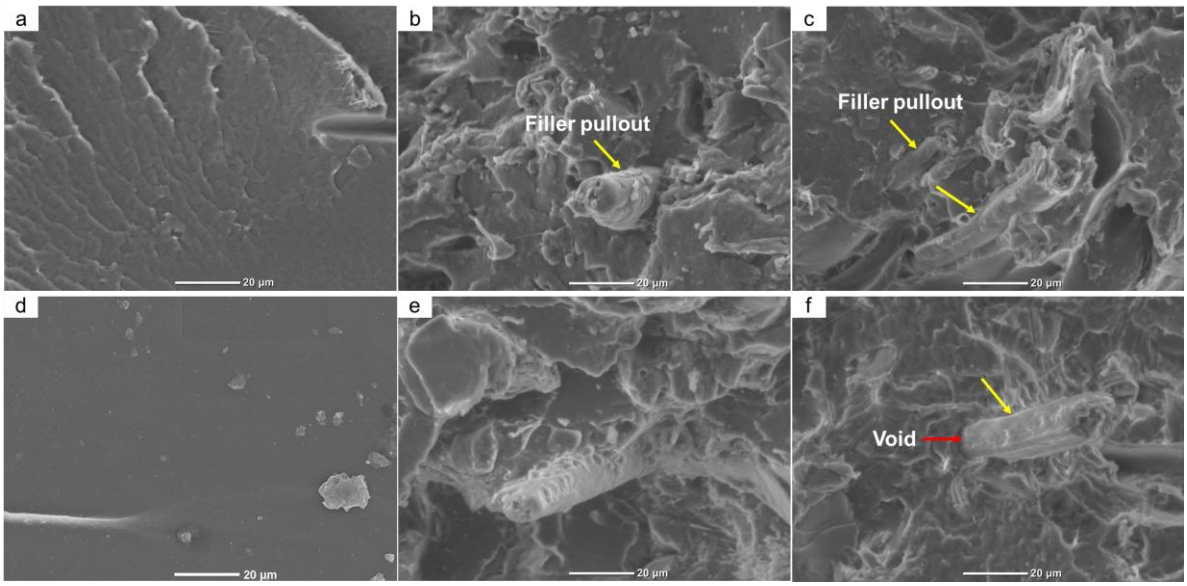

Figure 2: SEM images of impact fracture surfaces of: (a) PLA, (b) PLA/BP/PBAT, and (c) PLA/BP/BPM FDM specimens, and cryo-fractured surfaces of (d) PLA, (e) PLA/BP/PBAT, and (f) PLA/BP/BPM IM specimens.

3.3 Rheological and melt flow behaviour

The rheological properties of biocomposites are shown in Figure 3. The biocomposites showed shear-thinning behaviour (Figure 3b) and lower complex viscosity than PLA at a frequency between 0.4 rad/s and 25 rad/s. The shear-thinning behaviour can be utilized to reduce viscosity and obtain improved melt flow than PLA by adjusting the material throughput and the diameter of 3D printer nozzle [17]. The higher complex viscosity at low frequency are desired for holding the form of filament during extrusion [17]. PLA/BP/PBAT showed increased complex viscosity in the molten state than PLA/BP/BPM, indicating higher melt strength, and steadier extrusion during filament processing, which is advantageous to obtain a filament with consistent diameter and roundness [18]. There was no significant difference in storage (elastic) modulus and loss (viscous) modulus between PLA/BP/PBAT and PLA/BP/BPM, indicating the similar viscoelastic behaviour and mobility of polymer chains in the two biocomposites.

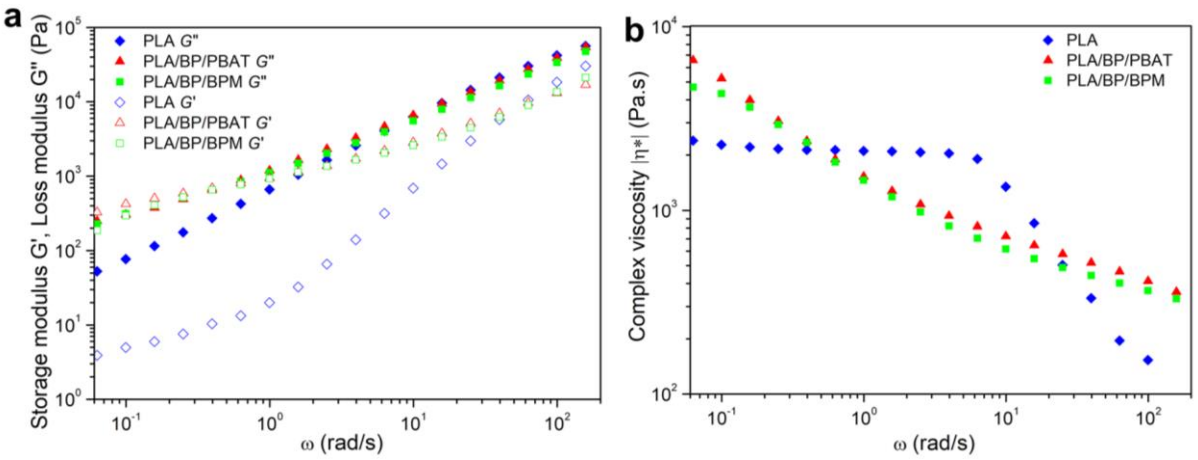

Figure 3: Dynamic frequency sweep plots for biocomposites: (a) storage modulus and loss modulus, (b) complex viscosity as a function of angular frequency at 190 °C.

The melt viscosity for a stabilized morphology were determined by the steady-state melt torque. Figure 4 shows the torque-rheometer plots as a function of time. PLA/BP/PBAT showed a lower melt torque than PLA/BP/BPM, indicating that less energy was required [19] during the process and better processability for PLA/BP/PBAT. The result was in accordance with the MFI (190 °C, 2.16 kg) results of 2.05 g/10 min for PLA/BP/PBAT and 1.55 g/10 min for PLA/BP/BPM.

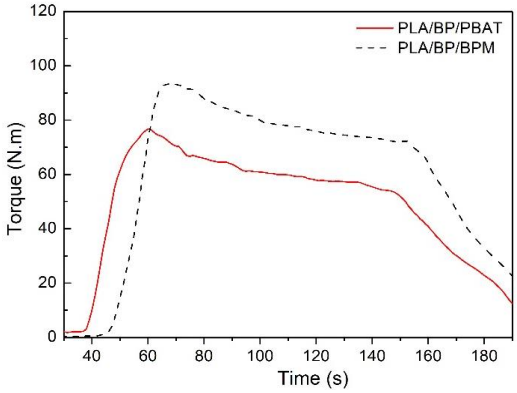

Figure 4: Melt torque versus time for processing biocomposites.

3.4 3D printing analysis

The filament diameter tolerance and roundness are shown in a box chart, as shown in Figure 5a, b. PLA/BP/PBAT filament exhibited a diameter tolerance and roundness at -0.05~0.04 mm and 0~0.02 mm respectively, demonstrating better quality than corresponding -0.14~0.13 mm and 0~0.06 mm of PLA/BP/BPM filament, because of the relatively higher complex viscosity of PLA/BP/PBAT biocomposite [18]. The surface roughness of FDM-printed specimens was determined and compared in Figure 5d. PLA/BP/BPM parts showed a higher surface roughness with higher value in R_a, R_q, R_z, and R_{max} than PLA/BP/PBAT parts, in agreement with the surface roughness as shown in Figure 5c.

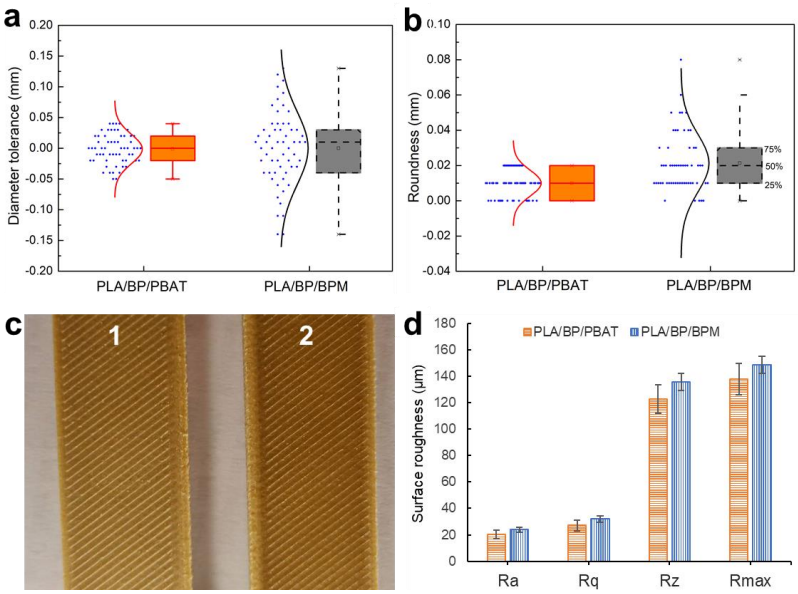

Figure 5: (a) Diameter tolerance, (b) roundness of PLA/BP/PBAT and PLA/BP/BPM filament, (c) 3D printed specimens (1-PLA/BP/PBAT, 2-PLA/BP/BPM), and (d) surface roughness of FDM-printed PLA/BP/PBAT and PLA/BP/BPM specimens.

4. CONCLUSIONS

PBAT/EGMA and BPM520 were used to improve the toughness of PLA/BP biocomposites and investigated the effect on the properties of PLA/BP biocomposites for FDM application. PLA/BP/PBAT and PLA/BP/BPM feedstock was prepared and compared with commercial PLA feedstock. The biocomposites showed higher impact strength than PLA. PLA/BP/PBAT showed highest ductility and impact strength for both IM and FDM products and possessed higher filament quality, smoother surface of FDM-printed parts, and better processability than PLA/BP/BPM. The results showed that PLA/BP/PBAT was a better material for FDM application than PLA/BP/BPM.

ACKNOWLEDGEMENTS

This work was supported by the Forest and Wood Products Australia [Grant # PNA360-1516] and China-Australia Institute for Advanced Materials and Manufacturing in Jiaxing University under Grant No. 701170120. The support received from Shenzhen Esun Industrial Co., Ltd is also appreciated.

REFERENCES

[1] N.A. Nguyen, C.C. Bowland, A.K. Naskar, A general method to improve 3D-printability and inter-layer adhesion in lignin-based composites, *Applied Materials Today*, **12**, 2018, pp. 138-152 (doi: 10.1016/j.apmt.2018.03.009).

[2] R. Tokoro, D.M. Vu, K. Okubo, T. Tanaka, T. Fujii, T. Fujiura, How to improve mechanical properties of polylactic acid with bamboo fibers, *Journal of Materials Science*, **43**(2), 2007, pp. 775-787 (doi: 10.1007/s10853-007-1994-y).

[3] X.-y. Song, M. Wang, Y.-x. Weng, Z.-g. Huang, Effect of Bamboo Flour Grafted Lactide on the Interfacial Compatibility of Polylactic Acid/Bamboo Flour Composites, *Polymers*, **9**(12), 2017, pp. 323 (doi: 10.3390/polym9080323).

[4] N. Petchwattana, S. Covavisaruch, Mechanical and morphological properties of wood plastic biocomposites prepared from toughened poly (lactic acid) and rubber wood sawdust (Hevea brasiliensis), *Journal of Bionic Engineering*, **11**(4), 2014, pp. 630-637 (doi: 10.1016/S1672-6529(14)60074-3).

[5] X. Xiao, Study on mechanical properties of two kinds of impact modifiers toughening PLA, *Plastics science and technology*, **42**(8), 2014, pp. 88-90. (in Chinese)

[6] X. Xiao, Q. Duan, Study on toughening modification of PBC with PLA, *Plastic Additives*, (3), 2016, pp. 63-66 (doi: 10.3969/j.issn.1672—6294.2016.03.013). (in Chinese)

[7] T. Yu, Y. Li, Influence of poly(butylenes adipate-co-terephthalate) on the properties of the biodegradable composites based on ramie/poly(lactic acid), *Compos. Pt. A-Appl. Sci. Manuf*, **58**, 2014, pp. 24-29 (doi: 10.1016/j.compositesa.2013.11.013).

[8] M. Hao, H. Wu, Z. Zhu, In situ reactive interfacial compatibilization of polylactide/sisal fiber biocomposites via melt-blending with an epoxy-functionalized terpolymer elastomer, *RSC Adv*, **7**(51), 2017, pp. 32399-32412 (doi: 10.1039/c7ra03513f).

[9] N. Wu, H. Zhang, Mechanical properties and phase morphology of super-tough PLA/PBAT/EMA-GMA multicomponent blends, *Materials Letters*, **192**, 2017, pp. 17-20 (doi: 10.1016/j.matlet.2017.01.063).

[10] M. Kumar, S. Mohanty, S.K. Nayak, M. Rahail Parvaiz, Effect of glycidyl methacrylate (GMA) on the thermal, mechanical and morphological property of biodegradable PLA/PBAT blend and its nanocomposites, *Bioresour Technol*, **101**(21), 2010, pp. 8406-15 (doi: 10.1016/j.biortech.2010.05.075).

[11] Y.-n. Wang, Y.-x. Weng, L. Wang, Characterization of interfacial compatibility of polylactic acid and bamboo flour (PLA/BF) in biocomposites, *Polymer Testing*, **36**, 2014, pp. 119-125 (doi: 10.1016/j.polymertesting.2014.04.001).

[12] B.A. Khan, V.S. Chevali, H. Na, J. Zhu, P. Warner, H. Wang, Processing and properties of antibacterial silver nanoparticle-loaded hemp hurd/poly(lactic acid) biocomposites, *Composites Part B: Engineering*, **100**, 2016, pp. 10-18 (doi: 10.1016/j.compositesb.2016.06.022).

[13] B.A. Khan, H. Na, V. Chevali, P. Warner, J. Zhu, H. Wang, Glycidyl methacrylate-compatibilized poly (lactic acid)/hemp hurd biocomposites: Processing, crystallization, and thermo-mechanical response, *Journal of Materials Science & Technology*, **34**(2), 2018, pp. 387-397 (doi: 10.1016/j.jmst.2017.03.004).

[14] Y. Bin, B. Yang, H. Wang, The effect of a small amount of modified microfibrillated cellulose and ethylene–glycidyl methacrylate copolymer on the crystallization behaviors and mechanical properties of polylactic acid, *Polymer Bulletin*, **75**(8), 2017, pp. 3377-3394 (doi: 10.1007/s00289-017-2215-8).

[15] Krishnan, S., Pandey, P., Mohanty, S. and Nayak, S.K., Toughening of polylactic acid: an overview of research progress, *Polymer-Plastics Technology and Engineering*, **55**(15), 2016, pp.1623-1652 (doi: 10.1080/03602559.2015.1098698).

[16] Feng, J.; Sun, Y.; Song, P.; Lei, W.; Wu, Q.; Liu, L.; Yu, Y.; Wang, H., Fire-Resistant, Strong, and Green Polymer Nanocomposites Based on Poly(lactic acid) and Core–Shell Nanofibrous Flame Retardants. ACS Sustainable Chemistry & Engineering 2017, **5**(9), 7894-7904 (doi: org/10.1021/acssuschemeng.7b01430).

[17] Nguyen, N.A., Barnes, S.H., Bowland, C.C., Meek, K.M., Littrell, K.C., Keum, J.K. and Naskar, A.K., A Path for Lignin Valorization via Additive Manufacturing of High-Performance Sustainable Composites with Enhanced 3D Printability, *Science advances*, **4**(12) , 2018, pp. eaat4967 (doi: 10.1126/sciadv.aat4967).

[18] Alzahrani, M., 2017. Modification of recycled poly (ethylene terephthalate) for FDM 3D-printing applications (Master's thesis, University of Waterloo).

[19] E. Freire, O. Bianchi, E. E. C. Monteiro, R. C. Reis Nunes and M. C. Forte, Processability of PVDF/PMMA blends studied by torque rheometry, *Materials Science and Engineering: C* **29**(2), 2009, pp. 657-661 (doi:10.1016/j.msec.2008.12.025).